IMPROVED THERMAL ENERGY UTILIZATION THROUGH COUPLED AND CASCADED COOLING CYCLES

A Thesis
Presented to
The Academic Faculty

by

Ashlie M. Brown

In Partial Fulfillment
Of the Requirements for the Degree
Master of Science in the
School of Engineering

Georgia Institute of Technology

December 2009

Improved Thermal Energy Utilization through Coupled and Cascaded Cooling Cycles

Approved by:

Dr. Srinivas Garimella, Advisor
College of Engineering
Georgia Institute of Technology

Dr. Sheldon Jeter
College of Engineering
Georgia Institute of Technology

Dr. Samuel Graham
College of Engineering
Georgia Institute of Technology

Date Approved: November 13, 2009

To my parents, JoEtta and Daryl Brown, for championing my cause.

ACKNOWLEDGEMENTS

I would like to thank Dr. Srinivas Garimella, director of the Sustainable Thermal Systems Laboratory at the Georgia Institute of Technology, for providing this research opportunity and serving as my advisor. I would also like to thank Dr. Sheldon Jeter and Dr. Samuel Graham for serving on my thesis committee and supporting me through the final stage of the thesis preparation.

Throughout this endeavor, the members of the Sustainable Thermal Systems Laboratory have provided advice and support beyond expectation; I am grateful for the opportunity to learn from and work with each of them. I would especially like to thank Brendon Keinath for exceptional reliability through many long hours and Vishwanath Subramaniam for endless encouragement and wisdom. I owe my deepest gratitude to Anand Nagavarapu, who freely contributed his time and expertise at many critical moments.

TABLE OF CONTENTS

LIST OF TABLES

LIST OF FIGURES

LIST OF SYMBOLS

A	Area, m^2
CAT	closest approach temperature, °C
COP	coefficient of performance
c_p	specific heat at constant pressure, J/kg-K
GAX	generator/absorber heat exchange
GWP	global warming potential
h	specific enthalpy, kJ/kg
LMTD	log mean temperature difference
m	mass flow rate, kg/s
ODP	ozone depletion potential
ORC	organic Rankine cycle
Q	thermal energy transfer, W
q	quality
p	pressure, kPa
RHX	refrigerant heat exchanger
s	specific entropy, kJ/kg-K
SHX	solution heat exchanger
T	temperature, °C
U	overall heat transfer coefficient, W/m^2
v	specific volume, m^3/kg
VOC	volatile organic compound

VX	vapor exchange
W	work input, W
x	LiBr mass fraction (kg LiBr/kg solution)

Greek Letters

ΔT	temperature differential, °C
η	efficiency
ω	humidity ratio

Subscripts

1 to 47	corresponding state points on appropriate diagrams
abs	absorber
all,electric	combined, electric input
all,energy	combined, total energy input
cond	condenser
desup	desuperheat
evap	evaporator
HCLD	high condenser/low desorber
HX	heat exchanger
HSHX	high-temperature solution heat exchanger
max	maximum
min	minimum
RHX	refrigerant heat exchanger

sat	saturation
SHX	solution heat exchanger
sub	subcool
sup	superheat
T	temperature

SUMMARY

Limited worldwide energy supplies demand the improved utilization of thermal energy, which is the dominant form of all primary energy sources used today. Large quantities of waste heat are routinely exhausted wherever thermo-mechanical energy conversion occurs, providing an obvious opportunity to improve utilization. Two waste-heat-driven cycles are analyzed: an absorption/compression cascade cooling cycle and a coupled Rankine/compression cycle. The absorption/compression cascade provides an environmentally-sound option not previously reported in the literature for low-temperature cooling using absorption cycles driven by waste heat. To achieve cooling at temperatures below 0ºC, ammonia-water is the overwhelming choice for the working fluid. However, concerns about the toxicity and flammability of ammonia sometimes limit its application in sensitive arenas. In this study, a lithium bromide-water absorption cycle is coupled with a carbon dioxide vapor compression cycle to realize the benefits of high-lift cooling without the concerns associated with ammonia. A waste heat stream at temperatures as low as 150°C is used to drive a Lithium Bromide/Water absorption cycle that generates evaporating water at about 5ºC. This evaporation is conducted in two components, one to directly provide chilled water. In the other evaporator, the water is evaporated using heat of condensation from a bottoming carbon dioxide vapor-compression cycle. This bottoming cycle in turn generates evaporating carbon dioxide at temperatures as low as -40°C. The topping absorption cycle achieves coefficients of performance (COPs) of about 0.77, while the bottoming cycle achieves a COP of about 2.2. The overall absorption/compression cascade cycle achieves a COP of 5.685 when

considering only electric power input. The coupled Rankine/compression cycle provides a mechanical expansion and compression approach to achieve thermally activated cooling, again driven by waste heat. The power produced in the turbine of the Rankine cycle is directly coupled to the compressor of a vapor-compression cooling cycle to generate cooling to be utilized for space-conditioning. In addition to the integrated turbo-compressor, the condensers of the power producing Rankine cycle and the bottoming vapor compression cycle are consolidated into one component to reduce the overall number of components required to achieve cooling from waste heat. The refrigerant R245fa is used throughout this cycle. Even with low grade waste heat sources (125°C), a Rankine cycle efficiency of about 10 percent can be achieved. When coupled to the bottoming compression cycle with a COP of about 2.7, this yields an overall waste heat-to-cooling conversion efficiency of about 32 percent at nominal conditions.

INTRODUCTION

The continuing rise in carbon-based energy utilization worldwide and the corresponding global climate change implications constitute the defining problem facing humankind today. Faced with this realization, the key question is not just finding new sources, but rather to ask, "How are the available energy sources *used*?" Two-thirds of the energy consumed nationally for electricity generation is wasted in conversion losses [1] (Fig. 1). It is obvious that energy demand will rise. Even if alternative energy technologies advance at the same rate as demand (an understated feat), fossil fuel input will, at best, remain constant. The most promising route to fossil fuel use reduction is to limit or reduce end use demand [18]. Revolutionary changes in energy *utilization* paradigms are clearly needed.

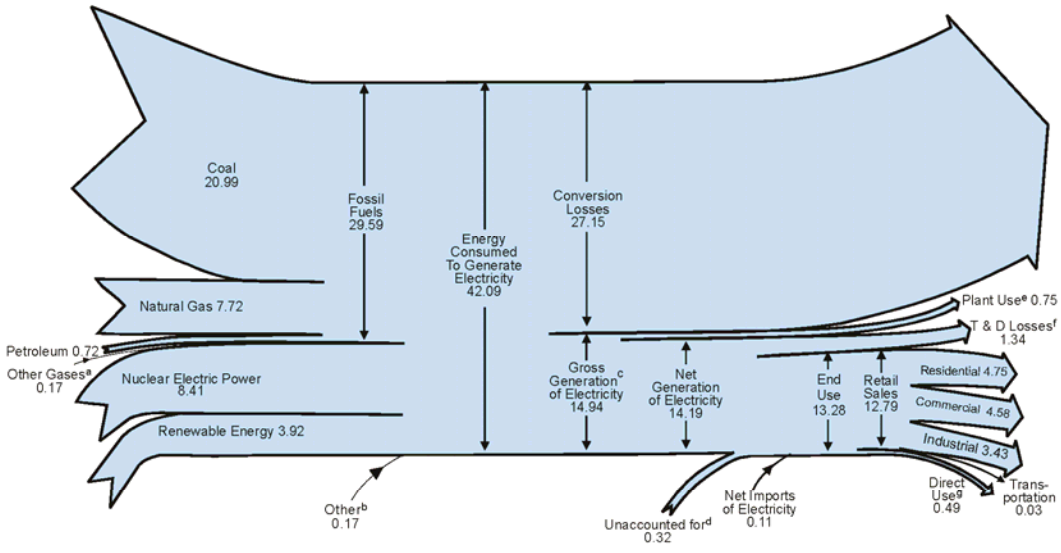

[a] Blast furnace gas, propane gas, and other manufactured and waste gases derived from fossil fuels.
[b] Batteries, chemicals, hydrogen, pitch, purchased steam, sulfur, miscellaneous technologies, and non-renewable waste (municipal solid waste from non-biogenic sources, and tire-derived fuels).
[c] Estimated as net generation divided by 0.95.
[d] Data collection frame differences and nonsampling error. Derived for the diagram by subtracting the "T & D Losses" estimate from "T & D Losses and Unaccounted for" derived from Table 8.1.
[e] Electric energy used in the operation of power plants, estimated as 5 percent of gross generation.
[f] Transmission and distribution losses (electricity losses that occur between the point of generation and delivery to the customer) are estimated as 9 percent of gross generation.
[g] Use of electricity that is 1) self-generated, 2) produced by either the same entity that consumes the power or an affiliate, and 3) used in direct support of a service or industrial process located within the same facility or group of facilities that house the generating equipment. Direct use is exclusive of station use.
Notes: • Data are preliminary. • See Note, "Electrical System Energy Losses," at the end of Section 2. • Values are derived from source data prior to rounding for publication. • Totals may not equal sum of components due to independent rounding.
Sources: Tables 8.1, 8.4a, 8.9, and A6 (column 4).

Fig. 1. 2007 Energy-to-Electricity Flow Data (Quadrillion Btu) [1].

Effective strategies to reduce energy consumption must rely on principles applicable to a wide range of situations. Thermal energy sources – oil, gas, coal, nuclear, some renewable – constitute over 93% of the primary energy supply in the US [19]. Thermodynamic laws governing the utilization of these sources dictate that a significant amount of input energy is rejected as heat. Efficiency improvements can nominally decrease heat rejected from individual processes. However, a far better strategy is to *avoid* rejecting heat by rearranging energy use worldwide so that reject heat from one process drives the next until the lowest grade energy is all that is discarded. Coupled and cascaded cooling cycles represent one example of a transformational approach to achieve this goal.

1.1 ENERGY SYSTEMS CASCADES

Cascading energy use across the entire temperature spectrum implies progressively using higher temperature processes as heat sources for lower temperature processes to thoroughly exhaust each unit of expended energy. Consider an idealized energy conversion cycle (Carnot cycle), represented by the temperature-entropy diagram in Fig. 2 (a). Energy is supplied to the cycle by the addition of heat (Process AB) and work (Process DA), and the cycle discards energy in the form of rejected heat (Process CD) and supplies work output (Process BC). The area ABCD represents the net work produced by the cycle and the area CDEF represents the amount of thermal energy rejected by the cycle. The cycle work output is usually fully utilized, while the thermal energy output is generally discarded and lost. In contrast, part (b) of Fig. 2 depicts additional cycles utilizing the discarded thermal energy. The heat rejected from the condenser of the high-temperature cycle provides heat to boil the working fluid in the

evaporator of the medium-temperature cycle. Likewise, the heat rejected from the medium-temperature cycle is used in the low-temperature cycle. Fluid properties and thermodynamics laws must be taken into account when designing such cascading cycles, but this approach does present the opportunity to progressively use external input energy for multiple uses down to the dead state. Such cascading of several processes under each high temperature thermal source can considerably improve overall thermal energy utilization efficiency.

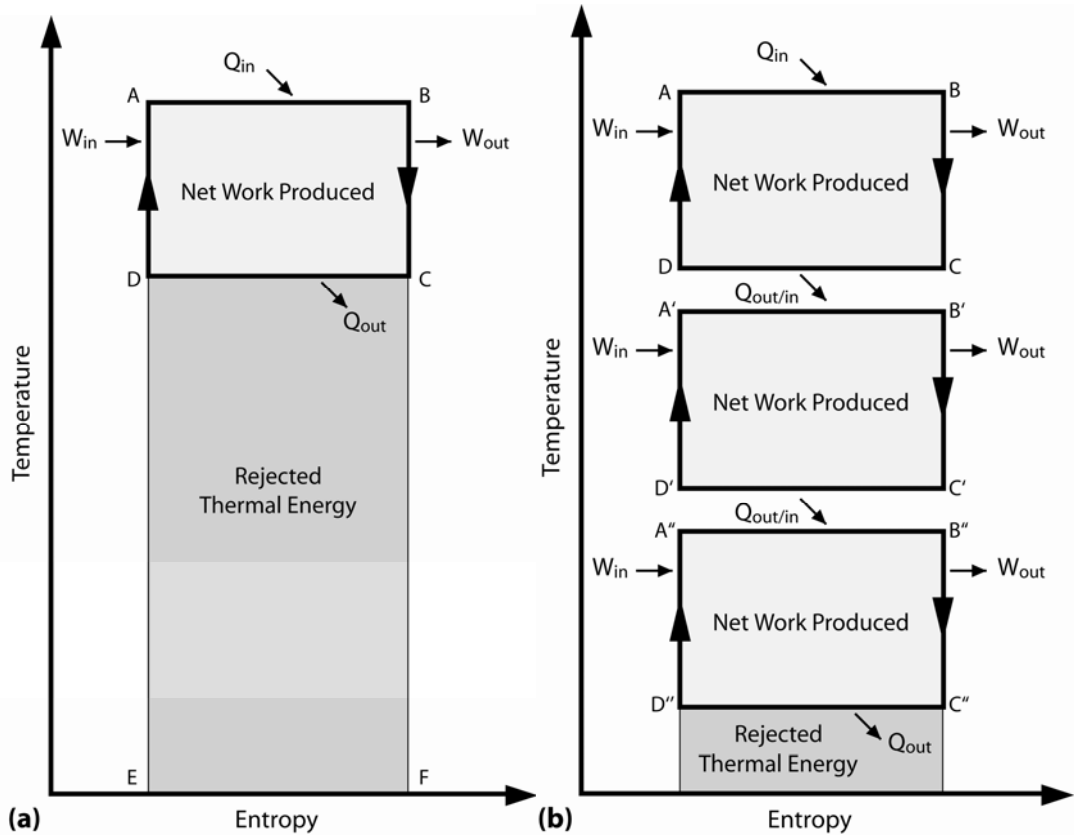

Fig. 2. Increased thermal energy utilization through cascaded energy systems.

Stationary power plants typically utilize evaporative cooling or once-through cooling systems, thereby maintaining low condenser temperatures and reducing the thermal energy rejected from the cycle. In these cases, the opportunity for cascaded

thermal energy utilization is primarily in the combustion exhaust stream rather than the heat rejected from the condenser. The thermal energy remaining in the flue gas can be used to drive cycles operating at temperatures lower than those in the main power cycle but higher than those at the condenser.

In a variety of applications, especially those in mobile cooling, residential energy systems, and others, combustion is used to provide space conditioning and water heating, whereas heat rejected from a different process could be used to drive these systems. Each application must be considered individually to identify opportunities for cascaded energy utilization.

1.2 HEAT-DRIVEN CYCLES

Techniques of waste heat recovery were considered and investigated even as early as the 19th century. Rudimentary implementations of the cascade systems described in section 1.1 include cogeneration plants, which, for example, already produce half of Denmark's electricity, contributing to its energy self-sufficiency [20]. The same techniques experienced popularity throughout the world in the 1920s and 1970s, but did not enjoy the sustained success they saw in Denmark [21]. Most of these techniques utilize discarded heat through heat-driven cycles, such as the absorption or Rankine cycles. The cascaded and coupled cycles in this study are based on an absorption cycle and a Rankine cycle, so the basic characteristics of each will be briefly discussed here.

1.2.1 Absorption Cycle

Absorption machines were first built in the mid-1800s for refrigeration purposes [22]. Near the turn of the 20th century, the spreading popularity of distributed electricity and the invention of the electricity-driven vapor-compression machines quickly relegated

absorption machines to niche markets. Absorption technology has historically experienced resurgences in popularity when energy resources are scarce, but has yet to compete with vapor-compression in the refrigeration market due to the convenience and low expense of electricity. However, absorption is particularly suited to the waste heat recovery sector and will likely become more popular as waste heat recovery techniques enjoy wider use.

A simple absorption cycle is shown in Fig. 3. Throughout the history of absorption, several refrigerant working pairs have been considered but only two are popularly used: ammonia-water (NH_3-H_2O) and water-lithium bromide (H_2O-LiBr). Here we will examine a machine using H_2O-LiBr because the system under consideration in this thesis also uses H_2O-LiBr. This diagram has been laid out on a pressure-temperature scale to emphasize the two cycle pressures and three cycle temperatures. Typical pressures for this cycle are about 10 kPa for the high pressure and 0.5 kPa for the low pressure. Typical temperatures are around 2°C, 40°C, and 100°C for the low, medium, and high temperatures, respectively.

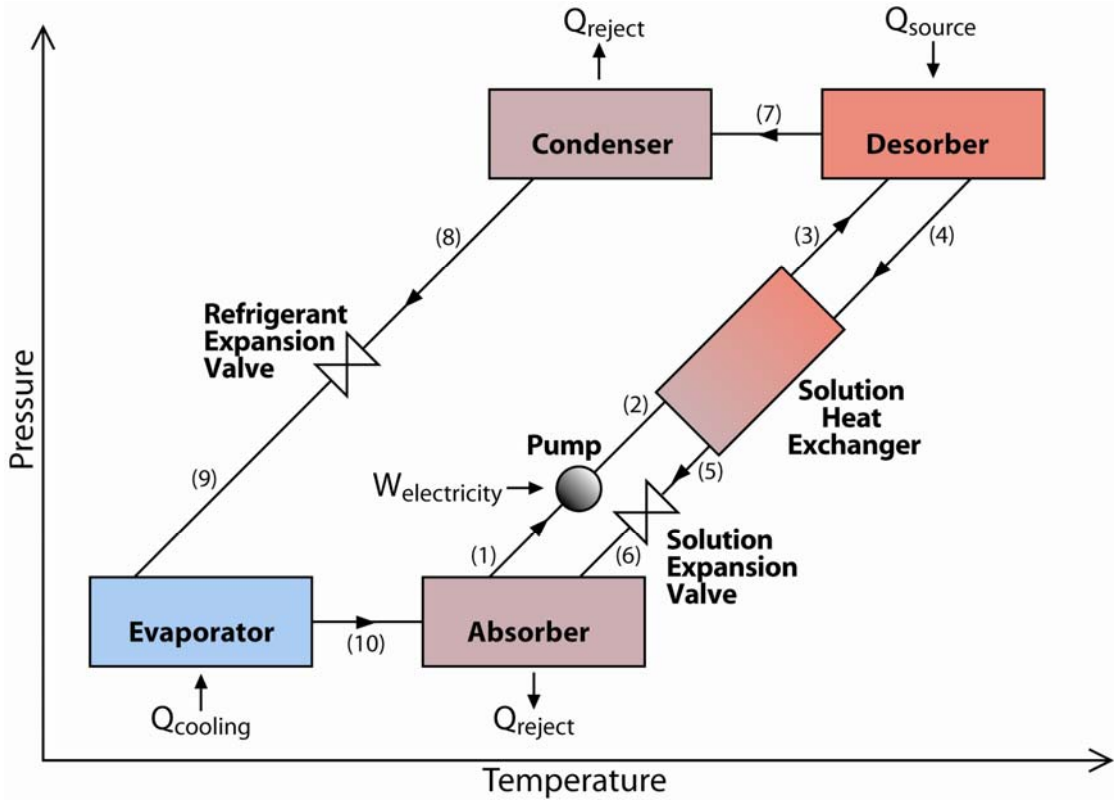

Fig. 3. Single-effect water/lithium bromide absorption chiller.

In this single-effect H_2O-LiBr absorption chiller, the absorber operates at the cycle low pressure and medium temperature. A solution of refrigerant (H_2O) and salt (LiBr) exits the absorber at its most dilute state, labeled on the diagram as state point 1. This dilute solution is pumped to the cycle high pressure, state 2, and often enters a solution heat exchanger. The solution heat exchanger is used to raise the temperature of the rich solution, from state 2 to state 3, before it enters the desorber. This pre-heating decreases the load required from the external heat source to evaporate the refrigerant from the solution, potentially improving system performance. In the desorber, some of the refrigerant (H_2O) is evaporated out of the salt solution, represented by state 7. The remaining concentrated solution, state 4, returns to the solution heat exchanger to provide heat to the dilute solution stream (state 2 to state 3). The cooled concentrated solution,

state 5, is expanded across the solution expansion valve to the cycle low pressure, state 6, and returns to the absorber. The desorbed refrigerant stream is cooled to a liquid state in the condenser, state 8, before being expanded across the refrigerant expansion valve to the cycle low pressure and low temperature (state 9). The refrigerant is evaporated at the cycle low temperature while supplying the desired cooling load and returns to the absorber, state 10, to be reabsorbed into the concentrated solution, state 6.

The two main differences from the H_2O-LiBr cycle found in a NH_3-H_2O machine are significantly higher cycle pressures and the addition of a rectifier downstream of the desorber. Typical cycle pressures for a NH_3-H_2O cycle are on the order of 200-500 kPa and 1200-2100 kPa for the low and high side pressures, respectively, depending on the desired cooling load and the heat source temperature. The vapor pressure of water is close enough to the vapor pressure of ammonia that the vapor generated in the desorber contains some amount of water. This water will accumulate in the evaporator and cause a rise in evaporator temperature as the evaporation proceeds, which affects the absorber and condenser cycle conditions to obtain a desired cooling. Alternately, depending on the controls employed, the evaporator pressure must decrease to enable an acceptably low evaporation temperature for cooling. However, the conditions of the other components must correspondingly drift to accommodate this lower evaporator pressure. This drift away from design conditions significantly decreases cycle efficiency. The rectifier is needed to further purify the evaporated ammonia downstream of the desorber. The vapor pressures of the NH_3-H_2O working pair are further discussed in Section 1.4.

The absorption cycle, with either working pair, is “heat-driven” because the main source of energy comes from the heat input to the desorber, $Q_{recovered}$, which could be

recovered thermal energy. Some electricity is needed to power the pump, but this is drastically lower than the electricity needed to power the compressor of a vapor-compression cycle. The work required to compress a vapor is significantly higher than the work needed to pump a liquid. The absorption and desorption of the evaporated refrigerant between state 10 and state 7 replaces the major portion of the electrical load needed to compress a vapor with the thermal load necessary to desorb a vapor from liquid solution. This characteristic is extremely useful when the required heat load, $Q_{recovered}$, comes from an inexpensive and readily available heat source such as rejected heat.

1.2.2 Rankine Cycle

The Rankine Cycle was first described by William John Macquorn Rankine in 1859. Rankine's original pressure-volume diagram is shown in Fig. 4. This cycle has been widely used to generate electricity from primary thermal sources *and* to recover wasted thermal energy from such processes.

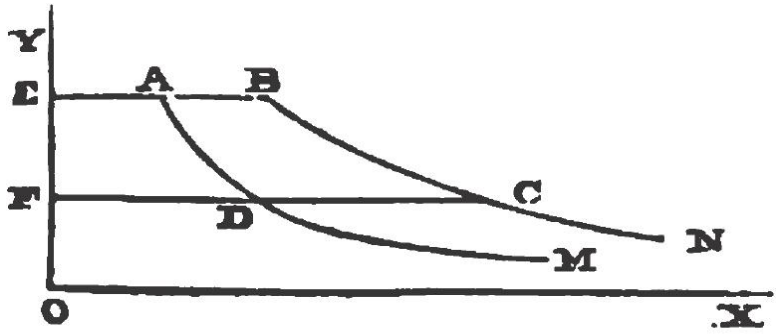

Fig. 4. Pressure-Volume diagram of the Rankine Cycle [2].

The basic components of the Rankine cycle are shown in Fig. 5, overlaid on the ideal temperature-entropy diagram of the cycle. In this cycle, the working fluid is expanded through a turbine, state 1 to state 2, producing work. The expanded vapor is then condensed to a saturated or subcooled liquid, state 3, by heat rejection. The liquid is pressurized through a pump, state 3 to state 4, and then enters the boiler. In the boiler,

the liquid is heated to the high temperature of the cycle, state 5, and then boiled and/or superheated, state 5 to state 1, completing the cycle.

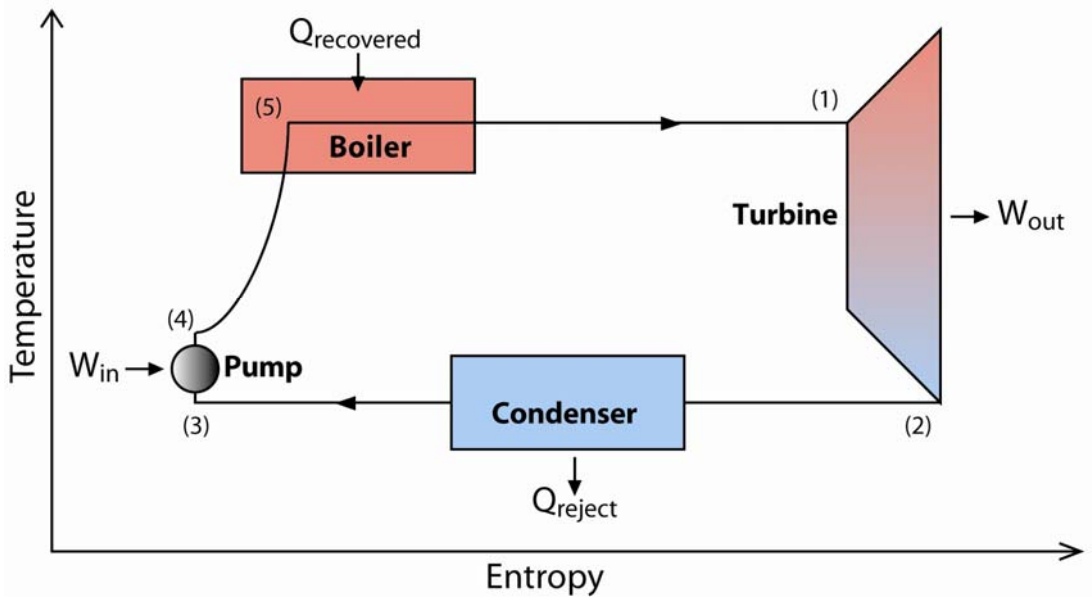

Fig. 5. Components of the Rankine cycle overlaid on the corresponding temperature entropy diagram.

As with the absorption cycle, the heat supplied to the boiler provides most of the energy required by the system, along with the electricity required in the pump. In contrast with the absorption cycle, the Rankine cycle produces work as its main output. This feature has made the cycle very useful for converting primary thermal sources to work. Again, when the heat source is readily available rejected heat, this cycle becomes especially attractive.

1.3 THE VAPOR-COMPRESSION CYCLE

The vapor-compression cycle is nearly ubiquitous in refrigeration applications, due to its simplicity, versatility, and the convenient nature of its energy source, electricity. The dependence of the cycle on inexpensive and readily available electricity can also cause problems. As pressure builds to decrease electricity use, the vapor-compression

system becomes less attractive. In this study, the goal is to move away from electricity use and both the cascaded and coupled cycles will be compared to a vapor-compression cycle as a measure of effectiveness. Somewhat ironically, the versatile nature of the vapor-compression cycle makes it a useful component *within* each of the studied cycles as well. The basic vapor-compression cycle is therefore reviewed here.

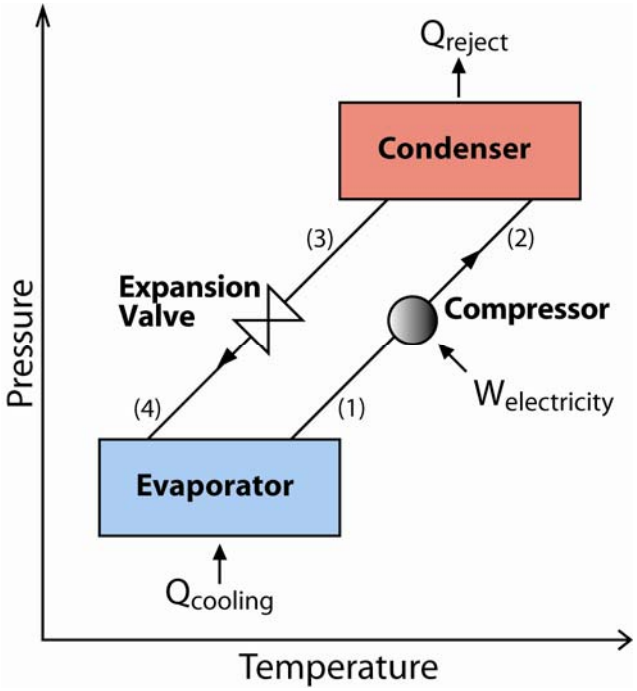

Fig. 6. Single-stage vapor-compression cycle.

Fig. 6 shows the basic vapor-compression cycle, laid out on pressure-temperature coordinates. When comparing this cycle to the absorption cycle in Fig. 3, the relative simplicity of the vapor-compression cycle is immediately obvious. In the vapor-compression cycle, the compressor takes the place of the absorber, pump, solution heat exchanger, desorber, and solution expansion valve. Refrigerant exits the evaporator of the vapor-compression cycle as a saturated vapor, state 1. The vapor is compressed to the cycle high pressure, state 1 to state 2. The compressed vapor is cooled in the condenser

to saturated liquid, state 3. The saturated liquid is expanded over the expansion valve to the cycle low pressure, state 3 to state 4. The refrigerant is evaporated in the evaporator to saturated vapor, state 1, completing the cycle. As mentioned in section 1.2.1, compressing a vapor requires a considerable amount of work. The large amounts of electricity needed to provide this work compared to the cascaded and coupled cycles will be discussed in later sections.

1.4 REFRIGERANTS

As stated at the beginning of this introduction, the primary concern leading to interest in coupled and cascaded cycles is environmental sustainability. Society must find a balance between the rate at which we use resources and the rate at which they are replenished to avoid resource depletion. Likewise, we must concern ourselves with the balance of chemicals in our environment to avoid dangerous depletions and build-ups. For this reason, only environmentally sound refrigerants are considered in this study.

Absorption Refrigerants

For the absorption based cycle, there are essentially two options for working pairs [23, 24]: ammonia-water (NH_3-H_2O) and water-lithium bromide (H_2O-LiBr). Table 1 summarizes the desirable working fluid properties for an absorption system and highlights the trade-offs between NH_3-H_2O and H_2O-LiBr.

Table 1. Absorption Working Fluid Properties [4].

Property	Ammonia/Water	Water/Lithium Bromide
Refrigerant		
High latent heat	Good	Excellent
Moderate vapor pressure	Too high	Too low
Low freezing temperature	Excellent	Limited application
Low viscosity	Good	Good
Absorbent		
Low vapor pressure	Poor	Excellent
Low viscosity	Good	Good
Mixture		
No solid phase	Excellent	Limited application
Low toxicity	Poor	Good
High affinity between refrigerant and absorbent	Good	Good

Both working pairs provide high levels of thermodynamic performance due to high latent heats (ammonia: 1370 kJ/kg at -33.33°C (101.3 kPa); water: 2257 kJ/kg at 100°C (101.3 kPa) [7]) and high affinity between their respective refrigerant and absorbent. High affinity between the refrigerant and absorbent is defined by a negative enthalpy change of mixing; this characteristic allows absorption to proceed without energy input. The enthalpy change of mixing for an NH_3-H_2O solution of 55% ammonia at 20°C and 1000 kPa is -236.20 J/g [4]. The enthalpy change of mixing for a H_2O-LiBr solution of 60% LiBr at 20°C and 1000 kPa is -149.63 J/g [4]. While a strong affinity induces

absorption, the negative enthalpy of mixing must be overcome by increased heat input in the desorber. Thus, stronger affinity does not necessarily translate to increased thermal efficiency.

Neither working fluid exhibits a convenient refrigerant vapor pressure: ammonia is too high and water is too low. At a refrigeration temperature of 10°C, the vapor pressure of ammonia is 615.05 kPa and the vapor pressure of water is 1.23 kPa. Therefore, NH_3-H_2O systems must operate at high pressures, requiring relatively thick-walled equipment. H_2O-LiBr systems must operate in a vacuum, at which the specific volume of the water vapor is very high (147.0 m^3/kg at 5.0°C and 0.87 kPa [25]), leading to high vapor velocities and requiring large volume equipment and special pressure drop considerations. Both systems are very sensitive to leaks. A leak in the pressurized NH_3-H_2O system will decrease the system pressure, which in turn decreases the evaporation temperature. In addition, a NH_3-H_2O system leak releases toxic ammonia into the ambient air. A leak in the H_2O-LiBr system vacuum will raise the system pressure, increasing evaporation temperature, and introduce noncondensable air into the system mixture, thus adding significant mass transfer resistances to the condensation and absorption processes.

Ammonia has a very low freezing temperature of -77°C at atmospheric conditions, which allows a wide range of applications for the NH_3-H_2O working pair. The mixture of ammonia and water does not enter the solid phase in the wide conditions of interest, giving it an advantage. However, while the vapor pressure of water is inconveniently low for a refrigerant, it is inconveniently high for an absorbent. The vapor pressure of water (270.28 kPa at 130°C) is much smaller, but not negligible, compared to the vapor

pressure of ammonia (10,897.70 kPa at 130°C). Thus, some amount of water will evaporate with the ammonia refrigerant in the desorber. Any fraction of water in the desorbed refrigerant vapor will pass through the system to the evaporator. At the refrigeration temperatures in the evaporator, the vapor pressure ratio is much higher; at 10°C, the vapor pressure of ammonia is 615.05 kPa and the vapor pressure of water is 1.23 kPa. A smaller fraction of water evaporates with the ammonia in the evaporator than in the desorber, thus water accumulates in the evaporator as mentioned in Section 1.2.1. The accumulated water causes an increase in evaporator temperature, decreasing the thermal performance of the cycle. The effect of small fractions of water in the desorbed ammonia refrigerant on evaporator temperature is shown in Fig. 7. A rectifier is often integrated into the NH_3-H_2O system downstream of the desorber to reduce the water content of the desorbed vapor.

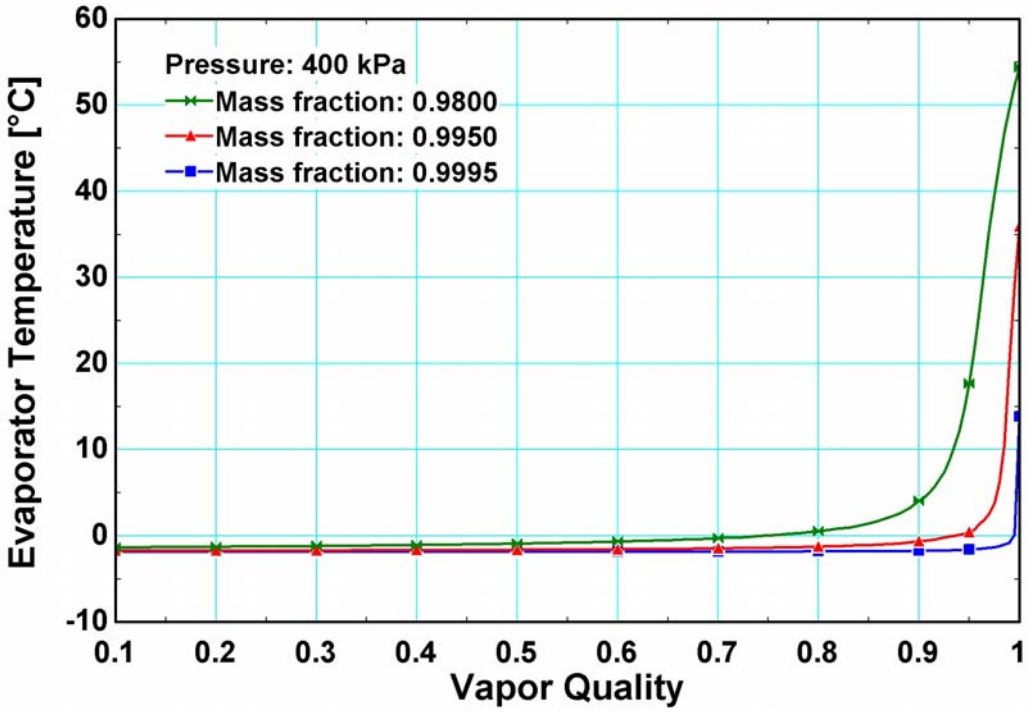

Fig. 7. Temperature glide in evaporator.

In addition, ammonia is a toxic chemical that must be handled with extreme care. In the case of a leak, ammonia is difficult to contain due to its gaseous form at ambient conditions. While a gaseous ammonia leak is diluted quickly in a large volume of ambient air, H_2O-LiBr represents a safer working fluid pair.

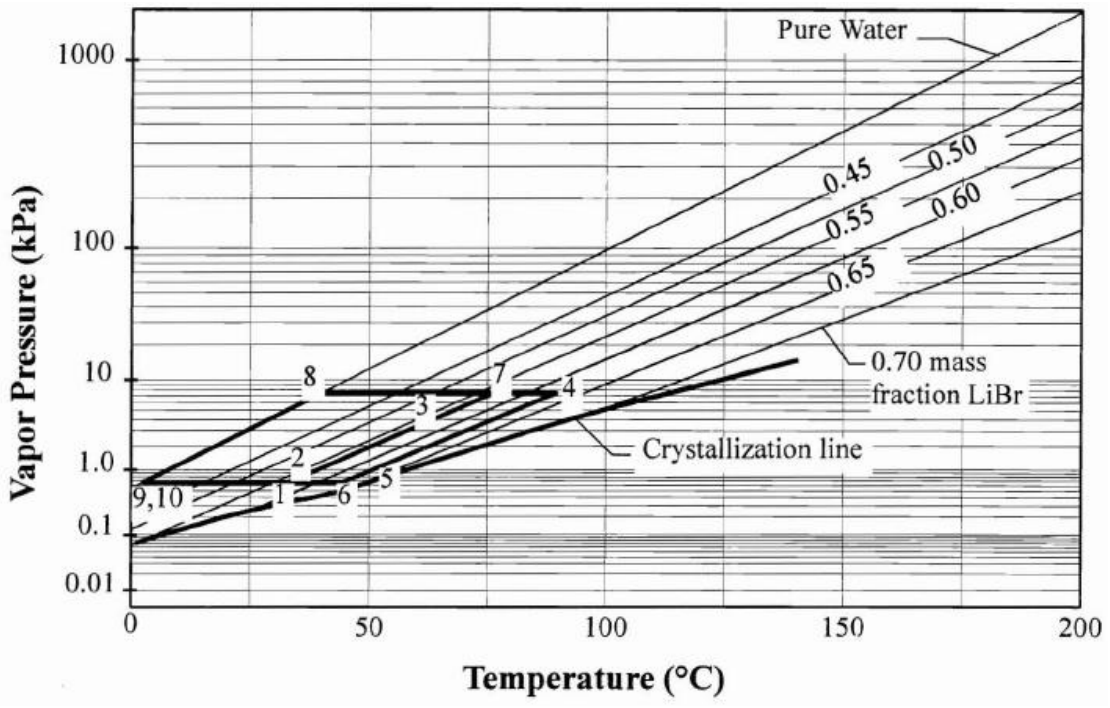

Fig. 8. Duhring plot of the single-stage absorption cycle [4].

However, the choice of H_2O-LiBr comes with two important limitations: the freezing point of water and the risk of solution crystallization. Water cannot be used as a refrigerant for cooling applications below 0°C, severely limiting the H_2O-LiBr cycles. Also, the H_2O-LiBr salt solution will crystallize if the mass fraction of LiBr exceeds the solubility limit [4]. This limit is heavily dependent on temperature and weakly dependent on pressure. As shown in the Dühring plot in Fig. 8, the operating temperatures and pressures of the single-stage absorption cycle lie close to the crystallization limit. This plot also makes clear the typical crystallization point in the cycle: the strong solution inlet

to the absorber. In Fig. 8, the close margin between state point 6 (44.7°C and 62.4% LiBr) and the crystallization limit near that point (approximately 47°C and 63% LiBr) is clear. In practice, crystallization issues usually occur at this point; a good design will pay close attention to the operating conditions and the crystallization limit there. A common method to avoid crystallization is to maintain low temperatures in the absorber. Lower absorber temperatures require lower solution concentrations and tend to avoid the crystallization limit [4]. However, to maintain low absorber temperatures, the H_2O-LiBr cycles must be water-cooled, rather than air-cooled.

Rankine Refrigerants

There are many more refrigerant options for the Rankine-based cycle. These are discussed in greater detail in Chapter 2. From the variety of fluids that possess acceptable thermodynamic characteristics, the refrigerant in this study is primarily selected by the global warming potential (GWP), the ozone depletion potential (ODP) and safety of the fluid. The GWP of a refrigerant is an index describing its potential to persist in the upper atmosphere and to trap the radiation emitted by the earth [7, 26]. The ODP of a refrigerant is a measure of its ability to destroy stratospheric ozone [7, 26]. Refrigerants that do not contain chlorine have ODPs of essentially zero. The GWP and ODP of a refrigerant are a comparison to the baseline refrigerants for each property, which are CO_2 and CFC-11, respectively. The GWP, ODP, and flammability of a few representative refrigerants are provided in Table 2 The refrigerant R245fa has been identified as an excellent choice for low-temperature Rankine cycle applications [27]. The fluid has a low GWP (950) [28], zero ODP, low-toxicity and is non-flammable [29]. When compared to typical Rankine cycle refrigerants R123 and R11 in an application

with boiler temperature of 149°C and condenser temperature of 38°C, R245fa shows slightly higher thermodynamic efficiency [29]. In addition, the fluid has excellent thermal stability. With competitive thermal properties and low environmental impact, R245fa is the clear choice for the Rankine-based cycle in this study.

Table 2. Refrigerant Environmental Properties.

Refrigerant	Global Warming Potential (GWP)	Ozone Depletion Potential (ODP)	Flammable?
11	4600	1	No
123	120	0.02	No
245fa	950	0	No
717 (NH_3)	0	0	Yes
744 (CO_2)	1	0	No

Source: 2006 ASHRAE Handbook – Refrigeration [7]

Vapor-compression Refrigerants

Finally, for the vapor-compression portion of the cascade cycles, the chosen refrigerant is carbon dioxide (CO_2). CO_2 is the baseline for the GWP scale, giving it a value of 1 by definition. The non-toxicity of the fluid is obvious, as it is a common component of the atmosphere. In addition to the environmental benefits, CO_2 has attractive thermodynamic and transport properties [7]: high thermal conductivity (0.112 W/m-K), high vapor density (94.1 kg/m^3), and low viscosity (0.101 mPa-s). The refrigerant is also inexpensive and readily available. For these reasons, CO_2 vapor-compression machines have been studied in recent years and are being introduced to the market. Two of the major disadvantages of CO_2 are the high operating pressures required for medium- and high-temperature refrigeration (3384 kPa at a saturation temperature of -1.1°C, 6685 kPa at a saturation temperature of 26.7°C) and low critical-point temperature (31.0°C) [7]. Refrigeration systems utilizing CO_2 exhibit low cycle performance when rejecting heat near or above the critical point. In the cascade cycle examined in this

work, the rejection temperature of the CO_2 vapor-compression portion is subcritical (near 5°C) and the efficiency losses of supercritical systems are avoided.

1.5 SCOPE OF RESEARCH

The focus of this work is to characterize and evaluate two cycles for low-grade heat recovery. A thermodynamic model of each cycle was developed on the Engineering Equation Solver [30] platform, with thermodynamic and mass balances at each state point. The models were used to estimate necessary flow rates and component sizes, and parametric analyses were carried out to identify critical components. The first cycle considered is a novel absorption/vapor-compression cascade cooling system with a high temperature lift (Fig. 33). The unique cascading of the absorption and vapor-compression systems provides efficiency advantages to both cycles, resulting in high overall coefficients of performance (COPs). The second cycle considered is a Rankine/vapor-compression coupled cooling system initially proposed over fifty years ago. Technology advances in critical components suggest that a renewed interest in this cycle may be warranted. This study explores fundamental issues essential to the realization of cascaded energy utilization through these two cycles.

1.5.1 Cascade Absorption/Compression Cycle

There is some prior work on absorption-compression systems, but primarily where compression is used simply to boost the pressure of the refrigerant vapor in the absorber downstream of the evaporation process. Here, a completely novel cascade cycle is analyzed, where a single-effect $LiBr/H_2O$ absorption cycle operating in a steady mode is used to generate a coolant stream of about 5°C. This coolant stream supplies medium temperature cooling at relatively low heat fluxes *and* serves as the heat sink for the low-

temperature vapor compression system using CO_2 as the working fluid. This cascade relationship circumvents a major issue with either the H_2O-LiBr absorption cycle or the CO_2 cycle alone:

I. As mentioned previously, the choice of H_2O-LiBr is environmentally sound, but limits the cycle to applications above 0°C; the CO_2 vapor-compression cycle has no such limitation and can cool at much lower temperatures.

II. Typical CO_2 vapor-compression applications call for transcritical cycles due to the low critical temperature of CO_2 (31°C). Transcritical cycles have relatively low COPs due to the non-isothermal supercritical heat rejection and the consequent departure from the Carnot cycle. However, with heat rejection at ~5°C (well below the critical point), subcritical operation occurs, with the corresponding high COPs.

The electric energy input to the absorption cycle of the cascaded system is very small and when there is an inexpensive source of heat readily available, the cost of running the absorption loop is very small. In this situation, the cascade cycle provides clear advantages over the likely competitor, a two-stage vapor-compression system using synthetic refrigerants. The two-stage cycle must provide a much larger temperature lift (conditioned space temperature to heat rejection temperature) than the vapor-compression loop of the cascade cycle (refrigeration temperature to ~5°C), and the corresponding electricity needed for the two-stage cycle will therefore be much larger. A quantitative comparison of these two cycles is provided after the analysis of the absorption/vapor-compression cascade is discussed in detail.

1.5.2 Coupled Rankine/Vapor-Compression Cycle

The second cycle analyzed is a cooling cycle that recovers waste heat using an organic Rankine cycle with refrigerant R245fa as the working fluid. The cycle configuration was initially reported by the Garrett Corporation [5]. The power produced in the turbine of this cycle is directly coupled to the compressor of a vapor-compression cooling cycle to generate cooling to be utilized for space-conditioning. In addition to the integrated turbo-compressor, the condensers of the power-producing Rankine cycle and the bottoming vapor compression cycle are integrated into one component to reduce the overall number of components required to achieve cooling from waste heat. Since 1966, advances in turbo-compression and the availability of new refrigerants warrants reconsideration of this cycle. It is shown that even with low grade waste heat sources, a Rankine cycle efficiency of about 11-12 percent can be achieved. This coupled to the bottoming cycle with a COP of about 2.7 yields an overall waste heat to cooling conversion efficiency of about 32 percent. This cycle provides an alternative to absorption systems that could require a larger and more heat exchangers to produce cooling from waste heat streams, although the cycle performance of absorption systems may be somewhat higher.

1.6 THESIS ORGANIZATION

The thesis is organized as follows:

- Chapter 2 discusses the research that has been done previously in areas related to absorption and Rankine cycles.
- Part 1, Chapter 3 provides detailed information about the performance model of the cascaded absorption/vapor-compression cycle.

- Part 1, Chapter 4 describes the results of the cascaded absorption/vapor-compression cycle performance model and the influence of key parameters on the model.
- Part 2, Chapter 5 provides detailed information about the performance model of the coupled Rankine/vapor-compression cycle.
- Part 2, Chapter 6 describes the results of the coupled Rankine/vapor-compression cycle performance model and the influence of key parameters on the model.
- Chapter 7 provides a summary of the conclusions obtained from the two performance models.
- Chapter 8 provides recommendations for future development.

CHAPTER TWO: PREVIOUS WORK

2.1 ADVANCED ABSORPTION AND RANKINE CYCLES

The basic absorption and Rankine cycles were first considered in the 1800s [2, 22]. After these basic cycles were well-developed and understood, they were used as building blocks to create more complex cycles with higher efficiencies. Some of these complex cycles have simply stacked similar basic cycles; others have created 'hybrids' by combining different types of cycles. Most of the 'hybrid' cycles discussed here are constructed with some combination of the three building blocks described in the introduction: the basic absorption, Rankine, and vapor-compression cycles. This stacking and combining of cycles is the foundation for cascaded and coupled cycle technology.

2.1.1 Advanced Absorption Cycles

Two categories encompassed the bulk of research on advanced cycles with absorption building blocks: multi-stage, multi-effect cycles and absorption/compression hybrids [10]. The absorption/compression hybrids (also known as sorption-compression systems) combine a mechanical compressor with a desorber/absorber loop, as shown in Fig. 9, in a similar configuration as the basic vapor-compression cycle. The desorber provides the cooling load while the absorber rejects heat from the cycle. The absorption/compression hybrids are driven by electrical work input to the compressor, rather than heat input, which is not a useful feature for low-temperature heat recovery and those cycles will therefore not be considered here.

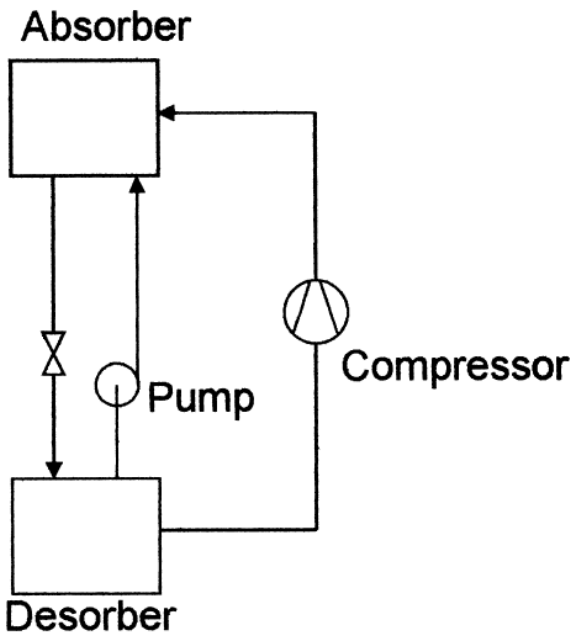

Fig. 9. Basic absorption-compression cycle [10].

Multi-stage and multi-effect cycles have been a major research focus in absorption technology for over one hundred years. The terms *stage* and *effect* have related, but distinct, definitions [4]. The number of *stages* refers to the number of absorption building blocks used in the advanced cycle. The number of *effects* refers to the number of times the initial driving heat is reused throughout the system, and can approximately predict the corresponding increase in COP. *Stage* is a description of the physical configuration of the cycle, while *effect* describes the cycle performance. The basic absorption cycle presented in Chapter 1 is a single-stage, single-effect (SE) cycle, which is often used as a baseline for comparison.

Open cycle

Open-cycle absorption systems utilize very low temperature heat sources to provide cooling at low lifts [13]. The open dehumidifier – evaporator – regenerator (DER) cycle is nearly identical to the single-stage cycle except for the lack of condenser, as shown in

Fig. 10. The condensation of the refrigerant is performed by the environment, instead of a condenser, reducing the number of components needed. Also, the DER cycle operates at ambient pressures, eliminating the need for pressure-sealed components. These factors significantly reduce the initial costs of the DER cycle. However, these advantages come at a significant performance cost. Hellman and Grossman [13] simulated a DER cycle that utilizes a hot water source at 57.2°C and operates with a cooling water temperature of 29.4°C and a chilled water temperature of 7.2°C. The predicted COP of this cycle was 0.43, only 60% of the typical single-stage COP of 0.7.

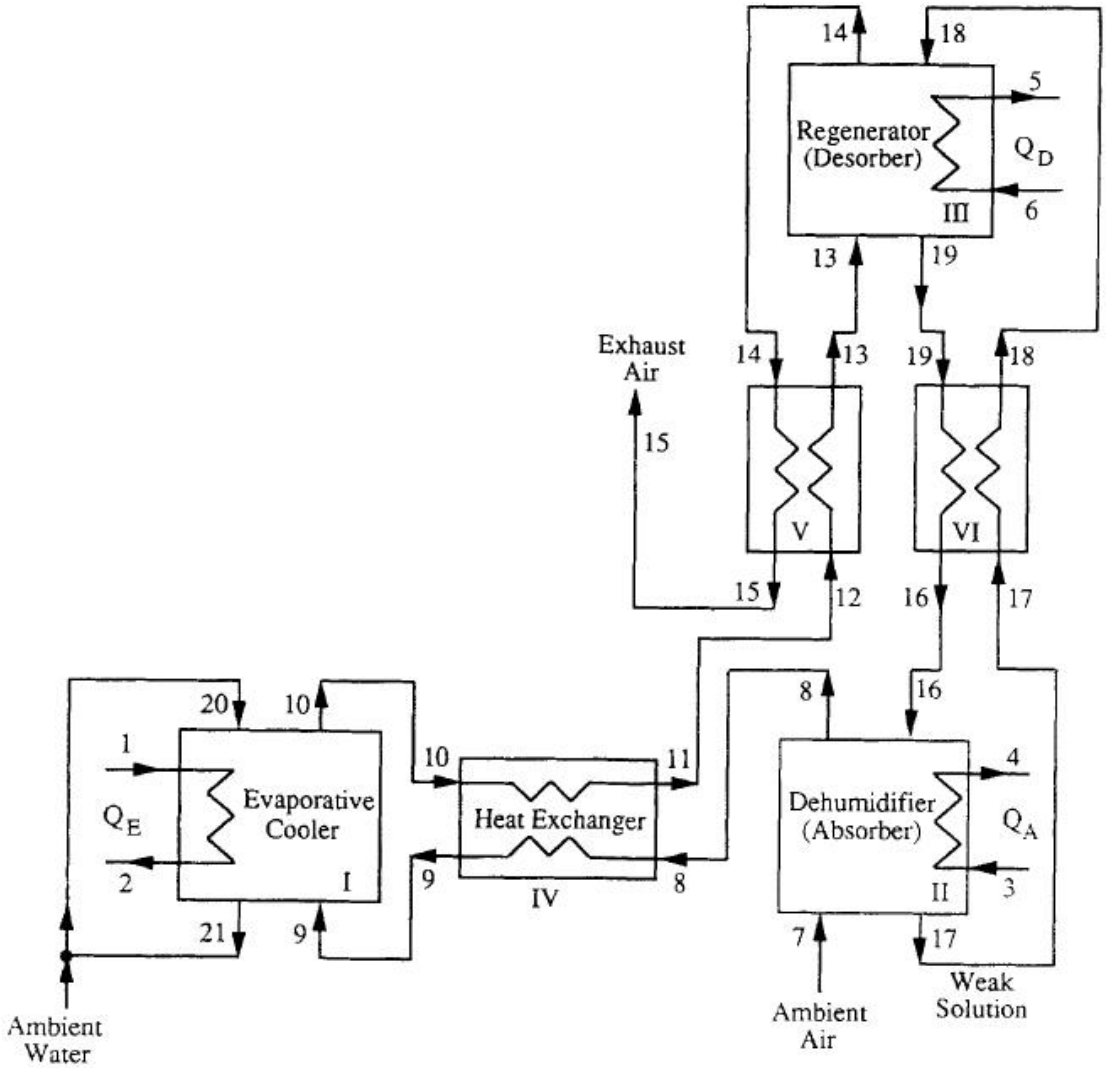

Fig. 10. The open dehumidifier – evaporator – regenerator (DER) cycle [13].

An experimental prototype was developed by Gommed and Grossman [31, 32] to test the concept and obtain realistic performance measures. The prototype was designed to be one piece of an air-conditioning system; the primary purpose of the open cycle in this system was dehumidification, rather than cooling. Ambient air was dehumidified in the absorber and cooled by additional systems before being provided to the conditioned space; ambient air was also used to evaporate water and concentrate the solution in the desober before being rejected to the environment. This configuration requires neither a condenser nor an evaporator. The thermal COP of the prototype was about 0.8, with a hot water heat source of 60-100°C and cooling water temperature of 22-27°C. The thermal COP of the system is defined as useful cooling/dehumidification produced over thermal energy supplied from the solar collectors and does not include parasitic losses. When parasitic losses are included, the COP appears to be around 0.6, but the average value of this measure is not explicitly provided. Another parameter not explicitly provided is the outlet temperature of the dehumidified air. It is assumed from the system description that the lift of this cycle is very small. The open cycle is more efficient in dealing with latent heat than with sensible heat, which explains the increased performance of the prototype when compared with the theoretical results of Hellman and Grossman [13]. If a high-temperature heat source is available, a closed cycle provides better cycle performance and lower cooling temperatures. Operation at ambient pressures limits the performance of an open cycle when compared to a closed-cycle operating at two pressures, due to the decreased ability of the open cycle to utilize input energy. However, the open cycle may have potential for providing air-conditioning from very low-temperature heat sources that cannot be utilized by other cycles.

Two-stage, Half-Effect (Double-Lift) Cycle

Especially when considering waste-heat applications, an available heat source temperature may be too low to drive an SE cycle. To address these cases, Maiuri [33] described a two-stage configuration that uses half of the prime energy to produce cooling and the other half to increase cycle lift. This cycle is called the "half-effect" or "double-lift" cycle for that reason. A schematic of this cycle is shown in Fig. 11. For the half-effect cycle, an intermediate-pressure absorber and desorber are added to the single-stage, single-effect cycle. The advantage of this addition can be seen in Fig. 12. The dotted lines represent the single-effect cycle, while the solid lines represent the half-effect cycle. The desorber operating temperatures for each cycle are the furthest right points on each plot. The single-effect desorber reaches a high of 90°C, requiring an input temperature of 100-110°C. The half-effect desorbers both reach a high of 65°C, allowing them to accept an input temperature of 70-80°C [4]. Both cycles produce refrigeration at the same temperature, shown by the lower-left point shared by both plots which represents the evaporator temperature.

However, this advantage of low temperature heat source utilization comes with major disadvantages: reduced performance and increased components and complexity. With the added absorber, the half-effect cycle rejects about 50% more heat than the single-effect cycle [4]. The COP of the half-effect cycle, 0.35, is roughly half of the single-effect COP, 0.7. Therefore, the half-effect cycle requires more thermal input to produce a specified cooling capacity. This drawback implies that this cycle is only practical when a large amount of low-grade waste heat that cannot be utilized by a single-effect cycle is available.

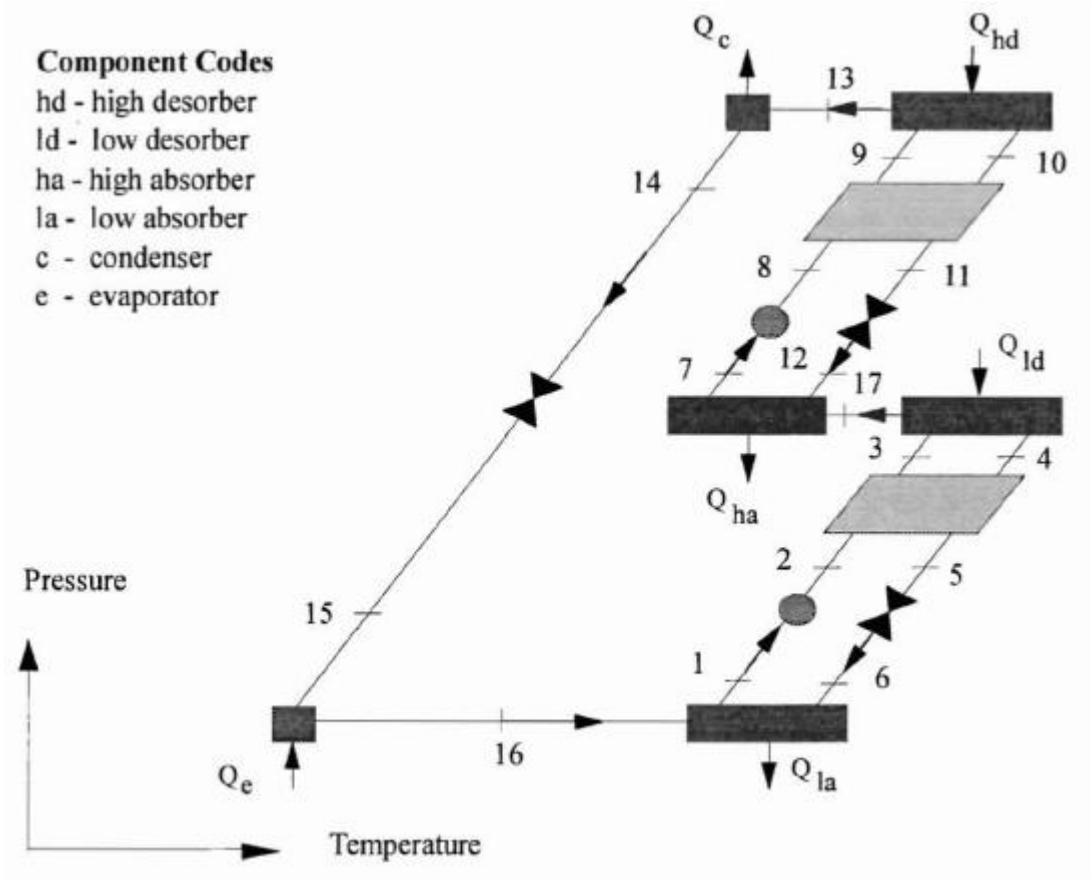

Fig. 11. Half-effect (Double-lift) Water-Lithium Bromide Absorption Cycle [4].

An ammonia-water half-effect cycle was implemented by Erickson [33] to produce ice in an isolated Alaskan fishing village. In this village, diesel generators are used to produce electricity. The jacket cooling water from those generators exits at 80°C. The half-effect ice-maker utilized that low-temperature heat source to reduce the load on the electrical capacity. With a condenser temperature of 19°C and an evaporator temperature of -17°C, the ice-maker operated at a COP of 0.306. This was lower than the design COP value of 0.35 due to subcooling in the absorbers, according to the authors. Again, increased heat rejection is the primary cause of low COPs in the half-effect cycle.

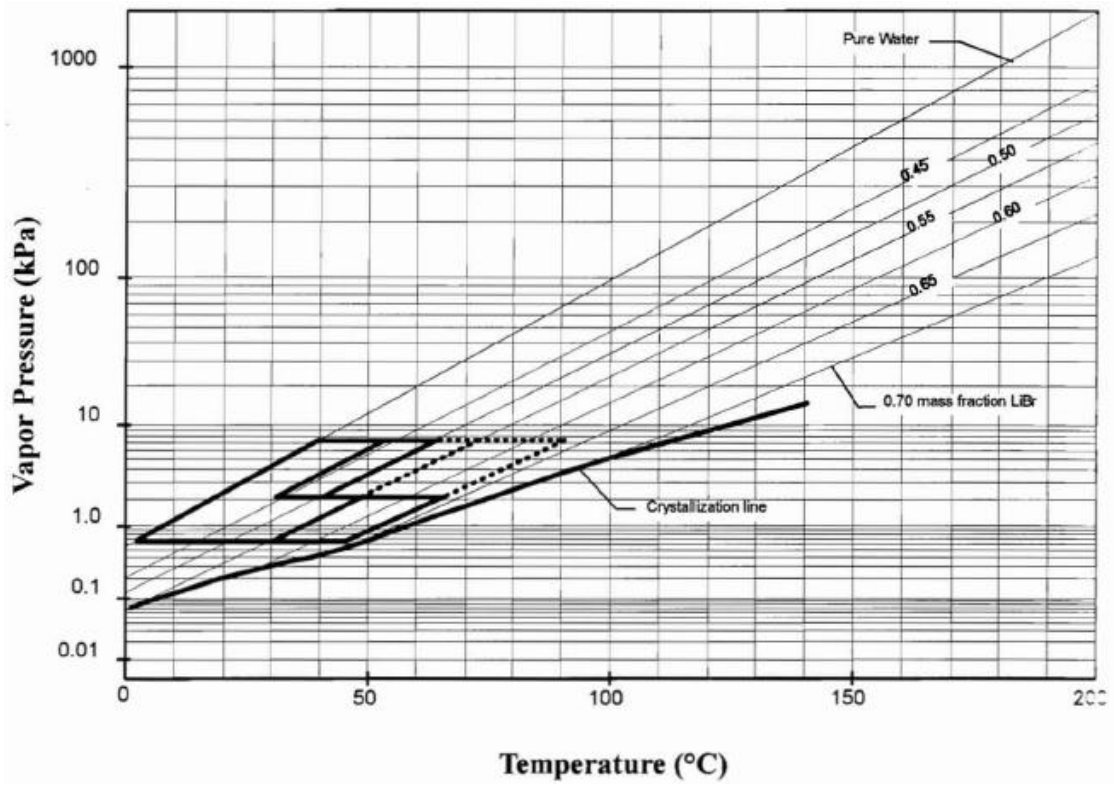

Fig. 12. Dühring plot for the half-effect cycle [4].

Water-lithium bromide half-effect cycles have been theoretically analyzed and experimentally validated by Ma and Deng [34]. On a 6 kW experimental prototype with a heat source temperature of 86°C and a cooling water temperature of 32°C, they obtained a COP of 0.35-0.38 for a range of chilled water temperatures 8-14°C. A detailed heat transfer model was developed for a much larger capacity H_2O/LiBr chiller by Goodheart [35]. The optimal performance for a 400-700 ton chiller predicted by that model was 0.39.

Single-Effect, Double-Lift Cycle

When the available heat source temperature is sufficiently high to drive a SE cycle, but the available heat source flow rates are low, a combination of the single-effect and half-effect cycles can be applied [11]. A schematic of this single-effect, double-lift (SE/DL) cycle is shown in Fig. 13. The framework of the cycle is similar to the single-

stage machine: evaporator (EO), absorber (AO), condenser (C2) and generator (G21). Within the framework, three additional heat exchangers are incorporated to provide the double-lift: G I, G22 (generators) and A1 (absorber). The advantage of the cycle can be seen by following the flow of the district heating hot water. First, the single-effect sub-cycle utilizes the highest temperatures of the heat source at G21, allowing a greater COP than if the half-effect cycle was used alone. The lower temperature stream exiting G21 then passes to the half-effect sub-cycle generators G1 and G22. The half-effect sub-cycle utilizes the lower temperature heat source, allowing the cycle to extract enough driving heat to provide a useful cooling capacity.

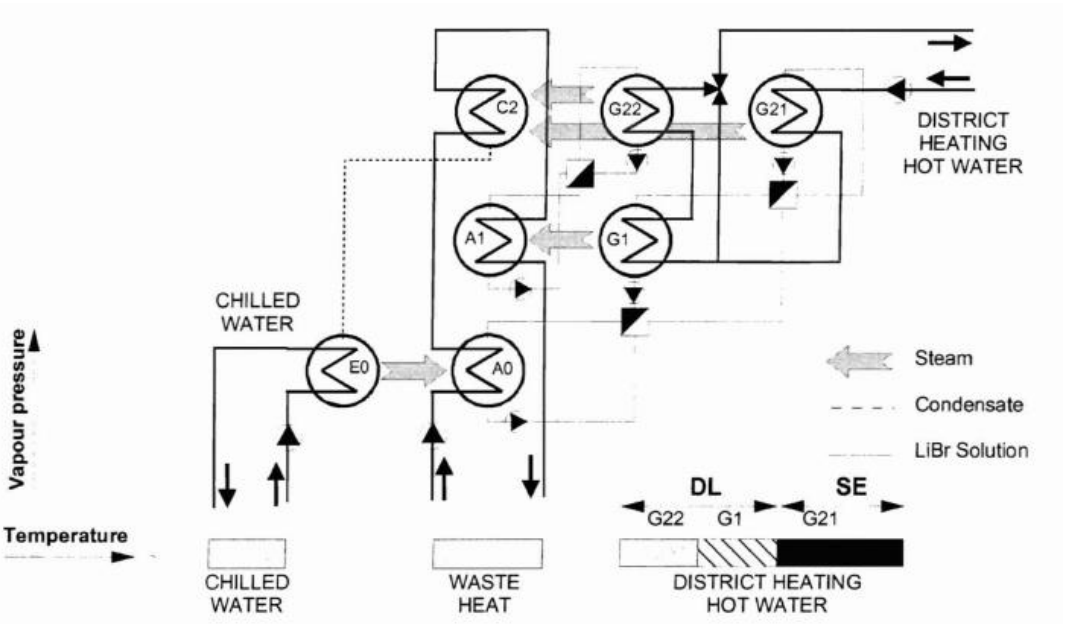

Fig. 13. Single-Effect/Double-Lift Cycle [11].

Three SE/DL cycles were implemented in Germany [11], to utilize the waste heat produced at a university, power plant, and airport. Each cycle chilled 12°C water to 6°C. At the university, waste heat was provided at 95°C and returned at 65°C. The university cycle provided 400 kW of cooling at a COP of 0.62. At the power plant, waste heat was provided at 85°C and returned at 60°C. The power plant cycle provided 300 kW of

cooling with a COP of 0.58. At the airport, waste heat was provided at 95°C and returned at 60°C. The power plant cycle provided 2500 kW of cooling with a COP of 0.65. As expected, these cycles show a level of performance (COP ~0.6) between the expected levels of half-effect (COP ~0.35) and single-effect cycles (COP ~0.7) alone. The SE/DL performance is comparable to the SE performance. If a heat source is available in adequate flow rates, an SE cycle provides the performance advantage. However, when flow rates are limited below those necessary for SE cycles, the SE/DL cycle can provide large cooling rates at a comparable performance level.

Two-stage, Double-Effect Cycles

If a heat source is available at very high temperatures, the SE cycle cannot fully utilize the driving heat available. The two-stage, double-effect (DE) absorption cycle discussed here aims to utilize the additional energy available. The first two-stage, DE absorption device was proposed by Edmund Altenkirch [22]. The typical theoretical COP of a DE absorption machine is in the range of 1.0 to 1.2, almost double the typical 0.7 COP of a single-stage machine. This significant increase in cycle efficiency is often well worth the extra components needed, leading to the popularity of two-stage cycles around the world [36]. The cycle is well-understood and often serves as a test cycle for new thermodynamic or thermoeconomic modeling software [37, 38].

The double-effect machine can be constructed in several configurations. Fig. 14 shows one configuration of a two-stage, double-effect water/lithium-bromide absorption chiller. The two stages are clearly labeled “low” and “high” and each of the components have a role similar to that described in section 1.2.1 for the single-stage cycle. The benefit of this cycle is the internal heat exchange between the high condenser and low

desorber, reusing the initial driving heat supplied to the high desorber. This reuse feature is the double effect of the cycle, which allows the cycle to fully utilize all of the thermal energy available.

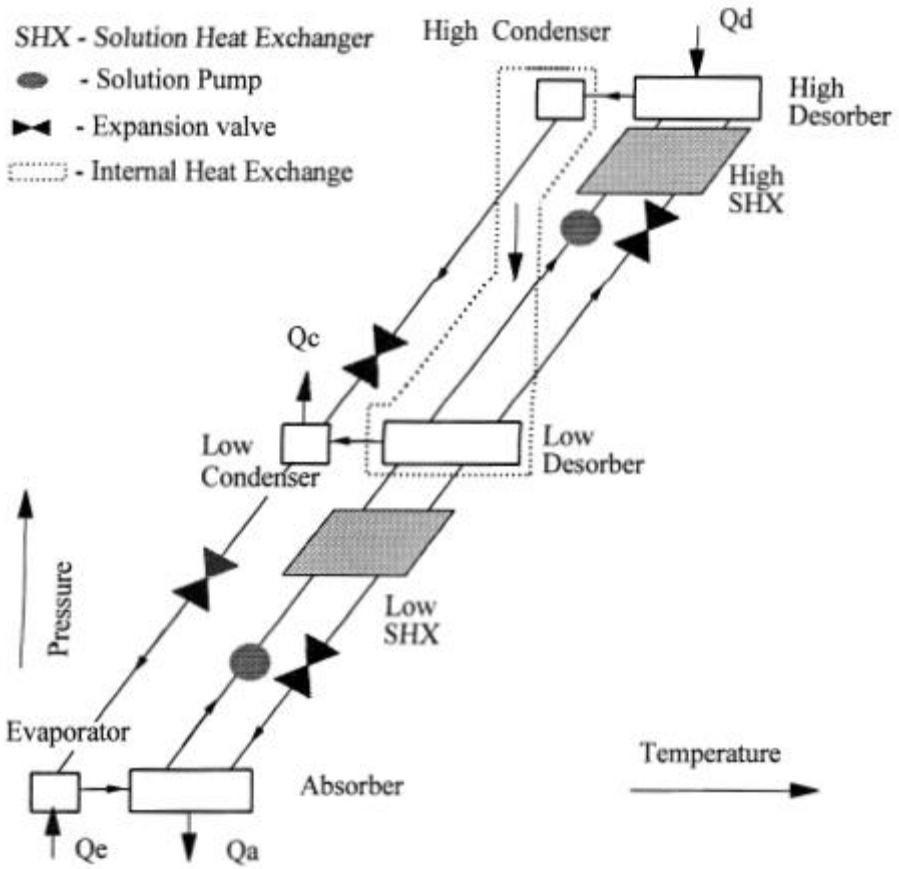

Fig. 14. Double-effect water/lithium bromide chiller [4].

The high and low solution circuits can be connected in either parallel or series flow [4]. The double-effect cycle example given previously, in Fig. 14, is parallel flow. In parallel flow, the weak solution leaving the low solution heat exchanger from the absorber is split into two streams: one flowing to the high desorber and the other to the low desorber. Active controls are required to maintain the proper split ratio between the two streams in parallel flow. In series flow, the entire weak solution stream flows through one desorber and then through the other, shown in Fig. 15, avoiding the need for

split flow controls. A series-flow cycle can be configured to direct flow either to the high or low desorber first. Sending the weak solution stream to the high desorber first tends to be the better performing series-flow cycle configuration. In either case, the flow rate through the high solution heat exchanger is larger in the series-flow configuration than in parallel flow. The larger flow rate implies higher load and also higher irreversibility in that component. For this reason, the typical COP of a series-flow cycle is lower than that of parallel flow. However, the capacity of the series-flow configuration is typically larger than that of parallel flow. The increased capacity is due to a better temperature match in the high desorber. The outlet temperature of the high desorber is hotter in series flow than in parallel flow; therefore the outlet temperature of the low desorber is also increased, evaporating more water from the solution. Ultimately, more mass flow passes through the evaporator which provides increased capacity. The trade-offs between parallel and series flow configurations are complex and through proper optimization and component sizing, the differences in performance between these configurations may be decreased.

Another double-effect cycle configuration, used with the ammonia/water working pair [4], adds second absorber and desorber operating at the single-stage pressures rather than adding a desorber and condenser at a higher pressure. In this configuration, shown in Fig. 16, the reused heat is transferred between the second absorber and the original desorber. This configuration is possible due to the wide solution field of ammonia/water and exhibits some performance benefits due to the high heat of absorption compared to the heat of condensation. However, increases in performance can be outweighed by other effects, such as the rectification requirements of the ammonia/water pair.

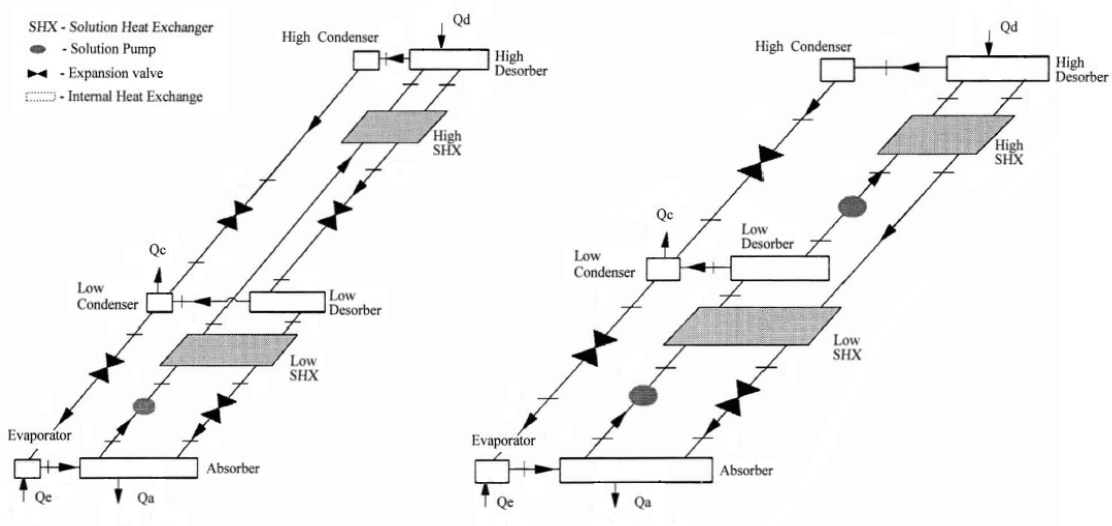

Fig. 15. Double-effect water/lithium bromide cycle series configuration with solution to high-temperature (left) or low-temperature (right) desorber first [4].

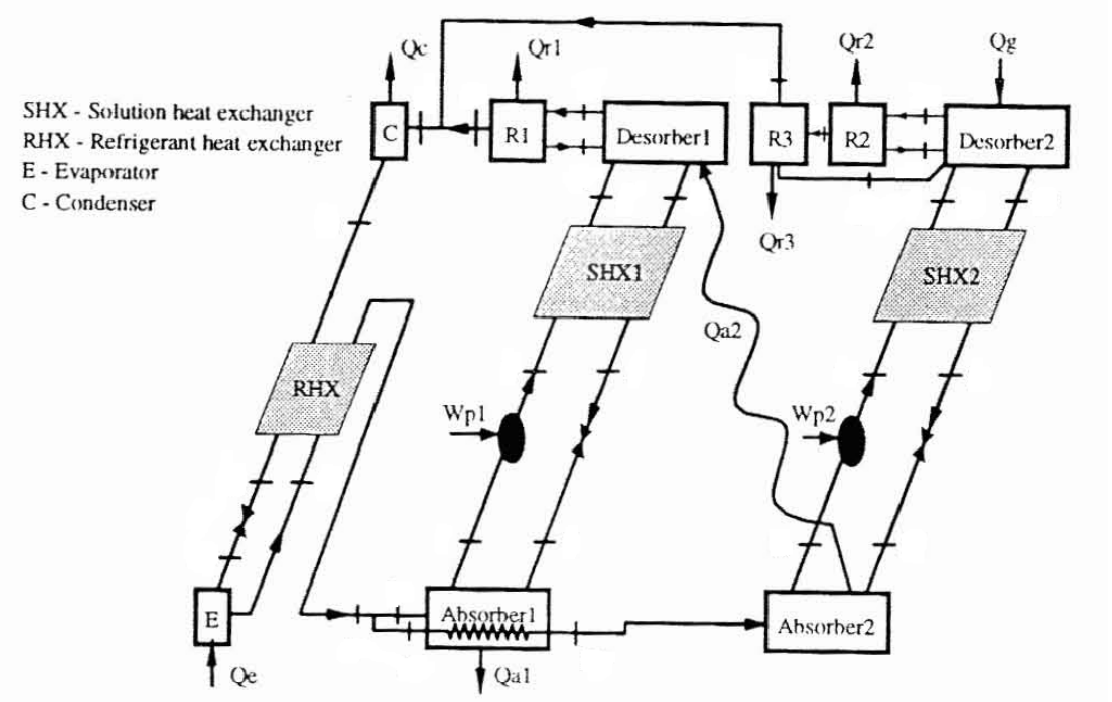

Fig. 16. Double-effect ammonia/water cycle configuration [4].

Two-Stage, Triple-Effect Cycle

A different two-stage configuration, first proposed by Georg Alefeld [39], is triple-effect. The cycle was first built using water/LiBr for the low-temperature stage and a water/zeolite working pair for the high-temperature stage. Ivester and Shelton [40] later showed that both stages could be operated with ammonia/water. Fig. 17 shows this two-stage, triple-effect configuration for an ammonia/water cycle. In this cycle, both the high condenser and absorber are operated at sufficiently high temperatures (about 88°C and 91-110°C, respectively) to provide internal heat exchange to the low desorber. Thus, every unit of heat supplied to the high desorber is used to evaporate refrigerant three times and therefore the cycle is triple-effect. Additionally, the high absorber can provide the heat input to the hotter parts of the low generator while the high condenser must only supply heat input to the cooler parts. The lower condenser temperature (88°C, compared to equivalent double-effect cycle temperature of 108°C) allows the cycle to run at a lower high cycle pressure (4830 kPa, compared to 6895 kPa), which decreases the work required and increases the COP. With efficient internal heat exchangers (an assumed ΔT of 3°C between all internal heat exchange streams), the predicted COP is 1.41 [4, 41]. The major disadvantage of the cycle is the high generator temperatures required (~220°C), which can cause corrosion problems and limit application. Devault et al. [41] show that this is the only triple-effect configuration that can be operated within the solubility limits of the ammonia/water pair. Garimella et al. [42] investigated the performance of the cycle over a wide range of cooling and heating mode ambient temperatures. In this study, representative heat exchanger configurations and UAs were used to ensure a practical system. The predicted cooling mode COP at an ambient

temperature of 35°C is approximately 0.78. This value is just over half the 1.41 COP value predicted with efficient internal heat exchangers.

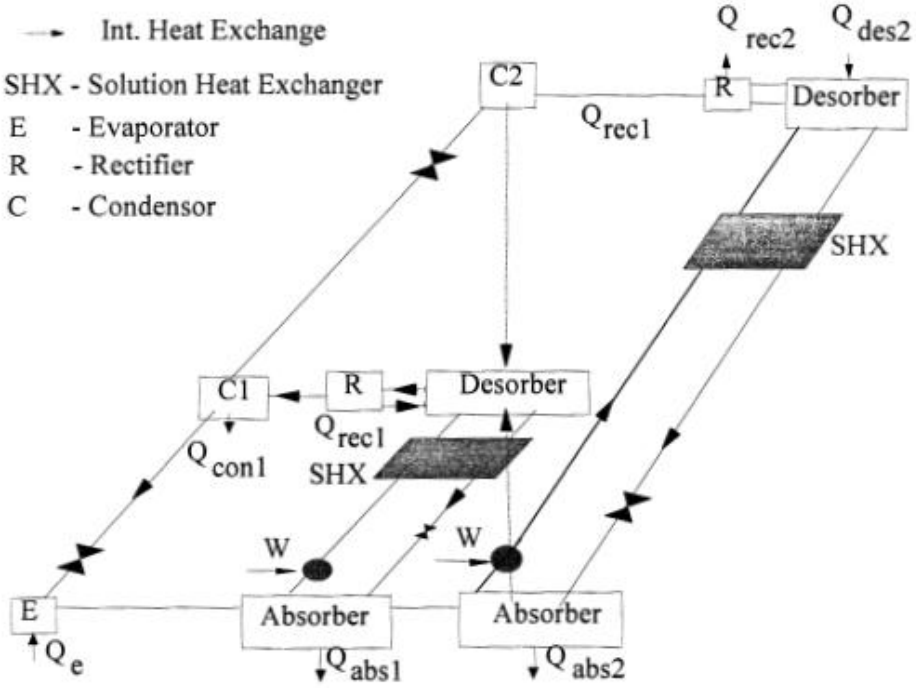

Fig. 17. Two-stage, triple-effect ammonia/water chiller [4].

Multi-effect, Multi-stage Cycles

A variety of cycle configurations with more stages and/or more effects have been considered in the literature, but the complexity of these cycles has limited implementation. Most configurations are characterized by the number of components needed, which is a measure of the complexity. For example, the two-stage, triple-effect cycle discussed above is also known as the two-condenser, two-absorber (2C2A) triple-effect cycle. Grossman et al. [12] considered three triple-effect cycles: the three-condenser, three-desorber (3C3D) cycle, the double condenser coupled (DCC) cycle, and the dual-loop cycle. The 3C3D cycle is simply an extension of the double-effect cycle described above and requires 16 components. The DCC cycle adds one component to the 3C3D cycle: a recuperative heat exchanger that cools the condensate leaving the high-

temperature condenser (Fig. 18). The dual-loop cycle consists of two separate single-effect loops, with the condenser and absorber of one cycle providing heat to the desorber of the other cycle (Fig. 19). Several variations of each cycle are analyzed and the calculated COPs range from 1.27 to 1.73. When compared to the 1.41 COP of the simpler 2C2A cycle described above, the increase in COP would in most cases not justify the additional complexity. Grossman [43] also considered a four-condenser, four-desorber (4C4D) quadruple-effect cycle. The calculated COP of the 4C4D cycle was around 2.0 for desorber heat input temperatures of over 200°C. The high temperature raises issues of corrosion and flue losses.

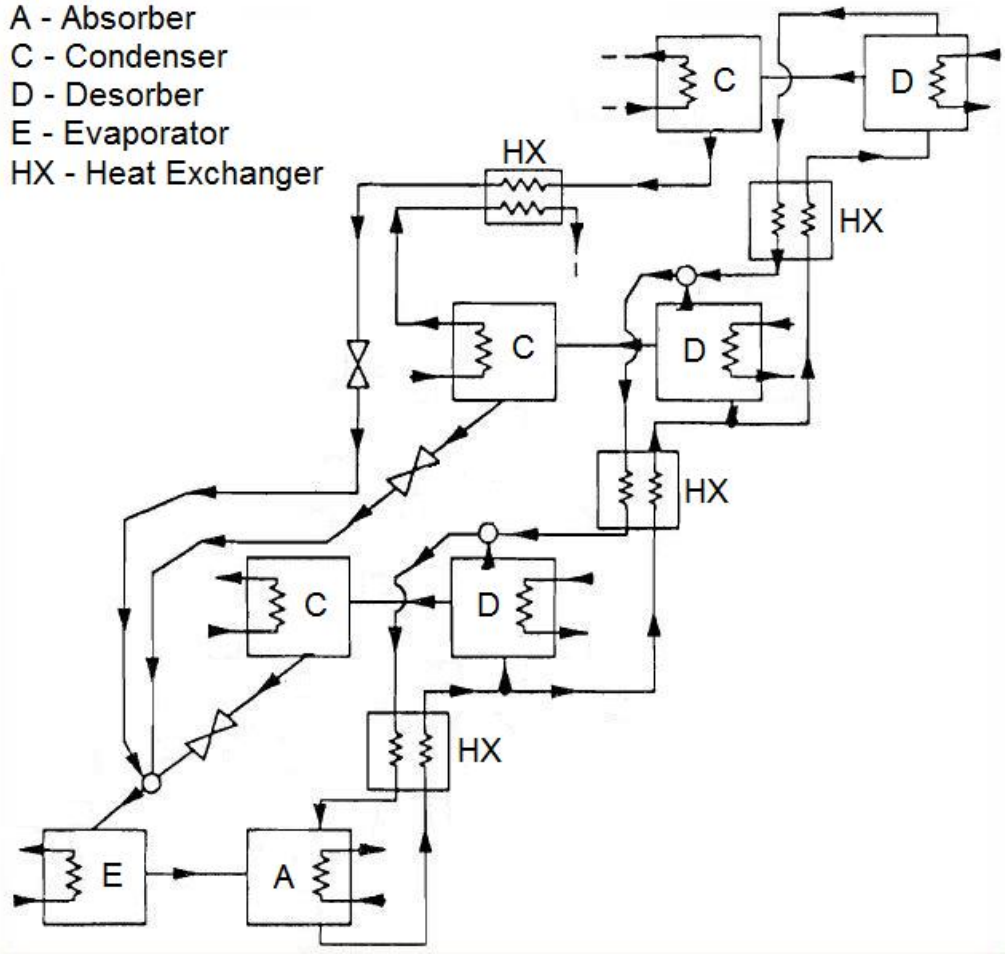

Fig. 18. Double-condenser-coupled (DCC) triple-effect chiller in parallel flow [12].

Many more cycle configurations are possible and Ziegler and Alefeld [44] developed a method to quickly evaluate the potential of novel configurations. They estimated (within 10%) the COP of an advanced cycle by considering the cycle a simple combination of single-stage cycles. This shortcut allows the screening of advanced cycles before significant research effort is invested.

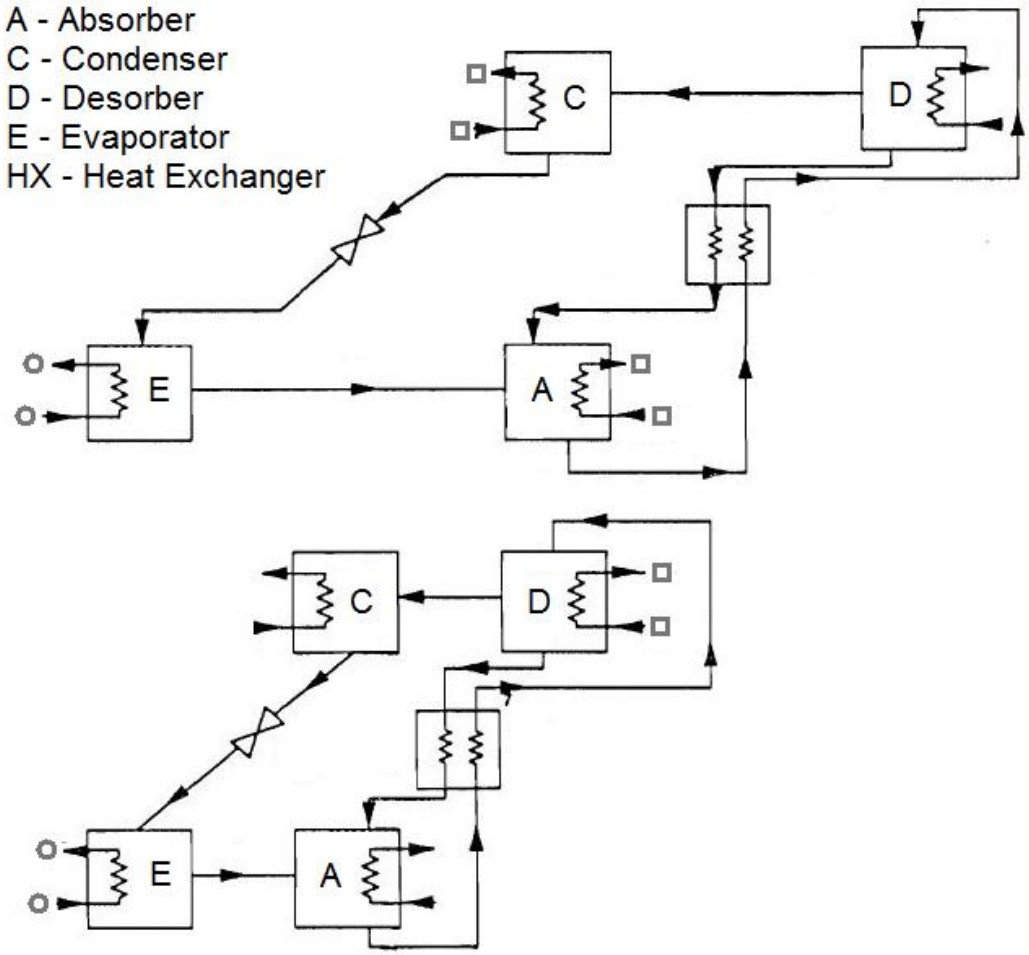

Fig. 19. Dual-loop triple-effect chiller [12]. Inlets and outlets marked with a square, □, or a circle, ○, are part of the same secondary loop.

Generator/Absorber Heat Exchange Cycles

The generator/absorber heat exchange (GAX) cycles provide multiple effects through a single stage configuration. The cycle was patented by Altenkirch and Tenckhoff [45]. The concept of a GAX cycle is illustrated by Herold et al. [4] in Fig. 20. Starting with a two-stage system shown by solid lines in Fig. 20, the flow rate in both solution pumps is reduced. This reduction increases the temperature of the low-stage poor solution stream and decreases the temperature of the high-stage rich solution stream, as shown by the dotted lines in Fig. 20. At some reduced flow rate, these streams will follow the same pressure and temperature changes; that is, the dashed lines in Fig. 20 will be the same. If the flow rate in these streams is equal, the streams cancel each other, and the cycle becomes the GAX cycle shown in Fig. 21. The original two absorbers and desorbers have now been merged into one component each, giving a single-stage configuration. The difference between the GAX cycle and the single-stage, single-effect cycle is the temperature gradients within the absorber and the desorber. These gradients are so large that the high-temperature end of the absorber, near state 4 in Fig. 21, is hotter than the low-temperature end of the desorber, near state 2. The high-temperature end of the absorber can now provide heat to the low-temperature end of the desorber. The starting cycle in Fig. 20 could have been triple-stage, triple-effect and the same GAX cycle would result, only with a larger temperature overlap between the absorber and desorber and therefore more internal heat transfer. In this way, the GAX cycle is a multi-effect, single-stage cycle.

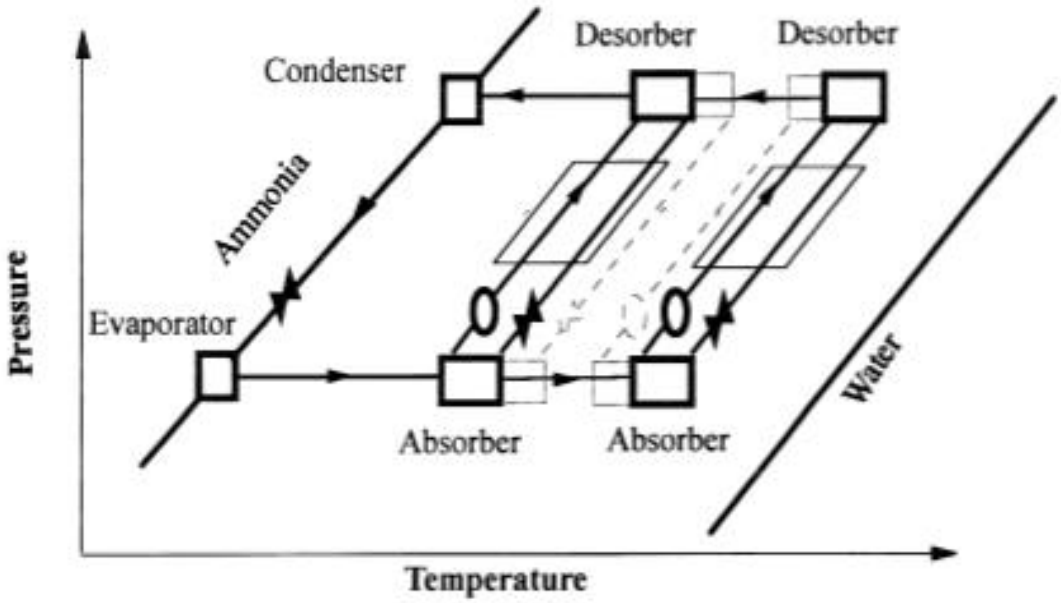

Fig. 20. Conceptual construction of the GAX cycle [4].

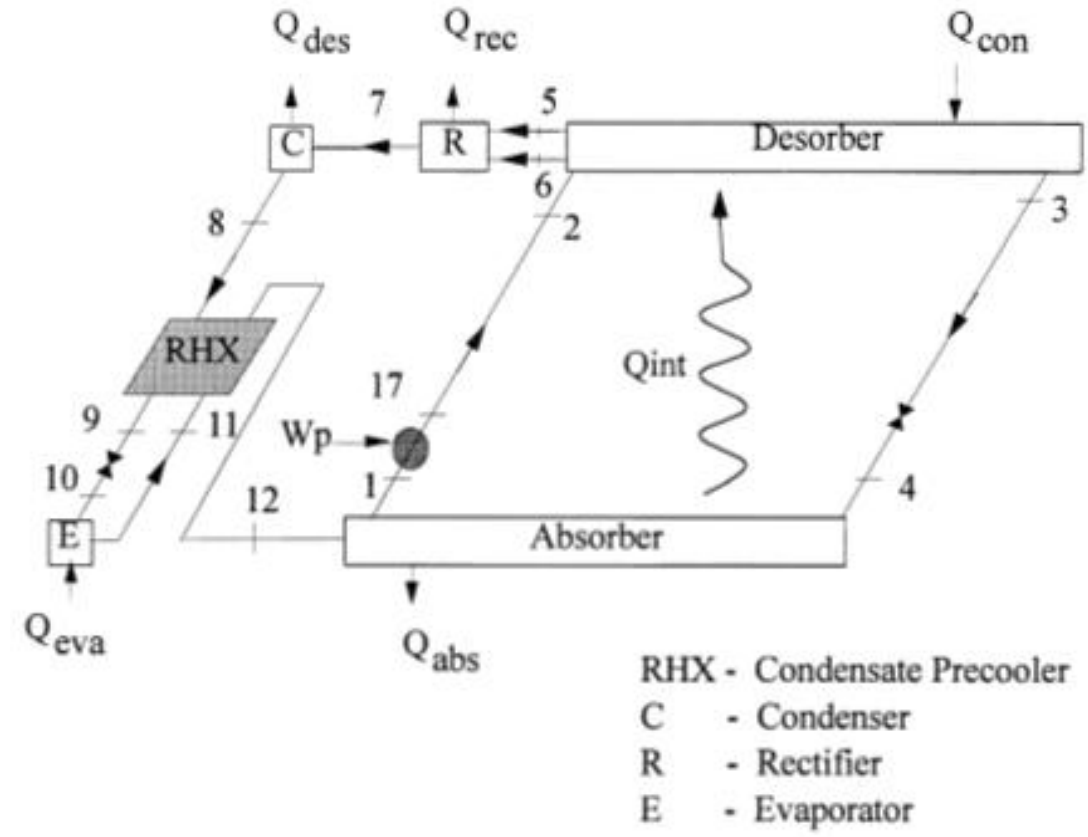

Fig. 21. GAX Cycle [4].

The apparent simplicity of the single-stage configuration and the increased COP of the multi-effect internal heat transfer have made the GAX cycle a very attractive concept. However, the potential COP of the cycle is limited by two complexities introduced by the absorber-desorber heat transfer.

First, the heat provided by the high-temperature part of the absorber is generally not sufficient to meet the heat input requirements of the low-temperature part of the desorber [46]. This deficiency is not usually considered in simple first-order calculations of the COP that do not account for component UAs and stream ΔTs required for such recuperative heat exchange with unbalanced streams. Therefore, the actual COP can be much lower than that predicted with such simple analyses. To combat this first challenge, the efficiency of the internal heat transfer must be maximized. In maximization, two additional challenges are encountered. One, the most efficient heat and mass transfer is achieved with counter-flow between the streams in the absorber and desorber and also counter-flow between the vapor and liquid streams in each component [4]. This arrangement is difficult to create in a real heat exchanger because of buoyancy/gravity driven vapor and liquid streams on both sides that could easily lead to flooding in the components at anything but the lowest of mass fluxes. A hydronic loop may be introduced to facilitate the arrangement, which introduces the second challenge: different approach temperatures between the hydronic loop and the absorption/desorption sides due to the mismatched thermal capacities.

Garimella et al. [14] and Engler et al. [16] investigated the performance of the GAX cycle over various operating conditions. In their ammonia-water GAX cycle model (Fig. 22), Garimella et al. included a realistic gas burner with flue losses and optimized the UA

of each heat exchange component for maximum cycle performance. In cooling mode with optimized component UAs, Garimella et al. predicted a COP of 0.925 at an ambient condition of 35°C. The COP of the cycle with baseline UAs decreases from 0.865 to 0.796 as ambient temperature increases from 18.3°C to 40.6°C. The ammonia-water GAX cycle simulated by Engler et al. [16] operates at an evaporator temperature of 10°C and a condenser temperature of 42.2°C (Fig. 23). As the desorber outlet temperature ranges from 149-205°C, the COP of the cycle increases from 0.75 to 1.05. At high heat source temperatures, the GAX cycle provides the efficiency of a double-effect system without the additional complexity.

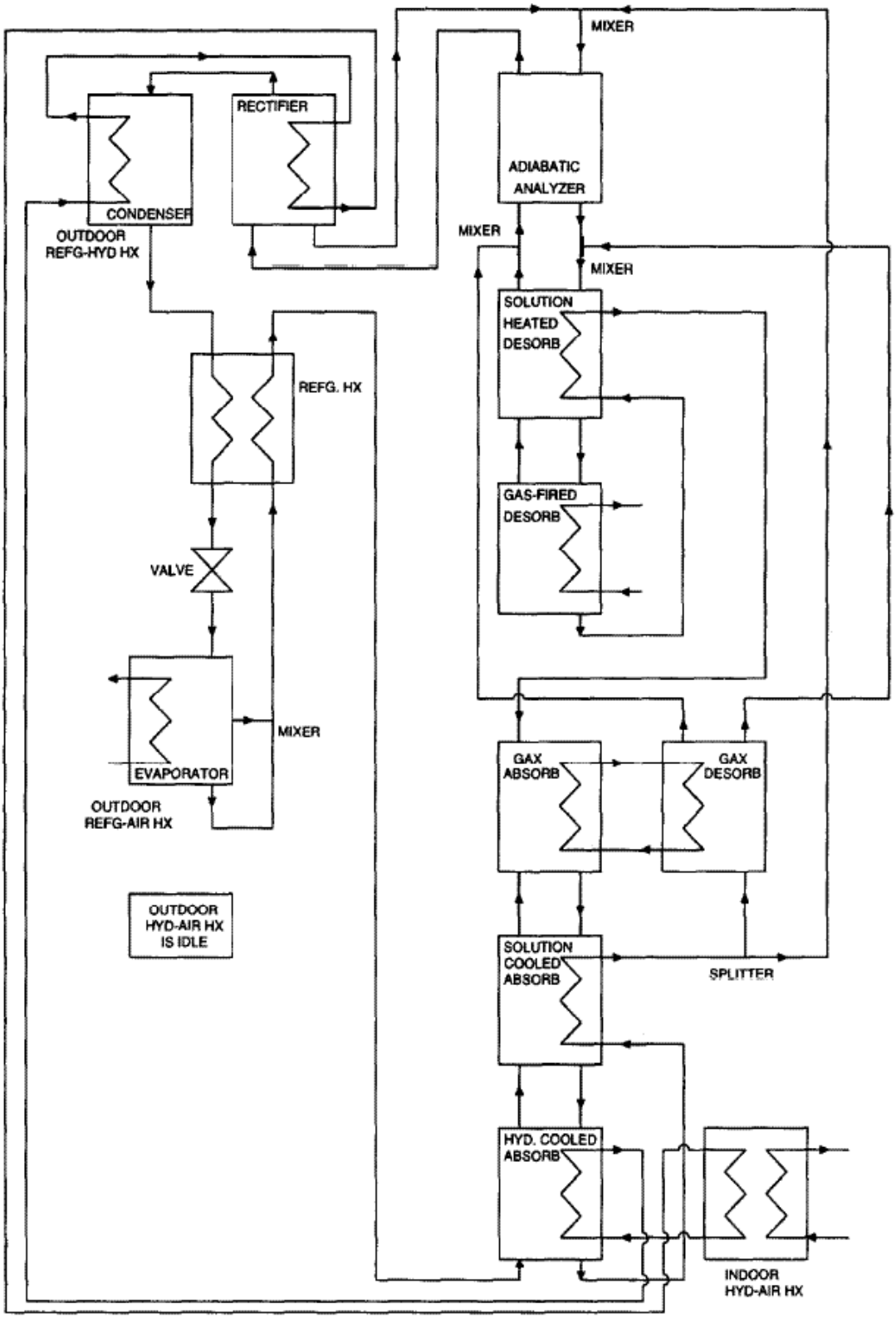

Fig. 22. GAX cycle schematic [14].

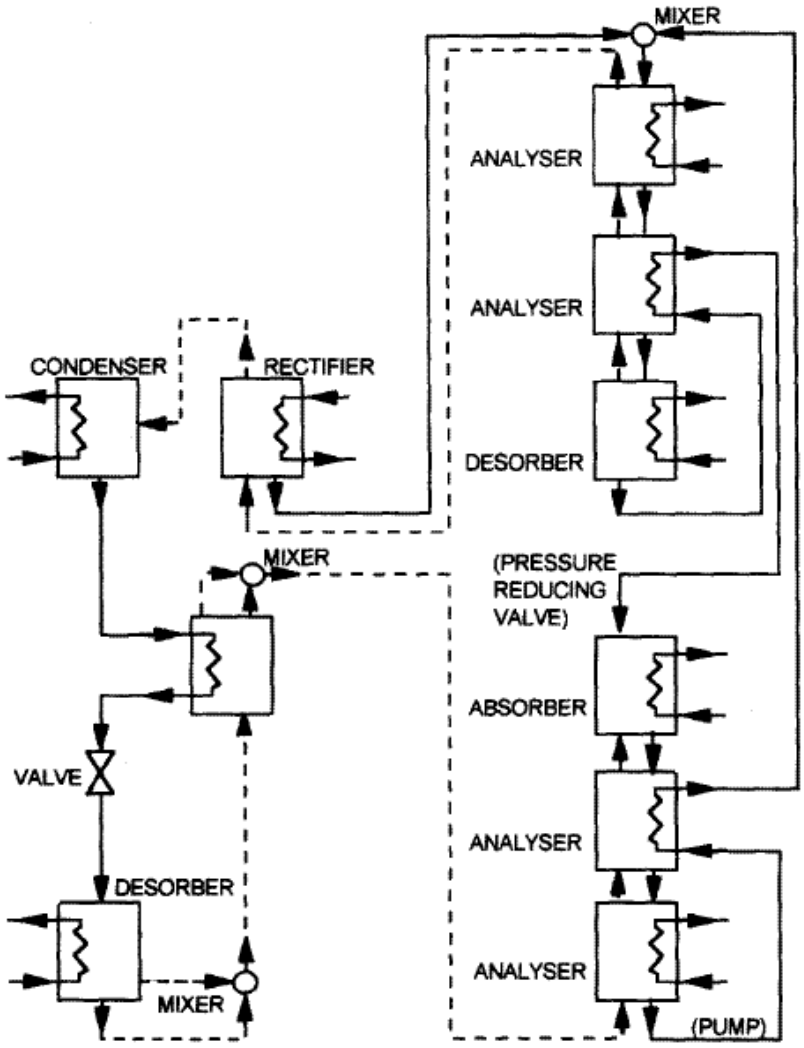

Fig. 23. Schematic description of the GAX cycle [16]

Branched GAX Cycle

A modified GAX cycle provides an alternative method to improve heat transfer between the absorber and generator (accomplished by the hydronic loop in the previous section). In this branched GAX cycle [4], shown in Fig. 24, a second solution pump is added to increase the mass flow rate in the high temperature portion of the absorber. This addition boosts the heat provided by the absorber to the low temperature end of desorber, decreasing the amount of external heat input required there. However, the branch also increases flow rate in the high temperature end of the desorber, which increases the

external heat required on that end. The balance between the decreased need of the low-temperature end and the increased need of the high-temperature end limits the potential performance improvement provided by the branch. It is possible to have more than one branch in a GAX cycle for increased improvement, but there are diminishing returns for each branch due to this balance.

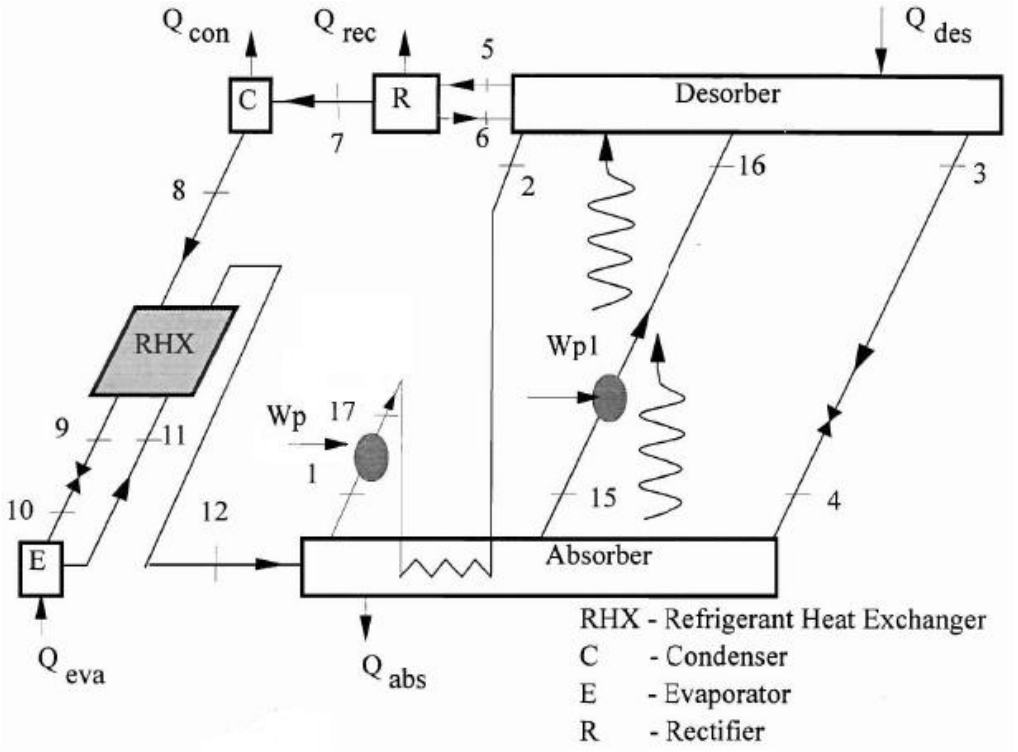

Fig. 24. Branched GAX Cycle [4].

Engler et al. [16] define the split ratio (SR) of the branched GAX cycle to be the ratio of mass flowrates between the recirculated stream and the total stream in the high-temperature end of the absorber (i.e. the flow ratio between the branch stream and the maximum stream in the absorber). Therefore, a GAX cycle with no branch would have an SR of 0.0, while a GAX cycle with one branch recycling the entire flow would have an SR of 1.0. For an ammonia-water branched GAX cycle with evaporator temperature of 10.0°C, condenser temperature of 42.2°C, and desorber outlet temperature of 195°C,

they found that a branch is only useful with SR between 0.0 and 0.65. Maximum performance occurs when SR = 0.3 with a COP of 1.08. For the equivalent GAX cycle without branch, they show a COP of 1.0. The improved thermal performance of the branched GAX cycle is somewhat offset by the increased electricity needed for the second pump. Erickson et al. [47] characterize another performance limitation in the ammonia-water branched GAX cycle. In an experimental comparison of a basic and a branched GAX cycle, both cycles are operated at a lift of 38.9°C and a cooling capacity of 14.6 kW. They found the steady-state basic GAX COP to be 1.06, while the branched GAX COP was only 1.04. They attribute the poor performance to sub-cooling in the absorber. Sub-cooling has a greater penalty for the branched GAX cycle, as the cooler liquid is recirculated, which negates the benefits of the branch. The results of Erickson et al. and Engler et al. show that the branched GAX cycle may provide a thermal advantage, but the corresponding disadvantages may outweigh the benefits.

Vapor Exchange GAX Cycle

The GAX and branched GAX offer increased thermal performance over the SE cycle for low and intermediate temperature lifts. However, when the GAX cycle is operated at high temperature lifts, there is no temperature overlap in the absorber and condenser. A three-pressure, vapor exchange (VX) GAX cycle was developed by Rane and Erickson [48] to provide improved COPs at high lifts. The VX GAX cycle incorporates an additional desorber and absorber at an intermediate pressure (Fig. 25), to enable heat exchange at high lifts. At lower lifts, a branch is added to the VX GAX and the resulting COP is greater than the corresponding branched GAX [48]. They simulated a VX GAX ammonia-water cycle at a lift of 70°C, with a -40°C evaporator temperature and a 30°C

condenser temperature. The COP of this cycle is predicted to be 0.66. For a VX GAX cycle at 30°C lift, with evaporator temperature of 3°C and condenser temperature of 33°C, the COP is predicted to be 1.88. The heat source temperature required for each of these cycles is about 215°C. If a high temperature heat source is available, the VX GAX cycle provides improved performance over other GAX cycles and SE cycles. For low temperature heat sources, the VX GAX cycle is not useful. Additionally, the VX GAX cycle is the most complex cycle discussed so far. The added complexity and additional components will increase the installation costs of VX GAX machines and reduce their appeal in the refrigeration market.

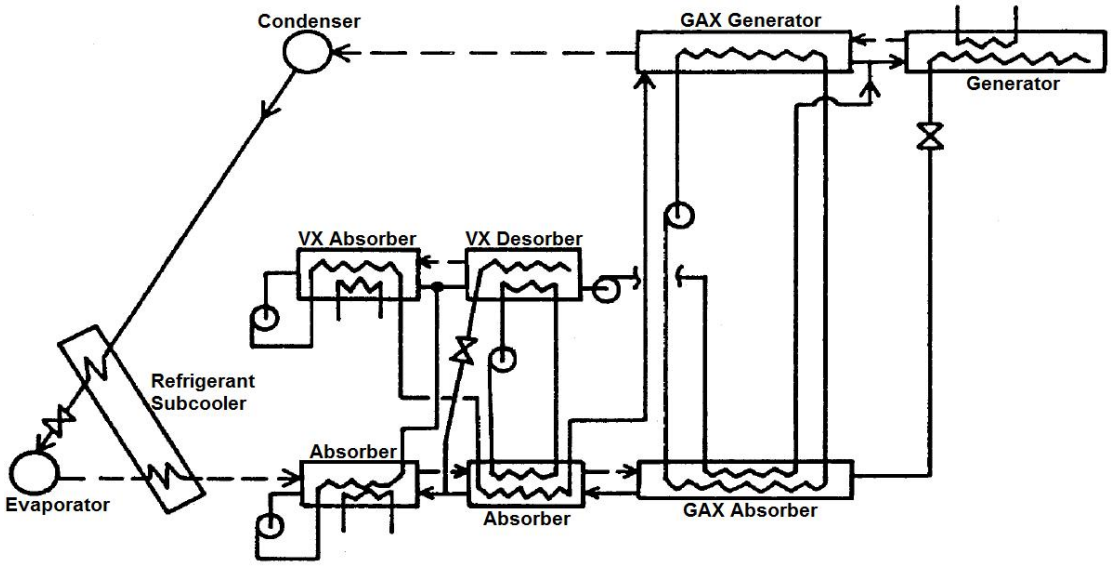

Fig. 25. Schematic of VX GAX cycle [3].

Summary

The multi-stage and multi-effect absorption cycles discussed here have been developed for applications that lie outside the practical range of the single-stage single-effect absorption cycle.

The open cycle and two-stage half-effect cycle utilize heat sources at temperatures too low to be utilized by the basic absorption cycle. The open cycle can utilize heat sources at temperatures around 60-70°C, providing low lift cooling at low COPs. The open cycle is particularly useful for the dehumidification of air, but cycle performance decreases when used to remove sensible heat as well. The two-stage half-effect cycle utilizes slightly higher temperatures (70-80°C). The two-stage half-effect cycle performs at about half the COP of the basic single-stage cycle, but can utilize large amounts of low-grade heat that may otherwise be wasted.

The single-effect, double-lift cycle was developed to utilize heat sources that are available at sufficient temperatures to drive a basic single-effect cycle, but at insufficient flow rates. The single-effect, double-lift cycle has been implemented in such conditions with a COP of around 0.6. Again, the decreased performance can be negated by the ability to use heat sources that could not be utilized by the basic single-effect cycle.

Many cycles are able to utilize heat sources that exist at temperatures higher than those required by the basic single-effect cycle. The aim of these cycles is to maximize the amount of energy extracted from the heat source; energy that would otherwise be underutilized by the basic single-effect cycle. The two-stage double-effect cycle can utilize temperatures of 150-200°C with COPs in the range of 1.0-1.2. The two-stage, triple-effect cycle utilizes slightly higher temperatures (~220°C) with a slightly higher predicted COP of 1.41. However, the two-stage, triple-effect cycle relies on efficient internal heat transfer and cycle performance is predicted to be around 0.78 when realistic heat exchanger models are used. Several other multi-stage, multi-effect configurations have been developed to utilize high heat source temperatures, but the additional

complexity and slight increases in cycle performance has limited the practicality of such cycles.

The generator/absorber heat exchange cycles also utilize high temperature heat sources. These cycles use a single-stage configuration to provide multiple effects by expanding the temperature ranges of the generator and absorber. When the absorber and generator ranges overlap, internal heat exchange between the two is used to provide multiple effects. The basic GAX cycles have a temperature range and performance similar to the two-stage, double-effect cycles. Branched and vapor exchange GAX configurations have been developed to improve the internal heat exchange and therefore cycle performance.

Advanced absorption cycles therefore cover a broad range of application. A wide variety of heat sources can be utilized by the appropriate cycle to provide useful cooling.

2.1.2 Rankine/Vapor-Compression Cycles

The Rankine cycle is a power generation cycle, and must be coupled to another cycle to provide cooling. The obvious choice for a coupling cycle that converts work to cooling is the vapor-compression cycle and the majority of Rankine-driven cooling cycles are Rankine/vapor-compression cycles. The basic configuration for the cycle is shown in Fig. 26. The coupling is straightforward: the turbine of the Rankine cycle described in section 1.2.2 is used to provide the compressor power for the vapor-compression cycle described in section 1.3.

Prigmore and Barber [49] described a solar-driven Rankine/vapor-compression prototype, using R-12 for the vapor-compression portion and R-113 for the Rankine portion. The configuration of this 3-ton system was similar to the one shown in Fig. 26,

with the addition of a regenerative heat exchanger using the outlet stream of the turbine to preheat the stream entering the boiler. In addition, an electric generator is used as a backup system for the solar-driven Rankine loop. The turbine and generator are connected by an overrunning clutch to the compressor of the vapor-compression system. This allows the cooling system to be run by either solar power or electricity, as well as enabling the solar-driven production of 1-kW of electricity when cooling is not needed. When the solar collector temperature is 102°C, the cycle COP is 0.5. As the solar collector temperature drops to 80°C, the COP decreases to 0.3.

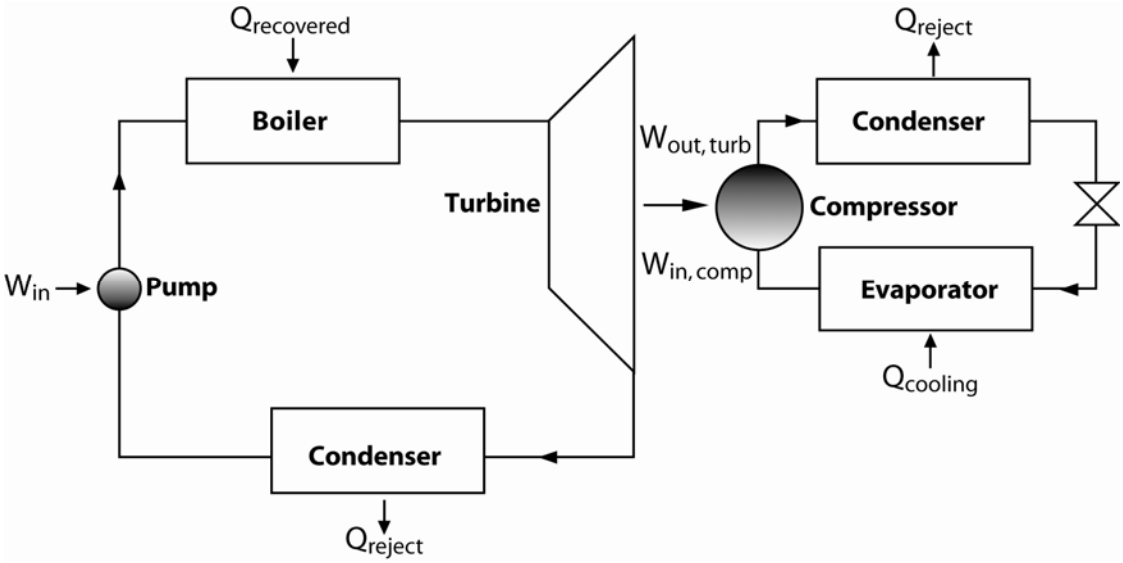

Fig. 26. Basic Rankine/vapor-compression cycle configuration.

A similar system was described by Lior [15], shown in Fig. 27. Lior added an additional recuperative heat exchanger, using the turbine outlet stream to heat the solar-collector outlet stream, and a fuel-powered superheater, upstream of the turbine, to the cycle described by Prigmore and Barber [49]. This solar-driven Rankine/vapor-compression cycle was considered in both cooling and heating modes, and includes an electric motor backup. The system did not provide electricity generation, a feature of

Prigmore and Barber's cycle. Under conditions similar to Prigmore and Barber's cycle with solar collector temperatures of ~100°C, the cooling COP of this cycle was 0.6. This is slightly better than Prigmore and Barber's cycle performance, due to the additional heating of the second RHX and superheater. However, the improvement may not justify the cost of the additional components. Compared to powering the heat pump with centralized electricity, Lior estimated 50-60% energy savings in the cooling mode. When comparing this cycle to conventional furnace heating, Lior estimated 3-4 fold energy savings in the heating mode.

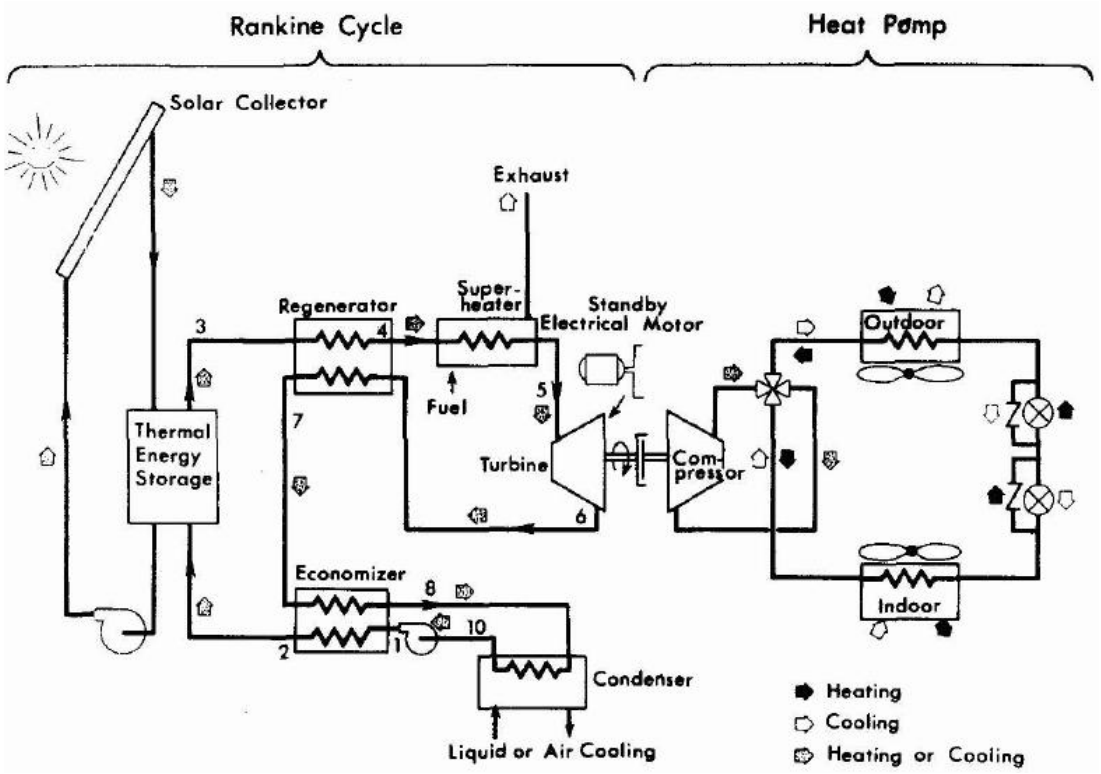

Fig. 27. Solar-driven Rankine/vapor-compression cycle configuration [15].

Christensen and Santoso [9] proposed a significant change to the Rankine cycle engine-driven heat pump. In this system, the Rankine power cycle uses R-113 as the working fluid and the vapor compression cycle heat pump uses R-22. The main development in this paper was the exchange of heat between the two cycles, as shown in

Fig. 28. As the working fluid of the vapor-compression cycle moves from the compressor to the condenser, heat is delivered to the Rankine loop. In the Rankine cycle, that heat is received upstream of the boiler to be further heated. The cycle was designed to be fuel-driven, instead of solar-driven, making comparison to the Prigmore and Barber [49] and Lior [15] results difficult. At roughly equivalent heat input temperatures (Rankine boiler temperature of 100°C), the cycle achieves a cooling COP of 0.65. This is only a slight improvement over the previous examples, but higher temperature heat sources yield increased cycle performance. At the boiler temperature design condition of 140°C, they predicted heating and cooling COPs of 2.01 and 1.06 respectively.

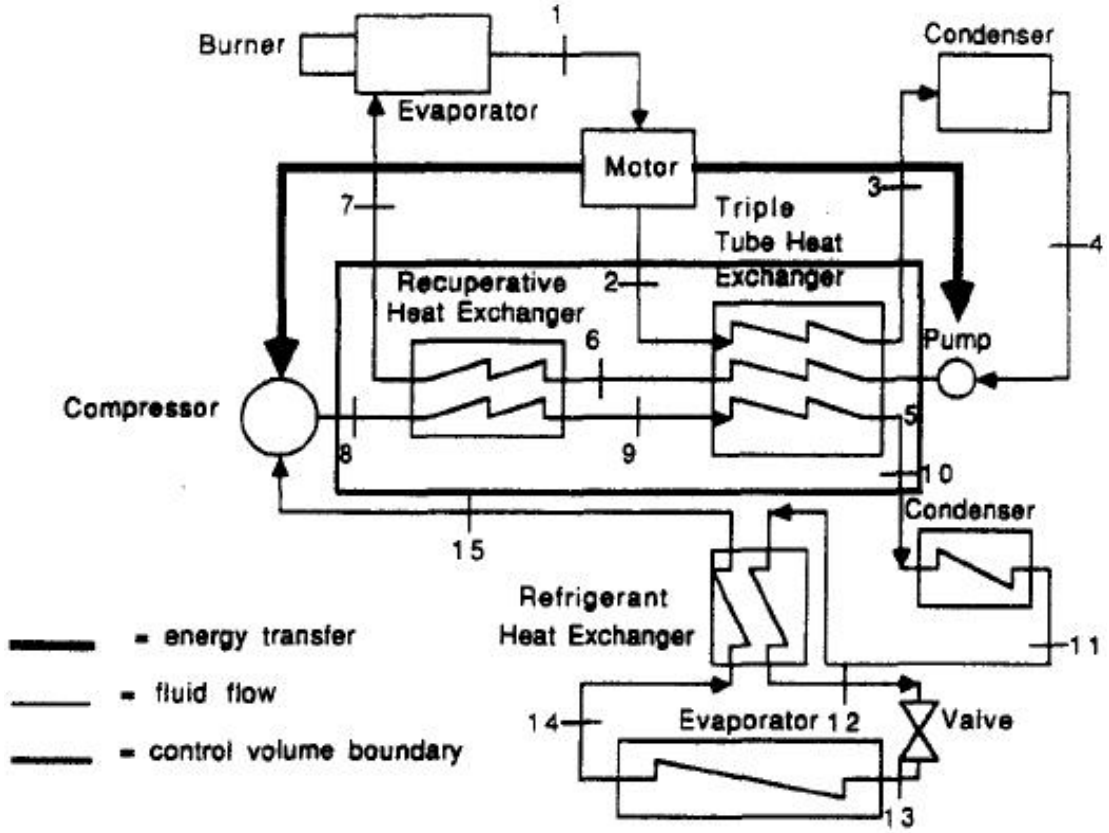

Fig. 28. Rankine/vapor-compression cycle configuration with recuperative heating between cycles [9].

A significantly different cycle was proposed by the Garrett Corporation [5] in an environmental control equipment design using a Rankine cycle to power a refrigeration cycle. In this Rankine/vapor-compression cycle, recuperative heating is abandoned in favor of integrating the cycles together and using one condenser. The system is shown in Fig. 29, with the Rankine portion of the system on the left and the vapor-compression loop on the right. The working fluid, R-11, is pumped as a liquid to the boiler pressure and heated to a vapor in the boiler. The vapor is expanded to the condenser pressure in a turbine coupled to a compressor. The compressor outlet stream of the cooling cycle is also at this same condenser pressure. The turbine and compressor outlets are mixed and condensed to liquid in the condenser. Directly after the condenser, the refrigerant is again separated into two streams in the receiver; one stream enters the pump of the Rankine loop, thus completing that cycle, and the other enters the vapor-compression cycle. The vapor-compression stream is expanded through a valve to the evaporator pressure, the lowest pressure of the system. The stream is evaporated to a vapor in the evaporator and enters the compressor side of the turbo-compressor, thus completing the vapor-compression loop. A detailed analysis of the cycle, including temperature, pressure, and cycle performance values, is not available. The only known design parameters are the nominal 17.6 kW of cooling and 35.2 kW of heating.

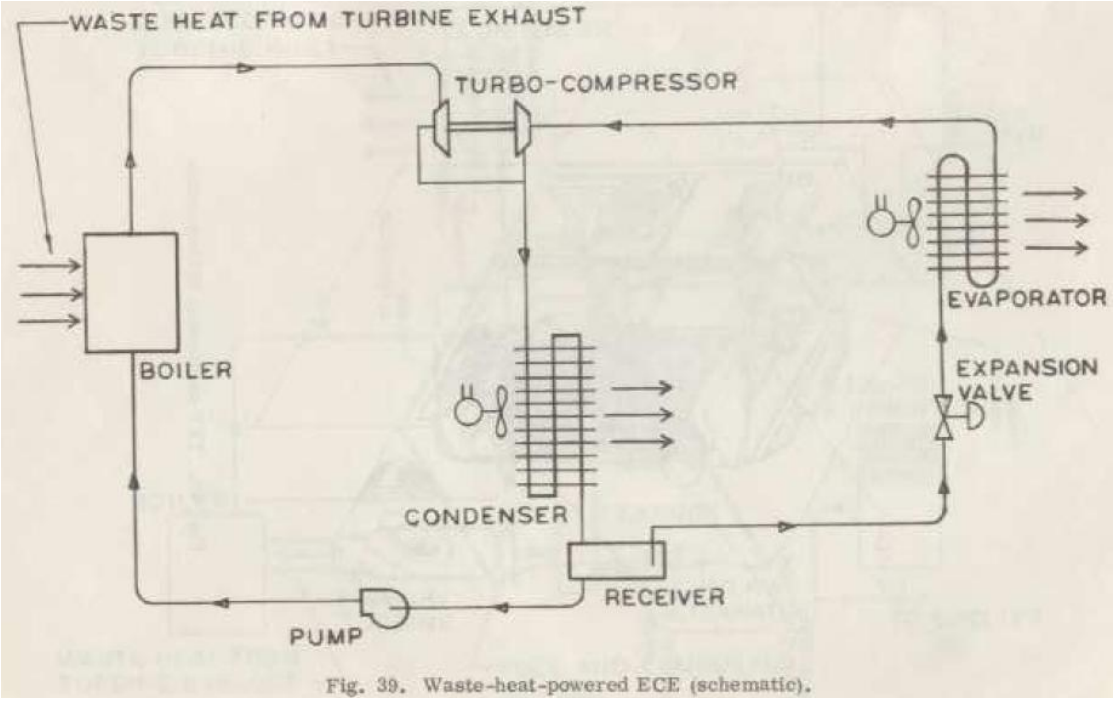

Fig. 29. Diagram of Rankine/Vapor-compression cycle designed in 1969 [5].

Wang et al. [17] evaluated this cycle for use as a portable cooling system. For portable applications, weight and size are important design variables. The authors minimized these variables by using microtechnology-based components: microchannel heat exchangers and a piston-based expander/compressor design. For a piston-based, miniature expander/compressor design, they cite expander and compressor efficiencies of 0.8 and 0.9, respectively. The cycle pressures dictated by this expander/compressor lead to the choice of isopentane for the working fluid. To increase cycle performance, they considered the effect of a regenerative heat exchanger in the power cycle. As shown in Fig. 30, the heat exchanger uses the expanded vapor exiting the turbine to preheat the compressed fluid entering the boiler, within the Rankine loop. This regenerative heating recovers underutilized heat from the expanded fluid. In a parametric study of superheat in the boiler, they discovered that cycle efficiency increases with superheat in the cycle with regenerative heating and decreases with increasing superheat in the basic cycle. The

regenerative heat exchanger recovers most of the extra heat input, leading to increased cycle performance. Without regenerative heating, the boiler input increases faster than the cooling capacity and cycle efficiency decreases. Due to this advantage, the regenerative heat exchanger allows for superheat and higher cycle efficiencies. To provide 150 W of cooling at 7°C, the regenerative cycle operates at a COP of 0.96 at boiler saturation temperatures of 116°C. With 111°C superheat (boiler temperature 227°C), the cycle reaches a predicted COP of 1.3. These cycle performance values are similar to values obtained by advanced absorption cycles utilizing similar heat source temperatures.

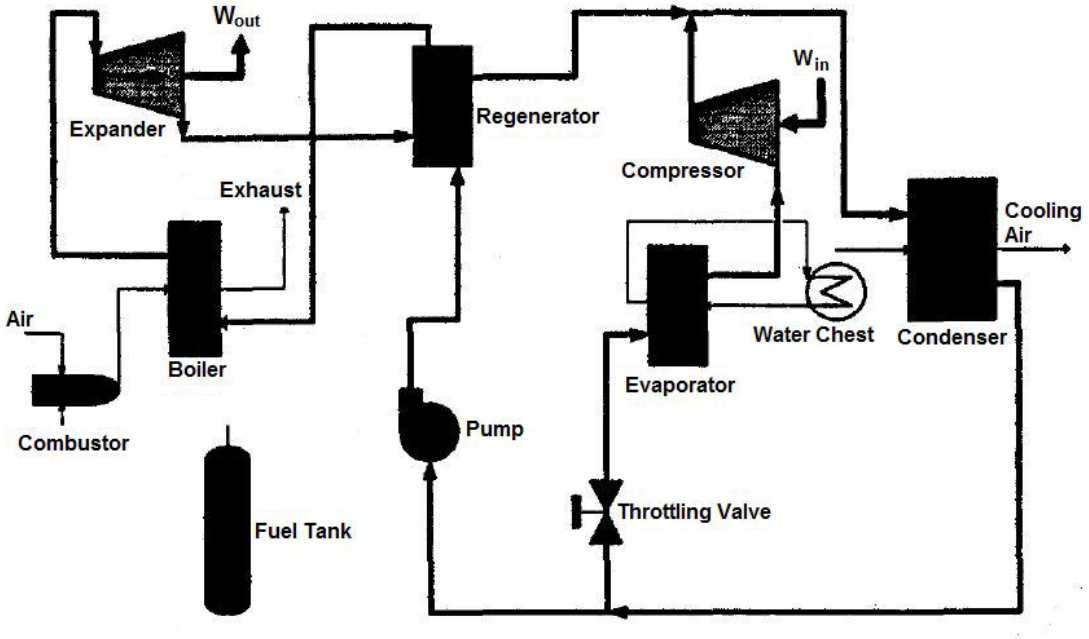

Fig. 30. Expander/compression heat pump diagram[17].

The studies by Wang et al. [17] were constrained by the goal to develop a miniature, portable system. A state-of-the-art magnetic bearing turbo-compressor described by Takizuka et al. [50] is too heavy for a portable application, but offers significant performance improvements. The analytical results of Takizuka et al. show a compressor efficiency of 90.5 percent and a turbine efficiency of 92.8 percent. These

state-of-the-art turbo-compressor efficiencies are higher than those used by Wang et al. in their cycle model. Wang et al. [17] describe an almost linear relationship between cycle efficiency and expander/compressor efficiency, so the COP of the cycle could be drastically raised by using a more efficient turbo-compressor. In addition, the turbo-compressor determines the vapor pressure properties required in the working fluid. Without the constraint of portability, more design freedom could be exercised in choosing the turbo-compressor which could allow a wider variety of choices for working fluid. Optimizing the turbo-compressor efficiencies and the working fluid properties should provide significant increases in cycle efficiency.

Finally, the miniaturization, portability goal also constrained the size of the condenser and evaporator in the cycle investigated by Wang et al. [17]. As condenser temperature drops, the cycle efficiency increases, but the size of the condenser must also increase to accommodate the smaller ΔT with the environment. As the evaporator temperature increases, more energy can be absorbed by the system, in latent heat and/or increased fluid mass flow rate, leading to increased cooling capacity. However, the evaporator size must also increase to accommodate the smaller ΔT between working fluid and heat source. If the evaporator and condenser are optimized for a non-portable application, which allows for larger components, the cycle efficiencies should rise over those shown by Wang et al. [17].

2.2 LOW-TEMPERATURE UTILIZATION

A major design choice in developing cycles to utilize low-temperature heat sources is choosing the proper refrigerant. In the case of absorption, with only two popular working pairs available, additional effort is needed to carefully balance design tradeoffs

when the operating conditions of the cycle approach the limits of the working pair solution fields.

2.2.1 Absorption

Using absorption cycles to upgrade waste heat was an idea first explored in the 1920s, and the practice remained a common application for absorption [22]. However, it was not until the energy crises of the 1970s that waste-heat utilization became a central point in the argument for absorption. Grossman and Perez-Blanco [51] considered the potential of absorption systems to recover low temperature waste heat at 60°C. Unlike the absorption cycles described here that provide useful cooling by utilizing a heat source, the absorption cycle considered by Grossman and Perez-Blanco converted a large low-temperature heat source into a smaller but higher temperature heat source. The resulting high-temperature heat source would then be used as process heat or perhaps used to drive another cycle. Grossman and Perez-Blanco considered both the water-lithium bromide and water-lithium chloride working pairs for this application, and found water-lithium bromide provided better results. Predicting a COP of 0.4 for a water-lithium bromide two-stage cycle, Grossman and Perez-Blanco endorse the technology for waste heat recovery. When considering the intent of this cycle, to recover wasted energy and provide a useful product, the low COP was promising because any amount of energy recovered would have otherwise been wasted.

Vliet et al. [52] investigated the influence of several variables on the performance of a low-temperature-driven water-lithium bromide, double-effect absorption cooling cycle providing chilled water at 6.7°C. They considered mass, species, and energy balances, as well as fluid flow, heat transfer, and mass transfer correlations, to

characterize the state of the refrigerant in each of the components. The variables investigated by Vliet et al. included coupling temperatures, flow rates, heat exchanger areas, two individual pumps, and the effect of orifice flow control. The heat source was varied from 104.5-160ºC. The maximum COP achieved was around 1.5, with a cooling water temperature of 24°C and a source hot water temperature of 104.5°C.

Vliet and Kim [53] investigated the double-effect absorption cycle in more depth, with a focus on optimizing the cycle. They determined that the best optimization process for the cycle considered COP, capacity, and cost. The resulting optimization values for heat exchanger areas were very different from typical values in practice: generator areas decreased 39-66%, condenser area increased 40%, evaporator area increased 12%, absorber area increased 19%, and recuperative heat exchanger areas increased 557-719% over typical values in practice. The COP increased from a nominal value of 1.2 to an optimized value of 1.5. Vliet and Kim's conclusion – that substantially more area should be allocated to the heat exchangers than the typical areas found in practice – highlights an important tradeoff. Increased heat exchanger surface areas do increase cycle performance, but also increase the cost, weight and size of the systems. Depending on the application, the additional cost and size of the system could negate the increased cycle performance obtained by this optimization.

Kaushik et al. [54] evaluated a double-effect water-lithium bromide system in a solar application. They discussed a trade-off in using a double-effect cycle for solar applications. The big concern for solar technology was efficiency; the same concern still plagues solar panels today. A double-effect cycle increases the efficiency of the overall system, but also requires a higher input temperature and the solar collector efficiency

decreases when operated at higher temperatures. Using a generator temperature of 87°C, they estimated that a double-effect cycle could maintain an evaporator temperature of 10°C with a COP of 1.65.

The low-temperature-driven absorption cycles discussed here use the water/LiBr working pair, which is the general choice for low-temperature heat recovery applications. The excellent thermal properties of water are especially useful in low-temperature applications when it is crucial that the energy extracted from the heat source is maximized. However, water is limited as a refrigerant by its relatively high freezing point (0°C). This limitation in turn limits the utilization of low-grade waste heat in applications requiring sub-zero cooling.

2.2.2 Rankine

There are several options for the Rankine cycle refrigerant and many authors concerned with low-temperature applications have discussed them in great detail [8, 27, 55]. Water is the predominant Rankine cycle working fluid, especially in primary energy power generation. However, a steam Rankine cycle does not efficiently utilize heat below 370°C. Organic working fluids can adapt the cycle to much lower input temperatures, making them suitable for waste-heat recovery. A crucial characteristic of a Rankine cycle working fluid is the saturation vapor curve [8]. When graphed on a temperature-entropy diagram, the slope of the saturation vapor curve of a fluid is either positive or negative. A negatively-sloped curve indicates a fluid that will tend to partially condense during the turbine expansion process. A positively-sloped "dry" fluid tends to remain a saturated vapor. Fluids that have a nearly vertical saturation vapor curve are very unlikely to condense and are termed "isentropic" fluids. Persistent saturation

throughout expansion is an extremely attractive quality for a Rankine cycle, as the enthalpy lost to condensation through the expansion process is avoided and maintenance related to moisture corrosion in the turbine is limited. Useful work is produced in the turbine by the increased velocity of the working fluid due to pressure and enthalpy decrease. Enthalpy reductions due to condensation do not produce useful work, and therefore represent a thermodynamic loss in the cycle which positively-sloped and isentropic fluids avoid. On the other hand, positively-sloped and "isentropic" fluids generally exhibit smaller enthalpy reductions due to expansion and therefore still produce less useful work despite avoiding losses to condensation. The advantage of reduced enthalpy drop over the turbine is that it allows a single-stage turbine to be used in ORCs instead of the multi-stage turbine needed for steam cycles, thereby simplifying the system. Organic fluids have lower heat capacities than water and tend to decompose and deteriorate at high temperatures and pressures. These properties decrease thermal performance and limit the range of applications for ORCs.

Hung et al. [8] reviewed the efficiencies of ORCs using benzene, ammonia, R11, R12, R134a and R113. The effect of turbine-inlet temperature on system efficiency for various working fluids in this study is shown in Fig. 31. The boiler pressure of each cycle is held constant at 2.5 MPa. The efficiency is a weak function of the turbine-inlet temperature when boiler pressure is held constant, i.e. an increase of superheat in the turbine inlet does not result in a significant increase in efficiency. Under these conditions, the choice of working fluid has significantly larger impact on system efficiency than increased superheat. For applications providing a turbine-inlet temperature greater than 227°C, benzene is the best refrigerant choice. Though water

appears to have higher efficiencies in this range, the volume ratio and enthalpy losses through the steam turbine make the benzene cycle less expensive and easier to implement. At temperatures between 187°C and 227°C, R113 is the best choice. Between 147°C and 187°C, R11 is best. Below 147°C, R12 prevails. However, many organic fluids such as R11 and R12 have very high CFC content, and have been phased out of use to combat global warming. As shown in Fig. 31, replacements such as R134a (substitute for R12) have similar performance characteristics but fall slightly short [8]. Fortunately, new refrigerants continue to be introduced with more and more favorable properties. In a recent refrigerant review, Saleh et al. [27] recommended the following refrigerants for low-temperature applications (<100°C): R236ea, R245ca, R245fa, R600, R600a, R601a, RE134, RE245, R143a, and R152a, which are all relatively new refrigerants.

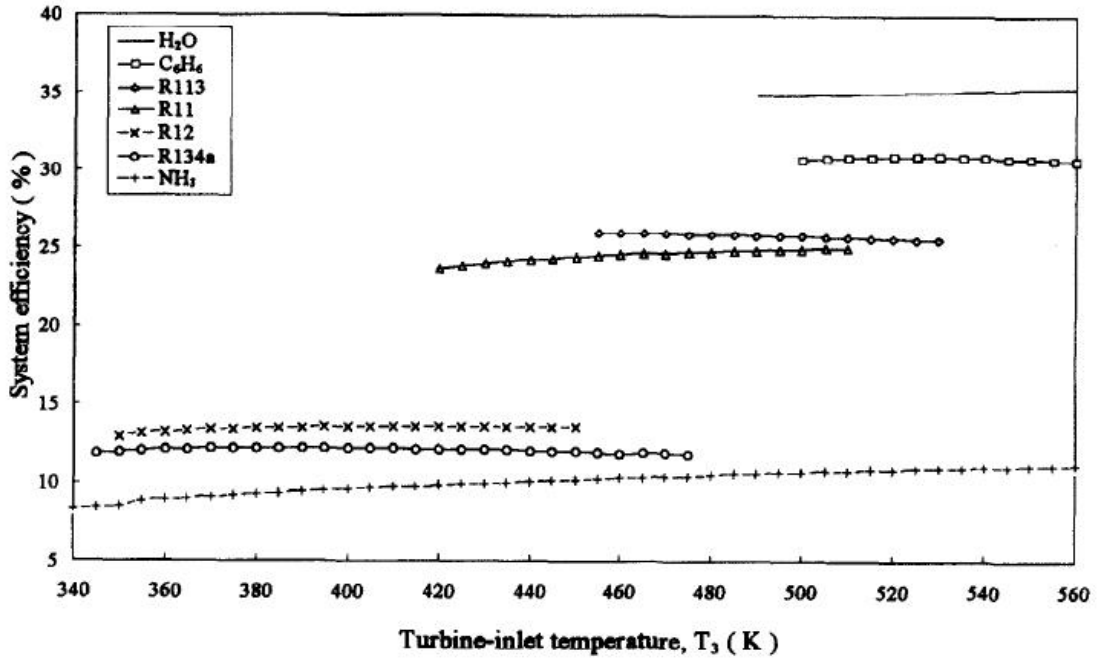

Fig. 31. Variations of ORC efficiencies as turbine-inlet temperature increases [8].

2.3 NEED FOR FURTHER RESEARCH

Advanced absorption and Rankine cycles have been developed to utilize low-temperature heat sources, in response to the growing appeal of waste heat utilization [56]. Another growing consideration is the effect of cycle working fluids on the environment. Further research into cycles that utilize low-grade heat and use environmentally benign working fluids may yield important contributions to the changing energy utilization landscape. Both absorption- and Rankine-based cycles can be further developed towards these goals.

In absorption, cycle designers are faced with the choice of ammonia/water or water/LiBr. As stated before, ammonia introduces some safety concerns and water cannot be used in sub-zero applications. In addition, water offers superior thermodynamic properties that are crucial to low-grade heat utilization. The cascaded absorption/vapor-compression cycle has the advantage of using water/LiBr while avoiding the freezing point issue and offering high COPs as well. This cycle utilizes waste heat to provide low-temperature cooling, medium-temperature space-conditioning, and water heating. Only non-toxic refrigerants are used: water-lithium bromide and carbon dioxide. One example of a sensitive environment that could not be served by an ammonia-water system is a naval ship. The proposed cycle can cut the fuel use of the ship without posing danger to the sailors or the environment.

Regarding the Rankine cycle, the new environmentally benign refrigerants have significantly improved thermal properties over the original replacement refrigerants for low-temperature applications. The integrated Rankine/vapor-compression cycle studied by the Garrett Corporation [5] and Wang et al. [17] may yield promising cycle

performance using one of the recommended new refrigerants, R245fa. Advances in turbo-compressor technology may also boost efficiency.

In view of the above discussion, the objectives for this work are the following:

- Develop accurate thermodynamic models of the cascaded absorption/vapor-compression cycle and coupled Rankine/vapor-compression cycle.
- Predict the cycle performance of each cycle over a range of postulated operating conditions.
- Determine the critical components of each cycle through parametric analysis.
- Evaluate the potential of each cycle in low-temperature applications.

PART ONE: CASCADED ABSORPTION/VAPOR-COMPRESSION CYCLE

CHAPTER THREE: CASCADE ABSORPTION/VAPOR-COMPRESSION CYCLE MODEL

The first cycle considered is the cascaded absorption/vapor-compression cycle (CAVC), described in previous chapters. A system simulation model that enables the prediction of component performance requirements given the cooling capacity needs for a range of anticipated operating conditions was developed. The anticipated conditions were determined for a particular application: a naval aircraft carrier. Although this is the intended application, the cycle and the modeling techniques can be adapted for a wide range of conditions that justify such cascaded arrangements. These conditions can greatly affect the cycle COP, as will be discussed in the next chapter. In this chapter, the development of the model will be discussed, including assumptions, cycle conditions, and results for the baseline case.

3.1 NAVAL AIRCRAFT CARRIER APPLICATION

A modern naval aircraft carrier has three distinct cooling and heating needs: high heat flux electronics cooling, air-conditioning, and water heating. Additionally, there is a large amount of waste heat available from the gas turbines used to propel the ship. The CAVC cycle can provide all three of the ship's needs using this available heat source and a minimal amount of additional electricity. Fig. 32 shows a conceptual flow diagram of the CAVC cycle, with major inputs, outputs, and heat transfer between cycles.

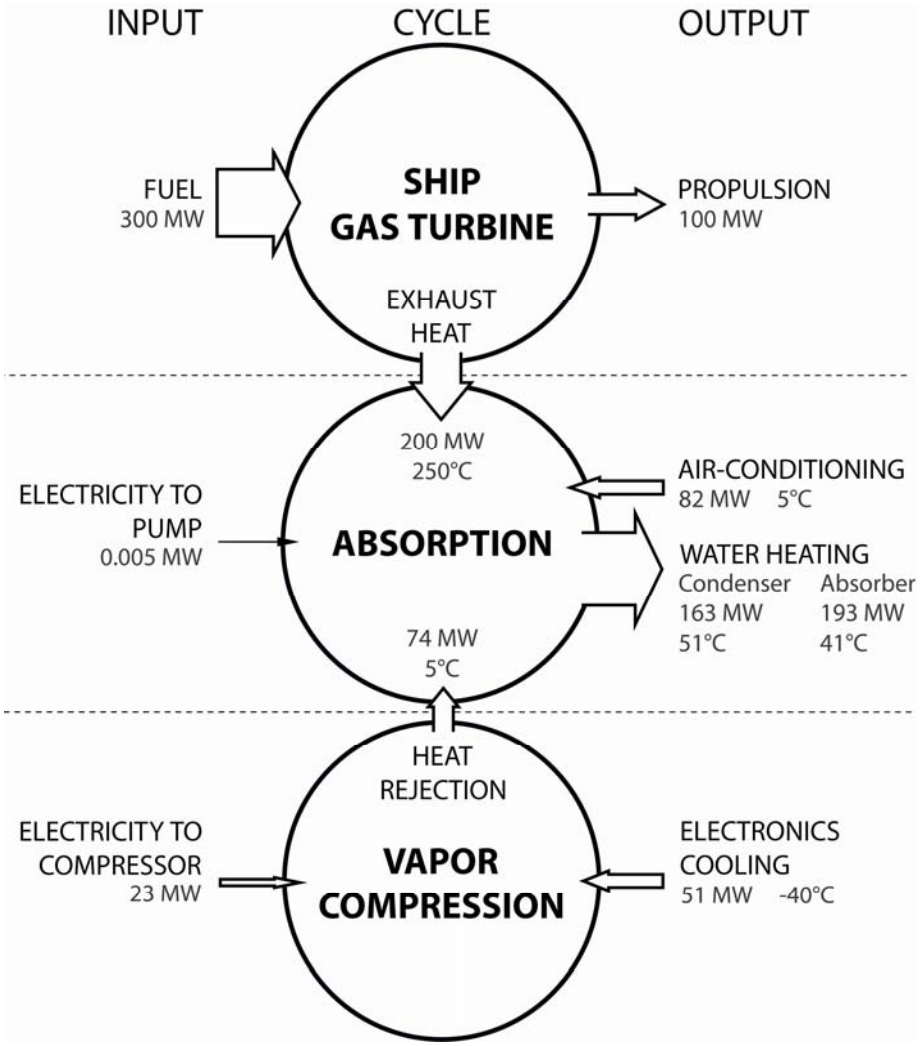

Fig. 32. Conceptual flow diagram of CAVC cycle.

The main design focus of the CAVC cycle in this study is effective electronics cooling. Advanced naval electronics require cooling at large heat fluxes over large surface areas, while maintaining low junction temperatures. Heat removal rates approach tens of Megawatts due to heat fluxes of ~1 kW/cm^2 acting over surfaces such as a nominal 1 m^2. For the cooling of shipboard electronics, although fundamental advances in chip, interface, and convective cooling could reduce the thermal resistances significantly, these alone will be inadequate for meeting the target of removing 1 kW/cm^2 over areas of the order of m^2. Even the most optimistic projections of decreases in

thermal resistance *R"* through advances in heat removal techniques, and increases in surface area *A* from the chip-to-ship progression do not enable dissipation of 1 kW/cm^2 over large areas while operating within the 35-50°C range. Therefore, a third dimension, i.e, reduced heat sink temperature, is essential to address the heat rejection problem. A nominal temperature of -40°C was chosen for the low-temperature coolant of the CAVC cycle, based on the consideration that such low coolant temperatures will enable cooling of the high flux electronic components to a desired temperature of 50°C with plausible technical advances in *R"* and *A*.

The cascade cycle also allows for air-conditioning and water heating as auxiliary functions. The absorption loop of the CAVC cycle can provide air-conditioning, through a double evaporator system that is described in more detail in the following chapters. Water heating is provided by the heat rejected by the absorber and condenser of the absorption loop.

Advanced naval ships require as much as ~100 MW of propulsive power, which translates to a thermal energy input to the gas turbines of ~300 MW, resulting in ~ 200 MW of wasted heat. The CAVC cycle utilizes this waste heat to supply a major portion of the cooling needs stated above, without any appreciable additional expenditure of fuel for generating power for cooling. Although much higher waste heat temperatures may be available in such ships, to limit the system to relatively simple single-effect absorption cycles, a waste heat temperature range of 175-275°C was chosen for this analysis, along with a heat input rate of 200 MW at the desorber.

One of the other significant advantages of implementing such waste heat driven cooling in naval ships is the proximity of an excellent heat sink: the ocean. Thus, the

heat of absorption and condensation is rejected to the sea water through a closed coolant loop. This cooling loop can also be used for the auxiliary water heating function of the cycle. The design conditions for heat rejection temperature used here were typical sea water temperatures of 25-40°C. This range roughly corresponds to the sea water temperatures from New England to the Middle East.

Table 3. Cycle Design Specifications.

Component	UA [MW/K]	Coupling Fluid Flow Rate [kg/s]	Coupling Fluid Inlet Temperature [°C]	Load [MW]
Absorber	35	8458	38.00	193
Condenser	33	8458	43.46	163
Coupled Evaporator/Condenser	25			74
Water Evaporator	15	4208	14.00	82
Desorber	3	1606	250.00	200
Recuperative Heat Exchanger (RHX)	0.4			5
Sea Heat Rejection	118	8466	35.00	356
Solution Heat Exchanger (SHX)	6			72
Compressor				23
Note: Shaded values are not set parameters, but rather values determined by the set parameters				

3.2 MODEL INPUTS: ASSUMPTIONS, DESIGN CONDITIONS AND COMPONENT SELECTIONS

The naval ship application provides the specific range of cycle conditions discussed above: 200 MW of waste heat input to the desorber (at 175-275°C), a heat rejection temperature equal to sea temperature (25-40°C), and the need for -40°C cooling temperatures. To conduct the analysis of the CAVC cycle, a baseline system coupling layout, several input parameters, operating conditions, and heat exchanger sizes have to be chosen and specified. Several of these key parameters are summarized in Table 3. The conceptual flow diagram of the CAVC cycle (Fig. 32) illustrates major input and output values of the baseline conditions. For the present analysis, the baseline system was assumed to receive waste heat input to the desorber directly from the exhaust gas

stream, without an intermediate heat transfer fluid loop. A representative value of 250°C was chosen as the exhaust gas temperature for the baseline case, but it should be noted that single-effect gas fired absorption systems can function with heat input temperatures as low as ~125°C. A flow rate of 1606 kg/s (2381 m^3/s) was chosen to enable a nominal waste heat input of 200 MW across an exhaust stream temperature drop of 122°C. The absorber and condenser are coupled to a hydronic fluid (50% ethylene glycol water mixture) stream in series. Thus, the hydronic fluid first receives the heat of absorption, and is then further heated in the condenser. Other alternatives considered here include condenser upstream of the absorber, and absorber and condenser in parallel, based on the design objective and operating conditions under consideration. The ethylene glycol-water solution that serves as the hydronic fluid can also be changed to water (which has the advantage of resulting in a smaller temperature difference for the same heat duty), depending on the actual application under consideration. The loop is coupled to ambient sea water at a worst-case-scenario temperature of 35°C. A nominal (total) 10°C rise in temperature across the absorber and condenser is used to determine the coolant flow rate in the closed loop as well as the open-loop sea water flow rate, which yields a nominal volumetric flow rate of 8.5 m^3/s (135,000 gpm) in each loop. Given these flow rates, the absorber and condenser coolant temperatures settle to values dictated by the sea water inlet temperature and the specified heat exchanger *UA*s. The pumped dilute LiBr-H_2O solution flow rate is set at 700 kg/s. Low flow rates are desired so that a larger fraction of the waste heat input is used to generate refrigerant (and therefore high COPs) rather than wasteful sensible heating of the solution, but at low enough solution flow rates, the concentration of the concentrated solution exiting the desorber exceeds the limits that

lead to crystallization. The value chosen here represents a tradeoff that yields the best COPs possible with the vapor-liquid equilibrium characteristics of the LiBr-H_2O fluid pair while preventing crystallization. The CO_2 vapor-compression cycle compressor power input determines the fraction of the absorption cycle refrigerating effect that is used as the heat sink for low temperature cooling. For the baseline case, the compressor load is set at 23 MW, which corresponds to a coupled evaporator outlet quality of 0.5, and roughly corresponds to an equal utilization of absorption cycle refrigerant for medium-temperature cooling and for providing a heat sink to the CO_2 cycle.

Without *a priori* knowledge of heat exchanger sizes necessary to achieve the desired heat transfer in each component that meets system performance requirements, an estimate of the acceptable closest approach temperature difference (*CAT*) between the respective streams of each heat exchanger is used as a specification for most of the heat exchangers. The larger the *CAT*, the smaller the size of the heat exchanger required, and vice versa. A large *CAT*, however, reduces the available temperature difference between source and sink in the cycle, and leads to lower system performance. On the other hand, a low *CAT* specification implies a large heat exchanger size and capital cost. Based on these considerations, a *CAT* of 3°C was chosen for the desorber, condenser, evaporator and absorber. The counterflow solution heat exchanger and the recuperative refrigerant heat exchanger were assumed to have a heat exchanger effectiveness of 90%. Once the system computations converged with these assumed *CAT*s and effectivenesses, the *UA* values required to achieve this performance were calculated and substituted as fixed input specifications for further analyses. It should be noted that these specifications are necessarily of a single-point type, and represent a first-order analysis of the overall

system. However, they do capture, in adequate measure, the driving potentials required for the interactions between the streams exchanging heat and/or mass, and also the effects of irreversible heat exchange between the source/sink and the working fluid across temperature differences that represent realistic component performances. Representing components with varying thermal capacities by a unique value of *UA* constitutes an approximation to facilitate a preliminary estimation of system performance.

The calculated *UA* values can provide some estimation of the size of components needed. To obtain an estimation of *A* in this manner, a value for *U* must be determined. Precise calculations of *U* cannot be completed without a considerable level of detailed component design, i.e., tube diameters, number of tubes, etc. However, some typical *U* values can be found in the literature and used for very rough, first approximation calculations. Perry's Chemical Engineers' Handbook [6] provides ranges of typical *U* values for a wide variety of heat transfer equipment, taking into account the heat transfer media. An abbreviated set of typical *U* values listed in this resource is provided in Table 4. This generic listing does not provide an exact match for each component in the CAVC cycle; for example, the H_2O evaporator/CO_2 condenser presents a situation that is not directly listed in the typical values. In such cases, typical values for the limiting medium were used. From the range of *U* values provided for the relevant media in a tubular heat exchanger, the highest value was used to estimate the *A* of the CAVC components. The most efficient heat transfer value provided was used to reflect the inclusion of highly efficient microchannel-based components in the cycle. The typical values obtained from Perry's Chemical Engineers' Handbook and the resulting estimation of *A* are tabulated in Table 5. The reference numbers listed in Table 5 correspond with the numbering in

Table 4, to clearly show the source of the *U* values used for each component. The heat transfer surface area estimates are quite large, but could possibly be translated to more manageable component sizes through the use of microchannels and compact heat exchanger configurations. Precise *U* calculations may also decrease the estimated component size.

Table 4. Typical Overall Heat-Transfer Coefficients in Tubular Heat Exchangers [6].

Type	Ref. #	Shell Side	Tube Side	Design *U* [Btu/(°F·ft2·hr)]
Liquid-liquid	1	Water	Water	200-250
	2	Organic solvents	Water	50-150
	3	Organic solvents	Organic solvents	20-60
Condensing vapor-liquid	4	Steam	Water	400-1000
	5	Low-boiling hydrocarbons (atmospheric)	Water	80-200
	6	High-boiling hydrocarbons (vacuum)	Water	20-50
	7	Organic solvents (atmospheric)	Water	100-200
Gas-liquid	8	Water	Air, N_2, etc. (compressed)	20-40
	9	Water	Air, N_2, etc. (atmospheric)	5-20
	10	Air, N_2, etc. (compressed)	Water	40-80
	11	Air, N_2, etc. (atmospheric)	Water	10-50
Vaporizers	12	Propane, butane, etc.	Steam condensing	200-300
	13	Water	Steam condensing	250-400

Source: Typical Overall Heat-Transfer Coefficients in Tubular Heat Exchangers, Perry's Chemical Engineers' Handbook (7th Edition)

Table 5. Estimated CAVC Component Heat Transfer Surface Areas

Heat Exchanger	Ref. #	Typical U [Btu/(°F·ft^2·hr)]	Typical U [W/(m^2·K)]	UA [W/K]	Heat Transfer Surface Area, A [m^2]
Refrigerant Heat Exchanger (RHX)	11	50	284	398,000	1,400
Solution Heat Exchanger (SHX)	1	250	1,420	6,178,000	4,400
Absorber	4	1000	5,678	34,678,000	6,100
Condenser	4	1000	5,678	32,906,000	5,800
Generator	9	20	114	2,660,000	23,400
Evaporator/Condenser	4	1000	5,678	24,689,000	4,300
H_2O Evaporator	4	1000	5,678	15,013,000	2,600
Sea Heat Exchanger	1	250	1,420	118,483,000	83,500

Note: Typical overall heat transfer coefficients are taken from Perry's Chemical Engineers' Handbook (7th Edition)
The highest U value (i.e., 1000 Btu/hr-ft^2-F) was chosen for phase-change heat exchangers coupled either to single-phase liquids or to phase-change processes to reflect the anticipated high heat transfer coefficients due to phase change of H_2O and CO_2.

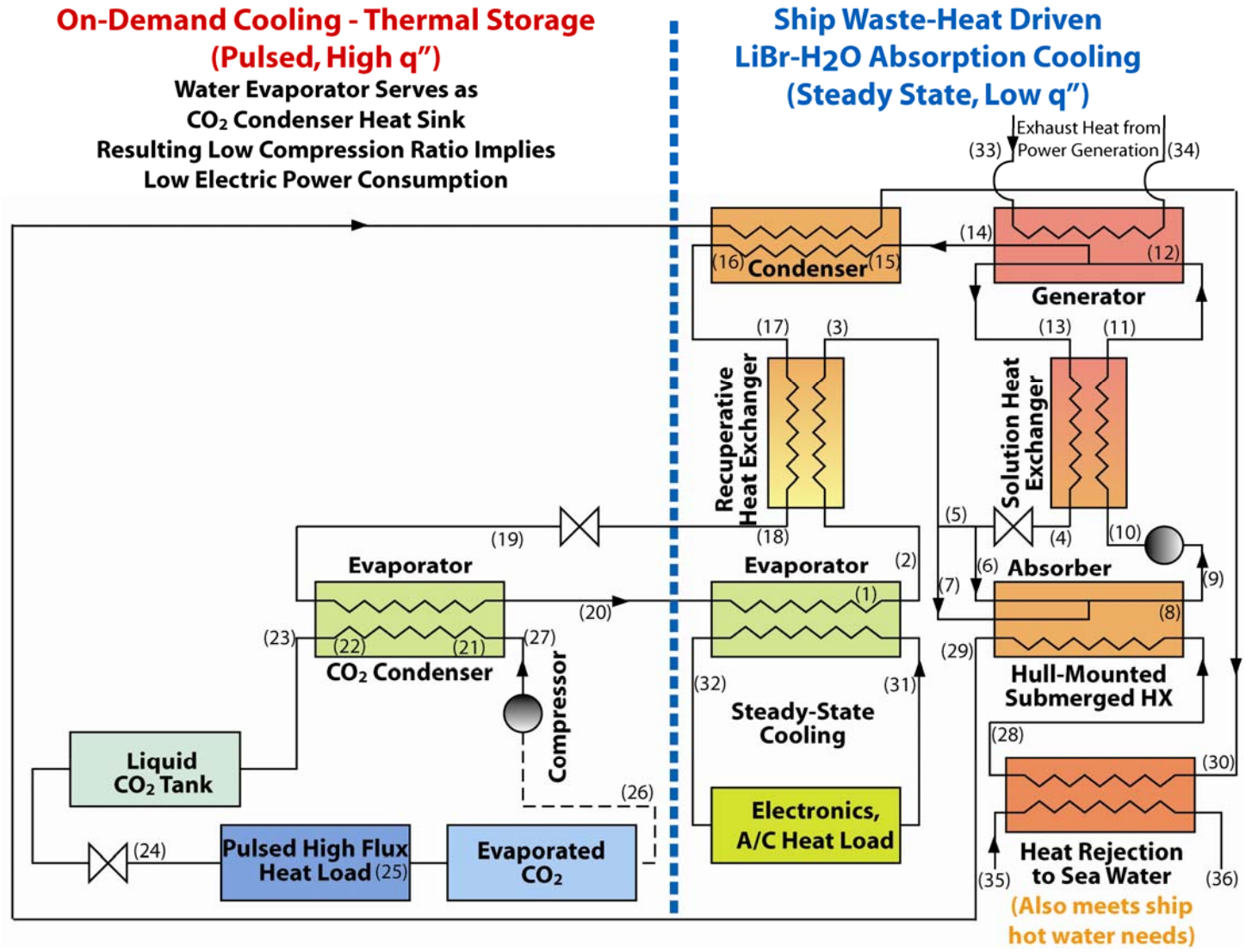

Fig. 33. The schematic diagram of the cascaded absorption/vapor-compression system.

Table 6. State points for the baseline CAVC system (Fig. 33).

State Point	LiBr Concentration [%]	Temperature [C]	Enthalpy [kJ/kg]	Mass Flow Rate [kg/s]	Pressure [kPa]	Quality	Entropy [kJ/kg-K]	Specific Volume [m^3/kg]
1		5.00	2510.08	65.6	0.87	1.000		
2		8.00	2515.73	65.6	0.87			
3		44.97	2585.02	65.6	0.87			
4	64.9	46.02	155.94	634.4	13.03			
5		52.76	2599.09	-2.7	0.87			
6	64.6	52.76	166.34	637.1	0.87			
7		44.64	2584.41	62.9	0.87			
8	58.8	41.00	111.58	700.0	0.87			
9	58.8	39.00	107.66	700.0	0.87			0.0006
10	58.8	39.00	107.67	700.0	13.03			
11	58.8	91.22	210.20	700.0	13.03			
12	58.8	94.21	216.09	700.0	13.03			
13	64.9	109.11	269.08	634.4	13.03			
14		101.66	2690.27	65.6	13.03			
15		51.07	2593.19	65.6	13.03	1.000		
16		51.07	213.83	65.6	13.03	0.000		
17		49.07	205.47	65.6	13.03			
18		32.50	136.18	65.6	13.03			
19		5.00	136.18	65.6	0.87	0.046		
20		5.00	1265.51	65.6	0.87	0.500		
21		8.00	-81.89	227.8	4283.00	1.000		
22		8.00	-286.44	227.8	4283.00	0.000		
23		6.00	-292.05	227.8	4283.00			
24		-40.00	-292.05	227.8	1004.52	0.316		
25		-40.00	-71.46	227.8	1004.52	1.000		
26		-38.00	-69.40	227.8	1004.52		-0.68	
27		94.01	33.05	227.8	4283.00		-0.58	
28		38.00		8458.0	413.69			
29		43.46		8458.0	413.69			
30		48.07		8458.0				
31		14.00		4208.0				
32	50.0	8.00		4208.0				
33		250.00		1606.0				
34		128.21						
35		35.00		8466.0	101.30			
36		45.06						

3.3 CAVC CYCLE DESCRIPTION AND BASELINE RESULTS

The detailed operation of the CAVC cycle is described here, along with baseline operating parameters. The CAVC system was modeled in the *Engineering Equation Solver* (EES) Software [30] platform by computing mass, species and energy conservation equations for each component shown schematically in Fig. 33. The properties of the working fluid at each state point of Fig. 33 are detailed in Table 6.

H_2O/LiBr Absorption Loop

Dilute H_2O/LiBr solution exits the absorber at state (9). The dilute solution concentration (58.82% LiBr) is determined by the absorber saturation temperature (41°C), which is in turn set by the heat rejection temperature (35°C). In addition, a saturation pressure is needed to obtain the concentration. This is established at the evaporator.

At state (9), the dilute solution has been subcooled by 2°C to 39.00°C:

$$T_9 = T_8 - \Delta T_{\text{subcool, absorber}} \tag{3.1}$$

$$39°\text{C} = 41°\text{C} - 2°\text{C}$$

This dilute, subcooled solution flows through the solution pump and exits at state (10), at the high-side pressure established at the condenser. The advantage of an absorption cycle lies in the relatively small amount of electricity required by the solution pump; by accomplishing the pressure rise in the liquid phase, the absorption cycle avoids the work-intensive compression of high specific volume vapor required in vapor-compression cycles. The pump sets the solution flow rate at 700 kg/s, and consumes a minuscule 5.14 kW:

$$v_9 = v_{\text{LiBr}}\left(T_9, x_9\right) \tag{3.2}$$

$$0.0006038\,\frac{\mathrm{m}^3}{\mathrm{kg}} = v_{\mathrm{LiBr}}\left(39°\mathrm{C},\,58.82\%\right)$$

$$W_{\mathrm{Pump}} = v_9 m_9\left(p_{10} - p_9\right) \tag{3.3}$$

$$5.14\ \mathrm{kW} = 0.0006038\,\frac{\mathrm{m}^3}{\mathrm{kg}} \cdot 700\,\frac{\mathrm{kg}}{\mathrm{s}} \cdot \left(13.03\ \mathrm{kPa} - 0.87\ \mathrm{kPa}\right)$$

$$W_{\mathrm{Pump}} = m_9\left(h_{10} - h_9\right) \tag{3.4}$$

$$5.14\ \mathrm{kW} = 700\,\frac{\mathrm{kg}}{\mathrm{s}} \cdot \left(107.66638\,\frac{\mathrm{kJ}}{\mathrm{kg}} - 107.65905\,\frac{\mathrm{kJ}}{\mathrm{kg}}\right)$$

The dilute solution temperature rises slightly (by 0.004°C) as it flows through the pump:

$$h_{10} = h_{\mathrm{LiBr}}\left(T_{10}, x_{10}\right) \tag{3.5}$$

$$107.66638\,\frac{\mathrm{kJ}}{\mathrm{kg}} = h_{\mathrm{LiBr}}\left(39.004°\mathrm{C},\,58.82\%\right)$$

The flow rate directly sets the cycle recirculation ratio, and affects the outlet concentration from the desorber; it was chosen to optimize cycle performance while avoiding crystallization in the concentrated solution.

After exiting the pump, the dilute solution is recuperatively heated to state (11) in the solution heat exchanger (SHX). The dilute solution then enters the desorber at 58.82% LiBr concentration and a temperature of 91.22°C. Thermal energy is provided to the dilute solution stream in the desorber using the waste heat gas stream entering at state (33) and leaving at state (34). Based on the input specifications and assumptions detailed above, the waste gas stream enters the desorber at 250°C and is cooled to 128.21°C:

$$Q_{\text{Exhaust Input}} = m_{33} c_{\mathrm{p,Exhaust}}\left(T_{33} - T_{34}\right) \tag{3.6}$$

$$200\ \mathrm{MW} = 1606\,\frac{\mathrm{kg}}{\mathrm{s}} \cdot 1.022\,\frac{\mathrm{kJ}}{\mathrm{kg}\cdot\mathrm{K}} \cdot \left(250°\mathrm{C} - 128.21°\mathrm{C}\right)$$

Initial heating in the desorber raises the solution temperatures to the saturation value, i.e., 94.21°C at state (12):

$$T_{12} = T_{\text{LiBr}}\left(p_{12}, x_{12}\right) \tag{3.7}$$

$$94.21°\text{C} = T_{\text{LiBr}}\left(13.03\ \text{kPa},\ 58.82\%\right)$$

The desorber then generates 65.59 kg/s of superheated water vapor that exits the desober at state (14). The desorber heat duty is 200 MW.

$$Q_{\text{Exhaust Input}} = m_{13}h_{13} + m_{14}h_{14} - m_{11}h_{11} \tag{3.8}$$

$$200\ \text{MW} = 634.4\frac{\text{kg}}{\text{s}}\cdot 269.1\frac{\text{kJ}}{\text{kg}} + 65.59\frac{\text{kg}}{\text{s}}\cdot 2690.3\frac{\text{kJ}}{\text{kg}} - 700\frac{\text{kg}}{\text{s}}\cdot 210.2\frac{\text{kJ}}{\text{kg}}$$

The remaining concentrated solution exits at state (13), at 64.90% LiBr concentration and 109.11°C, and enters the recuperative solution heat exchanger to provide heating for the desorber inlet stream (11).

$$h_{13} = h_{\text{LiBr}}\left(T_{13}, x_{13}\right) \tag{3.9}$$

$$269.1\frac{\text{kJ}}{\text{kg}} = h_{\text{LiBr}}\left(109.1°\text{C},\ 64.9\%\right)$$

$$T_{13} = T_{\text{LiBr}}\left(p_{13}, x_{13}\right) \tag{3.10}$$

$$109.1°\text{C} = T_{\text{LiBr}}\left(13.03\ \text{kPa},\ 64.90\%\right)$$

The log mean temperature difference (*LMTD*) is used to calculate the *UA* of the desorber. The saturated inlet and concentrated solution outlet temperatures are used in calculating the *LMTD* because the desorber heat duty is dominated by the phase-change portion of the total duty. The *UA* is then set constant at the resulting 2.7 MW/K:

$$LMTD\left(T_{33}, T_{34}, T_{12}, T_{13}\right) = \frac{\left(T_{33} - T_{13}\right) - \left(T_{34} - T_{12}\right)}{\ln\left\{\left(T_{33} - T_{13}\right)/\left(T_{34} - T_{12}\right)\right\}} \tag{3.11}$$

$$75.19°\text{C} = \frac{\left(250.00°\text{C} - 109.11°\text{C}\right) - \left(128.21°\text{C} - 92.21°\text{C}\right)}{\ln\left(\frac{250.00°\text{C} - 109.11°\text{C}}{128.21°\text{C} - 92.21°\text{C}}\right)}$$

$$Q_{\text{Exhaust Input}} = UA_{\text{Exhaust Input}} LMTD\left(T_{33}, T_{34}, T_{12}, T_{13}\right) \tag{3.12}$$

$$200\ \text{MW} = 2.7\frac{\text{MW}}{\text{K}} \cdot 75.19°\text{C}$$

The solution heat exchanger cools the concentrated LiBr solution stream exiting the desorber, while heating the dilute solution exiting the pump before it enters the desorber. An effectiveness of 90% is assumed for this component, yielding a heat duty of 72 MW:

$$h_{\text{SHX,hot}} = h_{\text{LiBr}}\left(T_{10}, x_{13}\right) \tag{3.13}$$

$$143.4\frac{\text{kJ}}{\text{kg}} = h_{\text{LiBr}}\left(39°\text{C},\ 64.9\%\right)$$

$$h_{\text{SHX,cold}} = h_{\text{LiBr}}\left(T_{13}, x_{10}\right) \tag{3.14}$$

$$245.4\frac{\text{kJ}}{\text{kg}} = h_{\text{LiBr}}\left(109.11°\text{C},\ 58.82\%\right)$$

The maximum possible heat duty on either side of the heat exchanger is calculated as follows:

$$Q_{\text{max,SHX hot}} = m_{13}\left(h_{13} - h_{\text{SHX,hot}}\right) \tag{3.15}$$

$$80\ \text{MW} = 634\frac{\text{kg}}{\text{s}}\left(269\frac{\text{kJ}}{\text{kg}} - 143\frac{\text{kJ}}{\text{kg}}\right)$$

$$Q_{\text{max,SHX cold}} = m_{10}\left(h_{\text{SHX,cold}} - h_{10}\right) \tag{3.16}$$

$$96\ \text{MW} = 700\frac{\text{kg}}{\text{s}}\left(245\frac{\text{kJ}}{\text{kg}} - 108\frac{\text{kJ}}{\text{kg}}\right)$$

From these values of the maximum heat duty and the assumed heat exchanger effectiveness, the actual solution heat exchanger duty is cacluated to be 72 MW:

$$Q_{\text{min,SHX}} = \min\left(Q_{\text{max,SHX hot}}, Q_{\text{max,SHX cold}}\right) \tag{3.17}$$

$$Q_{\text{SHX}} = \varepsilon_{\text{SHX}} Q_{\text{min,SHX}} \tag{3.18}$$

$$72\ \text{MW} = 90\% \cdot 80\ \text{MW}$$

Based on this heat duty, the dilute solution exiting the pump is heated from 39.00°C to the desorber inlet temperature of 91.22°C:

$$Q_{\text{SHX}} = m_{10}\left(h_{11} - h_{10}\right) \tag{3.19}$$

$$72\ \text{MW} = 700\frac{\text{kg}}{\text{s}}\left(210\frac{\text{kJ}}{\text{kg}} - 108\frac{\text{kJ}}{\text{kg}}\right)$$

Similarly, the concentrated LiBr solution stream exiting the desorber is cooled from 109.11°C to 46.02°C:

$$Q_{\text{SHX}} = m_{13}\left(h_{13} - h_{4}\right) \tag{3.20}$$

$$72\ \text{MW} = 634.4\frac{\text{kg}}{\text{s}}\left(269\frac{\text{kJ}}{\text{kg}} - 156\frac{\text{kJ}}{\text{kg}}\right)$$

The *UA* required to accomplish this heat duty in the SHX is 6.2 MW/K:

$$Q_{\text{SHX}} = UA_{\text{SHX}} LMTD\left(T_{13}, T_4, T_{10}, T_{11}\right) \tag{3.21}$$

$$72\ \text{MW} = 6.2\frac{\text{MW}}{\text{K}} \cdot 11.62°\text{C}$$

The concentrated solution stream exiting the solution heat exchanger, state (4), expands across the expansion valve from the high-side pressure (13.03 kPa) to the low-side pressure (0.87 kPa). The concentrated solution exits the valve and mixes with the vapor stream from the refrigerant heat exchanger (RHX) in the absorber, thus completing

the solution loop of the absorption cycle. The mixing process is modeled in detail; the results are further explained at a later point in this discussion.

The vapor generated by the desorber enters the refrigerant loop, state (14), at a superheated temperature of 101.66°C. As vapor is desorbed at varying temperatures through the desorber, the superheated vapor temperature is chosen as the average of the desorber saturation and outlet solution temperatures:

$$T_{14} = \frac{T_{13} + T_{12}}{2} \tag{3.22}$$

$$101.66°\text{C} = \frac{94.2°\text{C} + 109.1°\text{C}}{2}$$

Upon entering the condenser, the desorbed vapor is cooled to a saturated vapor at 51.07°C, represented by state (15):

$$T_{15} = T_{\text{H}_2\text{O}}\left(p_{15}, q_{15}\right) \tag{3.23}$$

$$51.07°\text{C} = T_{\text{H}_2\text{O}}\left(13.03\ \text{kPa}, 1\right)$$

The corresponding desuperheating duty is 6.4 MW:

$$Q_{\text{Condenser,Desup}} = m_{14}\left(h_{14} - h_{15}\right) \tag{3.24}$$

$$6.4\ \text{MW} = 65.59\frac{\text{kg}}{\text{s}}\left(2690\frac{\text{kJ}}{\text{kg}} - 2593\frac{\text{kJ}}{\text{kg}}\right)$$

The saturated vapor is then condensed to a saturated liquid, represented by state (16):

$$Q_{\text{Condenser,Sat}} = m_{15}\left(h_{15} - h_{16}\right) \tag{3.25}$$

$$156\ \text{MW} = 65.59\frac{\text{kg}}{\text{s}}\left(2593\frac{\text{kJ}}{\text{kg}} - 214\frac{\text{kJ}}{\text{kg}}\right)$$

A subcooling of 2°C is assumed at the condenser outlet, state (17):

$$T_{17} = T_{16} - \Delta T_{\text{Sub,Cond}} \tag{3.26}$$

$$49.07°\text{C} = 51.07°\text{C} - 2°\text{C}$$

The corresponding subcooling duty is 0.6 MW:

$$Q_{\text{Condenser,Sub}} = m_{16}\left(h_{16} - h_{17}\right) \tag{3.27}$$

$$0.6\text{ MW} = 65.59\frac{\text{kg}}{\text{s}}\left(214\frac{\text{kJ}}{\text{kg}} - 206\frac{\text{kJ}}{\text{kg}}\right)$$

Based on these constituent heat duties, the total condenser duty is calculated:

$$Q_{\text{Condenser,H}_2\text{O}} = Q_{\text{Condenser,Desup}} + Q_{\text{Condenser,Sat}} + Q_{\text{Condenser,Sub}} \tag{3.28}$$

$$163\text{ MW} = 6.4\text{ MW} + 156\text{ MW} + 0.6\text{ MW}$$

Cooling for the condenser is provided by a cooling loop coupled to sea water, entering the condenser at state (29) and exiting at state (30). The hydronic fluid inlet and outlet temperatures are 43.46° and 48.07°C, respectively. The resulting total condenser heat rejection load is 163 MW and the required condenser *UA* is 32.9 MW/K:

$$Q_{\text{Condenser,H}_2\text{O}} = m_{29}c_{\text{p,Condenser}}\left(T_{30} - T_{29}\right) \tag{3.29}$$

$$163\text{ MW} = 8458\frac{\text{kg}}{\text{s}}\cdot 4.18\frac{\text{kJ}}{\text{kg}\cdot\text{K}}\left(48.07°\text{C} - 43.46°\text{C}\right)$$

$$Q_{\text{Condenser,H}_2\text{O}} = UA_{\text{Condenser,H}_2\text{O}}LMTD\left(T_{15}, T_{16}, T_{29}, T_{30}\right) \tag{3.30}$$

$$163\text{ MW} = 32.9\frac{\text{MW}}{\text{K}}\cdot 4.95°\text{C}$$

The saturated temperature is used to calculate the condenser *LMTD*, as the desuperheating and subcooling represent a small fraction of the overall heat duty but would introduce a large difference in the calculated *LMTD* and *UA*. The cycle high-side pressure of 13.03 kPa is established here by the hydronic coupling fluid temperature:

$$p_{16} = p_{\text{H}_2\text{O}}\left(T_{16}, q_{16}\right) \tag{3.31}$$

$$13.03 \text{ kPa} = p_{H_2O}\left(51.1°\text{C}, 0\right)$$

where T_{16} is chosen to be at a 3 K *CAT* over the hydronic fluid outlet temperature of 48.07°C noted above. This established pressure also sets the desorber temperatures discussed above – for a given solution concentration, the higher the saturation pressure, the higher the desorber saturation temperature, which then reduces the driving temperature difference between the waste gas stream and the LiBr-H_2O solution in the desorber, and reduces the amount of heat that can be recovered from the waste stream. Conversely, a lower high-side pressure reduces the driving temperature difference between the refrigerant and the heat sink, thereby reducing the heat rejection capability.

The subcooled liquid stream (17) enters the refrigerant heat exchanger (RHX). A heat exchanger effectiveness of 90% is assumed for this component, leading to a heat duty of 4.5 MW:

$$h_{\text{RHX,hot}} = h_{H_2O}\left(T_2, p_{17}\right) \tag{3.32}$$

$$34\frac{\text{kJ}}{\text{kg}} = h_{H_2O}\left(8°\text{C}, 13.03 \text{ kPa}\right)$$

$$h_{\text{RHX,cold}} = h_{H_2O}\left(T_{17}, p_2\right) \tag{3.33}$$

$$2593\frac{\text{kJ}}{\text{kg}} = h_{H_2O}\left(49.07°\text{C}, 0.87 \text{ kPa}\right)$$

$$Q_{\text{max,RHX hot}} = m_{17}\left(h_{17} - h_{\text{RHX,hot}}\right) \tag{3.34}$$

$$11.3 \text{ MW} = 65.59\frac{\text{kg}}{\text{s}}\left(205\frac{\text{kJ}}{\text{kg}} - 34\frac{\text{kJ}}{\text{kg}}\right)$$

$$Q_{\text{max,RHX cold}} = m_2\left(h_{\text{RHX,cold}} - h_2\right) \tag{3.35}$$

$$5\ \text{MW} = 65.59\frac{\text{kg}}{\text{s}}\left(2593\frac{\text{kJ}}{\text{kg}} - 2516\frac{\text{kJ}}{\text{kg}}\right)$$

$$Q_{\text{min,RHX}} = \min\left(Q_{\text{max,RHX hot}}, Q_{\text{max,RHX cold}}\right) \tag{3.36}$$

$$Q_{\text{RHX}} = \varepsilon_{\text{RHX}} Q_{\text{min,RHX}} \tag{3.37}$$

$$4.5\ \text{MW} = 90\% \cdot 5\ \text{MW}$$

Upon exiting the RHX at state (18), the condensed stream has been cooled to 32.50°C by the refrigerant stream exiting the second absorption cycle evaporator. The corresponding vapor stream from the second evaporator is heated from 8.00°C to 44.97°C:

$$Q_{\text{RHX}} = m_{17}\left(h_{17} - h_{18}\right) \tag{3.38}$$

$$4.5\ \text{MW} = 65.59\frac{\text{kg}}{\text{s}}\left(205\frac{\text{kJ}}{\text{kg}} - 136\frac{\text{kJ}}{\text{kg}}\right)$$

$$Q_{\text{RHX}} = m_{2}\left(h_{3} - h_{2}\right) \tag{3.39}$$

$$4.5\ \text{MW} = 65.59\frac{\text{kg}}{\text{s}}\left(2585\frac{\text{kJ}}{\text{kg}} - 2516\frac{\text{kJ}}{\text{kg}}\right)$$

The calculated UA to achieve this duty in the RHX is 0.4 MW/K:

$$Q_{\text{RHX}} = UA_{\text{RHX}} LMTD\left(T_{17}, T_{18}, T_{2}, T_{3}\right) \tag{3.40}$$

$$4.5\ \text{MW} = 0.4\frac{\text{MW}}{\text{K}} \cdot 11.42°\text{C}$$

The recuperative RHX enables the liquid refrigerant to enter the evaporator at a lower enthalpy than the condenser outlet enthalpy, so that very little flashing occurs across the expansion valve. Thus, more of the latent heat is available in the evaporator for cooling. The water flows across the expansion valve, entering a first evaporator as a

low-quality, two-phase mixture at state (19). The water pressure decreases from 13.03 kPa to the low-side pressure of 0.87 kPa across the valve, with the refrigerant exiting at a quality of 4.6%:

$$h_{19} = h_{18} = 136 \frac{\text{kJ}}{\text{kg}} \tag{3.41}$$

$$q_{19} = q_{\text{H}_2\text{O}}\left(p_{19}, h_{19}\right) \tag{3.42}$$

$$0.046 = q_{\text{H}_2\text{O}}\left(0.87 \text{ kPa}, 136 \frac{\text{kJ}}{\text{kg}}\right)$$

The two-phase refrigerant mixture enters the coupled absorption cycle evaporator at a temperature of 5.00°C. The heating load is provided to this evaporator by the condenser of the cascaded CO_2 vapor-compression cycle. The water exits the first evaporator at state (20) as a two-phase mixture of a higher quality than at the evaporator inlet. The exact value of the quality at state (20) is determined by cycle parameters balancing the cooling load between the low-temperature, high-flux vapor-compression cycle, and the medium temperature, steady-state cooling loop. In the baseline case, the stream is evaporated to a quality of 50.0%:

$$T_{20} = T_{\text{H}_2\text{O}}\left(q_{20,} p_{20}\right) \tag{3.43}$$

$$5.00°\text{C} = T_{\text{H}_2\text{O}}\left(0.5, 0.87 \text{ kPa}\right)$$

$$Q_{\text{H}_2\text{O Evaporator/CO}_2\text{ Condenser}} = m_{19}\left(h_{20} - h_{19}\right) \tag{3.44}$$

$$74 \text{ MW} = 65.59 \frac{\text{kg}}{\text{s}}\left(1266 \frac{\text{kJ}}{\text{kg}} - 136 \frac{\text{kJ}}{\text{kg}}\right)$$

This mixture (20) enters a second evaporator, which provides steady, medium temperature cooling to a hydronic fluid loop. The two-phase water vapor is further

evaporated to saturation and a superheated temperature of 8.00°C in the second evaporator. States (1) and (2) represent the saturated and superheated vapor states, respectively, in the second evaporator:

$$h_1 = h_{H_2O}(T_1, q_1) \tag{3.45}$$

$$2510\frac{\text{kJ}}{\text{kg}} = h_{H_2O}\left(5.00°\text{C}, 1\right)$$

$$Q_{\text{Evaporator,Medium T,Sat}} = m_{20}\left(h_1 - h_{20}\right) \tag{3.46}$$

$$81.6\ \text{MW} = 65.59\frac{\text{kg}}{\text{s}}\left(2510\frac{\text{kJ}}{\text{kg}} - 1266\frac{\text{kJ}}{\text{kg}}\right)$$

$$T_2 = T_1 + \Delta T_{\text{sup}} \tag{3.47}$$

$$8.00°\text{C} = 5.00°\text{C} + 3.00°\text{C}$$

$$Q_{\text{Evaporator,Medium T,Sup}} = m_1\left(h_2 - h_1\right) \tag{3.48}$$

$$0.4\ \text{MW} = 65.59\frac{\text{kg}}{\text{s}}\left(2516\frac{\text{kJ}}{\text{kg}} - 2510\frac{\text{kJ}}{\text{kg}}\right)$$

$$Q_{\text{Evaporator,Medium T}} = Q_{\text{Evaporator,Medium T,Sat}} + Q_{\text{Evaporator,Medium T,Sup}} \tag{3.49}$$

$$82\ \text{MW} = 81.6\ \text{MW} + 0.4\ \text{MW}$$

This evaporator is coupled to the medium-temperature, steady-state cooling loop of 50% ethylene glycol water mixture flowing at 4208 kg/s (3.9 m^3/s). This hydronic fluid is cooled from 14°C to 8.00°C, yielding a medium temperature cooling duty of 82 MW:

$$Q_{\text{Evaporator,Medium T}} = m_{31}c_{\text{p,Hydronic}}\left(T_{31} - T_{32}\right) \tag{3.50}$$

$$82\ \text{MW} = 4208\frac{\text{kg}}{\text{s}} \cdot 3.25\frac{\text{kJ}}{\text{kg}\cdot\text{K}}\left(14.00°\text{C} - 8.00°\text{C}\right)$$

The *UA* of the medium-temperature evaporator is established to maintain a *CAT* of 3°C. Again, the saturated vapor temperature is used to calculate the *LMTD* rather than the superheated vapor outlet temperature because superheating represents a small portion of the total heat duty and using the superheated temperature would result in an exaggerated ΔT:

$$Q_{\text{Evaporator,Medium T}} = UA_{\text{Evaporator,Medium T}} LMTD\left(T_{31}, T_{32}, T_{20}, T_{1}\right) \tag{3.51}$$

$$82 \text{ MW} = 15 \frac{\text{MW}}{\text{K}} \cdot 5.46°\text{C}$$

The absorption cycle low-side pressure is established in this evaporator, i.e., by the hydronic fluid temperature, flow rate, and the evaporator *UA* of 15 MW/K:

$$p_1 = p_{H_2O}\left(T_1, q_1\right) \tag{3.52}$$

$$0.87 \text{ kPa} = p_{H_2O}\left(5.00°\text{C}, 1\right)$$

Upon exiting the second evaporator, the water vapor flows through the refrigerant pre-cooler, receiving the heat rejected by the condenser outlet stream, and leaves the pre-cooler at state (3). This vapor stream flows to the absorber, where it combines with the returning concentrated solution (4) from the solution heat exchanger.

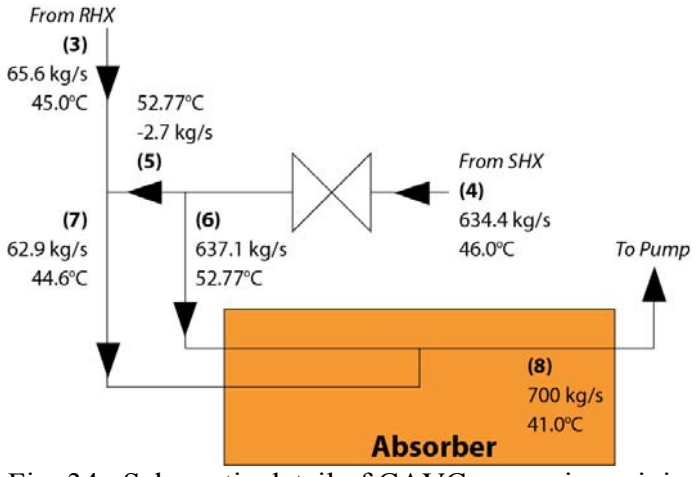

Fig. 34. Schematic detail of CAVC expansion mixing.

The solution exiting the solution heat exchanger is typically not in a saturated state. Therefore, upon expanding to the low pressure state, either some water vapor can flash from this stream and combine with stream (3) from the refrigerant heat exchanger, or some adiabatic absorption of the vapor from stream (3) can occur. The mixing between the vapor and liquid streams is modeled in considerable detail. A schematic detail of the mixing process is shown in Fig. 34. Vapor stream (7) represents this new state of the vapor, while state (6) is the new state of the LiBr/H_2O solution. In the baseline case, a small amount (2.71 kg/s) of the water vapor stream is adiabatically absorbed into the solution stream:

$$q_{\text{Outlet,LiBr Valve}} = q_{\text{LiBr}}\left(h_4, p_5, x_4\right) \tag{3.53}$$

$$-0.43\% = q_{\text{LiBr}}\left(156\frac{\text{kJ}}{\text{kg}}, 0.87\ \text{kPa}, 64.9\%\right)$$

$$m_5 = m_4 \frac{q_{\text{Outlet,LiBr Valve}}}{100\%} \tag{3.54}$$

$$-2.71\frac{\text{kg}}{\text{s}} = 634.4\frac{\text{kg}}{\text{s}} \cdot \frac{-43\%}{100\%}$$

The resulting vapor stream has a flow rate of 62.88 kg/s at 44.64°C:

$$m_7 = m_3 + m_5 \tag{3.55}$$

$$62.88\frac{\text{kg}}{\text{s}} = 65.59\frac{\text{kg}}{\text{s}} - 2.71\frac{\text{kg}}{\text{s}}$$

$$m_7 h_7 = m_3 h_3 + m_5 h_5 \tag{3.56}$$

$$62.88\frac{\text{kg}}{\text{s}} \cdot 2584\frac{\text{kJ}}{\text{kg}} = 65.59\frac{\text{kg}}{\text{s}} \cdot 2585\frac{\text{kJ}}{\text{kg}} - 2.71\frac{\text{kg}}{\text{s}} \cdot 2599\frac{\text{kJ}}{\text{kg}}$$

$$T_7 = T_{\text{H}_2\text{O}}\left(h_7, p_7\right) \tag{3.57}$$

$$44.6°\text{C} = T_{\text{H}_2\text{O}}\left(2584\frac{\text{kJ}}{\text{kg}}, 0.87\ \text{kPa}\right)$$

The resulting solution stream has a concentration of 64.62%, with a flow rate of 637.1 kg/s at 52.77°C (whereas the solution heat exchanger outlet was at 91.22°C):

$$m_6 = m_4 - m_5 \tag{3.58}$$

$$637.1\frac{\text{kg}}{\text{s}} = 634.4\frac{\text{kg}}{\text{s}} + 2.71\frac{\text{kg}}{\text{s}}$$

$$T_6 = T_5 = 52.77°\text{C} \tag{3.59}$$

This detailed modeling of the mixing process yields a more representative estimate of the actual solution inlet temperature for the absorber, which is subsequently used for the calculation of the driving temperature difference between the solution and coolant streams.

The vapor and solution streams mix in the absorber, and while flowing through the absorber, the vapor phase is absorbed into the liquid phase due to heat rejection to the sea water-coupled coolant loop, which enters at state (28) and exits at state (29). Vapor absorption in the absorber yields a 58.82% LiBr solution at a saturation temperature of 41.00°C:

$$m_8 = m_6 + m_7 \tag{3.60}$$

$$700\frac{\text{kg}}{\text{s}} = 637.1\frac{\text{kg}}{\text{s}} + 62.9\frac{\text{kg}}{\text{s}}$$

$$x_8 m_8 = x_6 m_6 \tag{3.61}$$

$$58.82\% \cdot 700\frac{\text{kg}}{\text{s}} = 64.62\% \cdot 637.1\frac{\text{kg}}{\text{s}}$$

$$T_8 = T_{\text{LiBr}}\left(p_8, x_8\right) \tag{3.62}$$

$$41.00°\text{C} = T_{\text{LiBr}}\left(0.87\ \text{kPa}, 58.82\%\right)$$

$$Q_{\text{Absorber,Sat}} = m_6 h_6 + m_7 h_7 - m_8 h_8 \tag{3.63}$$

$$190.4\ \text{MW} = 637.1\frac{\text{kg}}{\text{s}}\cdot 166\frac{\text{kJ}}{\text{kg}} + 62.9\frac{\text{kg}}{\text{s}}\cdot 2584\frac{\text{kJ}}{\text{kg}} - 700\frac{\text{kg}}{\text{s}}\cdot 111.6\frac{\text{kJ}}{\text{kg}}$$

The dilute solution is further subcooled to 39.00°C, resulting in a total absorber load of 193.1 MW:

$$T_9 = T_8 - \Delta T_{\text{Sub}} \tag{3.64}$$

$$39.00°\text{C} = 41.00°\text{C} - 2.00°\text{C}$$

$$Q_{\text{Absorber,Sub}} = m_8\left(h_8 - h_9\right) \tag{3.65}$$

$$2.7\ \text{MW} = 700\frac{\text{kg}}{\text{s}}\left(111.6\frac{\text{kJ}}{\text{kg}} - 107.7\frac{\text{kJ}}{\text{kg}}\right)$$

$$Q_{\text{Absorber}} = Q_{\text{Absorber,Sat}} + Q_{\text{Absorber,Sub}} \tag{3.66}$$

$$193.1\ \text{MW} = 190.4\ \text{MW} + 2.7\ \text{MW}$$

The hydronic fluid (at 8458 kg/s or 8.5 m^3/s) enters the absorber at 38.00°C and is heated to an outlet temperature of 43.46°C:

$$Q_{\text{Absorber}} = m_{28} c_{\text{p,Absorber}}\left(T_{29} - T_{28}\right) \tag{3.67}$$

$$193.1\ \text{MW} = 8458\frac{\text{kg}}{\text{s}}\cdot 4.2\frac{\text{kJ}}{\text{kg}\cdot\text{K}}\left(43.46°\text{C} - 38.00°\text{C}\right)$$

The LMTD is again calculated with the saturated, rather than subcooled, outlet temperature. A *UA* value of 35 MW/K is required to maintain a 3°C *CAT* in this component:

$$Q_{\text{Absorber}} = UA_{\text{Absorber}} LMTD\left(T_6, T_8, T_{28}, T_{29}\right) \tag{3.68}$$

$$193.1\ \text{MW} = 35\frac{\text{MW}}{\text{K}} \cdot 5.57°\text{C}$$

The hydronic cooling fluid continues to the condenser, where it is heated to 48.07°C, before rejecting heat to sea water. The sea water flow rate is also set to 8.5 m^3/s (8466 kg/s) and is heated from 35°C to 45.06°C by the hydronic fluid:

$$Q_{\text{SeaHX}} = m_{30} c_{\text{p,Hydronic}} \left(T_{30} - T_{28}\right) \tag{3.69}$$

$$356\ \text{MW} = 8458\frac{\text{kg}}{\text{s}} \cdot 4.2\frac{\text{kJ}}{\text{kg} \cdot \text{K}}\left(48.07°\text{C} - 38.00°\text{C}\right)$$

$$Q_{\text{SeaHX}} = m_{35} c_{\text{p,Sea}} \left(T_{36} - T_{35}\right) \tag{3.70}$$

$$356\ \text{MW} = 8466\frac{\text{kg}}{\text{s}} \cdot 4.2\frac{\text{kJ}}{\text{kg} \cdot \text{K}}\left(45.06°\text{C} - 35.00°\text{C}\right)$$

The sea water heat exchanger requires a *UA* of 118.5 MW/K to transfer the 356 MW heat duty:

$$Q_{\text{SeaHX}} = UA_{\text{SeaHX}} LMTD\left(T_{30}, T_{28}, T_{35}, T_{36}\right) \tag{3.71}$$

$$356\ \text{MW} = 118.5\frac{\text{MW}}{\text{K}} \cdot 3.01°\text{C}$$

The total heat rejection load is 356 MW, a portion of which could be used to supply water heating needs within the ship. Typically, this heat load would serve to *preheat* the water that needs to be heated for a variety of functions in the ship.

CO_2 Vapor-Compression Loop

As described above, the first evaporator in the LiBr-H_2O absorption cycle serves as the heat sink for the condenser of the CO_2 vapor-compression cycle. The low pressure refrigerant from the absorption cycle evaporates across the evaporator/condenser component coupling the absorption and vapor-compression cycles, while condensing

227.8 kg/s of CO_2 from the vapor-compression cycle. Superheated CO_2 vapor enters the condenser at 94.00°C, state (27). The CO_2 stream is cooled to the saturation temperature of 8.00°C:

$$Q_{\mathrm{H_2O\ Evaporator/CO_2\ Condenser,Desup}} = m_{27}\left(h_{27} - h_{21}\right) \tag{3.72}$$

$$26\ \mathrm{MW} = 227.8\frac{\mathrm{kg}}{\mathrm{s}}\left(33\frac{\mathrm{kJ}}{\mathrm{kg}} - \left(-82\frac{\mathrm{kJ}}{\mathrm{kg}}\right)\right)$$

The condenser pressure in the vapor-compression cycle, 4283.00 kPa, is set by the temperature of the coupled two-phase water mixture (much like the condenser pressure in the absorption cycle, which is set by its own heat sink temperature):

$$p_{21} = p_{\mathrm{CO_2}}\left(T_{21}, q_{21}\right) \tag{3.73}$$

$$4283.00\ \mathrm{kPa} = p_{\mathrm{CO_2}}\left(8.00°\mathrm{C}, 1\right)$$

The condenser saturated vapor and liquid states are represented by states (21) and (22), respectively, representing a condensation load of 47 MW:

$$Q_{\mathrm{H_2O\ Evaporator/CO_2\ Condenser,Sat}} = m_{21}\left(h_{21} - h_{22}\right) \tag{3.74}$$

$$47\ \mathrm{MW} = 227.8\frac{\mathrm{kg}}{\mathrm{s}}\left(\left(-82\frac{\mathrm{kJ}}{\mathrm{kg}}\right) - \left(-286\frac{\mathrm{kJ}}{\mathrm{kg}}\right)\right)$$

Subcooled CO_2 exits the condenser at state (23) at 6.00°C:

$$Q_{\mathrm{H_2O\ Evaporator/CO_2\ Condenser,Sub}} = m_{22}\left(h_{22} - h_{23}\right) \tag{3.75}$$

$$1\ \mathrm{MW} = 227.8\frac{\mathrm{kg}}{\mathrm{s}}\left(\left(-286\frac{\mathrm{kJ}}{\mathrm{kg}}\right) - \left(-292\frac{\mathrm{kJ}}{\mathrm{kg}}\right)\right)$$

The evaporator/condenser component therefore has a total heat duty of 74 MW:

$$Q_{\mathrm{H_2O\ Evap/CO_2\ Cond}} = Q_{\mathrm{H_2O\ Evap/CO_2\ Cond,Desup}} + Q_{\mathrm{H_2O\ Evap/CO_2\ Cond,Sat}} + Q_{\mathrm{H_2O\ Evap/CO_2\ Cond,Sub}} \tag{3.76}$$

$$74\ \mathrm{MW} = 26\ \mathrm{MW} + 47\ \mathrm{MW} + 1\ \mathrm{MW}$$

The coupled evaporator/condenser is designed to maintain a 3°C temperature difference between the saturated water and carbon dioxide streams, requiring a *UA* of 25 MW/K:

$$Q_{\mathrm{H_2O\ Evaporator/CO_2\ Condenser}} = UA_{\mathrm{H_2O\ Evaporator/CO_2\ Condenser}} \Delta T_{\mathrm{H_2O\ Evaporator/CO_2\ Condenser}} \tag{3.77}$$

$$74\ \mathrm{MW} = 25 \frac{\mathrm{MW}}{\mathrm{K}} \cdot 3.00°\mathrm{C}$$

The subcooled liquid stream may be stored for pulsed, high-flux, on-demand use before flowing to the expansion valve. When the cooling cycle is in use, the stored liquid CO_2 flows through the expansion valve and enters the evaporator as a two-phase mixture at state (24). The subcooled CO_2 liquid is expanded from the high-side pressure to the low-side pressure of 1004.52 kPa, resulting in a CO_2 mixture of 32% quality, which enters the evaporator at -40.00°C:

$$h_{24} = h_{23} = -292 \frac{\mathrm{kJ}}{\mathrm{kg}} \tag{3.78}$$

$$T_{24} = T_{\mathrm{CO_2}} \left(p_{24}, h_{24} \right) \tag{3.79}$$

$$-40.00°\mathrm{C} = T_{\mathrm{CO_2}} \left(1004.52\ \mathrm{kPa}, -292 \frac{\mathrm{kJ}}{\mathrm{kg}} \right)$$

$$q_{24} = q_{\mathrm{CO_2}} \left(p_{24}, h_{24} \right) \tag{3.80}$$

$$0.32 = q_{\mathrm{CO_2}} \left(1004.52\ \mathrm{kPa}, -292 \frac{\mathrm{kJ}}{\mathrm{kg}} \right)$$

The evaporator provides a heat sink at a nominal -40°C for the low-temperature cooling load. The two-phase mixture is fully evaporated in the evaporator to yield a cooling duty of 51 MW at -40.00°C for high-flux electronics cooling. The saturated vapor state is represented by state (25):

$$Q_{\mathrm{Evaporator,\ Low\ T,\ Sat}} = m_{24} \left(h_{26} - h_{24} \right) \tag{3.81}$$

$$50.5\text{ MW} = 227.8\frac{\text{kg}}{\text{s}}\left(\left(-71\frac{\text{kJ}}{\text{kg}}\right)-\left(292\frac{\text{kJ}}{\text{kg}}\right)\right)$$

The vapor is superheated to -38.00°C at state (26):

$$T_{26} = T_{25} + \Delta T_{\text{Sup}} \tag{3.82}$$

$$-38.00°\text{C} = -40.00°\text{C} + 2.00°\text{C}$$

$$Q_{\text{Evaporator, Low T, Sup}} = m_{25}\left(h_{26} - h_{25}\right) \tag{3.83}$$

$$0.5\text{ MW} = 227.8\frac{\text{kg}}{\text{s}}\left(\left(-69\frac{\text{kJ}}{\text{kg}}\right)-\left(-71\frac{\text{kJ}}{\text{kg}}\right)\right)$$

The resulting total low temperature evaporator heat duty is 51 MW:

$$Q_{\text{Evaporator, Low T}} = Q_{\text{Evaporator, Low T, Sat}} + Q_{\text{Evaporator, Low T, Sub}} \tag{3.84}$$

$$51\text{ MW} = 50.5\text{ MW} + 0.5\text{ MW}$$

The superheated CO_2 enters the compressor, state (26), and is compressed to state (27), completing the vapor-compression cycle. The compressor is modeled with 65% isentropic efficiency and uses 23 MW of power:

$$\eta_{\text{Compressor}} = \frac{h_{27,\text{isentropic}} - h_{26}}{h_{27} - h_{26}} \tag{3.85}$$

$$0.65 = \frac{\left(-3\frac{\text{kJ}}{\text{kg}}\right)-\left(-69\frac{\text{kJ}}{\text{kg}}\right)}{\left(33\frac{\text{kJ}}{\text{kg}}\right)-\left(-69\frac{\text{kJ}}{\text{kg}}\right)}$$

$$W_{\text{Compressor}} = m_{26}\left(h_{27} - h_{26}\right) \tag{3.86}$$

$$23\text{ MW} = 227.8\frac{\text{kg}}{\text{s}}\left(33\frac{\text{kJ}}{\text{kg}}-\left(-69\frac{\text{kJ}}{\text{kg}}\right)\right)$$

The required compressor power is essentially the only energy cost in the entire cascade system. (It should be noted that coupled fluid pumps also will consume some energy, but this would be the case for any cycle used to provide cooling.) Herein lies the main benefit of the system: low-temperature cooling with natural refrigerants and low energy costs.

It should be noted that efficiencies of relatively small capacity compressors such as these typically range from 50-65%. Here, a value of 65% is chosen to illustrate the upper end of the performance that can be expected from this cycle.

3.4 BASELINE SYSTEM PERFORMANCE SUMMARY

The cascade absorption/vapor-compression baseline results detailed above yield a combined, total-energy-input-based *COP* of 0.594. The combined, total energy input *COP* is defined as:

$$COP_{\text{All, Energy}} = \frac{Q_{\text{Evaporator, Low T}} + Q_{\text{Evaporator, Medium T}}}{Q_{\text{Exhaust Input}} + W_{\text{Compressor}} + W_{\text{Pump}}} \tag{3.87}$$

$$0.594 = \frac{51\ \text{MW} + 82\ \text{MW}}{200\ \text{MW} + 23\ \text{MW} + 0.005\ \text{MW}}$$

It should be noted that low and medium temperature cooling represent considerably different availabilities, which is masked by this addition of heat loads. However, this representation provides a simple aggregate measure of cycle performance. Similarly, in the denominator, the mechanical and thermal energy inputs are combined, even though they too represent different thermodynamic availabilities. Because the waste heat input included above does not require any new investment in energy, a more revealing picture of the system performance is obtained by considering only the electric power input in the definition of *COP* as follows:

$$COP_{\text{All, Electric}} = \frac{Q_{\text{Evaporator, Low T}} + Q_{\text{Evaporator, Medium T}}}{W_{\text{Compressor}} + W_{\text{Pump}}} \tag{3.88}$$

$$5.685 = \frac{51\ \text{MW} + 82\ \text{MW}}{23\ \text{MW} + 0.005\ \text{MW}}$$

This definition yields an overall *COP* of 5.685 based on the electrical input. Considering the relative value of low-temperature cooling and also the neglected additional benefits of water heating, these baseline results are very promising. The performances of the component absorption and vapor-compression cycles are evaluated on a stand-alone basis as follows:

$$COP_{\text{Absorption}} = \frac{Q_{\text{H}_2\text{O Evaporator/CO}_2\text{ Condenser}} + Q_{\text{Evaporator, Medium T}}}{Q_{\text{Exhaust Input}} + W_{\text{Pump}}} \tag{3.89}$$

$$0.780 = \frac{74\ \text{MW} + 82\ \text{MW}}{200\ \text{MW} + 0.005\ \text{MW}}$$

$$COP_{\text{Vapor Compression}} = \frac{Q_{\text{Evaporator, Low T}}}{W_{\text{Compressor}}} \tag{3.90}$$

$$2.173 = \frac{51\ \text{MW}}{23\ \text{MW}}$$

These two COPs provide an understanding of how well each of the component cycles is performing in comparison to typical absorption and vapor-compression cycles alone. The absorption COP is 0.780, while the vapor-compression COP is 2.173 despite the high lift from -40°C to 8°C. Without the absorption cycle, this lift would be from -40°C to 40°C, resulting in much lower cycle *COP*s. In summary, at an assumed high temperature, 35°C, of sea water for heat rejection, the baseline cascade cycle is able to use 200 MW of waste heat and provide 82 MW of cooling at 5°C, and 51 MW of cooling at -40°C with an investment of only 23 MW of compressor power.

CHAPTER FOUR: CAVC CYCLE PARAMETRIC ANALYSES

The analysis and the results described above provide the baseline system state points that can be used as the desired inlet and outlet conditions for the respective components, and could in turn be used for the detailed design of the individual components using heat and mass transfer principles. The system model also enables a variety of parametric studies; for example, investigations of:

a) the effect of component sizes on system performance

b) variation in cooling capacity and coefficient of performance with operating conditions

c) the effect of system coupling loop configuration (condenser and absorber in series or parallel), heat source (direct-fired or intermediate loop coupled), and heat rejection mechanisms (direct sea water coupling, intermediate hydronic loop coupling, or air coupling), and several other related considerations.

Thus, the model provides a consistent framework for the performance evaluation of systems of different capacities, and also provides a tool for the selection of the most optimal system configuration for each candidate blend of steady and pulsed loads and other design goals. Representative parametric analyses have been performed to understand the performance of this system, and key results are described below. The four critical cycle input parameters considered in these analyses are as follows:

- heat rejection temperature
- exhaust heat temperature
- compressor power,

• LiBr-H_2O solution flow rate

Also, three configurations of the coupling loop between the absorber, condenser and sea water heat exchanger are investigated here: series configuration with absorber receiving cooling water first, series configuration with condenser first, and a parallel configuration.

Crystallization is a concern in H_2O/LiBr systems and has been considered in these analyses. The concentration and temperature at the desorber solution outlet and absorber solution inlet are graphed against H_2O/LiBr solution crystallization data, published by Cyprus Foote Mineral [57], in Fig. 38, Fig. 42, and Fig. 47.

In addition, a CAVC cycle model incorporating a double-effect configuration of the absorption loop is developed to investigate the cycle performance improvements that could be achieved if high exhaust heat temperatures were available. Baseline double-effect CAVC cycle performance was investigated and a parametric analysis was done to evaluate the effect of exhaust heat temperature on the double-effect CAVC cycle.

The last section of this chapter describes an equivalent two-stage vapor-compression cycle and provides cycle performance parameters for comparison with the CAVC results.

4.1 HEAT REJECTION TEMPERATURE

Heat rejection temperatures ranging from 25° to 40°C were chosen to investigate system performance, representing a range of worldwide operating environments for the advanced naval ship. The variation of the cycle coefficients of performance is shown in Fig. 35. As the heat rejection temperature rises, $COP_{\text{All,Electric}}$ remains at a high value, but decreases from 6.67 to 5.21. Due to the relatively constant medium temperature

evaporator temperature, the component absorption and vapor compression cycles do not see an appreciable decrease in performance, with $COP_{\text{Absorption}}$ decreasing from 0.81 to 0.77, and $COP_{\text{Vapor Compression}}$ decreasing from 2.32 to 2.11.

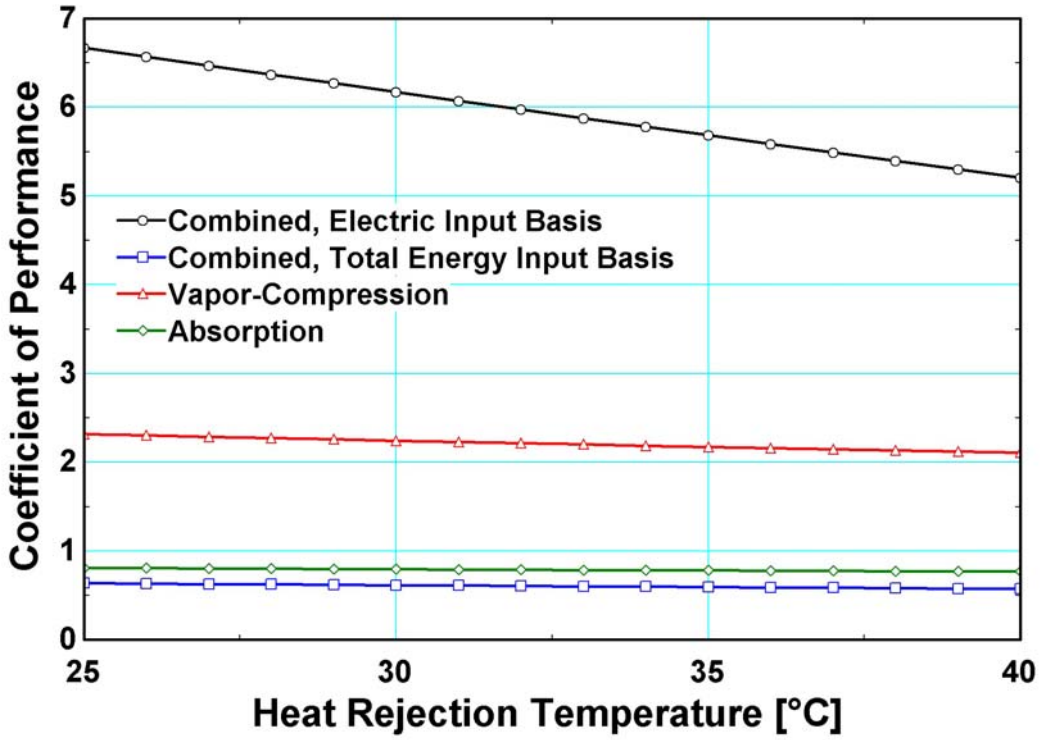

Fig. 35. Effect of Heat Rejection Temperature on Cycle Performance.

Likewise, $COP_{\text{All, Energy}}$ decreases from 0.64 to 0.57. These decreases in *COP* are caused by a decreased ability to reject heat as the heat rejection temperature increases, as shown in Fig. 35. The heat rejection load decreases from 401 MW to 334 MW over this temperature range. This is in turn reflected in an increase in temperature of LiBr-H_2O solution entering the desorber (75.60°C to 99.40°C), which reduces the waste heat input from 222 MW to 189 MW, and decreases the water generation rate. The reduced refrigerant flow decreases the total available cooling load from 156 MW to 122 MW. In contrast, the compressor power input is held constant at 23 MW. The decrease in total cooling load over the constant compressor load causes the decrease in $COP_{\text{All, Electric}}$ seen

in Fig. 35. The other *COP*s ($COP_{Absorption}$, $COP_{All,\ Energy}$) show less drastic decreases because they include the exhaust heat input; its decrease outweighs the effect of constant compressor power.

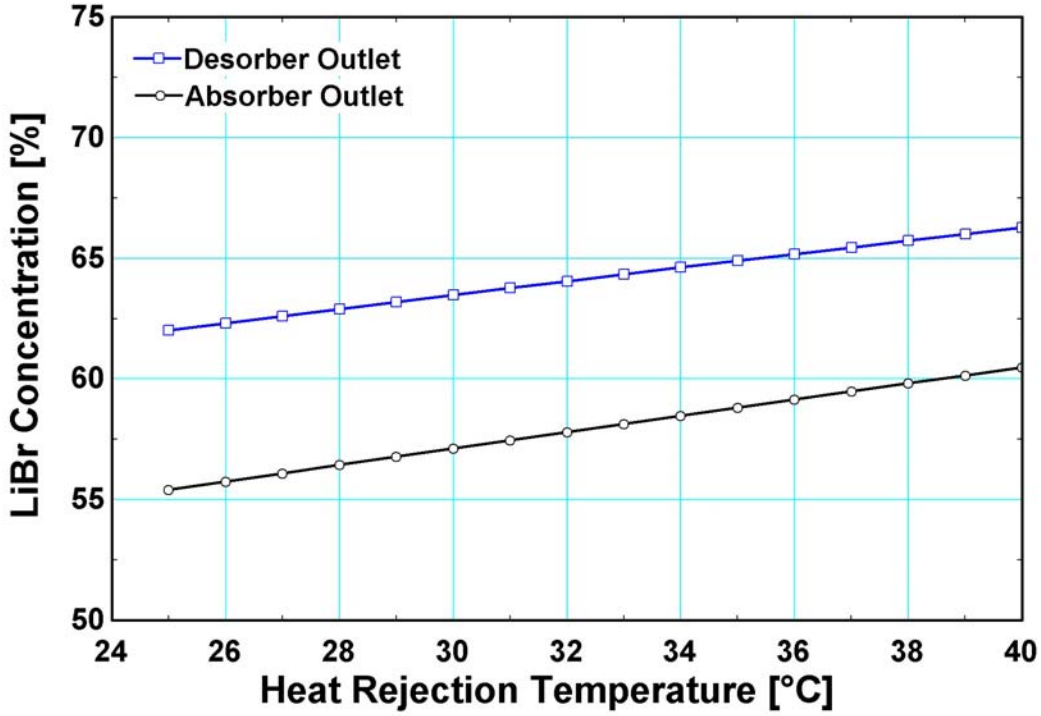

Fig. 36. Effect of Heat Rejection Temperature on LiBr Solution Concentrations.

As the heat rejection temperature rises, the absorber outlet concentration rises to be enable higher absorber temperatures that enable heat rejection (Fig. 36). An increased absorber outlet (and therefore desorber inlet) concentration leads to an increase in the desorber outlet concentration for a given waste heat input at the desorber. However, the desorber heat input does not remain the same, because the desorber operates at higher temperatures, reducing the driving temperature difference with the exhaust gas. Thus, less water is generated, as indicated by the decrease in the change in concentration across the desorber from 6.62% LiBr to 5.79% LiBr. The reduced refrigerant flow rate in the

absorption cycle leads to reduced cooling availability, thus decreasing the cooling loads of the entire cycle as seen in Fig. 37.

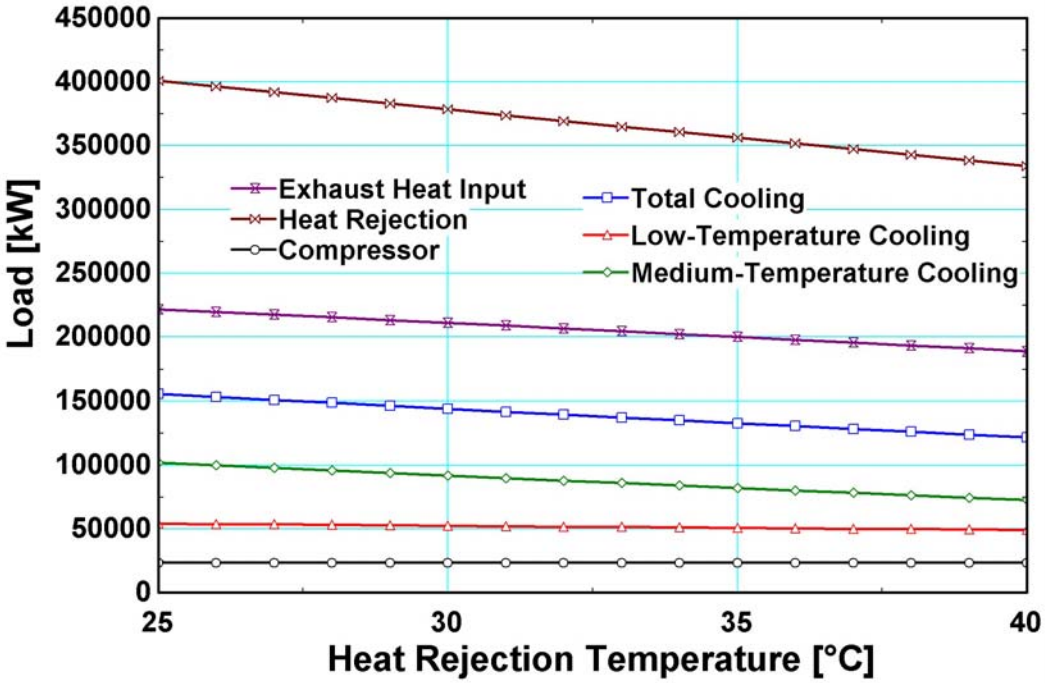

Fig. 37. Effect of Heat Rejection Temperature on System Capacities.

The effect of heat rejection temperature on the risk of crystallization in the cycle is show in Fig. 38. Though an increase in heat rejection temperature does cause an increase in LiBr concentration, temperatures and pressures at the absorber inlet and desorber outlet, conditions at each point remain safely removed from the crystallization limit.

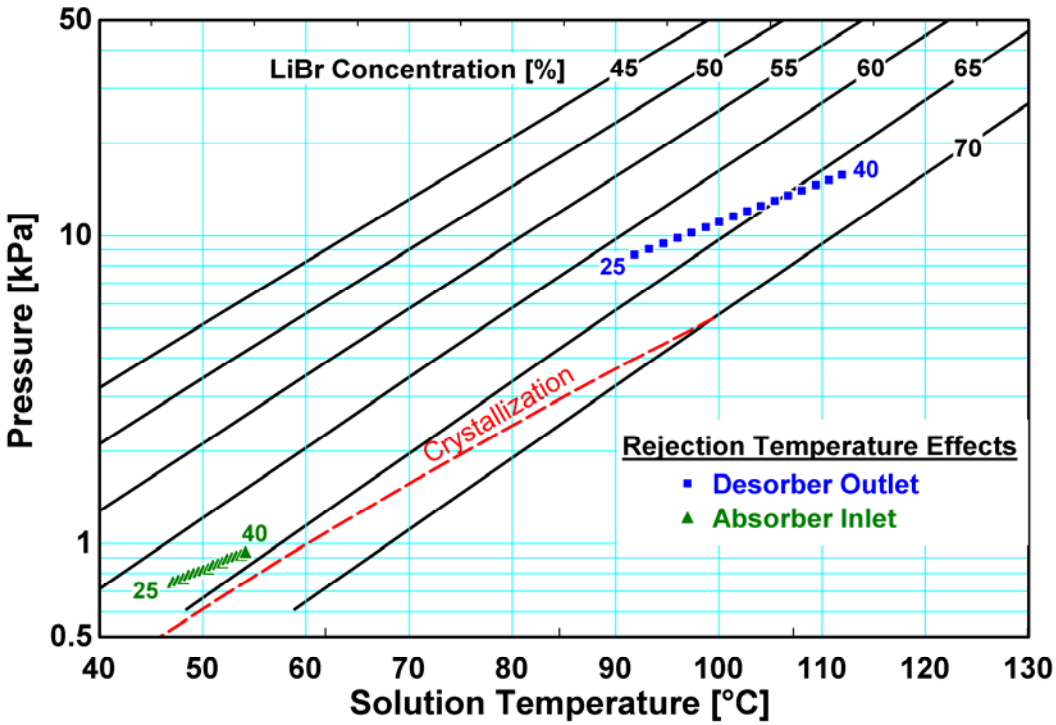

Fig. 38. Dühring Plot of Heat Rejection Temperature Effects on Cycle Temperatures and Crystallization Risk.

4.2 EXHAUST HEAT TEMPERATURE

The effect of exhaust heat temperature on cycle performance was also investigated over the range 175°C to 275°C (Fig. 39). As exhaust heat temperature increases, so do the combined electric, combined total energy, and vapor-compression *COP*s. The compressor input is constant, while the exhaust heat input increases at higher temperatures. Therefore, $COP_{\text{All, Electric}}$, which considers only electric energy inputs, increases from 3.52 to 6.32, as exhaust heat input increases. Even on a total energy input basis, $COP_{\text{All, Energy}}$ increases slightly from 0.53 to 0.61. $COP_{\text{Vapor Compression}}$ increases from 1.89 to 2.27 due to the decreasing heat rejection temperature for that cycle, as the water evaporator temperature decreases from 9.79°C to 3.60°C. The absorption cycle *COP* varies only slightly, decreasing from 0.80 to 0.78.

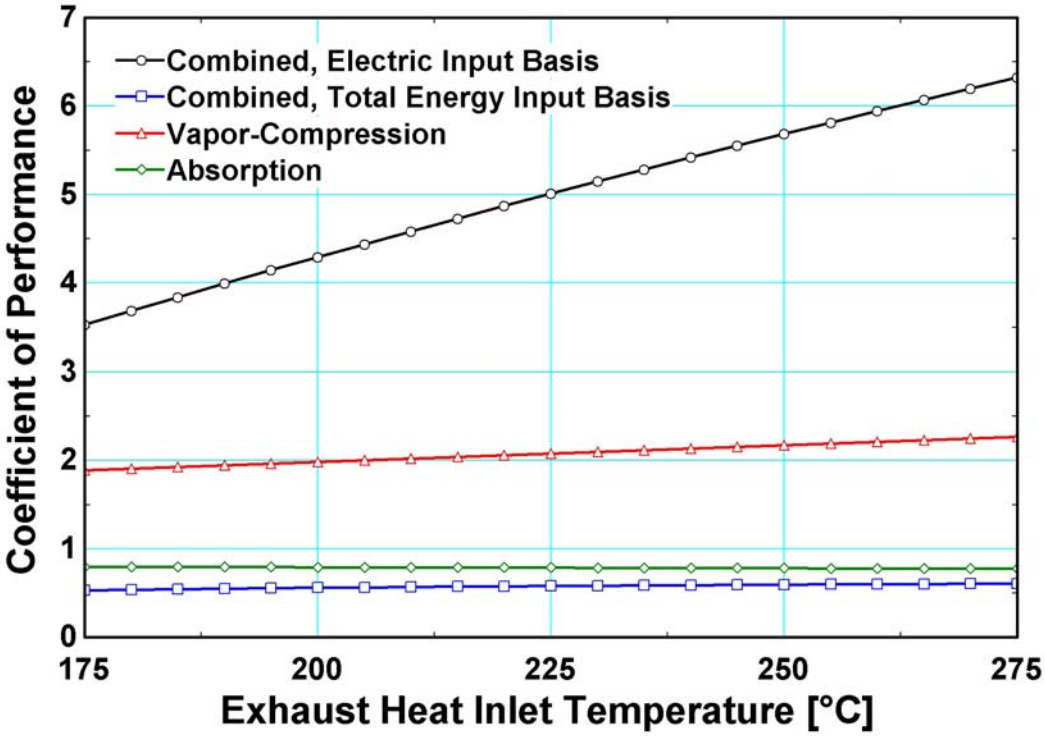

Fig. 39. Effect of Exhaust Inlet Temperature on Cycle Performance.

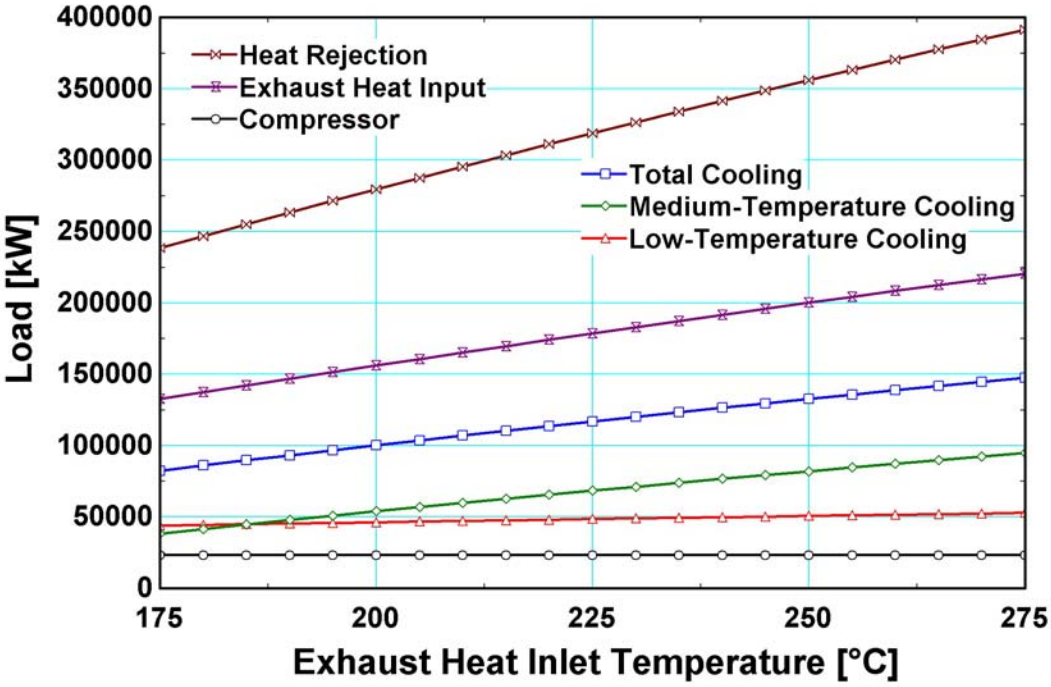

Fig. 40. Effect of Exhaust Inlet Temperature on Cycle Capacities.

Across this temperature range, the exhaust input load increases from 133 MW to 221 MW (Fig. 40), a 66% increase, while the total cooling load increases from 82 to 148 MW, a 79% increase, which corresponds to the increase in $COP_{\text{All, Energy}}$. Due to the fixed compressor power input of 23 MW, the low temperature cooling duty is also relatively constant, ranging from 44 to 53 MW, increasing only 20%. Because the constant compressor input limits the increase in low-temperature cooling load, the increase in total cooling is mostly absorbed by the medium-temperature cooling load, which rises from 39 to 95 MW, a 147% increase. Increasing the compressor power with exhaust gas temperature would better utilize this additional heat input for low-temperature cooling.

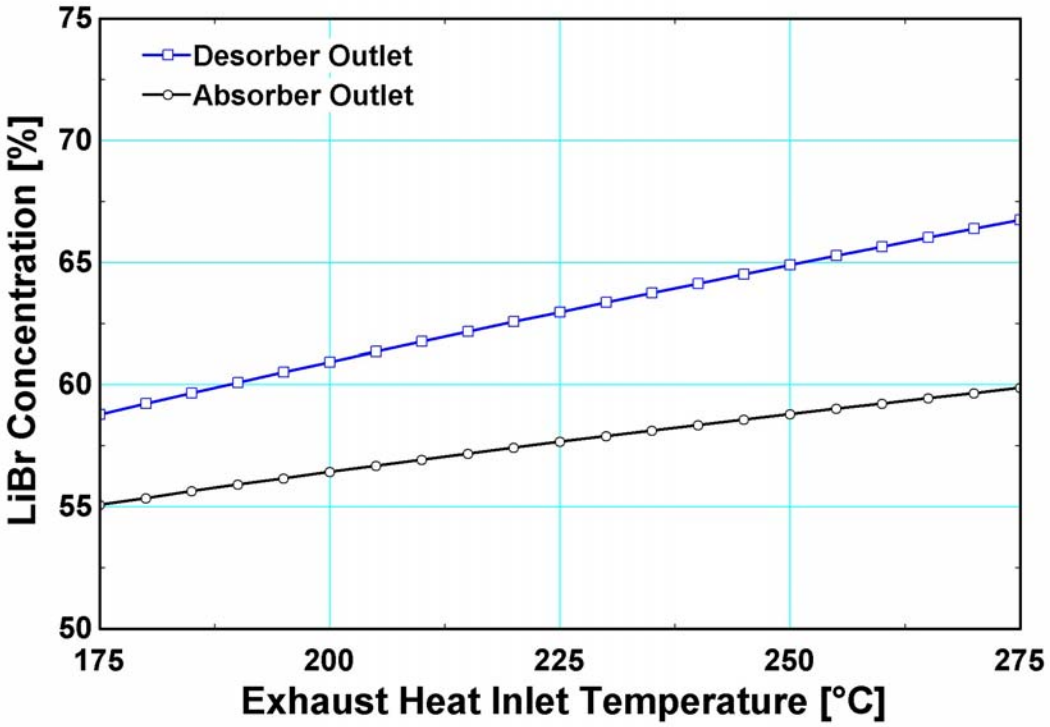

Fig. 41. Effect of Exhaust Inlet Temperature on LiBr Solution Concentration.

The increase in the exhaust heat input causes an increase in the amount of water generated in the desorber, reflected in the diverging slopes of the desorber inlet and outlet concentrations shown in Fig. 41. The trends in COP and capacity (Fig. 39 and Fig. 40)

discussed above are essentially because of this increasing refrigerant generation at the larger exhaust heat temperatures. The sizes established for each component were based on a nominal 250°C exhaust heat inlet temperature; therefore, the system is unable to use the additional thermal availability at the higher temperatures optimally because the components are undersized for the available heat duties. Therefore, the COP decreases because additional energy is input to the cycle but it cannot be utilized effectively. Also, higher cooling capacities with the same system design lead to water temperatures approaching the freezing point in the evaporator, which is not advisable from an implementation standpoint. However, with design modifications, mostly in *UA* values, flow rates and control algorithms that vary coupling fluid flow rates, expansion valve characteristics and compressor settings, this cycle could utilize higher temperatures more effectively. Furthermore, at the higher end of this exhaust temperature range, a much larger improvement in cycle performance can be obtained by utilizing a double-effect absorption cycle instead of the single-effect system considered here. The tradeoff between increased complexity and improved performance would govern this decision.

Additionally, an increase in exhaust inlet temperature is accompanied by some risk of crystallization, as shown in Fig. 42. At the high exhaust inlet temperature of 275°C, conditions at the absorber inlet are certainly in the crystallization range. An exhaust temperature of 260°C results in an absorber inlet pressure of 0.84 kPa, an inlet temperature of 53.57°C, and a 65.35% LiBr concentration. These absorber conditions are not in the crystallization range but are close to the crystallization limit, which could be exceeded with slight perturbations in the operating conditions. A limit of <65.0% LiBr concentration is imposed in this investigation to avoid crystallization. An exhaust inlet

temperature of 250°C results in absorber inlet conditions of 0.87 kPa, 52.76°C, and 64.62% LiBr concentration, providing the highest *COP* available (0.59 $COP_{\text{All, Energy}}$) within the crystallization constraint.

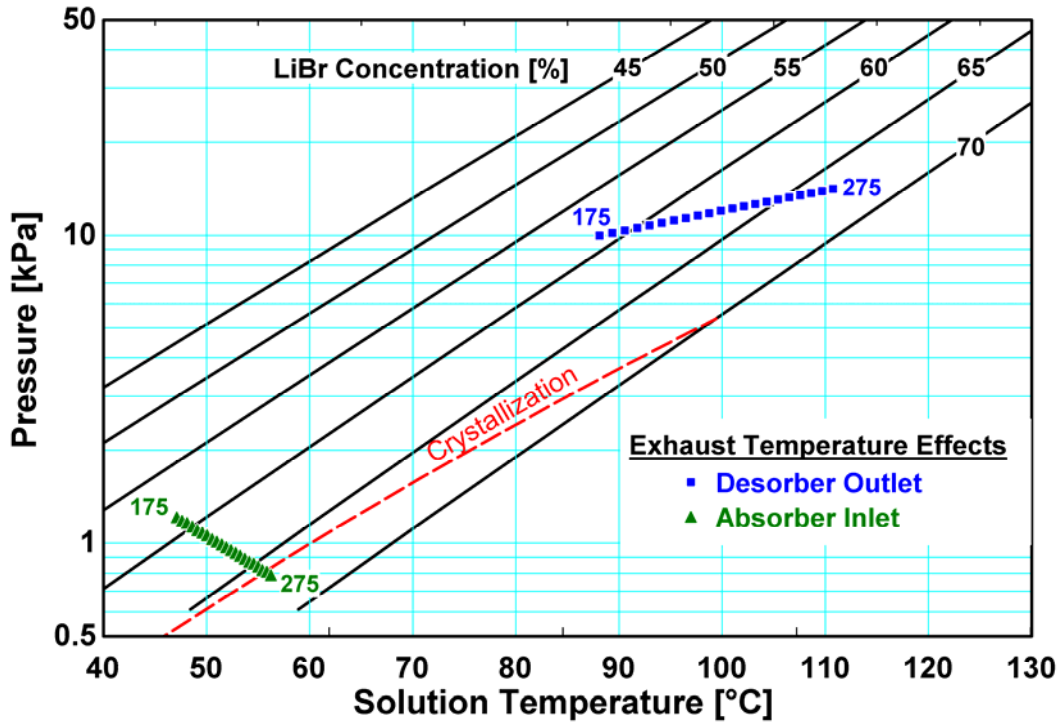

Fig. 42. Dühring Plot of Exhaust Inlet Temperature Effects on Cycle Temperatures and Crystallization Risk.

4.3 COMPRESSOR POWER

The compressor power input is a control parameter that directly affects the cooling load of the coupling evaporator/condenser between the two cascaded cycles. A compressor power input range of 17 to 48 MW was investigated, which yields a coupling evaporator outlet quality of 0.4 to 0.8. This outlet quality indicates the relative fractions of the low-temperature and medium-temperature loads. As the compressor power increases, $COP_{\text{All, Electric}}$ decreases predictably from 8.04 to 2.45 (Fig. 43) due to the increasing dependence on electrical power input compared to waste heat. The other

electric input related indicators follow suit ($COP_{\text{All, Energy}}$ decreases from 0.64 to 0.46, $COP_{\text{Vapor Compression}}$ from 2.34 to 1.72). $COP_{\text{Absorption}}$ increases slightly from 0.78 to 0.80 as the compressor power increases, due to less cooling duty being required in the second evaporator that was sized for larger capacities.

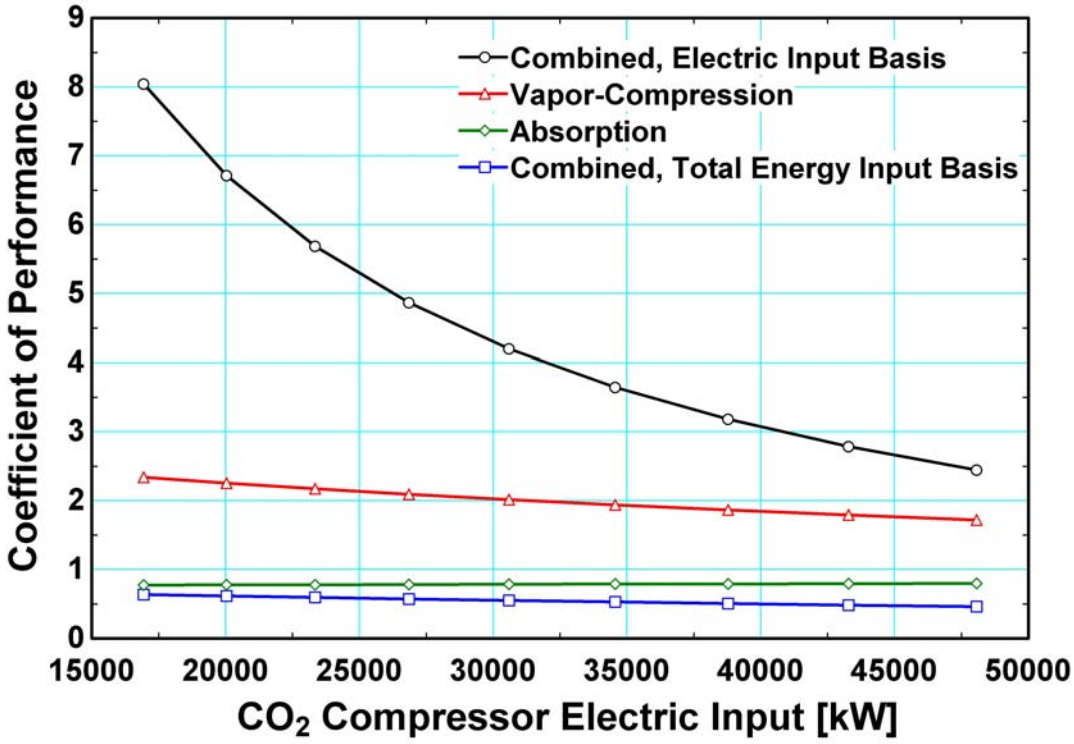

Fig. 43. Effect of Compressor Input Power on Cycle Performance.

The control of the cooling load balance using compressor power can be easily observed in Fig. 44. At a compressor power of 17 MW, the low-temperature cooling load (40 MW) accounts for 29% of the total cooling. The corresponding medium-temperature cooling load is 97 MW (71%). At a compressor power of 31 MW, the total cooling load is balanced between the two loads, with 62 MW of low-temperature cooling (48% of total) and 67 MW of medium-temperature cooling (52% of total). At a compressor power of 48 MW, the low-temperature cooling dominates with 83 MW, taking 70% of the total cooling load. The medium-temperature load is left with 35 MW (30% of the total). The

total cooling load decreases from 137 to 118 kW as more cooling is directed through the low-temperature cycle due to the increased fraction of high temperature lift cooling in the CO_2 cycle compared to the direct use of the medium-temperature cooling. This balance between cooling loads is an important cycle control and parameter and therefore the compressor input power is chosen based on this balance instead of COP optimization. Thus, the compressor power setting offers a simple way to infinitely vary the distribution between high-flux low-temperature and steady-state medium-temperature cooling fractions in a controlled manner based on the instantaneous operating conditions experienced on the naval ship. (It should be noted that the other parametric analyses reported here fix the compressor power at 23 MW, which, at nominal conditions, corresponds to a coupled evaporator outlet quality of 0.5, roughly representing an equal cooling load distribution.)

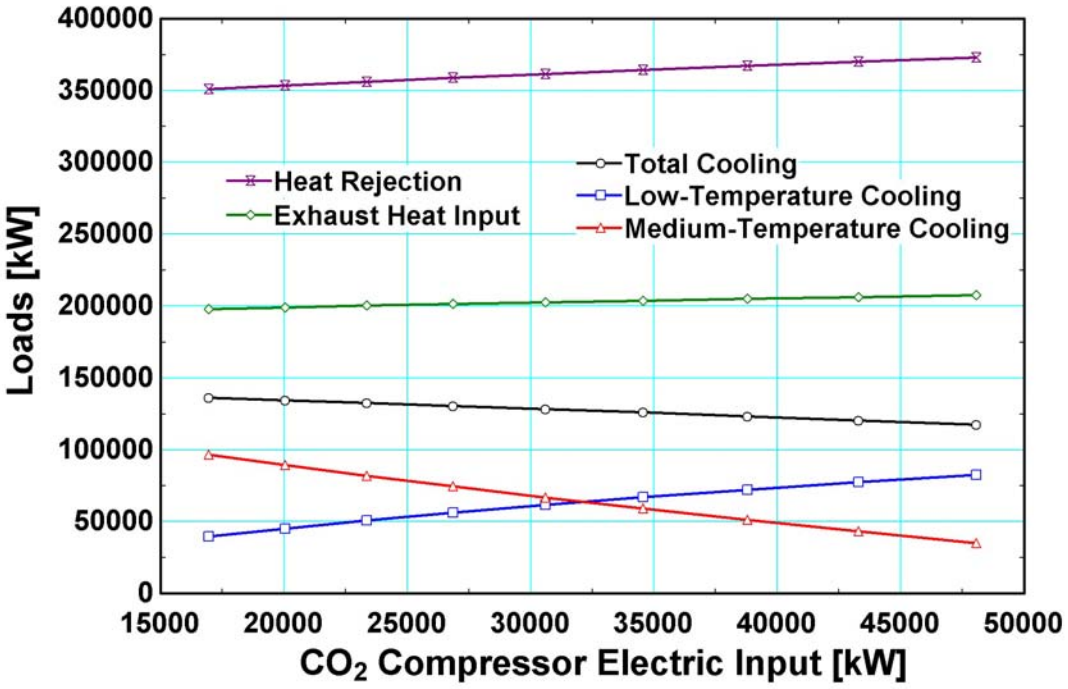

Fig. 44. Effect of Compressor Input Power on Cycle Capacities.

4.4 H_2O-LIBR SOLUTION FLOW RATE

The optimal solution flow rate that can be used in this cycle is determined based on cycle performance and the potential for crystallization. The H_2O-LiBr flow rate was varied from 350 to 1300 kg/s to investigate these parameters. Fig. 45 shows that each of the *COP* trends peak at 450 kg/s. $COP_{\text{All, Electric}}$ peaks at 450 kg/s with a value of 5.80, while $COP_{\text{Absorption}}$, $COP_{\text{Vapor Compression}}$, and $COP_{\text{All, Energy}}$ peak at 0.80, 2.19, and 0.61 respectively.

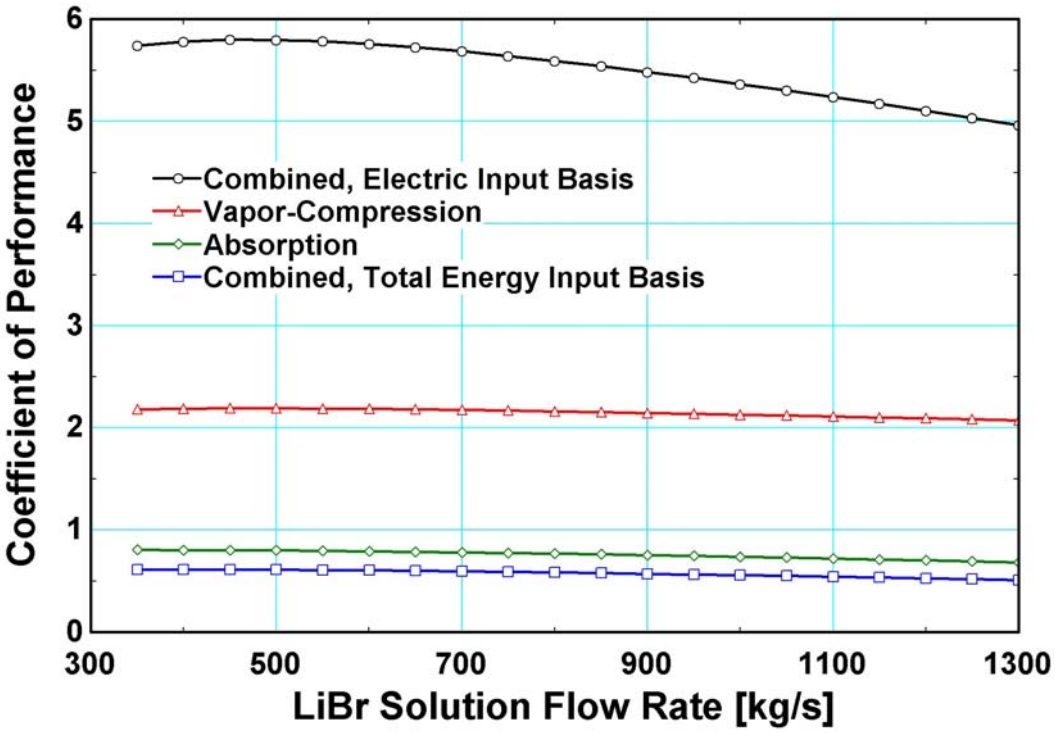

Fig. 45. Effect of LiBr Solution Flow Rate on Cycle Performance.

As the solution flow rate is varied, the exhaust heat input load is relatively constant due to the specified exhaust inlet temperature and desorber parameters, increasing by only 4% (196 to 204 MW) with increasing solution flow rate. At lower solution flow rates, the input heat load is used more to generate water than for sensible heating of the solution. Therefore, overall water production actually decreases from 66.1

to 58.4 kg/s as solution flow rate increases, and the concentration change in the desorber drops from 13.4 to 2.8% (Fig. 46). The LiBr concentration of the concentrated solution stream exiting the desorber is 71.0% at 350 kg/s, and decreases to 61.8% at 1300 kg/s.

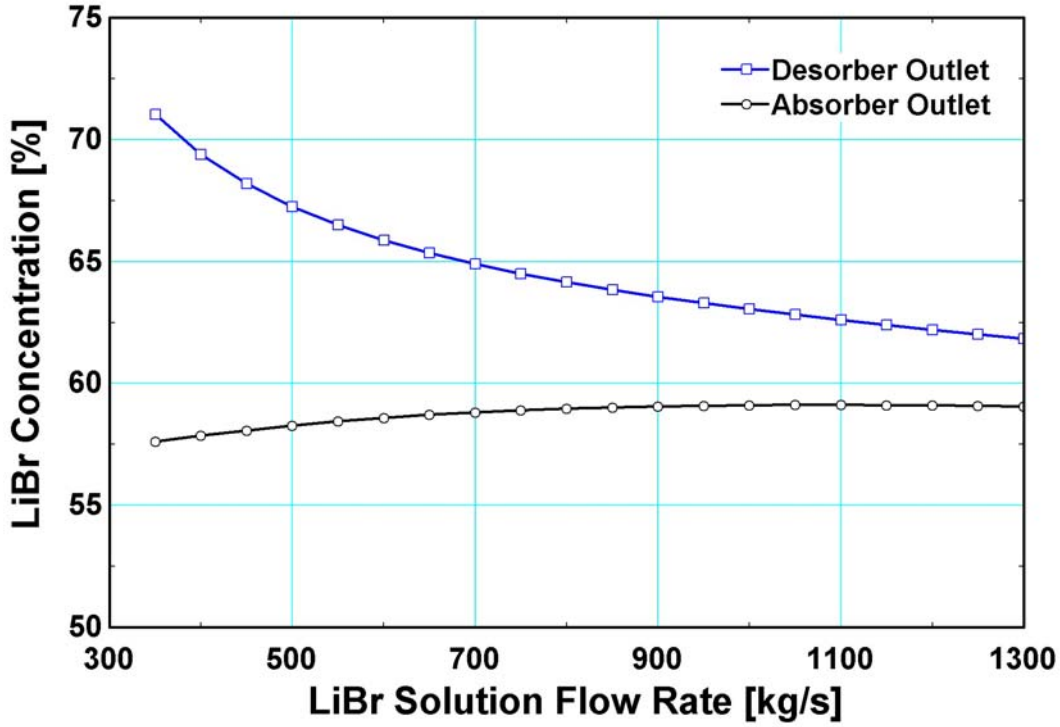

Fig. 46. Effect of LiBr Solution Flow Rate on LiBr Concentrations.

At high concentrations, the solution could crystallize, with the crystallization limits being dependent on the saturation temperature and pressure. As shown in Fig. 47, the lowest flow rate, 350 kg/s, clearly results in crystallization conditions. As the flow rate is increased in increments of 50 kg/s, the flow rate of 450 kg/s yields optimal *COP*s and results in an absorber inlet pressure of 0.86 kPa, a temperature of 58.18°C and a 67.41% LiBr concentration. These conditions are close to the crystallization limit, which could be exceeded with slight perturbations in the operating conditions. Based on these considerations, a limiting LiBr concentration of <65.0% is imposed in this investigation,

which establishes a solution flow rate of 700 kg/s chosen as the baseline, and provides the highest *COP* available within the crystallization constraint.

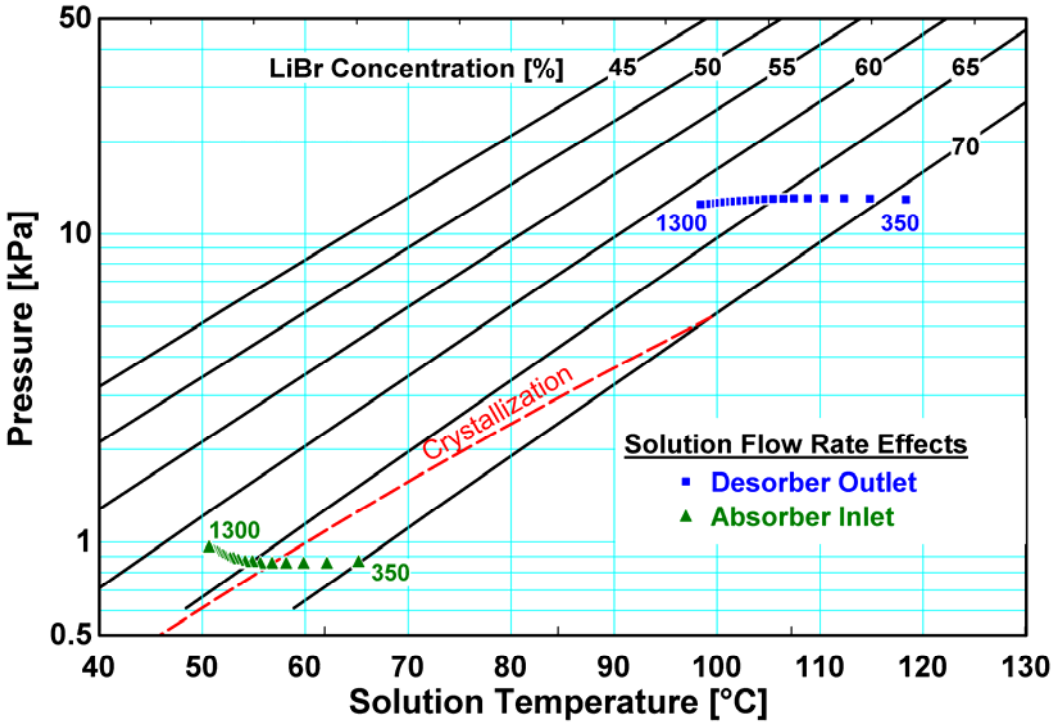

Fig. 47. Dühring Plot of LiBr Solution Flow Rate Effects on Cycle Temperatures and Crystallization Risk.

4.5 CONFIGURATION OF COUPLING LOOP FOR HEAT REJECTION TO SEA WATER

The coupling loop between the absorber and condenser and sea heat exchanger can be configured in three ways: series configuration with absorber receiving cooling water first, series configuration with condenser first, and a parallel configuration. The baseline cycle discussed in Chapter 3 utilizes a series configuration that provides cooling water to the absorber before cooling the condenser. The two other configurations are analyzed here using the *UA*s and flow rates determined for the baseline configuration, to facilitate consistent comparison between the cycles. For convenient comparison, the schematic of the each configuration is provided in Fig. 48-Fig. 50 with temperature,

pressure, LiBr concentration, quality, and heat duty information overlaid on each component.

The series configuration providing cooling water to the absorber before cooling the condenser (the baseline configuration) is shown in Fig. 48. Water cooled to 38.0°C by the sea heat exchanger flows directly to the absorber, where it is heated to 43.5°C. After cooling the absorber, the water flows through the condenser, where it is heated to 48.1°C. The water then returns to the seawater heat exchanger, completing the loop. The flow rate of the loop is determined by the requirements of the absorber and set to 8458 kg/s. The results of this configuration are detailed in Chapter 3.

The series configuration providing cooling water to the condenser before cooling the absorber is shown in Fig. 49. Water cooled to 38.0°C by the seawater heat exchanger flows directly to the condenser, where it is heated to 42.7°C. After cooling the condenser, the water flows through the absorber, where it is heated to 48.2°C. The water then returns to the seawater heat exchanger, completing the loop. The flow rate of the loop is 8458 kg/s, as in the baseline configuration. Holding the *UA*s constant at the values determined for the baseline configuration, the condenser-to-absorber series results are calculated. The $COP_{\text{All, Energy}}$ and $COP_{\text{All, Electric}}$ of the cycle are 0.599 and 5.748, respectively. This overall cycle performance is very similar to the baseline absorber-to-condenser configuration $COP_{\text{All, Energy}}$ and $COP_{\text{All, Electric}}$ of 0.594 and 5.685. The $COP_{\text{Absorption}}$ and $COP_{\text{Vapor Compression}}$ of the two cycles is also comparable: 0.785 and 2.182 for the condenser-to-absorber configuration, and 0.780 and 2.173 for the baseline absorber-to-condenser configuration. The slightly improved cycle performance of the condenser-to-absorber configuration reflects increased heat duties in the low and medium

temperature evaporators. Compared to the baseline absorber-to-condenser configuration, the lower temperature of the coupling fluid entering the condenser in the condenser-to-absorber configuration reduces the condenser saturation pressure from 13.03 kPa to 9.96 kPa. The desorber solution saturation temperature corresponding to the lower absorption cycle high pressure then decreases from 94.2°C to 93.4°C. The exhaust heat inlet temperature remains constant at 250°C and the increased temperature differential across the desorber increases the desorber duty from 200.0 MW to 200.6 MW. The desorber then generates more water vapor, increasing the refrigerant stream mass flow rate from 65.59 kg/s to 65.84 kg/s. The increased refrigerant flow results in increased heat rejection duty in the condenser (from 163.0 MW to 165.1 MW) and increased cooling duties in the low and medium temperature evaporators. Additionally, the temperature of the refrigerant exiting the RHX at state (18) is decreased from 32.5°C to 29.3°C. The lower refrigerant temperature reduces flashing as the refrigerant is expanded to the absorption cycle low pressure at state (19), with vapor exiting the valve at a quality of 0.041 compared to 0.046 in the baseline configuration. Therefore, more latent heat is available in the absorption evaporators for cooling. The increased refrigerant flow and reduced flashing increase the H_2O evaporator/CO_2 condenser duty from 74.1 MW to 74.3 MW and the medium-temperature evaporator duty from 82.0 MW to 83.3 MW. The increased H_2O evaporator/CO_2 condenser duty increases the CO_2 refrigerant flow rate from 227.8 kg/s to 228.4 kg/s. Also, the lower condenser saturation temperature reduces flashing in the CO_2 cycle expansion, so that refrigerant exits the valve at a quality of 0.315 rather than 0.316. Correspondingly, the low-temperature evaporator duty increases from 50.7 MW to 50.9 MW. As the compressor load remains constant and the increase

in desorber duty is proportionally small, cycle performance improves due to the increased cooling duties. However, there is an important disadvantage to the condenser-to-absorber configuration. The higher coupling fluid temperature entering the absorber will increase the absorber solution saturation temperature from 41.0°C to 45.5°C, also raising the saturation LiBr concentration from 58.82% to 61.16%. Therefore, the concentrated solution enters the absorber at 67.51% LiBr rather than the 64.9% LiBr concentration of the baseline cycle. The increase temperature and LiBr concentration at the absorber solution inlet raise concerns about crystallization at that point. The absorber heat rejection duty decreases by only 7 kW, from 193.113 MW to 193.106 MW.

It can be seen from the above discussion that the overall cooling and COP changes between the two configurations are relatively small. Therefore, choice of the configuration used in actual practice should be based on implementation issues, such as crystallization limits.

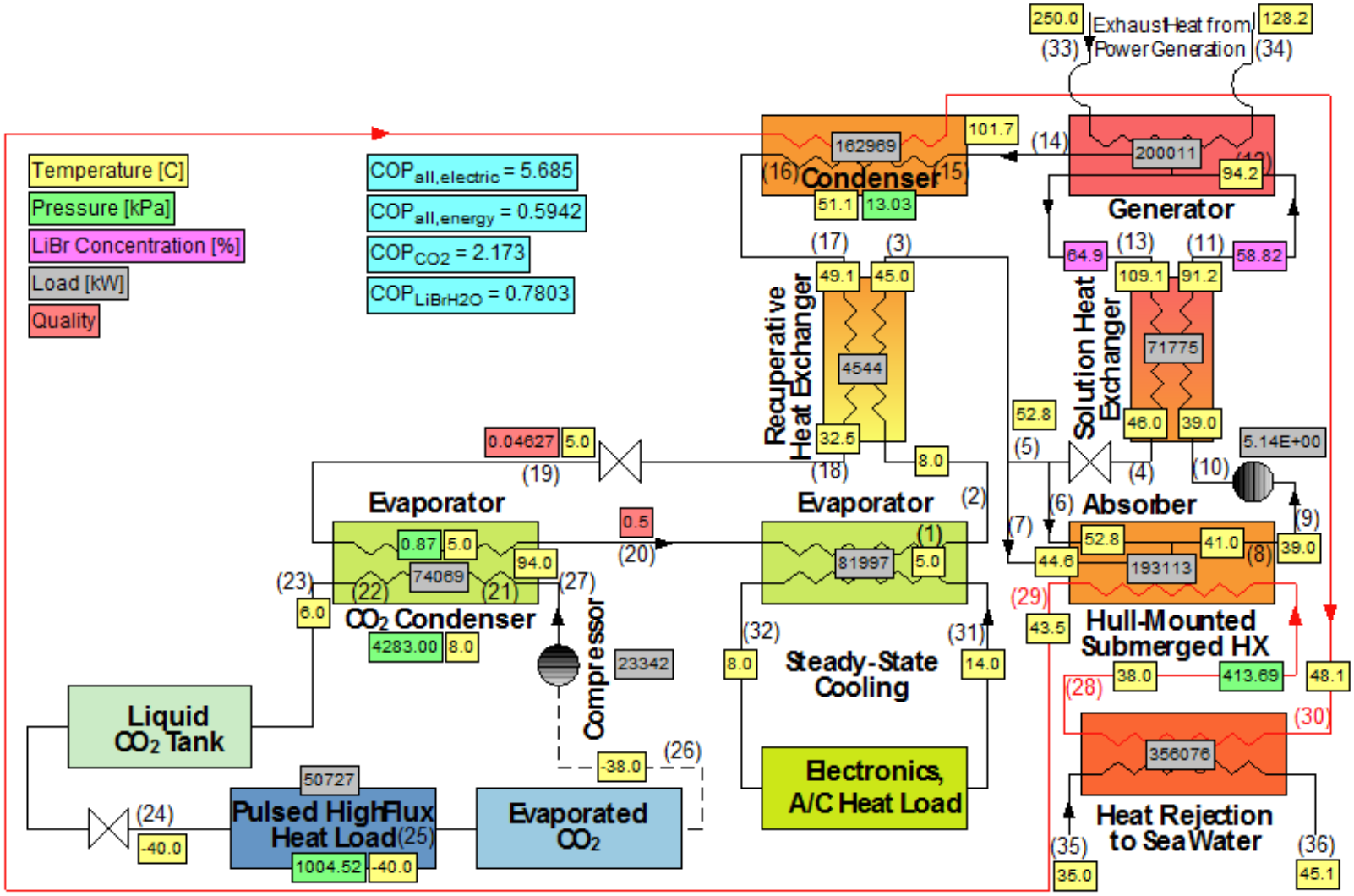

Fig. 48. Seawater Coupling Loop in Absorber-to-Condenser Series Configuration.

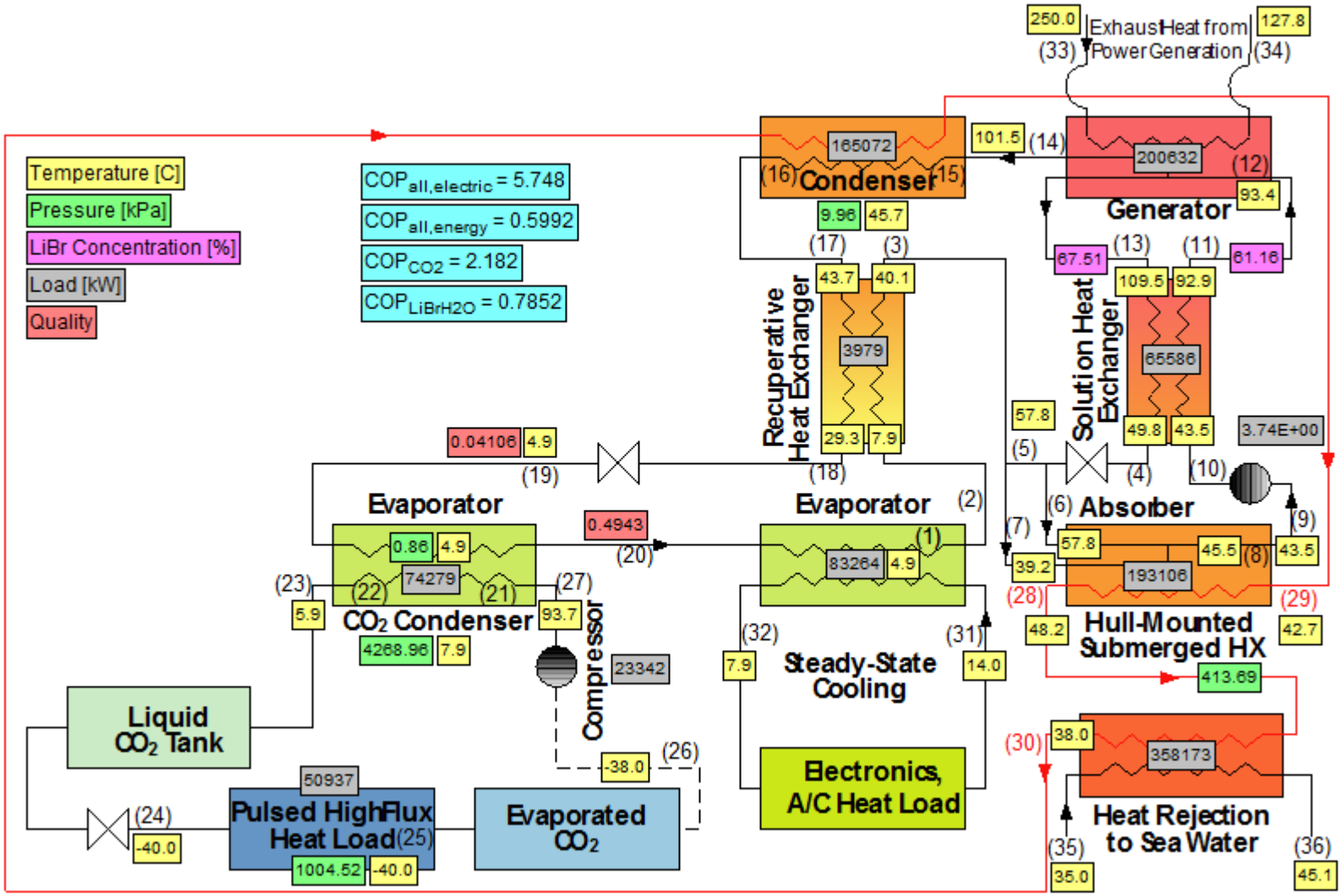

Fig. 49. Seawater Coupling Loop in Condenser-to-Absorber Series Configuration.

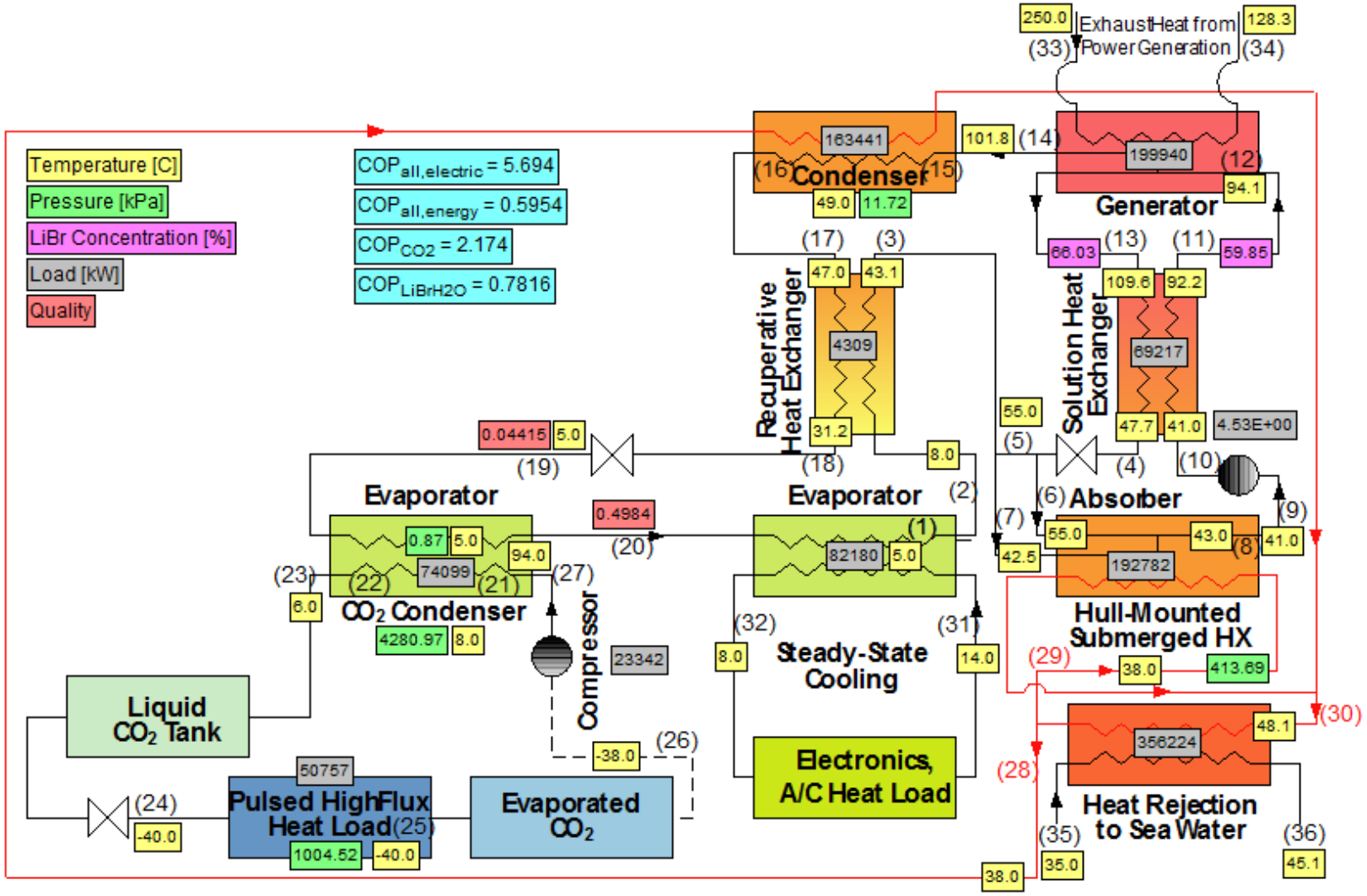

Fig. 50. Seawater Coupling Loop in Parallel Configuration.

Table 7. Seawater Coupling Loop Configuration Analysis Results

Coupling Loop Configuration	$COP_{All,\ Energy}$	$COP_{All,\ Electric}$	COP_{VC}	COP_{Abs}	Q_{low} [MW]	Q_{Medium} [MW]	Q_{Absorb} [MW]	Q_{Desorb} [MW]	$Q_{Condense}$ [MW]	q_{19} [%]	x_8 [%]	x_4 [%]	$\dot{m}_{water}$ [kg/s]
Absorber-to-condenser series	0.594	5.685	2.173	0.780	50.73	82.00	193.11	200.01	162.97	4.6	58.8	64.9	65.59
Condenser-to-absorber series	0.599	5.748	2.182	0.785	50.94	83.26	193.11	200.63	165.07	4.1	61.2	67.5	65.84
Parallel	0.595	5.694	2.174	0.782	50.76	82.18	192.78	199.94	163.44	4.4	59.9	66.0	65.53

The parallel configuration, which provides cooling water to both condenser and absorber at the same temperature, is shown in Fig. 50. The coupling fluid flow rate determined for the baseline configuration is held constant in the seawater heat exchanger and split equally to the condenser and absorber. Therefore, coolant flows to each component at 4229 kg/s and a temperature of 38.0°C. In the absorber, the coolant is heated to 48.9°C. The coolant is heated to 47.3°C in the condenser. The absorber and condenser outlet streams mix to produce a coolant flow at 48.1°C before reentering the seawater heat exchanger and completing the loop. The $COP_{\text{All, Energy}}$ and $COP_{\text{All, Electric}}$ of the cycle are 0.595 and 5.694, respectively. This overall cycle performance is, again, very similar to the baseline absorber-to-condenser configuration $COP_{\text{All, Energy}}$ and $COP_{\text{All, Electric}}$ of 0.594 and 5.685. The $COP_{\text{Absorption}}$ and $COP_{\text{Vapor Compression}}$ of the two cycles are also comparable: 0.782 and 2.174 for the parallel configuration and 0.780 and 2.173 for the baseline absorber-to-condenser configuration. In the parallel configuration, the benefits of lower heat rejection temperatures for the condenser and absorber are nearly negated by the drawback of reduced coolant flow in these components, which causes a greater temperature rise for the same heat load. The condenser saturation pressure decreases from 13.03 kPa to 11.72 kPa and the condenser heat rejection duty increases 163.0 MW to 163.4 MW. The corresponding desorber solution saturation temperature decreases from 94.2°C to 94.1°C. Despite the incrementally increased temperature differential over the desorber, the water vapor flow rate generated in the desorber decreases slightly from 65.59 kg/s to 65.53 kg/s, due to the decreased ability to reject heat from the absorber. The increase in evaporator duties is therefore due solely to the reduced flashing in the H_2O expansion valve. The temperature of the refrigerant exiting

the RHX at state (18) decreases from 32.5°C to 31.2°C. The quality of the refrigerant exiting the expansion valve is 0.044, compared to a quality of 0.046 in the baseline configuration. The reduced flashing increases the H_2O evaporator/CO_2 condenser duty from 74.07 MW to 74.1 MW and the medium-temperature evaporator duty from 82.0 MW to 82.2 MW. The increased H_2O evaporator/CO_2 condenser duty increases the CO_2 refrigerant flow rate from 227.8 kg/s to 227.9 kg/s. Correspondingly, the low-temperature evaporator duty increases from 50.73 MW to 50.76 MW. As in the condenser-to-absorber series configuration, crystallization is a concern in the parallel configuration. The reduced coupling fluid flow rate in the absorber increases the absorber solution saturation temperature from 41.0°C to 43.0°C, also raising the saturation LiBr concentration from 58.82% to 59.85%. Therefore, the concentrated solution enters the absorber at 66.03% LiBr rather than the 64.9% LiBr concentration of the baseline cycle. The absorber heat rejection duty decreases from 193.1 MW to 192.8 MW. As the heat duties are nearly equal for the parallel and baseline absorber-to-condenser configurations, the two configurations exhibit very similar cycle performance

The cycle performance and heat duties of each seawater coupling loop configuration will be dependent on the component *UA*s specified and the environmental operating conditions. The key results of the seawater coupling loop configuration analysis are summarized in Table 7. For the conditions and *UA*s considered here, the condenser-to-absorber series configuration offers slightly improved cycle performance and cooling loads but also increases the risk of crystallization in the cycle.

4.6 DOUBLE-EFFECT ABSORPTION LOOP CONFIGURATION

A double-effect configuration of the absorption cycle was analyzed to determine the cycle performance improvement that could be achieved if high exhaust heat temperatures (≥275°C) were available. As discussed in Chapter 2.1.1, several double-effect absorption cycle configurations have been developed. The double-effect configuration in this analysis is a series flow configuration with solution flowing to the high temperature desorber first. As in the baseline CAVC single-effect configuration analysis described in Chapter 3.2, the double-effect cycle was developed using assumed *CAT* and/or effectiveness values for each heat exchange component. Once the system computations converged with these assumed *CAT*s and effectivenesses, the *UA* values required to achieve this performance were calculated and substituted as fixed input specifications for parametric analyses based on the exhaust heat input temperature.

Baseline Cycle Development

As discussed in Chapter 2.1.1, one parallel flow and two series flow double-effect H_2O/LiBr absorption cycle configurations are typically used in industry. The parallel flow configuration generally exhibits higher COPs but provides less cooling capacity than the series flow configurations, as discussed in Chapter 2.1.1. Between the two series flow configurations, the configuration with solution flowing to the high desorber and then the low desorber exhibits higher COPs and provides more cooling capacity than the configuration with solution flowing to the low desorber first. Due to the increased complexity and added controls required for the parallel flow configuration, the series flow configuration with solution flow to the high desorber first was chosen for this analysis. The double-effect CAVC cycle configuration is shown in Fig. 51.

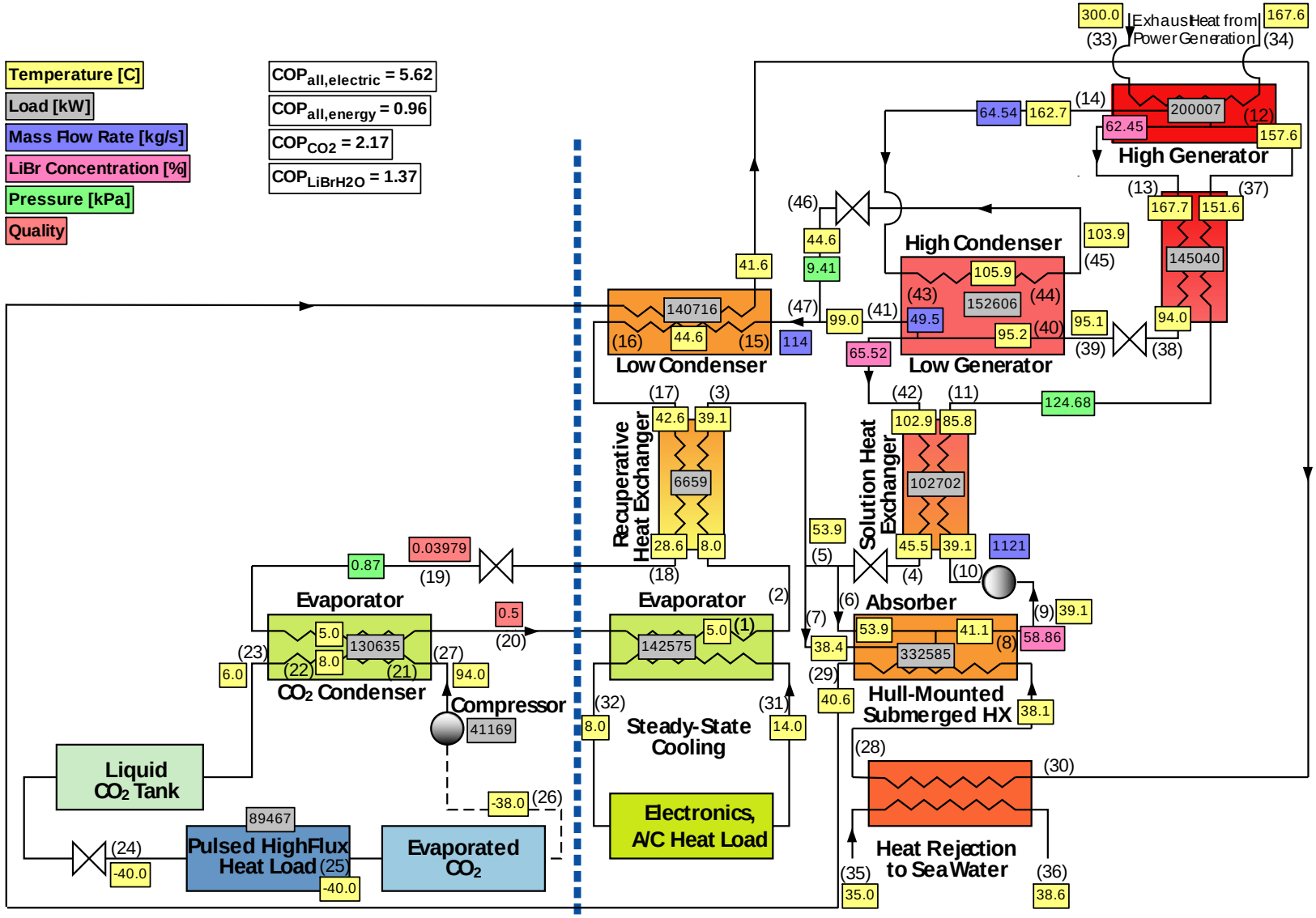

Fig. 51. Double-effect CAVC Cycle Schematic and Baseline Results

Table 8. Double-effect CAVC Cycle Optimization

Exhaust Heat Temperature [C]	Combined COP (Electric Input Basis)	Combined COP (Total Energy Input Basis)	COP (Absorption Cycle)	Total Cooling Load [kW]	Concentrated Solution LiBr Concentration [%]
275	5.284	0.380	0.483	96926	59.06
280	5.468	0.909	1.288	257781	60.52
285	5.474	0.944	1.348	269641	61.94
290	5.476	0.956	1.369	273897	63.33
295	5.478	0.961	1.376	275380	64.69
300	5.478	0.961	1.378	275652	66.02
305	5.478	0.960	1.376	275360	67.32
310	5.478	0.959	1.374	274808	68.58
315	5.478	0.957	1.370	274164	69.81
320	5.478	0.955	1.367	273526	71.01
325	5.477	0.953	1.364	272950	72.18

The double-effect model was initially developed using assumed *CAT* and effectiveness values for each heat exchange component, as in the single-effect configuration model (Chapter 3.2). Using these assumed values, the cycle performance was evaluated over a range of exhaust heat input temperatures. The highest temperature (275°C) considered in the single-effect CAVC exhaust heat temperature parametric analysis was the lowest temperature considered for the double-effect analysis. The optimal COP and total cooling capacity occurred at an exhaust heat temperature of 300°C, as shown in Table 8. Additionally, the concentrated solution LiBr concentration rises with exhaust heat temperature to a value of 66.0% at 300°C. As discussed in Chapters 4.1 and 4.4, a limit of 65.0% LiBr concentration has been assumed in this analysis to avoid crystallization issues. Exhaust temperatures above 300°C result in LiBr concentrations far above this limit. Therefore, the double-effect configuration UA values were set using an exhaust heat temperature of 300°C.

Baseline Configuration and Results

The double-effect CAVC cycle configuration, with baseline results, is shown in Fig. 51. A high-temperature condenser/low-temperature desorber (HCLD) heat exchanger and an additional SHX are added to the single-effect CAVC baseline cycle configuration. The double-effect CAVC cycle operates at a high pressure of 124.68 kPa, an intermediate pressure of 9.41 kPa, and a low pressure of 0.87 kPa. As described in Chapter 3.3, the single-effect CAVC cycle operates at a high pressure of 13.03 kPa and a low pressure of 0.87 kPa. The single-effect CAVC model equations detailed in Chapter 3.3 are also applicable for the double-effect CAVC model. Additional equations required by the HCLD and SHX are detailed here.

Dilute solution leaving the low-temperature SHX at state (11) enters the high-temperature SHX where it is heated by the intermediate concentrated solution exiting the high-temperature desorber at state (13). An effectiveness of 90% is assumed for this component, yielding a heat duty of 145 MW. First, the lowest enthalpy ($h_{\text{HSHX,hot,out}}$) achievable by the intermediate solution stream as it flows from state (13) to state (38) is evaluated:

$$h_{\text{HSHX,hot,out}} = h_{\text{LiBr}}\left(T_{11}, x_{13}\right) \tag{4.1}$$

$$214.9\frac{\text{kJ}}{\text{kg}} = h_{\text{LiBr}}\left(85.8°\text{C},\ 62.5\%\right)$$

Next, the highest enthalpy ($h_{\text{HSHX,cold,out}}$) achievable by the dilute solution stream as it flows from state (11) to state (37) is evaluated:

$$h_{\text{HSHX,cold,out}} = h_{\text{LiBr}}\left(T_{13}, x_{11}\right) \tag{4.2}$$

$$361\frac{\text{kJ}}{\text{kg}} = h_{\text{LiBr}}\left(167.7°\text{C},\ 58.86\%\right)$$

These enthalpies establish the maximum possible heat duty on either side of the heat exchanger as follows:

$$Q_{\text{max,HSHX hot}} = m_{13}\left(h_{13} - h_{\text{HSHX,hot,out}}\right) \tag{4.3}$$

$$161\,\text{MW} = 1056\frac{\text{kg}}{\text{s}}\left(367\frac{\text{kJ}}{\text{kg}} - 215\frac{\text{kJ}}{\text{kg}}\right)$$

$$Q_{\text{max,HSHX cold}} = m_{11}\left(h_{\text{HSHX,cold,out}} - h_{11}\right) \tag{4.4}$$

$$181\,\text{MW} = 1121\frac{\text{kg}}{\text{s}}\left(361\frac{\text{kJ}}{\text{kg}} - 200\frac{\text{kJ}}{\text{kg}}\right)$$

From these values of the maximum heat duty and the assumed heat exchanger effectiveness, the actual solution heat exchanger duty is cacluated to be 145 MW:

$$Q_{\text{min,HSHX}} = \min\left(Q_{\text{max,HSHX hot}}, Q_{\text{max,HSHX cold}}\right) \tag{4.5}$$

$$Q_{\text{HSHX}} = \varepsilon_{\text{HSHX}} Q_{\text{min,HSHX}} \tag{4.6}$$

$$145\ \text{MW} = 90\% \cdot 161\ \text{MW}$$

Based on this heat duty, the dilute solution exiting the low-temperature SHX is heated from 85.8°C to the desorber inlet temperature of 157.6°C in the HSHX:

$$Q_{\text{HSHX}} = m_{11}\left(h_{37} - h_{11}\right) \tag{4.7}$$

$$145\ \text{MW} = 1121\frac{\text{kg}}{\text{s}}\left(329\frac{\text{kJ}}{\text{kg}} - 200\frac{\text{kJ}}{\text{kg}}\right)$$

Similarly, the intermediate concentration LiBr solution stream exiting the high-temperature desorber is cooled from 167.7°C to 94.0°C:

$$Q_{\text{HSHX}} = m_{13}\left(h_{13} - h_{38}\right) \tag{4.8}$$

$$145\ \text{MW} = 1056\frac{\text{kg}}{\text{s}}\left(367\frac{\text{kJ}}{\text{kg}} - 230\frac{\text{kJ}}{\text{kg}}\right)$$

The *UA* required to accomplish this heat duty in the HSHX is 12.4 MW/K:

$$Q_{\text{HSHX}} = UA_{\text{HSHX}} LMTD\left(T_{13}, T_{38}, T_{11}, T_{37}\right) \tag{4.9}$$

$$145\ \text{MW} = 12.4\frac{\text{MW}}{\text{K}} \cdot 11.72°\text{C}$$

After exiting the high-temperature HSHX, the intermediate concentration solution expands across the high solution valve from the high cycle pressure of 124.68 kPa at state (38) to the intermediate cycle pressure of 9.41 kPa at state (39). The quality of the

solution exiting the valve is checked to determine the solution state at the low desorber inlet:

$$q_{\text{Outlet,High LiBr Valve}} = q_{\text{LiBr}}\left(h_{38}, p_{39}, x_{38}\right) \tag{4.10}$$

$$-0.0007\% = q_{\text{LiBr}}\left(230\frac{\text{kJ}}{\text{kg}}, 9.41\text{ kPa}, 62.5\%\right)$$

The intermediate concentration solution at state (39) then enters the low-temperature desorber at 62.45% LiBr concentration and a temperature of 95.1°C. Thermal energy is provided to the intermediate concentrated solution stream in the low-temperature desorber using the vapor stream entering the high-temperature condenser at state (14) and leaving at state (45). Initial heating in the desorber raises the solution temperatures to the saturation value, i.e., 95.2°C at state (40) from the inlet temperature of 95.1°C at state (39):

$$T_{40} = T_{\text{LiBr}}\left(p_{40}, x_{40}\right) \tag{4.11}$$

$$95.2°\text{C} = T_{\text{LiBr}}\left(9.41\,\text{kPa},\ 62.45\%\right)$$

The desorber then generates 49.5 kg/s of superheated water vapor that exits the low-temperature desorber at state (41). The low-temperature desorber heat duty is 153 MW.

$$Q_{\text{HCLD}} = m_{42}h_{42} + m_{41}h_{41} - m_{39}h_{39} \tag{4.12}$$

$$153\text{ MW} = 1007\frac{\text{kg}}{\text{s}}\cdot 261\frac{\text{kJ}}{\text{kg}} + 49.5\frac{\text{kg}}{\text{s}}\cdot 2686\frac{\text{kJ}}{\text{kg}} - 1056\frac{\text{kg}}{\text{s}}\cdot 232\frac{\text{kJ}}{\text{kg}}$$

The remaining concentrated solution exits at state (42), at 65.52% LiBr concentration and 102.9°C, and enters the low-temperature SHX to provide heating for the pump outlet stream (10).

The vapor generated by the high-temperature desorber enters the high-temperature condenser, state (14), at a superheated temperature of 162.7°C. The vapor is first cooled to a saturated vapor (43) at 105.9°C, then condensed to a saturated liquid (44), and subcooled by 2°C to 103.9°C at the condenser outlet (17). The total high-temperature condenser duty is calculated as follows:

$$Q_{\text{High Condenser,H}_2\text{O}} = m_{14}\left(h_{14} - h_{45}\right) \tag{4.13}$$

$$153\ \text{MW} = 64.54\frac{\text{kg}}{\text{s}}\left(2800\frac{\text{kJ}}{\text{kg}} - 436\frac{\text{kJ}}{\text{kg}}\right)$$

The *UA* required to accomplish this heat duty in the HCLD is 25.2 MW/K:

$$Q_{\text{HCLD}} = UA_{\text{HCLD}}LMTD\left(T_{43}, T_{44}, T_{40}, T_{42}\right) \tag{4.14}$$

$$153\ \text{MW} = 25.2\frac{\text{MW}}{\text{K}}\cdot 6.06°\text{C}$$

As in the single-effect model, the saturated temperature is used to calculate the HCLD *LMTD*, as the superheating, desuperheating and subcooling on either side of the component represent a small fraction of the overall heat duty but would introduce a large difference in the calculated *LMTD* and *UA*.

After exiting the high-temperature condenser, the water flows across the high pressure H_2O expansion valve. The water pressure decreases from the high cycle pressure of 124.68 kPa at state (45) to the intermediate cycle pressure of 9.41 kPa at state (46), with the refrigerant exiting at a quality of 10.4%:

$$h_{45} = h_{46} = 436\frac{\text{kJ}}{\text{kg}} \tag{4.15}$$

$$q_{46} = q_{\text{H}_2\text{O}}\left(p_{46}, h_{46}\right) \tag{4.16}$$

$$0.104 = q_{H_2O}\left(9.41\text{ kPa}, 436\frac{\text{kJ}}{\text{kg}}\right)$$

The low-quality, two-phase mixture exiting the valve mixes with the vapor stream exiting the low-temperature desorber side of the HCLD. The resulting H_2O stream (47) has a flow rate of 114 kg/s at 44.6°C and a quality of 51.2%:

$$m_{47} = m_{46} + m_{41} \tag{4.17}$$

$$114\frac{\text{kg}}{\text{s}} = 64.54\frac{\text{kg}}{\text{s}} + 49.5\frac{\text{kg}}{\text{s}}$$

$$m_{47}h_{47} = m_{46}h_{46} + m_{41}h_{41} \tag{4.18}$$

$$114\frac{\text{kg}}{\text{s}}\cdot 1412\frac{\text{kJ}}{\text{kg}} = 64.54\frac{\text{kg}}{\text{s}}\cdot 436\frac{\text{kJ}}{\text{kg}} + 49.5\frac{\text{kg}}{\text{s}}\cdot 2686\frac{\text{kJ}}{\text{kg}}$$

$$T_{47} = T_{H_2O}\left(h_{47}, p_{47}\right) \tag{4.19}$$

$$44.6°\text{C} = T_{H_2O}\left(1412\frac{\text{kJ}}{\text{kg}}, 9.41\text{ kPa}\right)$$

$$q_{47} = q_{H_2O}\left(h_{47}, p_{47}\right) \tag{4.20}$$

$$0.512 = q_{H_2O}\left(1412\frac{\text{kJ}}{\text{kg}}, 9.41\text{ kPa}\right)$$

The two-phase mixture enters the low-temperature condenser at state (47). The remainder of the cycle is calculated with the assumptions and equations described in Chapter 3.3 for the single-effect CAVC model. Various output results differ between the single-effect and double-effect models, as shown by a comparison between Fig. 48and Fig. 51.

Double-Effect CAVC Cycle Performance

The double-effect CAVC baseline results detailed above yield a combined, total-energy-input-based *COP* of 0.96. The combined, total energy input *COP* is defined as:

$$COP_{\text{All, Energy}} = \frac{Q_{\text{Evaporator, Low T}} + Q_{\text{Evaporator, Medium T}}}{Q_{\text{Exhaust Input}} + W_{\text{Compressor}} + W_{\text{Pump}}} \tag{4.21}$$

$$0.96 = \frac{89\ \text{MW} + 143\ \text{MW}}{200\ \text{MW} + 41\ \text{MW} + 0.084\ \text{MW}}$$

This COP value represents a 60% increase in overall cycle performance from the single-effect COP of 0.594 based on total energy input.

As in Chapter 3.4, a revealing insight into the system performance is obtained by considering only the electric power input in the definition of *COP* as follows:

$$COP_{\text{All, Electric}} = \frac{Q_{\text{Evaporator, Low T}} + Q_{\text{Evaporator, Medium T}}}{W_{\text{Compressor}} + W_{\text{Pump}}} \tag{4.22}$$

$$5.62 = \frac{89\ \text{MW} + 143\ \text{MW}}{41\ \text{MW} + 0.084\ \text{MW}}$$

This definition yields an overall *COP* of 5.62 based on the electrical input, which is slightly lower than the overall electric input COP of 5.685 calculated for the single-effect cycle. The overall COP based on electrical input is not improved by the increased double-effect absorption cycle performance because the cooling capacity and required electrical input both increase proportionally. The single-effect cycle provides 51 MW of low-temperature cooling and 82 MW of medium-temperature cooling using 23 MW of electricity in the compressor and pump. The double-effect cycle provides 89 MW of low-temperature cooling and 143 MW of medium-temperature cooling using 41 MW of electricity in the compressor and pump. The increase in cooling capacity is 74.4% while the increase in required electricity is 78.3%, resulting in a slightly lower electricity-based

overall COP for the double-effect cycle. As discussed in Chapter 2.1.1, the main advantage of the double-effect cycle configuration is the double use of the absorption cycle heat input. When heat input is considered a cost for cycle performance, as in Eqn. (4.21), the double use advantage is clearly captured in higher COPs due to the relatively steady value of the COP denominator when heat input is included. When the heat input is freely available and not considered a cost for cycle performance, this advantage provides only increased capacity and does not increase cycle COPs.

The performances of the component double-effect absorption and vapor-compression cycles are evaluated on a stand-alone basis as follows:

$$COP_{\text{Absorption}} = \frac{Q_{\text{H}_2\text{O Evaporator/CO}_2\text{ Condenser}} + Q_{\text{Evaporator, Medium T}}}{Q_{\text{Exhaust Input}} + W_{\text{Pump}}} \tag{4.23}$$

$$1.37 = \frac{131\text{ MW} + 143\text{ MW}}{200\text{ MW} + 0.084\text{ MW}}$$

$$COP_{\text{Vapor Compression}} = \frac{Q_{\text{Evaporator, Low T}}}{W_{\text{Compressor}}} \tag{4.24}$$

$$2.17 = \frac{89\text{ MW}}{41\text{ MW}}$$

These two COPs provide an understanding of how well each of the component cycles is performing in comparison to typical absorption and vapor-compression cycles alone. The absorption COP is 1.37, while the vapor-compression COP is 2.17 despite the high lift from -40°C to 8°C. Without the absorption cycle, this lift would be from -40°C to 40°C, resulting in much lower cycle *COP*s. In summary, at an assumed high temperature, 35°C, of sea water for heat rejection, the double-effect cycle is able to use 200 MW of waste heat and provide 143 MW of cooling at 5°C and 89 MW of cooling at -40°C with an investment of only 41 MW of compressor power. At the same sea water temperature,

the single-effect CAVC cycle uses 200 MW of waste heat to provide 82 MW of cooling at 5°C and 51 MW of cooling at -40°C, using 23 MW of compressor power. When the cycle input is considered a free source of energy, the main advantage of the double-effect cycle is the greatly increased cooling capacities.

Double-Effect CAVC Cycle Component Sizes

The calculated *UA* values are used to estimate the size of components needed for the double-effect CAVC cycle baseline configuration, as in the single-effect CAVC cycle baseline configuration analysis (see Chapter 3.2). Typical *U* values provided by Perry's Chemical Engineers' Handbook [6] are used for very rough, first approximation calculations of required heat transfer surface area. An abbreviated set of typical *U* values listed in this resource is provided in Table 4. This generic listing does not provide an exact match for each component in the double-effect CAVC cycle; for example, the HCLD presents a situation that is not directly listed in the typical values. In such cases, typical values for the limiting medium were used. From the range of *U* values provided for the relevant media in a tubular heat exchanger, the highest value was used to estimate the *A* of the CAVC components. The most efficient heat transfer value provided was used to reflect the inclusion of highly efficient microchannel-based components in the cycle. The typical values obtained from Perry's Chemical Engineers' Handbook and the resulting estimation of *A* are tabulated in Table 9. The reference numbers listed in Table 9 correspond with the numbering in Table 4, to clearly show the source of the *U* values used for each component.

Table 9. Estimated Double-Effect CAVC Heat Transfer Surface Areas.

Heat Exchanger	Ref. #	Typical U [Btu/(°F·ft^2·hr)]	Typical U [W/(m^2·K)]	UA [W/K]	Heat Transfer Surface Area, A [m^2]
Refrigerant Heat Exchanger (RHX)	11	50	284	692,000	2,400
Low Solution Heat Exchanger (LSHX)	1	250	1,420	9,449,000	6,700
High Solution Heat Exchanger (HSHX)	1	250	1,420	12,374,000	8,700
Absorber	4	1000	5,678	47,970,000	8,400
Low Condenser	4	1000	5,678	40,218,000	7,100
High Condenser/Low Desorber (HCLD)	4	1000	5,678	25,188,000	4,400
High Generator	9	20	114	4,224,000	37,200
Evaporator/Condenser	4	1000	5,678	43,545,000	7,700
H_2O Evaporator	4	1000	5,678	26,105,000	4,600
Sea Heat Exchanger	1	250	1,420	155,716,000	109,700

Note: Typical overall heat transfer coefficients are taken from Perry's Chemical Engineers' Handbook (7th Edition)
The highest U value (i.e., 1000 Btu/hr-ft^2-F) was chosen for phase-change heat exchangers coupled either to single-phase liquids or to phase-change processes to reflect the anticipated high heat transfer coefficients due to phase change of H_2O and CO_2.

Table 10. Increased Surface Area Required for Double-Effect CAVC Configuration.

Heat Exchanger	Heat Transfer Surface Area, A [m^2]		Increased Surface Area Required [%]
	Double-Effect CAVC	Single-Effect CAVC	
Refrigerant Heat Exchanger (RHX)	2,400	1,400	71.4%
Low Solution Heat Exchanger (LSHX)	6,700	4,400	52.3%
High Solution Heat Exchanger (HSHX)	8,700		
Absorber	8,400	6,100	37.7%
Low Condenser	7,100	5,800	22.4%
High Condenser/Low Desorber (HCLD)	4,400		
High Generator	37,200	23,400	59.0%
Evaporator/Condenser	7,700	4,300	79.1%
H_2O Evaporator	4,600	2,600	76.9%
Sea Heat Exchanger	109,700	83,500	31.4%

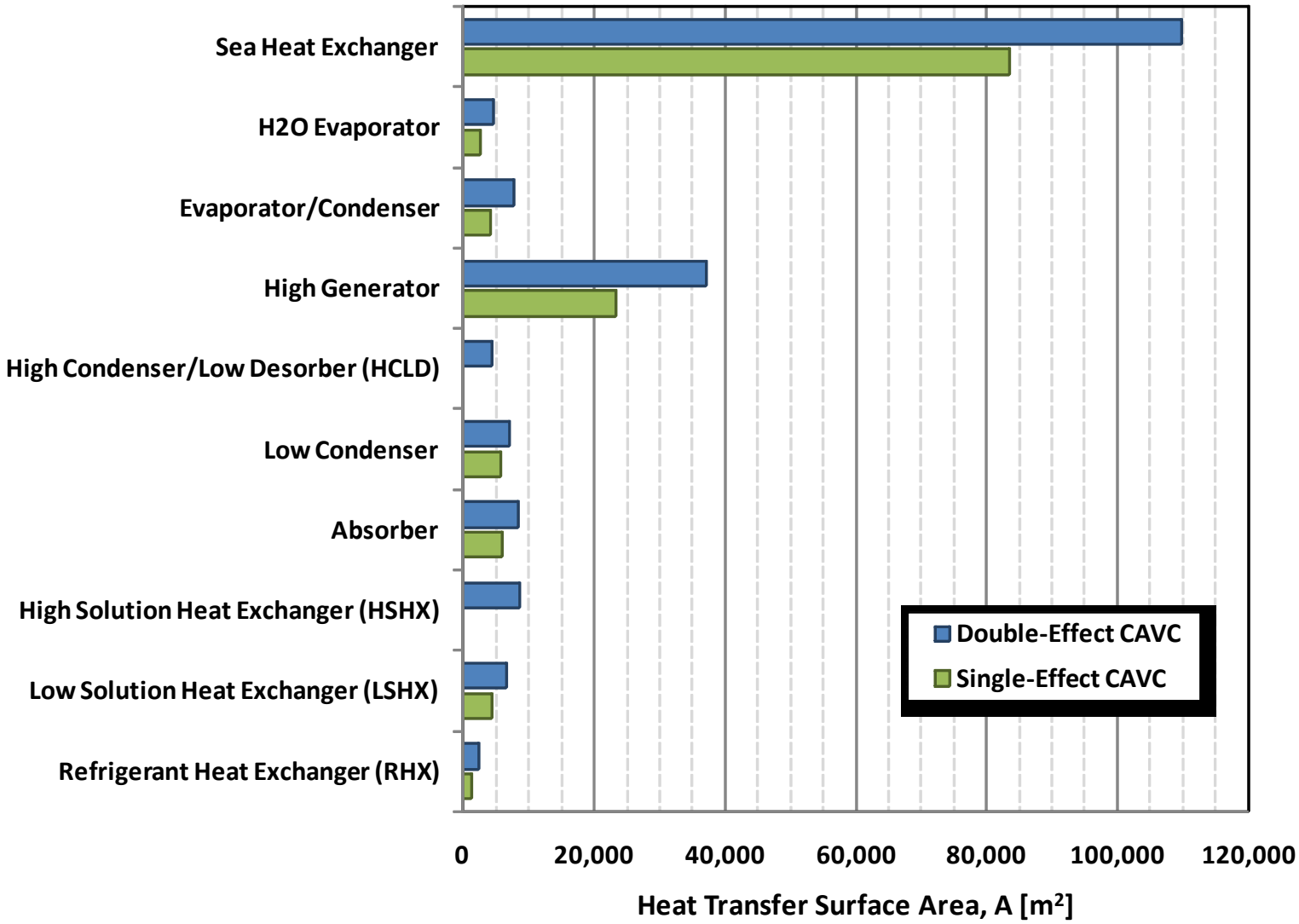

Fig. 52 Increased Surface Area Required for Double-Effect CAVC Configuration.

To provide the increased cooling capacity described above, the double-effect CAVC cycle requires significantly increased heat transfer surface areas when compared to the single-effect CAVC cycle. As shown in Table 10 and Fig. 52, the required increase in surface area ranges from a 22.4% increase in the low pressure heat rejection condenser of the LiBr/H2O cycle to a 79.1% increase in the H_2O evaporator/CO_2 condenser. Two additional heat exchangers also add to the required increase; the HSHX and the HCLD require 8,700 m^2 and 4,400 m^2, respectively. The required HSHX surface area is 197.7% of the single-effect SHX area, while the required HCLD surface area is 75.9% of the single-effect condenser area. Therefore, to provide a cooling capacity increase of 74.4%, the double-effect CAVC cycle requires an average overall increase of roughly 70% in heat transfer surface area.

Exhaust Heat Temperature Parametric Analysis

The effect of exhaust heat temperature on double-effect CAVC cycle performance and capacities was investigated over the range 275°C to 400°C. As noted earlier in this Chapter, the maximum solution LiBr concentration reaches the established limit of 65.0% when the exhaust heat input reaches approximately 300°C with a set mass flow rate. Therefore, to utilize temperatures above 300°C, a solution pump control system must be used to adjust the solution flow rate to maintain the maximum concentration at ≤65.0% LiBr. In this analysis, a set total solution flow rate of 1121 kg/s was used to investigate the effect of exhaust heat temperature over the range of 275°C to 300°C (Fig. 53 and Fig. 54), while a set maximum LiBr concentration of 65.0% was used over the range of 300°C to 400°C (Fig. 55 and Fig. 56).

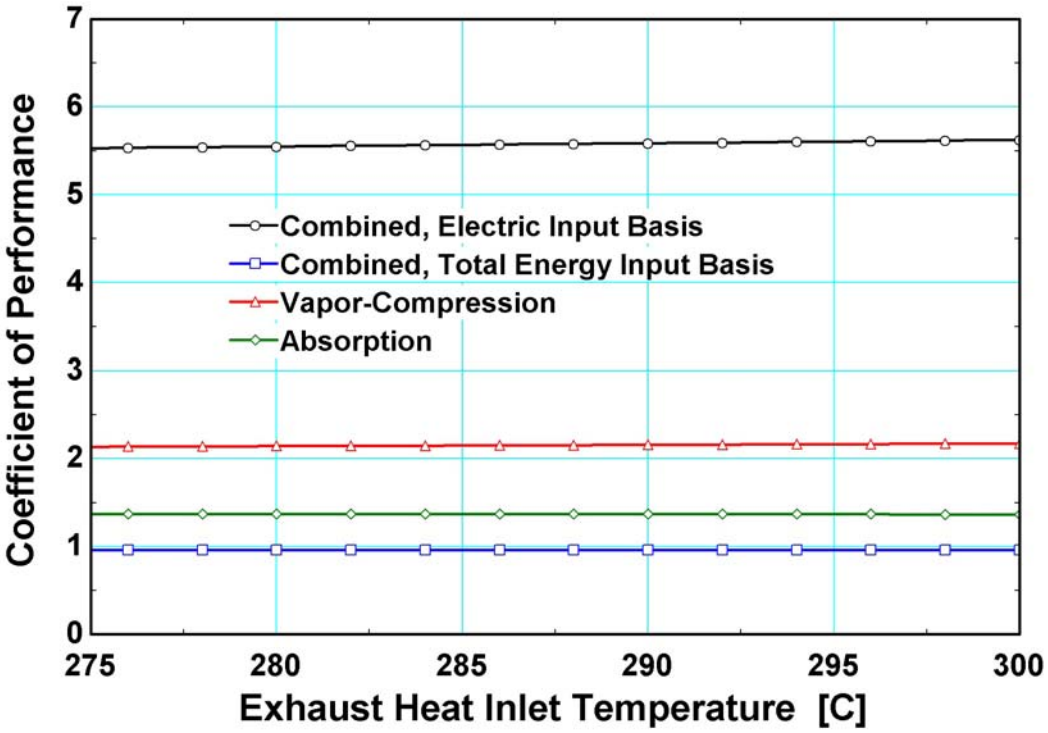

Fig. 53. Effect of Exhaust Inlet Temperature on Double-Effect CAVC Cycle Performance (275°C to 300°C).

As exhaust heat temperature increases from 275°C to 300°C, the combined electric and vapor-compression *COP*s also rise (Fig. 53). The low-temperature evaporator cooling capacity increases more than the compressor input rises, increasing $COP_{\text{All, Electric}}$ from 5.53 to 5.62 and $COP_{\text{Vapor Compression}}$ from 2.14 to 2.17. The compressor power input rises from 38 MW to 41 MW, an 8.1% increase, while the low temperature cooling duty rises from 81 to 89 MW, a 10.0% increase, which corresponds to the increase in $COP_{\text{All, Electric}}$ and $COP_{\text{Vapor Compression}}$. As exhaust heat temperature increases, the absorption cycle cooling temperature decreases from 5.8°C to 5.0°C. The lower temperature vapor-compression cycle heat sink increases the low-temperature cooling capacity while allowing a smaller increase in compressor power input needed to provide that capacity. In the absorption loop, the effective use of exhaust heat input in the double-effect cycle configuration maintains a proportional increase in total cooling

capacity as exhaust heat temperature rises, keeping $COP_{\text{All, Energy}}$ and $COP_{\text{Absorption}}$ steady at 0.96 and 1.37, respectively. As shown in Fig. 54, the exhaust input load increases from 181 MW to 200 MW, a 10.3% increase, while the total cooling load increases from 249 to 273 MW, a 9.7% increase. The similar increase in each capacity corresponds to the relatively constant $COP_{\text{All, Energy}}$ and $COP_{\text{Absorption}}$.

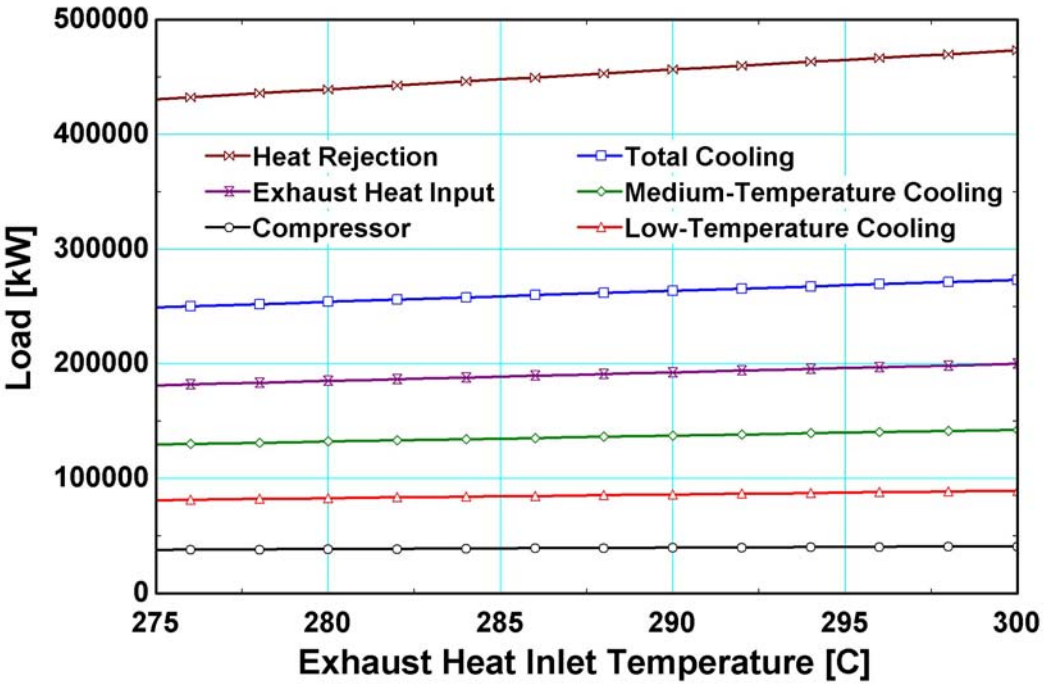

Fig. 54. Effect of Exhaust Inlet Temperature on Double-Effect CAVC Cycle Capacities (275°C to 300°C).

As exhaust heat temperature increases from 300°C to 400°C, with a set maximum solution LiBr concentration of 65.0%, the combined electric and vapor-compression *COP*s continue to rise (Fig. 55). As before, the low-temperature evaporator cooling capacity increases more than the compressor input rises (Fig. 56), increasing $COP_{\text{All, Electric}}$ from 5.62 to 5.73 and $COP_{\text{Vapor Compression}}$ from 2.17 to 2.22. The required compressor power input rises from 41 MW to 44 MW, an 8.2% increase, while the low temperature cooling duty rises from 89 to 98 MW, a 10.5% increase, which corresponds

to the increase in $COP_{\text{All, Electric}}$ and $COP_{\text{Vapor Compression}}$. As exhaust heat temperature increases, the absorption cycle cooling temperature decreases from 5.1°C to 4.1°C. As before, the lower temperature vapor-compression cycle heat sink increases the low-temperature cooling capacity while allowing a smaller increase in compressor power input needed to provide that capacity. In the absorption loop, the increase in exhaust heat input outweighs the increase in cooling capacity, due to large solution mass flow rate and desorber temperature increases when compared to the total vapor mass flow rate increase and evaporator temperature decrease.

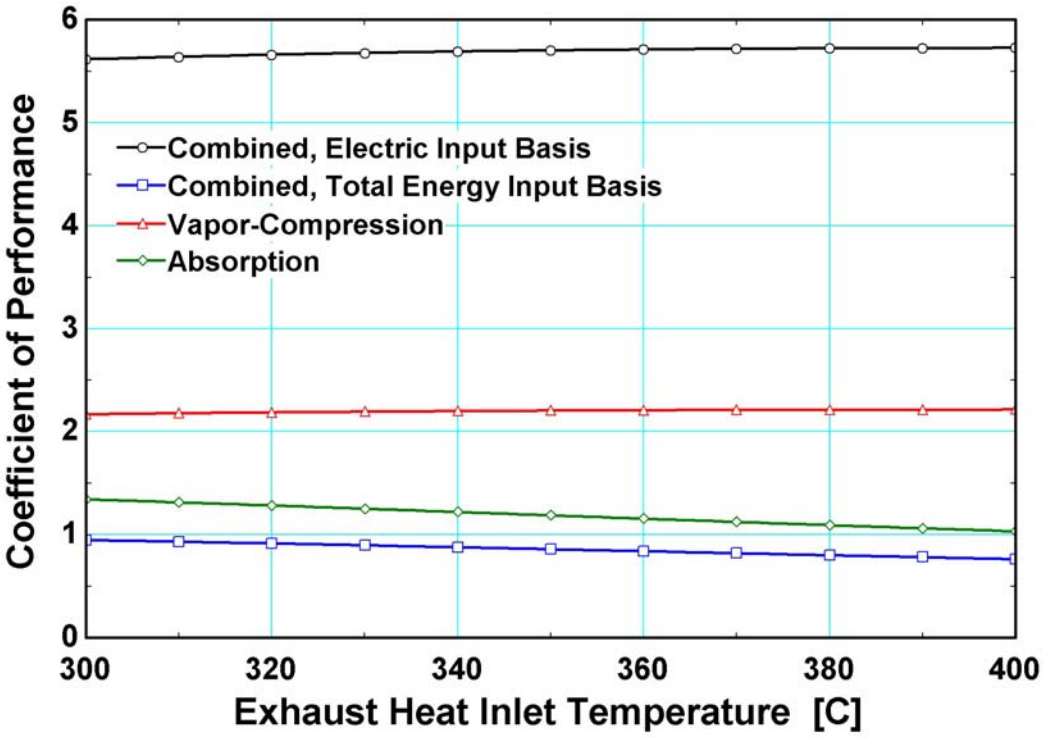

Fig. 55. Effect of Exhaust Inlet Temperature on Double-Effect CAVC Cycle Performance (300°C to 400°C).

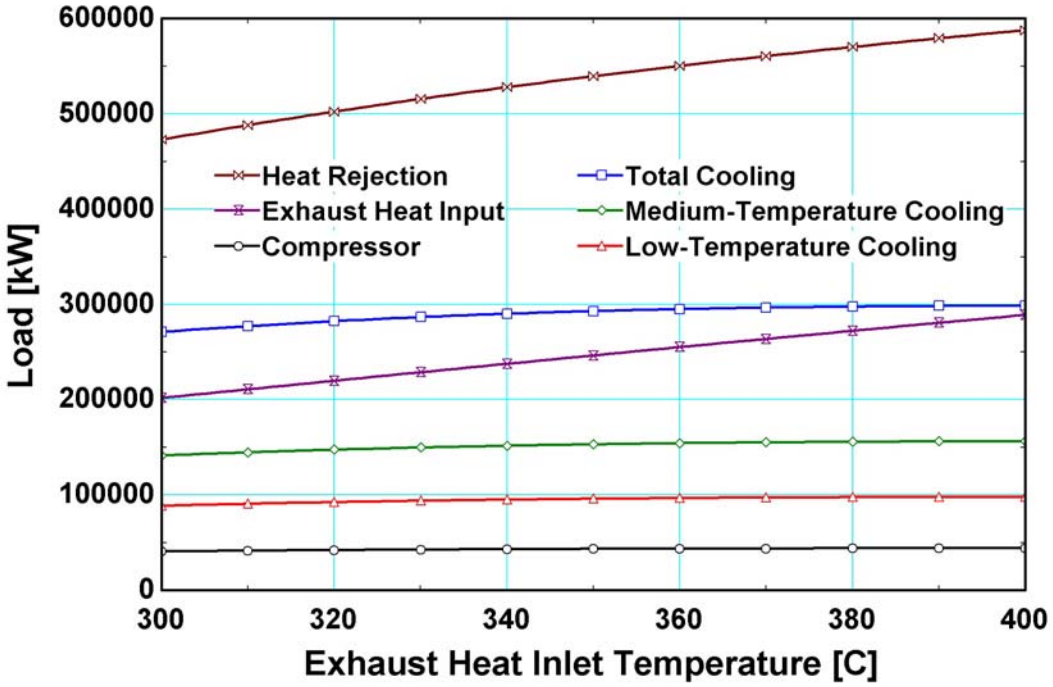

Fig. 56. Effect of Exhaust Inlet Temperature on Double-Effect CAVC Cycle Capacities (300°C to 400°C).

The total solution mass flow rate required to maintain the concentration limit and the resulting vapor mass flow rates are shown in Fig. 57. Total solution flow rate rises from 1221 kg/s to 2432 kg/s, a 99.2% increase, while total vapor flow rate increases from 113 kg/s to 125 kg/s, a 10.6% increase. The increased solution flow rate demands greater heat transfer duty from the SHXs. Due to the fixed *UA* of each SHX, the SHX cold stream outlet temperatures, T[11] and T[37], decrease as solution flow rate increases. Therefore, more sensible heating is required in the high-temperature desorber due to the decreasing solution inlet temperature. The increasing sensible heating load results in a relatively small increase in vapor production when compared to the increase in total solution flow rate. The $COP_{\text{All, Energy}}$ decreases from 0.95 to 0.76 and $COP_{\text{Absorption}}$ decreases from 1.34 to 1.03. As shown in Fig. 56, the exhaust input load increases from 202 MW to 289 MW, a 43.1% increase, while the total cooling load increases from 271

to 298 MW, a 10.0% increase. The larger increase in exhaust heat input compared to cooling capacity corresponds to the decrease in $COP_{\text{All, Energy}}$ and $COP_{\text{Absorption}}$.

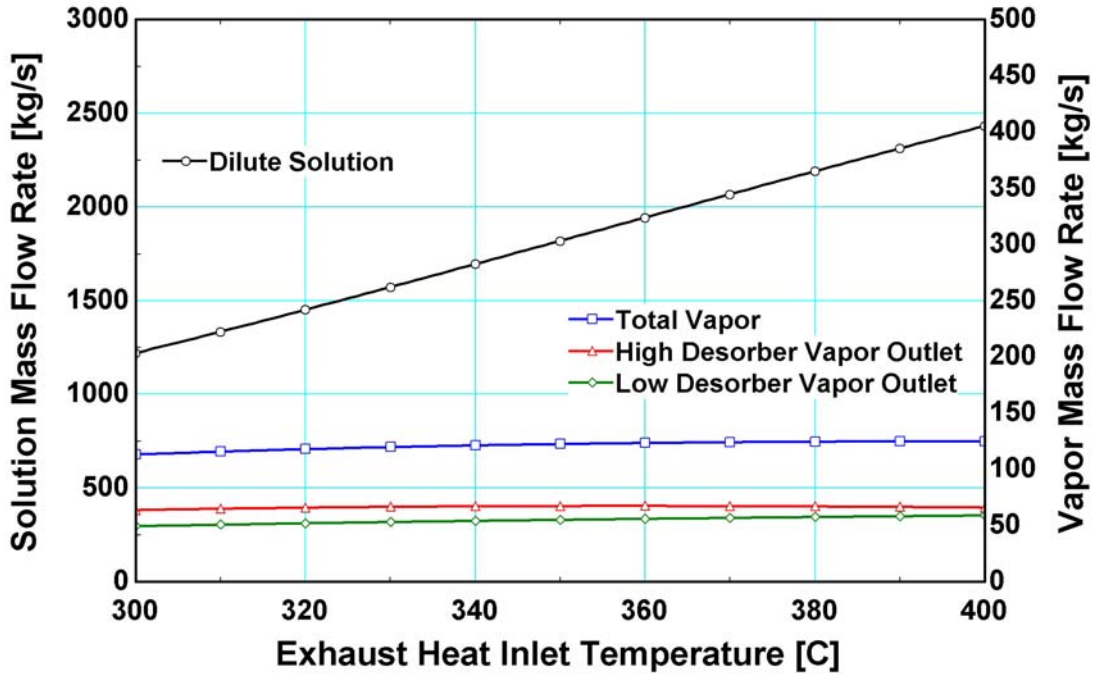

Fig. 57. Effect of Exhaust Heat Inlet Temperature on Double-Effect CAVC Cycle Mass Flow Rates (300°C to 400°C).

Based on these results, the double-effect CAVC configuration would improve cycle performance and cooling capacity if high temperature exhaust heat sources were available. However, crystallization issues may limit the temperatures that can be utilized if sophisticated cycle controls are not implemented.

Heat Rejection Temperature Parametric Analysis

The effect of heat rejection temperatures ranging from 25° to 40°C on double-effect cycle performance was investigated. This temperature range is identical to that investigated on the single-effect cycle in Chapter 4.1. The variation of the double-effect cycle coefficients of performance is shown in Fig. 58. As the heat rejection temperature rises, $COP_{\text{All,Electric}}$ decreases from 7.01 to 4.95 and $COP_{\text{All, Energy}}$ decreases from 1.06 to

0.91. The component absorption and vapor compression cycles also decrease slightly, with $COP_{\text{Absorption}}$ decreasing from 1.43 to 1.33, and $COP_{\text{Vapor Compression}}$ decreasing from 2.38 to 2.08. The relatively large decrease in $COP_{\text{All,Electric}}$ is due to the constant compressor power input; cooling load decreases due to increased heat rejection temperature, while electric input remains constant.

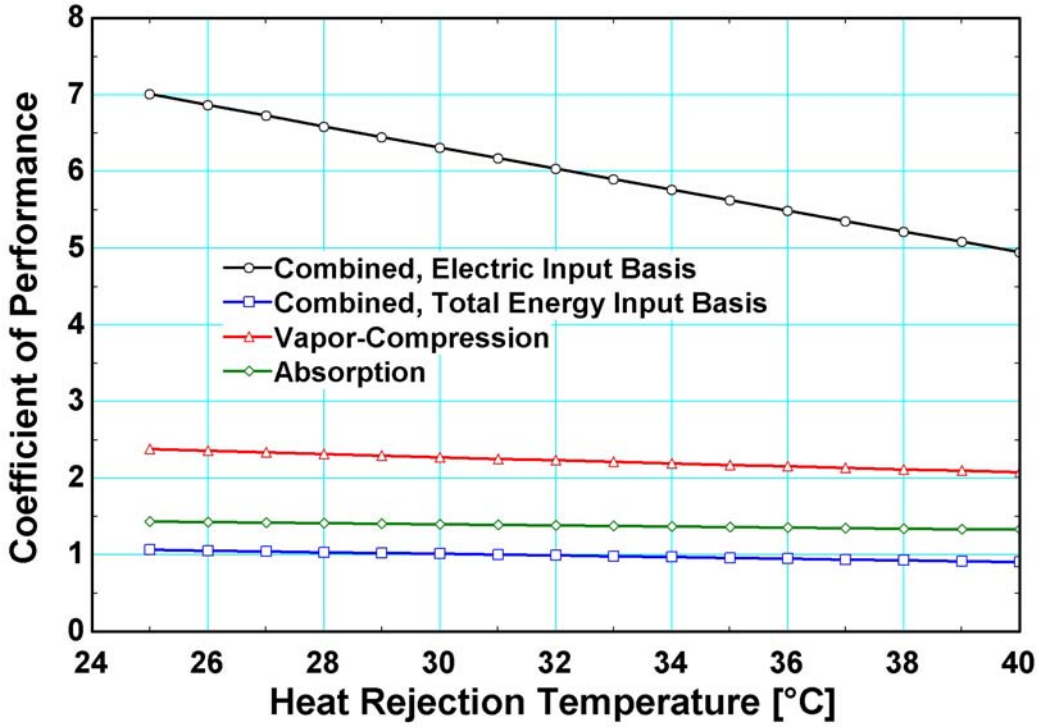

Fig. 58. Effect of Heat Rejection Temperature on Double-Effect CAVC Cycle Performance

The decreases in *COP* are caused by a decreased ability to reject heat as the heat rejection temperature increases, as shown in Fig. 59. The heat rejection load decreases from 560 MW to 430 MW over this temperature range. This is in turn reflected in an increase in temperature of LiBr-H_2O solution entering the high desorber (130.7°C to 162.4°C), which reduces the waste heat input from 230 MW to 184 MW, and decreases the water generation rate in the high desorber. The water generation rate in the HCLD also decreases as the temperature differential across the component decreases with

increasing heat rejection temperature. The high condenser and low desorber saturation temperatures converge, decreasing the heat transfer rate between the two streams and therefore the water generation rate in the low desorber stream. The reduced refrigerant flow decreases the total available cooling load from 330 MW to 245 MW. The compressor power input is held constant at 41 MW. The total cooling load decreases 25.8% while the waste heat input decreases only 20.0%, resulting in the slight decrease in $COP_{\text{All, Energy}}$. In constrast, the compressor input remains constant, resulting in the relatively large decrease in $COP_{\text{All,Electric}}$.

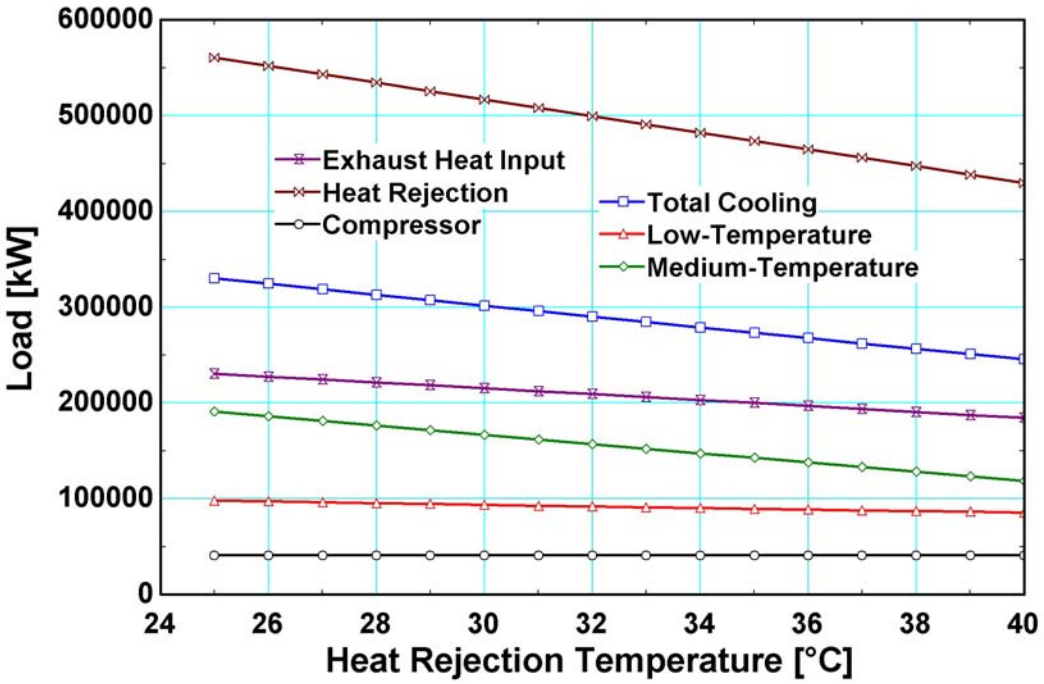

Fig. 59. Effect of Heat Rejection Temperature on Double-Effect CAVC Cycle Capacities.

The increased heat rejection temperature raises the risk of crystallization, with a maximum absorber inlet solution concentration of 66.0% at sea water temperatures of 40°C. While this concentration exceeds the limit of 65.0% set for these analyses, the

corresponding increase in absorber solution inlet temperature (57.4°C) would maintain a small safety margin between operating conditions and the actual crystallization limit.

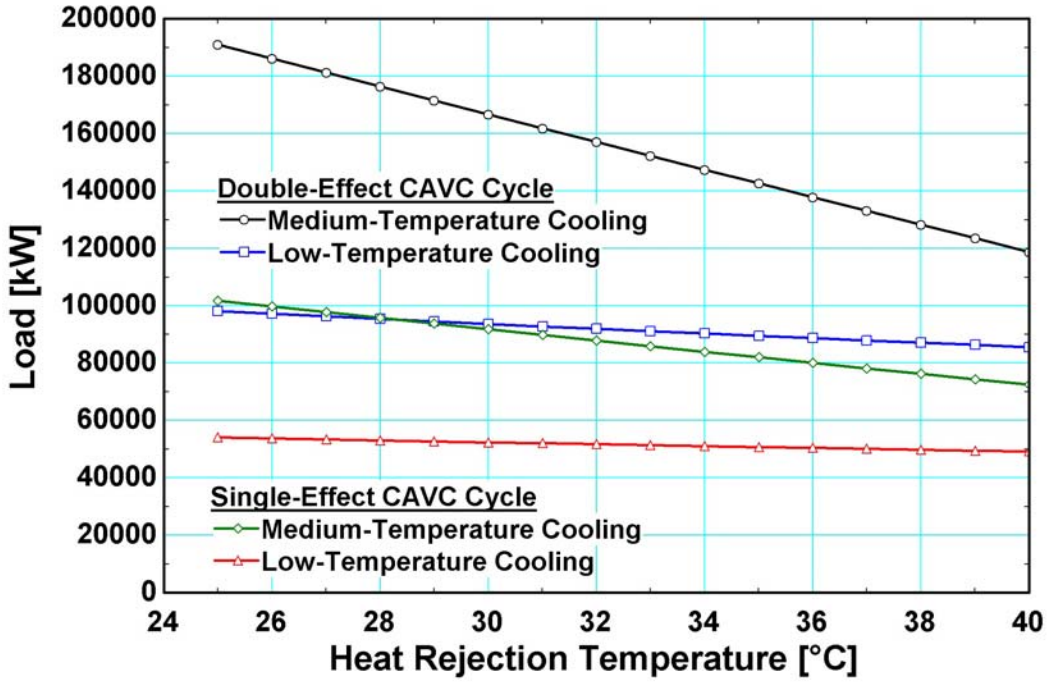

Fig. 60. Comparison of Double-Effect and Single-Effect CAVC Cycle Cooling Capacities.

The cooling capacities of the single-effect CAVC cycle and the double-effect CAVC cycle are compared in Fig. 60. At the low end of the heat rejection temperature range, 25°C, the single-effect CAVC cycle provides 102 MW of medium-temperature cooling and 54 MW of low-temperature cooling. At the same heat rejection temperature, the double-effect CAVC cycle provides 190 MW of medium-temperature cooling and 98 MW of low-temperature cooling, representing an 86.3% and 81.5% increase over the single-effect cycle, respectively. At the high end of the heat rejection temperature range, 40°C, the single-effect CAVC cycle provides 72 MW of medium-temperature cooling and 49 MW of low-temperature cooling. At 40°C, the double-effect CAVC cycle provides 119 MW of medium-temperature cooling and 86 MW of low-temperature

cooling, representing a 65.3% and 75.5% increase over the single-effect cycle, respectively. The increased heat rejection temperature has a greater effect on the double-effect cycle due to the decreasing temperature differential across the HCLD as sea water temperatures increase. As the difference between the high condenser and low desorber temperatures decreases, the heat transfer across the component decreases and less exhaust heat input energy is reused to produce vapor. The primary advantage of the double-effect cycle over the single-effect cycle is the reuse of input energy within the HCLD; therefore, the performance advantage decreases as the ability to reuse input energy decreases. Therefore, in applications utilizing a relatively cold heat rejection temperature, the double-effect CAVC cycle provides a greater advantage in cooling capacity over the single-effect CAVC cycle than in applications with warmer heat rejection temperatures.

4.7 COMPARISON WITH TWO-STAGE VAPOR-COMPRESSION CYCLE

To quantify the advantages of the cascade absorption/vapor-compression cycle over solely electrically driven vapor-compression cycles, the performance of a two-stage vapor-compression cycle (Fig. 61) operating under similar conditions was analyzed. In this cycle, refrigerant R507A evaporates at -40°C and 140.8 kPa (1). Leaving the evaporator at a superheated temperature of -37°C (2), the refrigerant flows through the first compressor to the intermediate pressure of 629 kPa (3). The cold stream of the recuperative heat exchanger (12) mixes with the refrigerant downstream of the first compressor (3), resulting in state (4). The combined stream (4), flows through the second compressor to the cycle high pressure of 1869 kPa (5). The stream then desuperheats to state (6) and condenses (7), rejecting heat to the 35°C ambient, and exits the condenser at a subcooled temperature (8). After exiting the condenser, the refrigerant is split into two streams. One stream expands to the intermediate pressure (9) and becomes the cold stream of the recuperative heat exchanger (12). The other stream becomes the hot stream of the recuperative heat exchanger (10) and is cooled (11) before expanding to the low pressure (13) and entering the evaporator.

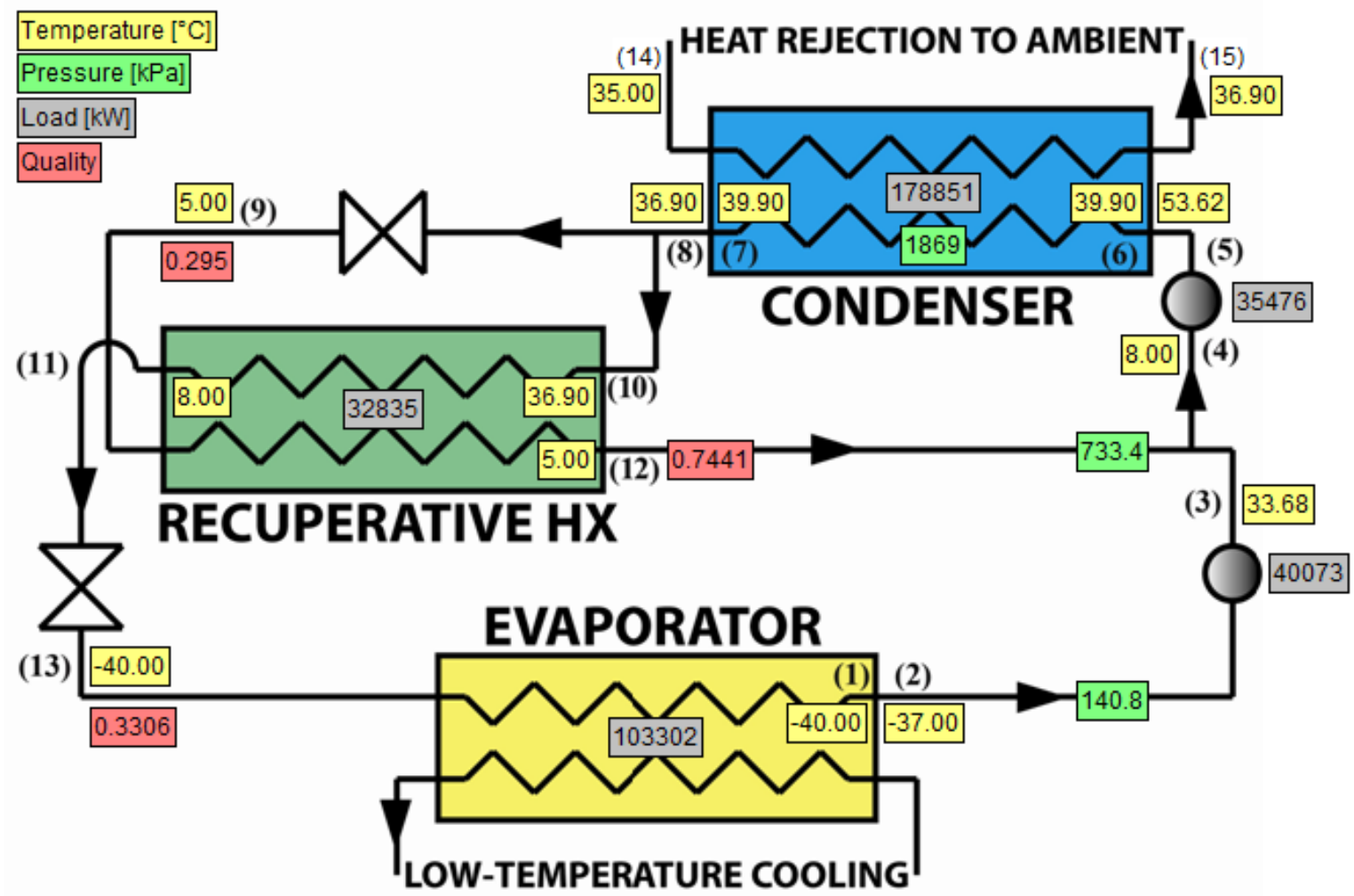

Fig. 61. Two-Stage Vapor-Compression Cycle.

The *CAT* in the condenser and recuperative heat exchanger were specified to be 3.00°C. From this specification, the component *UA*s were calculated and set constant for all analyses. The condenser *UA* is 26 MW/K. The recuperative heat exchanger has a *UA* of 3 MW/K. The calculated *UA* values are used to estimate the sizes of the components needed for the two-stage vapor-compression cycle, as in the CAVC cycle analyses (see Chapters 3.2 and 4.6). Typical *U* values provided by Perry's Chemical Engineers' Handbook [6] are used for very rough, first approximation calculations of required heat transfer surface area. An abbreviated set of typical *U* values listed in this resource is provided in Table 4. From the range of *U* values provided for the relevant media in a tubular heat exchanger, the highest value was used to estimate the *A* of the components. The most efficient heat transfer value provided was used to reflect the inclusion of highly efficient microchannel-based components in the cycle, as in the CAVC cycle analyses. The typical values obtained from Perry's Chemical Engineers' Handbook and the resulting estimates of *A* are shown in Table 11. The reference numbers listed in Table 11 correspond with the numbering in Table 4, to clearly show the source of the *U* values used for each component.

Table 11. Estimated Two-Stage Vapor-Compression Heat Transfer Surface Areas.

Heat Exchanger	Ref. #	Typical U [Btu/(°F·ft^2·hr)]	Typical U [W/(m^2·K)]	UA [W/K]	Heat Transfer Surface Area, A [m^2]
Recuperative HX	12	300	1,703	2,686,000	1,577
Condenser	5	200	1,136	26,256,000	23,120

Notes: Typical overall heat transfer coefficients are taken from Perry's Chemical Engineers' Handbook (7th Edition)

The two-stage vapor-compression cycle requires significantly less heat transfer surface areas when compared to either the single-effect or double-effect CAVC cycles. While the estimated two-stage vapor-compression heat exchanger sizes are comparable to the sizes of similar components in the CAVC cycles, the two-stage vapor-compression

cycle requires only three such heat exchangers rather than the nine heat exchangers required by the single-effect CAVC cycle. It is important to note, however, that the two-stage vapor-compression cycle requires two compressors rather than the one compressor required by the CAVC cycle, and uses primary mechanical energy rather than waste heat to drive the cycle.

For comparison with this two-stage vapor-compression cycle, the cascade cycle was stripped of its second absorption cycle evaporator and therefore produced only low temperature cooling. The two-stage vapor-compression cycle was then supplied with input parameters taken directly from the performance of this low-temperature-only cascade cycle. The cooling load provided by the low-temperature-only CAVC cycle with a fixed compressor power input as rejection temperature varied was first determined by parametric analysis. The results were then used in the two-stage vapor-compression model for two comparisons. First, the CAVC heat rejection temperatures and cooling loads were used to determine the compressor power required by the two-stage cycle to produce the same cooling load as rejection temperature varied. Second, the CAVC heat rejection temperatures and fixed compressor power input were used to determine the corresponding cooling load provided by the two-stage cycle as heat rejection temperature varied. The comparison between the performance of these cycles for the same cooling load is shown in Fig. 62, while the comparison at equal compressor power input is shown in Fig. 63.

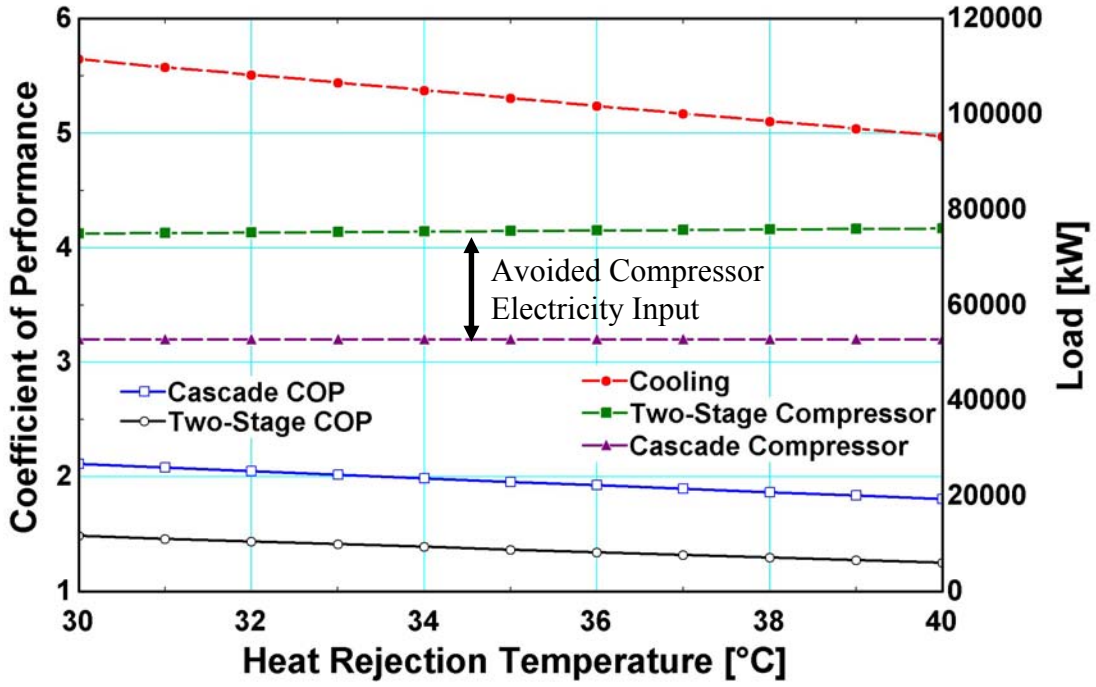

Fig. 62. COP and Load Comparison for Equal Cooling Load.

With 52.7 MW of compressor input power, the cascade cycle provides 111.5 MW cooling at 30°C and 95.4 MW cooling at 40°C. As seen in Fig. 62, the two-stage cycle requires 75 MW of compressor power input at 30°C and 76 MW at 40°C to provide the same cooling capacities. The difference in electricity demand between the two-stage compressors and the cascade compressor yields the avoided electricity consumption, which rises from 22 MW at 30.00°C to 23 MW at 40.00°C. The two-stage *COP* decreases from 1.5 to 1.3 as the heat rejection temperature increases, while the cascade cycle *COP* decreases from 2.1 to 1.8. In Fig. 63, the difference in cooling capacities achieved for the same compressor power input can be readily seen. Given the same input power as the CAVC cycle, the two-stage cycle provides only 81.4 MW at 30°C and 68.3 MW at 40°C. The cascade cycle provides 30 MW more cooling than the two-stage compression cycle at 30.00°C, and 27 MW more at 40.00°C, showing that the advantage remains fairly constant over the whole range of heat rejection temperatures. The two-

stage *COP* decreases from 1.5 to 1.3 as the heat rejection temperature increases, while the cascade *COP* decreases from 2.1 to 1.8.

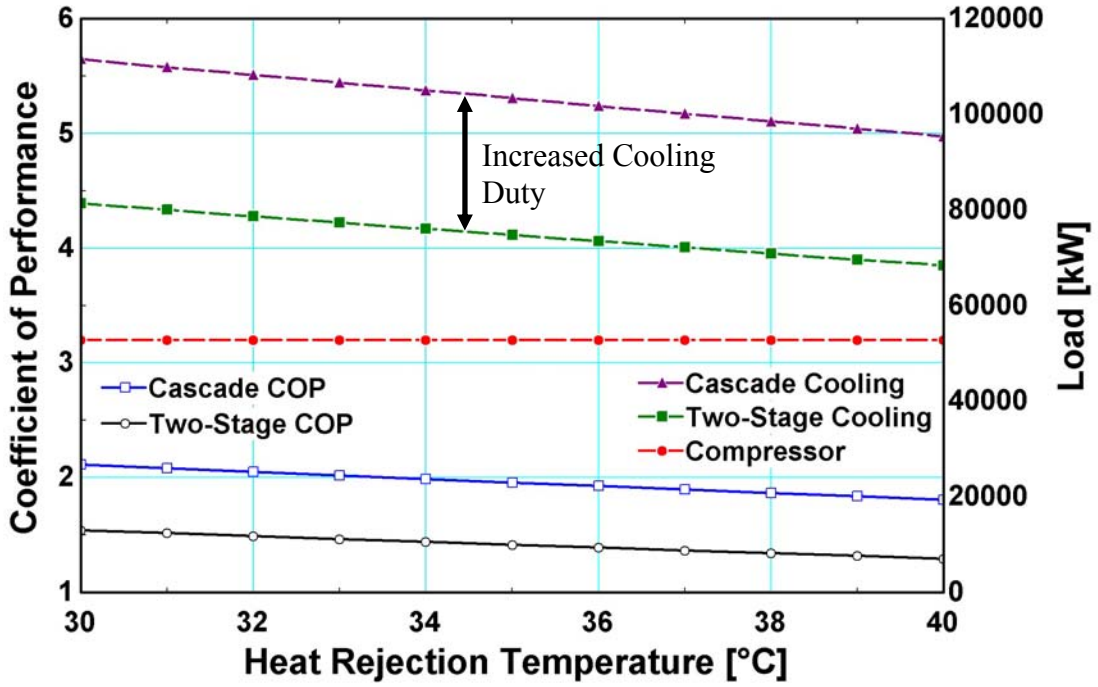

Fig. 63. COP and Load Comparison for Equal Compressor Input.

An additional advantage of the cascade cycle is shown in Fig. 64. At low heat rejection temperatures, for example, 30°C, the pressure ratio required by the two-stage cycle is almost 3 times larger than that required by the cascade cycle. As heat rejection temperatures rise to 40°C, the difference widens as the two-stage cycle requires a pressure ratio of 14.8 and the cascade cycle requires only 4.9. Higher pressure ratios require larger and heavier equipment, as well as increasing cycle inefficiencies due to increased temperatures in the compressors.

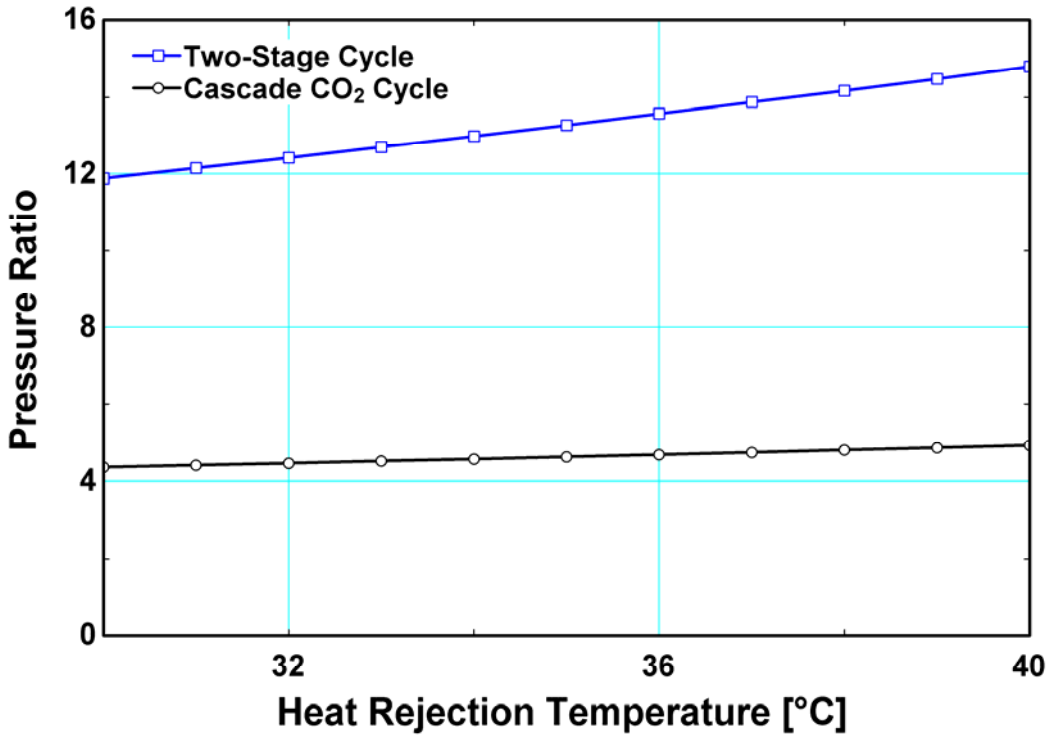

Fig. 64. Effect of Heat Rejection Temperature on Cycle Pressure Ratios.

PART TWO: ORGANIC RANKINE CYCLE

CHAPTER FIVE: ORGANIC RANKINE/VAPOR-COMPRESSION CYCLE MODELING

5.1 INPUT PARAMETERS

The organic Rankine/vapor-compression cycle (ORVC), shown in Fig. 65, is suited to utilize low-grade thermal energy for cooling. For the modeling of this cycle, inputs were chosen based on typical rating conditions for cooling systems and to enable low-grade thermal energy utilization. The values listed here are inputs for the baseline operation; subsequent parametric analyses investigate various ranges of each input, keeping all other inputs at baseline values.

- Waste Heat Source Temperature, T[19]: 125°C, 2.093 kg/s (2.36 m^3/s)

  The waste heat gas stream directly supplies heat to the R245fa stream in the boiler. In an actual application, a fluid coupling loop may be introduced to allow control and optimization of the boiler temperature, and minimize corrosion as applicable.

- Evaporator Return Air, T[14]: 26.67°C, 51% RH, 1.365 kg/s (1.18 m^3/s)

  The baseline temperature and relative humidity of the conditioned air input flow to the evaporator is chosen based on Air-Conditioning and Refrigeration Institute (ARI) standards. The conditioned air inlet flow rate is determined based on the desired cooling load.

- Condenser Return Air, T[5]: 35°C, 0.022 Humidity Ratio, 9.402 kg/s (8.495 m^3/s)

The baseline temperature and relative humidity of the ambient air inlet flow to the condenser is again determined by ARI rating conditions. The ambient air inlet flow rate is determined based on the heat rejection load.

- Turbine efficiency: 90%
- Compressor efficiency: 65%

  The turbine and compressor efficiencies have a significant impact on cycle performance. Therefore, the use of highly efficient components has been assumed in this analysis.

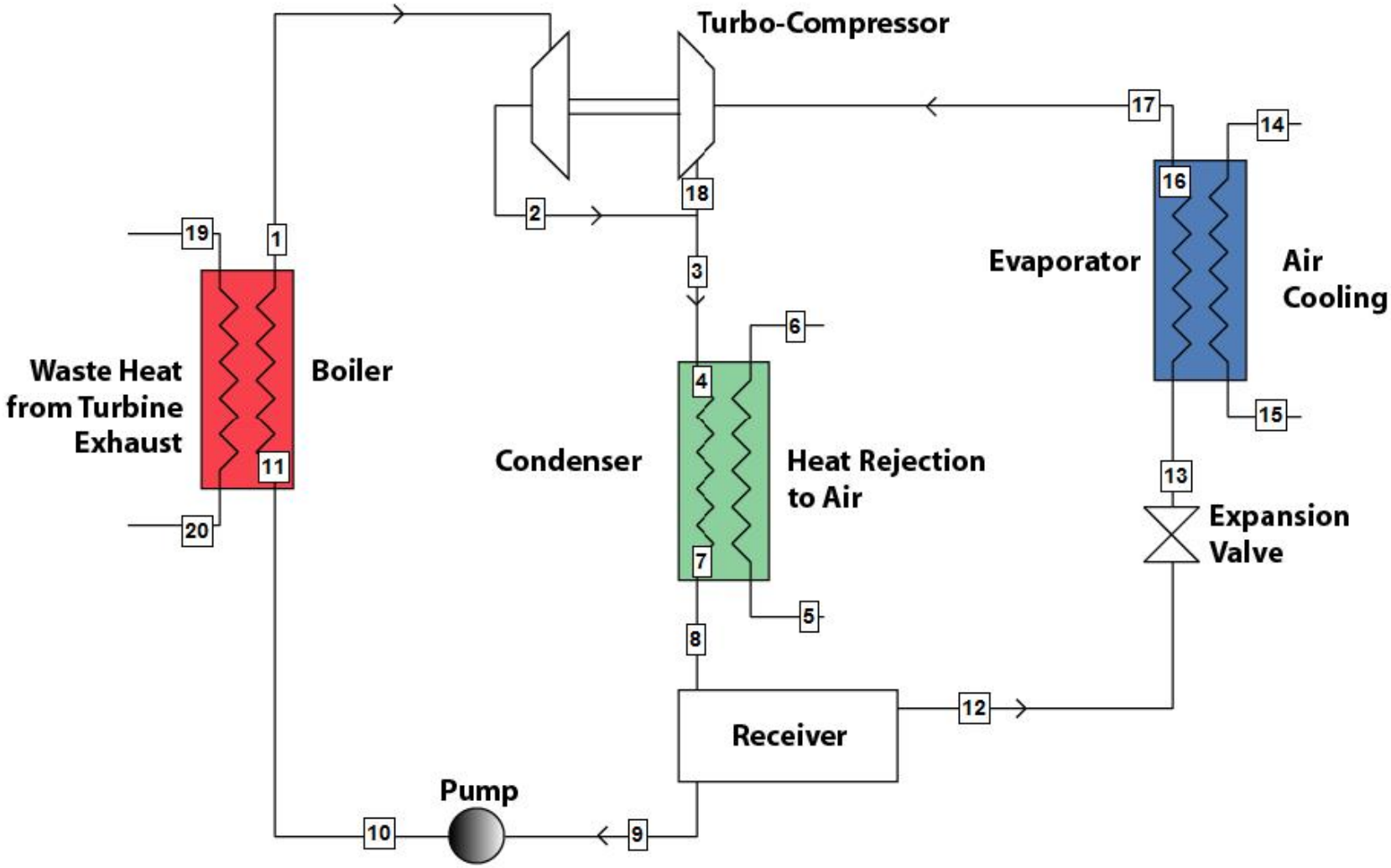

Fig. 65. Rankine/Vapor-Compression Cycle Schematic.

5.2 REFRIGERANT

The refrigerant R245fa is expressly suited for low-grade heat recovery with a boiling point slightly below room temperature (14.9°C) at atmospheric pressure. The operating pressure is 301.2 kPa for a condenser temperature of 45.59°C and 85.38 kPa for an evaporator temperature of 10.7°C. The freezing point of the liquid is less than -107°C, allowing plenty of room in the temperature scale for cycle operation. The operational range of the cycle can be seen on the R245fa temperature-entropy diagram (Fig. 66) and pressure-enthalpy diagram (Fig. 67). As discussed in Chapter 2, a crucial characteristic of a Rankine cycle working fluid is the saturation vapor curve. R245fa exhibits a positively-sloped saturation vapor curve, indicating that the fluid will remain in a vapor state throughout expansion instead of flashing, thereby reducing the possibility for cavitation and damage to the turbine. For this reason, the fluid does not need to be superheated in the boiler to ensure persistent saturation through expansion, thus enabling the utilization of low-temperature waste heat sources. The low enthalpy drop exhibited by 245fa over the expansion process allows the use of a single-stage turbine, rather than the multi-stage turbines required in steam cycles. Additionally, R245fa has zero Ozone Depletion Potential (ODP) and has a low Global Warming Potential. The refrigerant is not considered a Volatile Organic Compound (VOC) in the United States. These thermodynamic properties combined with the benign environmental properties make R245fa an excellent choice for this cycle, and it will be used throughout the analyses.

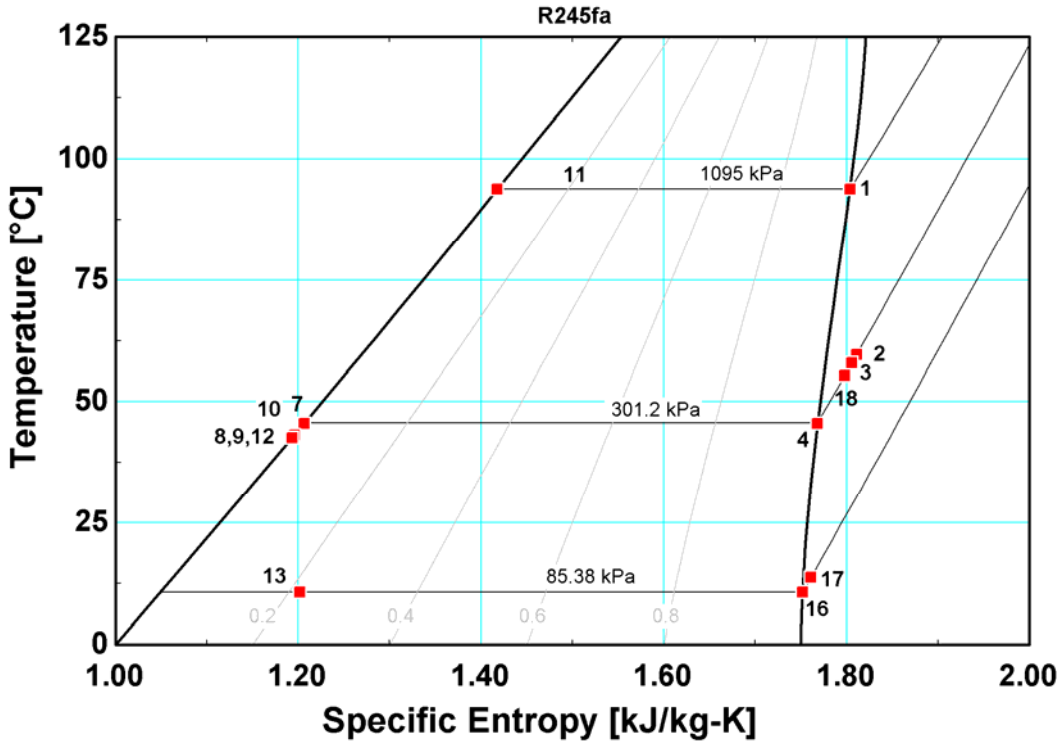

Fig. 66. R245fa T-s Diagram with ORVC Cycle State Points.

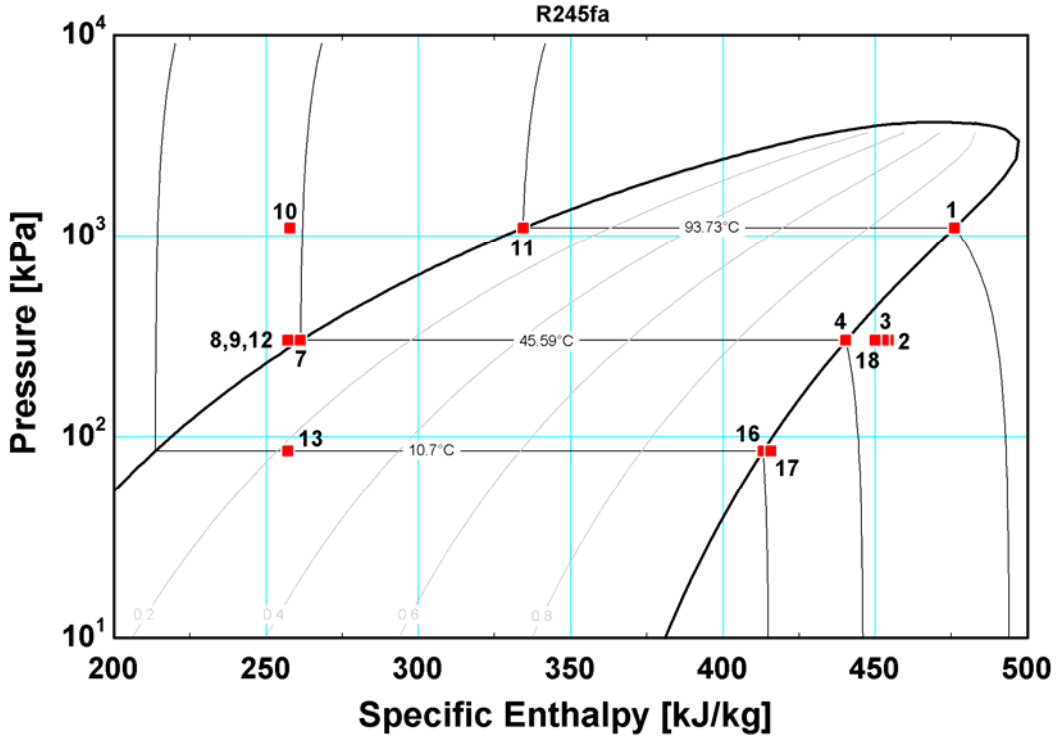

Fig. 67. R245fa P-h Diagram with ORVC Cycle State Points.

5.3 ORVC CYCLE DESCRIPTION AND BASELINE RESULTS

A simulation model was developed to establish a consistent set of state points for the ORVC cycle. A representative schematic of the basic cycle is shown in Fig. 65. The cycle consists of two overlapping loops: the boiler/turbine loop (left side of Fig. 65) and the evaporator/compressor loop (right side of Fig. 65).

The cycle refrigerant, R245fa, enters the boiler at a temperature of 43.19°C (10). The subcooled refrigerant stream is heated and evaporated by the thermal energy from the waste heat stream. The waste gas stream enters the boiler at 125°C (19) and is cooled to 101.3°C (20) as it heats the R245fa stream:

$$Q_{boiler} = m_{19}\left(h_{19} - h_{20}\right) \tag{5.1}$$

$$50.15\ \text{kW} = 2.093\frac{\text{kg}}{\text{s}}\left(399.4\frac{\text{kJ}}{\text{kg}} - 375.4\frac{\text{kJ}}{\text{kg}}\right)$$

The refrigerant stream is first heated from 43.19°C to the saturation temperature of 93.73°C (11) at the high cycle pressure of 1095 kPa. Saturated vapor exits the boiler (1) at 93.73°C:

$$T_{11} = T_{\text{R245fa}}\left(p_{11}, q_{11}\right) \tag{5.2}$$

$$93.73°\text{C} = T_{\text{R245fa}}\left(1095\ \text{kPa}, 0\right)$$

The refrigerant flow rate through the boiler is 0.23 kg/s. The heat duty required to bring the refrigerant to saturation temperature in the boiler is 17.59 kW:

$$Q_{\text{Boiler, Sensible}} = m_{10}(h_{11} - h_{10}) \tag{5.3}$$

$$17.59\ \text{kW} = 0.23\frac{\text{kg}}{\text{s}}\left(334.3\frac{\text{kJ}}{\text{kg}} - 257.8\frac{\text{kJ}}{\text{kg}}\right)$$

The heat duty required to evaporate the refrigerant in the boiler is 32.47 kW:

$$Q_{\text{Boiler, Sat}} = m_{11}\left(h_1 - h_{11}\right) \tag{5.4}$$

$$32.57\ \text{kW} = 0.23\frac{\text{kg}}{\text{s}}\left(475.9\frac{\text{kJ}}{\text{kg}} - 334.3\frac{\text{kJ}}{\text{kg}}\right)$$

The total boiler duty is therefore 50.15 kW:

$$Q_{\text{Boiler}} = Q_{\text{Boiler, Sensible}} + Q_{\text{Boiler, Sat}} \tag{5.5}$$

$$50.15\ \text{kW} = 32.57\ \text{kW} + 17.59\ \text{kW}$$

The log mean temperature difference (*LMTD*) is used to calculate the *UA* of the boiler. The saturated inlet and outlet temperatures are used in calculating the *LMTD* due to the larger phase-change portion of the total boiler duty. To maintain a *CAT* of 7.5°C in the boiler, the *UA* is set at 3 kW/K:

$$Q_{\text{Boiler}} = UA_{\text{Boiler}} LMTD\left(T_{19}, T_{20}, T_{11}, T_1\right) \tag{5.6}$$

$$50.15\ \text{kW} = 3\frac{\text{kW}}{\text{K}} \cdot 16.72°\text{C}$$

Downstream of the boiler, the refrigerant in the high-pressure Rankine cycle flows through the turbine component of the turbo-compressor. Assuming 90% efficiency, the refrigerant produces 4.987 kW of power as it flows through the turbine to the cycle intermediate pressure (301.2 kPa):

$$\eta_{\text{Turbine}} = \frac{h_1 - h_2}{h_1 - h_{2,isentropic}} \tag{5.7}$$

$$0.90 = \frac{475.9\frac{\text{kJ}}{\text{kg}} - 454.2\frac{\text{kJ}}{\text{kg}}}{475.9\frac{\text{kJ}}{\text{kg}} - 451.8\frac{\text{kJ}}{\text{kg}}}$$

$$W_{\text{Turbine}} = m_1\left(h_1 - h_2\right) \tag{5.8}$$

$$4.987\ \text{kW} = 0.23\frac{\text{kg}}{\text{s}}\left(475.9\frac{\text{kJ}}{\text{kg}} - 454.2\frac{\text{kJ}}{\text{kg}}\right)$$

The turbine power is transmitted directly to the compressor component of the turbo-compressor:

$$W_{\text{Turbine}} = W_{\text{Compressor}} \tag{5.9}$$

Refrigerant leaving the turbine (2) at 59.63°C mixes with the refrigerant leaving the compressor at 55.33°C to form a 0.3758 kg/s stream at 57.97°C:

$$m_3 = m_2 + m_{18} \tag{5.10}$$

$$0.376\frac{\text{kg}}{\text{s}} = 0.23\frac{\text{kg}}{\text{s}} + 0.146\frac{\text{kg}}{\text{s}}$$

$$m_3 h_3 = m_2 h_2 + m_{18} h_{18} \tag{5.11}$$

$$0.376\frac{\text{kg}}{\text{s}} \cdot 452.6\frac{\text{kJ}}{\text{kg}} = 0.23\frac{\text{kg}}{\text{s}} \cdot 454.2\frac{\text{kJ}}{\text{kg}} + 0.146\frac{\text{kg}}{\text{s}} \cdot 449.9\frac{\text{kJ}}{\text{kg}}$$

The mixed stream leaving the turbo-compressor enters the condenser with a superheat of 12.38°C (3) over the saturation temperature of 45.59°C. The corresponding desuperheating duty in the condenser is 4.59 kW:

$$Q_{\text{Condenser,Desup}} = m_3\left(h_3 - h_4\right) \tag{5.12}$$

$$4.59\ \text{kW} = 0.376\frac{\text{kg}}{\text{s}}\left(452.6\frac{\text{kJ}}{\text{kg}} - 440.3\frac{\text{kJ}}{\text{kg}}\right)$$

After cooling to the saturated vapor at 45.59°C (4), the refrigerant condenses completely (7) while rejecting 67.29 kW:

$$Q_{\text{Condenser,Sat}} = m_4\left(h_4 - h_7\right) \tag{5.13}$$

$$67.29\ \text{kW} = 0.376\frac{\text{kg}}{\text{s}}\left(440.3\frac{\text{kJ}}{\text{kg}} - 261.3\frac{\text{kJ}}{\text{kg}}\right)$$

The refrigerant stream exits the condenser (8) with a subcooling of 3°C, at 42.59°C:

$$T_8 = T_7 - \Delta T_{Sub} \tag{5.14}$$

$$42.59°\text{C} = 45.59°\text{C} - 3.00°\text{C}$$

The corresponding subcooling duty is 1.60 kW:

$$Q_{\text{Condenser,Sub}} = m_7 \left(h_7 - h_8 \right) \tag{5.15}$$

$$1.60 \text{ kW} = 0.376 \frac{\text{kg}}{\text{s}} \left(261.3 \frac{\text{kJ}}{\text{kg}} - 257 \frac{\text{kJ}}{\text{kg}} \right)$$

The total condenser load is therefore 73.49 kW:

$$Q_{\text{Condenser}} = Q_{\text{Condenser,Desup}} + Q_{\text{Condenser,Sat}} + Q_{\text{Condenser,Sub}} \tag{5.16}$$

$$73.49 \text{ kW} = 4.59 \text{ kW} + 67.29 \text{ kW} + 1.60 \text{ kW}$$

The refrigerant is cooled in the condenser by a 9.402 kg/s stream of ambient air (5), entering at 35°C and rising to 42.46°C (6) in the condenser. The ambient air stream maintains a humidity ratio of 0.022:

$$h_5 = h_{\text{Air-H}_2\text{O}} \left(T_5, \omega_5, p_5 \right) \tag{5.17}$$

$$91.68 \frac{\text{kJ}}{\text{kg}} = h_{\text{Air-H}_2\text{O}} \left(35°\text{C}, 0.022, 101.4 \text{ kPa} \right)$$

$$Q_{Condenser} = m_5 \left(h_6 - h_5 \right) \tag{5.18}$$

$$73.49 \text{ kW} = 9.402 \frac{\text{kg}}{\text{s}} \left(99.5 \frac{\text{kJ}}{\text{kg}} - 91.7 \frac{\text{kJ}}{\text{kg}} \right)$$

The condenser *UA* required to maintain a *CAT* of 3°C is 12 kW/K:

$$Q_{\text{Condenser}} = UA_{\text{Condenser}} LMTD \left(T_4, T_7, T_5, T_6 \right) \tag{5.19}$$

$$73.49 \text{ kW} = 12 \frac{\text{kW}}{\text{K}} \cdot 6.12°\text{C}$$

The subcooled refrigerant stream enters the receiver. Here, the refrigerant stream is split into the two loops of the cycle, the high-pressure Rankine loop and the low-pressure vapor-compression loop. The pump determines the amount of refrigerant that flows into the Rankine cycle (9). For the baseline analysis, the pump power input is set at 0.1906 kW and is assumed to have 90% efficiency. At this setting, the pump draws 0.23 kg/s from the receiver:

$$\eta_{\text{Pump}} = \frac{h_{10,\text{isentropic}} - h_9}{h_{10} - h_9} \tag{5.20}$$

$$0.90 = \frac{257.76\,\frac{\text{kJ}}{\text{kg}} - 257\,\frac{\text{kJ}}{\text{kg}}}{257.84\,\frac{\text{kJ}}{\text{kg}} - 257\,\frac{\text{kJ}}{\text{kg}}}$$

$$W_{\text{Pump}} = m_9\left(h_{10} - h_9\right) \tag{5.21}$$

$$0.1906\ \text{kW} = 0.23\,\frac{\text{kg}}{\text{s}}\left(257.84\,\frac{\text{kJ}}{\text{kg}} - 257\,\frac{\text{kJ}}{\text{kg}}\right)$$

Due to the work addition, the temperature of the refrigerant stream flowing through the pump rises from 42.59°C to 43.19°C. Downstream of the pump, the refrigerant enters the boiler (10), thus completing the Rankine loop.

The remaining 0.1458 kg/s of the refrigerant stream at the condenser outlet flows into the vapor-compression cycle (12). The refrigerant stream flowing to the vapor-compression loop from the receiver flows through an expansion valve, decreasing in pressure from the cycle intermediate pressure, 301.2 kPa, to the cycle low pressure, 85.38 kPa (13). Due to the flashing across the valve, the refrigerant temperature drops from 42.59°C to 10.7°C, the saturation temperature for the cycle low pressure. The refrigerant then enters the evaporator at a quality of 0.2175:

$$q_{13} = q_{\text{R245fa}}\left(p_{13}, h_{13}\right) \tag{5.22}$$

$$0.2175 = q_{\text{R245fa}}\left(301.2\text{ kPa}, 257\frac{\text{kJ}}{\text{kg}}\right)$$

The refrigerant is evaporated at 10.7°C to a saturated vapor state (16), followed by superheating to 13.7°C (17), with the corresponding heat duties calculated as follows:

$$Q_{\text{Evaporator,Sat}} = m_{13}\left(h_{16} - h_{13}\right) \tag{5.23}$$

$$22.76\text{ kW} = 0.1458\frac{\text{kg}}{\text{s}}\left(413.1\frac{\text{kJ}}{\text{kg}} - 257\frac{\text{kJ}}{\text{kg}}\right)$$

$$T_{17} = T_{16} + \Delta T_{\text{Sup}} \tag{5.24}$$

$$13.7°\text{C} = 10.7°\text{C} + 3.0°\text{C}$$

$$Q_{\text{Evaporator,Sup}} = m_{16}\left(h_{17} - h_{16}\right) \tag{5.25}$$

$$0.38\text{ kW} = 0.1458\frac{\text{kg}}{\text{s}}\left(415.7\frac{\text{kJ}}{\text{kg}} - 413.1\frac{\text{kJ}}{\text{kg}}\right)$$

The total heat duty in the evaporator is therefore 23.14 kW:

$$Q_{\text{Evaporator}} = Q_{\text{Evaporator,Sat}} + Q_{\text{Evaporator,Sup}} \tag{5.26}$$

$$23.14\text{ kW} = 22.76\text{ kW} + 0.38\text{ kW}$$

The refrigerant is cooled in the evaporator by a conditioned return air stream (14) of 1.365 kg/s at 26.67°C. The relative humidity of the air entering the evaporator is 51.1%:

$$h_{14} = h_{\text{Air-H}_2\text{O}}\left(T_{14}, p_{14}, RH_{14}\right) \tag{5.27}$$

$$55.32\frac{\text{kJ}}{\text{kg}} = h_{\text{Air-H}_2\text{O}}\left(26.67°\text{C}, 101.4\text{ kPa}, 51.1\%\right)$$

The refrigerant cools the air stream to 13.66°C and it leaves the evaporator (15) at a relative humidity of 100%:

$$Q_{\text{Evaporator}} = m_{14}\left(h_{14} - h_{15}\right) \tag{5.28}$$

$$23.14\ \text{kW} = 1.365\frac{\text{kg}}{\text{s}}\left(55.32\frac{\text{kJ}}{\text{kg}} - 38.37\frac{\text{kJ}}{\text{kg}}\right)$$

The resulting evaporator cooling load is 23.14 kW. A *UA* of 3 kW/K is required in the evaporator to maintain a *CAT* of 3°C:

$$Q_{\text{Evaporator}} = UA_{\text{Evaporator}} LMTD\left(T_{14}, T_{15}, T_{13}, T_{16}\right) \tag{5.29}$$

$$23.14\ \text{kW} = 3\frac{\text{kW}}{\text{K}} \cdot 7.71°\text{C}$$

The refrigerant exiting the evaporator outlet (17) enters the compressor component of the turbo-compressor, where it is compressed from 85.38 kPa to 301.2 kPa (18):

$$\eta_{\text{Compressor}} = \frac{h_{18,\text{isentropic}} - h_{17}}{h_{18} - h_{17}} \tag{5.30}$$

$$0.65 = \frac{438\frac{\text{kJ}}{\text{kg}} - 415.7\frac{\text{kJ}}{\text{kg}}}{449.9\frac{\text{kJ}}{\text{kg}} - 415.7\frac{\text{kJ}}{\text{kg}}}$$

$$W_{\text{Compressor}} = m_{17}\left(h_{18} - h_{17}\right) \tag{5.31}$$

$$4.987\ \text{kW} = 0.1458\frac{\text{kg}}{\text{s}}\left(449.9\frac{\text{kJ}}{\text{kg}} - 415.7\frac{\text{kJ}}{\text{kg}}\right)$$

The compressor output (18) mixes with the turbine output (2), thus completing the vapor-compression loop.

The calculated *UA* values can provide some estimation of the size of components needed. The sizes of the ORVC cycle components are estimated in the same manner as the CAVC component size estimates, using the typical *U* values from Perry's Chemical Engineers' Handbook [6] shown in Table 4. Again, these typical values provide for very

rough, first approximation calculations, in lieu of detailed design specifications for each component. As in the CAVC size estimations, the highest value in the range of U values provided for the relevant media in a tubular heat exchanger was used to estimate the A of the ORVC components. The most efficient heat transfer value provided was used to reflect the inclusion of highly efficient microchannel-based components in the cycle. The typical values obtained from Perry's Chemical Engineers' Handbook and the resulting estimates of A are tablulated in Table 12. The ORVC heat exchangers are all air-coupled at atmospheric pressure, which limits the typical U value to 284 W/m^{2}K. Despite this low value, the ORVC heat transfer surface area estimates are much smaller than for the CAVC system, because of the substantially lower waste heat duties under consideration here.

Table 12. Estimated ORVC Heat Transfer Surface Areas.

Heat Exchanger	Ref. #	Typical U [Btu/(°F·ft^2·hr)]	Typical U [W/(m^2·K)]	UA [W/K]	Heat Transfer Surface Area, A [m^2]
Boiler	11	50	284	3,000	11
Condenser	11	50	284	12,000	42
Evaporator	11	50	284	3,000	11

Notes: Typical overall heat transfer coefficients are taken from Perry's Chemical Engineers' Handbook (7th Edition)
Ref. #11 denotes heat exchange with gas-liquid media of Air (atm) and Water or Brine.

5.4 CYCLE PERFORMANCE

Two coefficients of performance and one efficiency value were defined for the Rankine/vapor-compression cycle. The overall COP is defined by the ratio of evaporator cooling load to exhaust heat input duty:

$$COP_{Overall} = \frac{Q_{Evaporator}}{Q_{Exhaust}} \tag{5.32}$$

For the baseline conditions, the overall COP is 0.4614. The second COP measures the performance of the vapor-compression cycle alone and is defined by the ratio of evaporator cooling load to the work input of the compressor:

$$COP_{Vapor-Compression} = \frac{Q_{Evaporator}}{W_{Compressor}} \tag{5.33}$$

For the baseline conditions, the vapor-compression COP is 4.64. The final measure of cycle performance is the performance of the Rankine cycle alone, which is defined by the ratio of the net work produced to exhaust heat input duty:

$$\eta_{\text{Rankine}} = \frac{W_{\text{Turbine}} - W_{\text{Pump}}}{Q_{\text{Exhaust}}} \tag{5.34}$$

The Rankine efficiency for the baseline case is 9.563%.

CHAPTER SIX: ORGANIC RANKINE/VAPOR-COMPRESSION CYCLE PARAMETRIC ANALYSES

The Rankine/vapor-compression cycle is affected by several input parameters: heat rejection temperature (ambient air temperature), waste heat source temperature, component efficiencies (turbine and compressor), and component air flow rates (evaporator and condenser). Appropriate ranges for each parameter were determined and the effect of variations in each of these parameters was illustrated through parametric analyses.

6.1 WASTE HEAT SOURCE TEMPERATURE

The most critical input parameter in the Rankine/vapor-compression cycle is the waste heat source temperature. A range of temperatures from 80°C to 170°C is considered. The low end, 80°C, is the minimum exhaust temperature that provides sufficient thermodynamic lift from reasonable ambient temperatures. This limit is due to the coupling of the turbine and compressor. The conditioned air temperature and ambient temperature are set by ARI standards and the compressor must provide for this predetermined lift; therefore, the exhaust temperature must be sufficiently high to provide turbine work equal to the minimum compressor work required by the air temperatures. The high end, 170°C, is an arbitrary limit, motivated by the intended use of the cycle in low-grade heat recovery. The exhaust heat input load rises with the exhaust heat temperature, from 44.55 kW to 53.93 kW, as seen in Fig. 68.

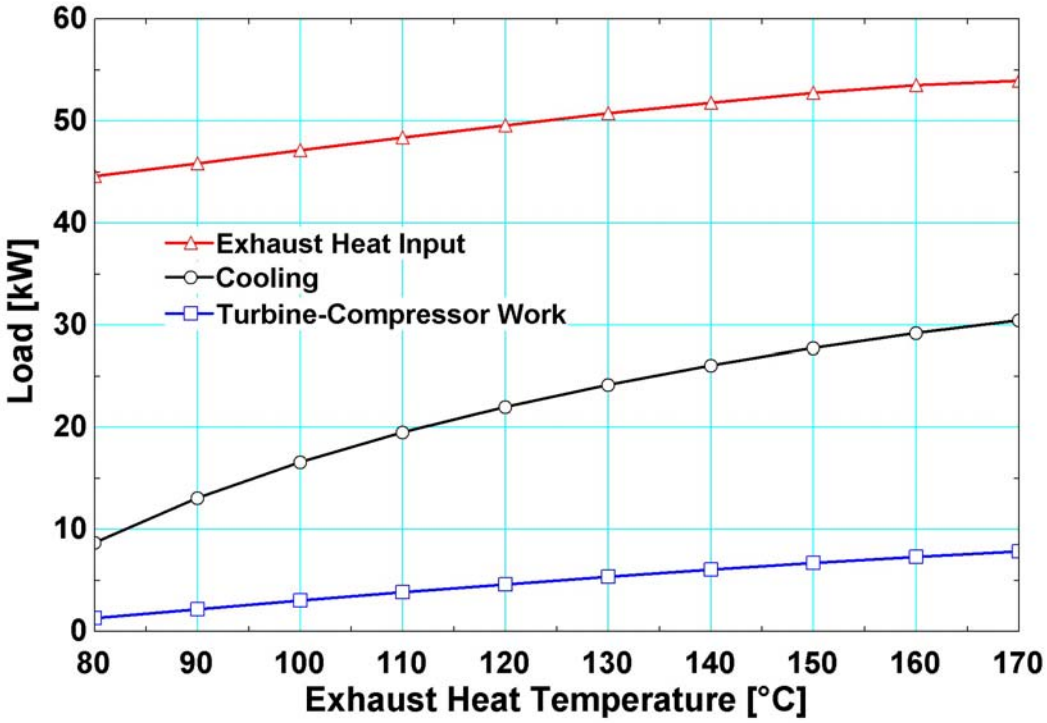

Fig. 68. Effect of Exhaust Heat Temperature on Cycle Capacities.

As the exhaust temperature rises, the boiler saturation temperature rises for a given *UA*, which in turn raises the boiler pressure. The increased pressure in the high-pressure cycle produces more work in the turbine, increasing the power generated from 1.301 kW to 7.851 kW. As the turbine power increases, the coupled compressor load also increases. Since both the compressor and turbine produce refrigerant streams at the same intermediate pressure, the pressure difference between the high- and low-pressure loops increases if the turbo-compressor power increases. The lower low pressures dictated by the compressor yield lower refrigerant saturation temperatures in the evaporator, which increases the temperature difference between the refrigerant stream and the conditioned air and therefore raises the evaporator cooling load from 8.736 kW to 30.48 kW. The increased pressure on the high side of the turbine increases the intermediate pressure as well, causing higher saturation temperatures in the condenser. As the temperature

difference between the ambient air and the condensing refrigerant stream increases, so does the heat rejection duty. Increased heat rejection allows increased heat source capabilities in the evaporator, and the cooling load rises. The variations in load shown in Fig. 68 directly explain the variations in performance shown in Fig. 69.

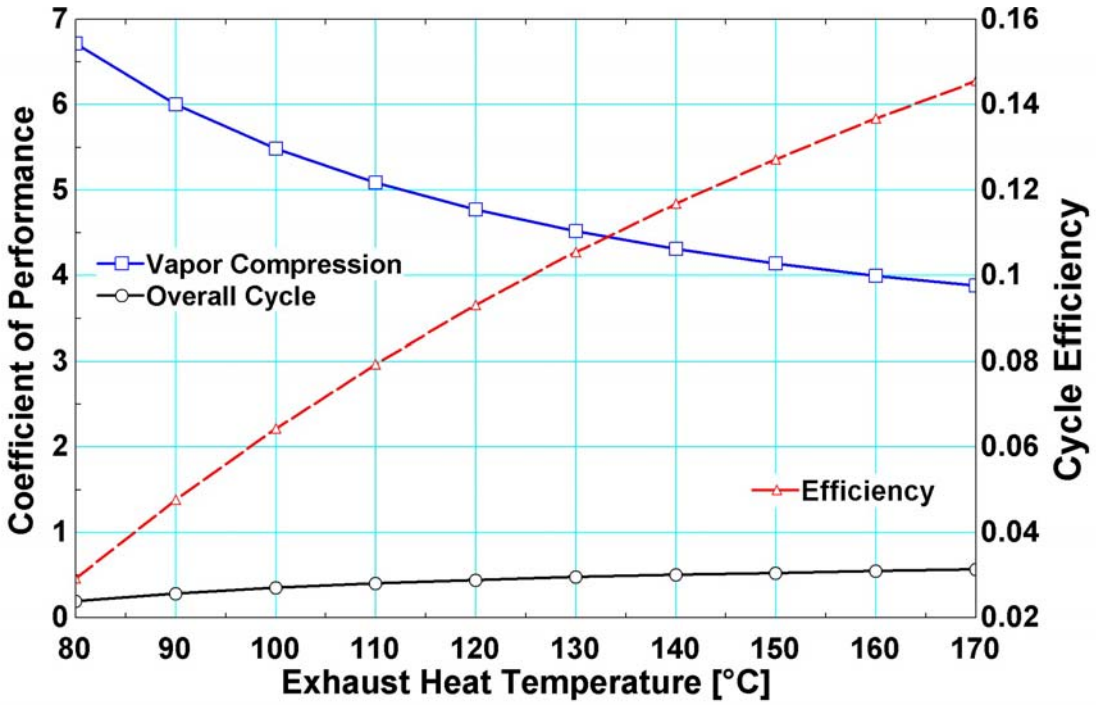

Fig. 69. Effect of Exhaust Heat Temperature on Cycle Performance.

To understand the variations in performance, the definitions of COP and efficiency are considered. The overall COP is defined as the ratio between evaporator cooling load and exhaust heat input. As the exhaust heat temperature changes from 80°C to 170°C, the cooling load increases by 249%, while the exhaust heat input rises by only 21%, so the overall *COP* increases, from 0.196 to 0.565 (188% increase). The vapor-compression *COP*, however, is defined by the ratio of evaporator cooling load to compressor work, which increases by 504%. Hence, the vapor-compression *COP* decreases from 6.715 to 3.883 (42.2% decrease). The Rankine cycle efficiency is defined by the ratio of the net turbine work to exhaust heat input, and rises from 2.86% to 13.35% (~350% increase).

From these results, it is clear that the cycle performance is highly dependent on the turbo-compressor. When the turbo-compressor load increases, the pressure ratio in both turbine and compressor increases. On the turbine side in the Rankine loop, this pressure ratio increase produces more work and leads to greater efficiencies. On the compressor side in the vapor-compression loop, the larger power available for compression leads to an increased cooling duy, but also a higher pressure ratio and a higher lift. This leads to a decreased vapor-compression *COP*, from 6.715 to 3.883, as the exhaust temperature changes from 80°C to 170°C, even as the cooling capacity increases from 8.736 kW to 30.48 kW. The relatively significant increase in turbine power combined with the relatively lower increase in exhaust heat input leads to a substantial increase in the topping cycle efficiency, which more than compensates for the smaller decrease in vapor-compression COP, therefore increasing the overall *COP*.

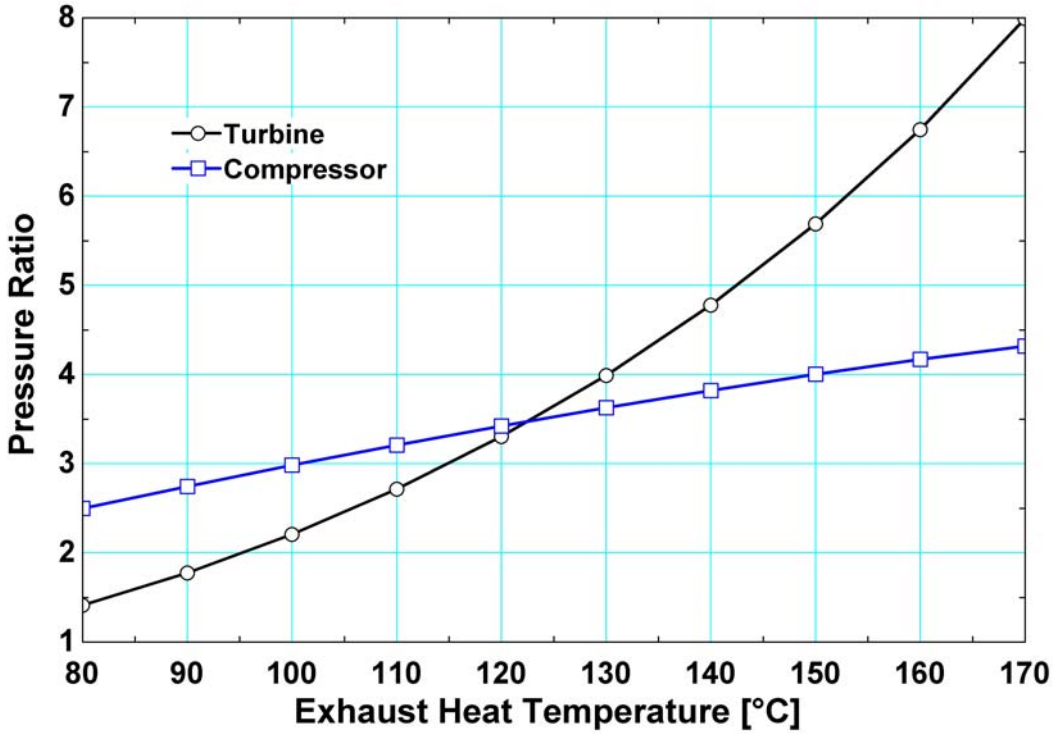

Fig. 70. Effect of Exhaust Heat Temperature on Cycle Pressure Ratios.

6.2 HEAT REJECTION TEMPERATURE

The second input parameter considered is heat rejection temperature in the condenser, or the ambient air temperature. Reasonable ambient air temperatures range from 20°C to 40°C, in environments that require cooling applications. As the rejection temperature increases, the heat rejection capability decreases. This decreased heat rejection also decreases the compressor power input and the evaporator cooling capacity.

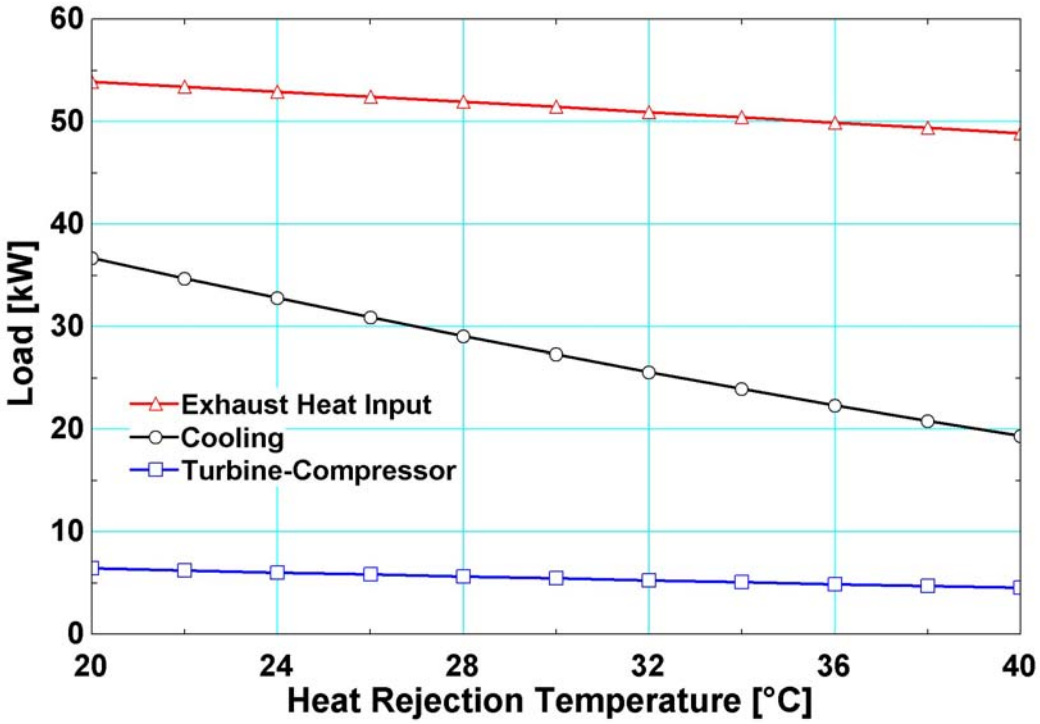

Fig. 71. Effect of Rejection Temperature on Cycle Capacities.

Fig. 71 shows the effect of reject heat temperature on cycle loads. The increasing refrigerant saturation temperatures corresponding to increasing ambient air temperatures raise the cycle intermediate pressure. The increasing intermediate pressure decreases the pressure ratio in the turbine, which therefore provides less power to the compressor, dropping from 6.43 kW to 4.53 kW. The decreased power causes a decreased pressure ratio in the compressor as well, and due to the increased intermediate pressure, low cycle

pressure increases. The corresponding higher evaporator saturation temperature decreases the cooling load from 36.68 kW to 19.37 kW. In the high-pressure cycle, decreased heat rejection means the fluid reaches the boiler at hotter temperatures and decreases the temperature difference between the refrigerant and the exhaust stream, thereby decreasing the exhaust heat input from 53.9 kW to 48.85 kW.

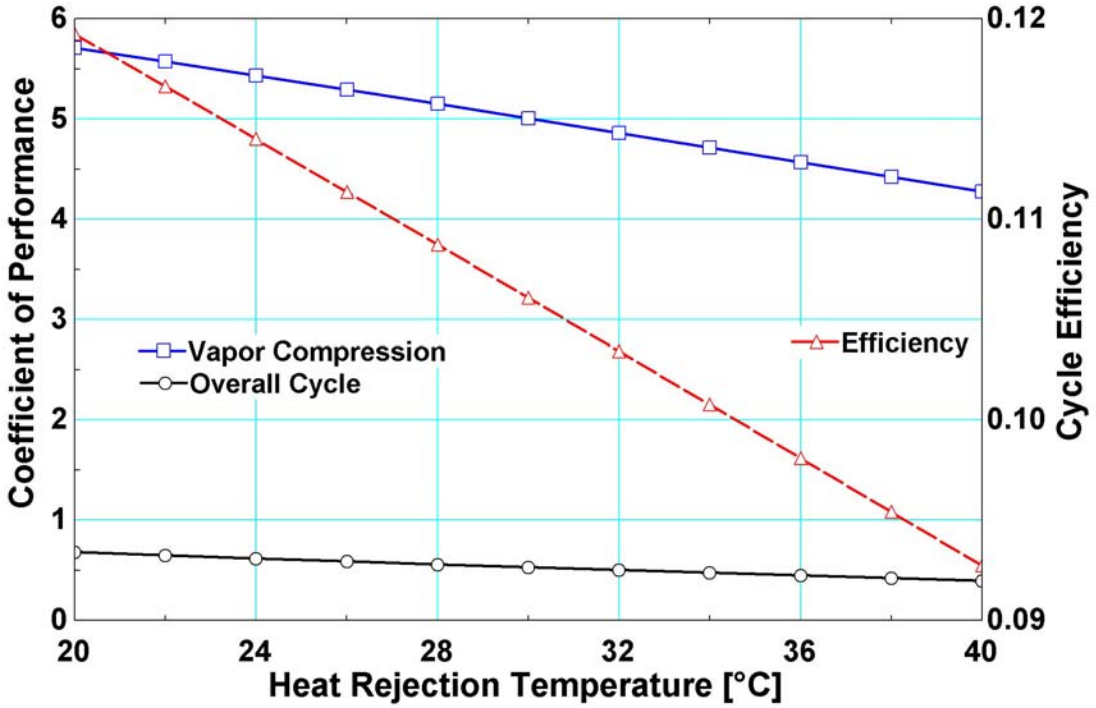

Fig. 72. Effect of Rejection Temperature on Cycle Performance.

Many of the explanations for COP variation in the waste heat temperature analyses are valid here as well. Variations in three critical outputs – exhaust input duty, turbine work, and evaporator cooling duty – again determine COP variations (Fig. 72). The exhaust input duty decreases by 9.4%, the turbine work decreases by 29.5%, and the cooling duty decreases by 47.2% as the ambient temperature rises from 20°C to 40°C. In this analysis, the decreased cooling duty is the most significant change, so the overall and vapor-compression COPs drop, from 0.680 to 0.396 (41.7% decrease) and from 5.706 to

4.275 (25.1% decrease), respectively. The overall COP drops more drastically because the exhaust input duty decrease is small compared to the turbine work decrease. For the same reason, the Rankine efficiency decreases from 11.56% to 8.89% (23% decrease) as the ambient temperature rises from 20°C to 40°C.

6.3 COMPONENT EFFICIENCIES

The Rankine/vapor-compression cycle performance is sensitive to the efficiencies of two components: turbine and compressor. The effects of a typical range in each efficiency are considered separately.

Turbine Efficiency

The turbine plays an important role in both loops of this cycle. It is the main output of the Rankine cycle and provides the compressor power, the main input for the vapor-compression cycle. As seen in the waste heat temperature and reject heat temperature analyses, increases or decreases in turbine work output are generally correlated with similar trends in overall cycle performance. Typical turbine efficiencies range from 80% to 95%. As turbine efficiency increases, so does the turbine work output. Fig. 73 shows the effect of increased turbine work output on cycle performance. It should be noted that compressor efficiency is maintained constant here, therefore, increases in the topping cycle propagate to a lesser extent to the bottoming cycle. Here, the turbine work variation is caused by the turbine efficiency and the cycle high pressure is relatively constant. The increased work output decreases the turbine pressure ratio slightly and increases the compressor pressure ratio. Therefore the Rankine efficiency rises, from 8.49% to 10.1% (18.9% increase), and the vapor-compression *COP* decreases, from 4.817 to 4.559 (5.4% decrease). The increase in Rankine efficiency outweighs the

smaller decrease in vapor-compression *COP* to result in an increase in the overall *COP*, from 0.427 to 0.478 (11.8% increase).

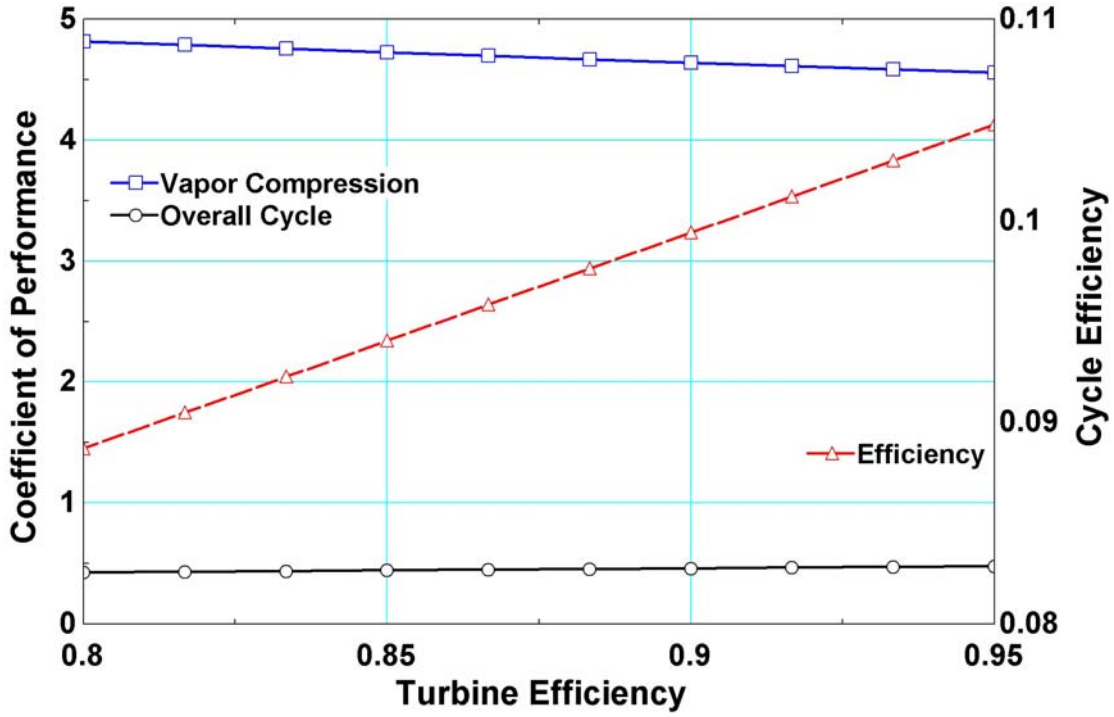

Fig. 73. Effect of Turbine Efficiency on Cycle Performance.

Compressor Efficiency

Over the assumed compressor efficiency range of 50% to 80%, the turbine output remains fairly constant (decreasing slightly from 5.0 to 4.95 kW), keeping the high and intermediate pressures relatively constant. Therefore, as the compressor efficiency rises, the compressor pressure ratio increases and decreases the low-side pressure. Low evaporator pressures result in low refrigerant saturation temperatures which translate into greater cooling loads. As shown in Fig. 74, the increased cooling load boosts the vapor-compression *COP* from 3.87 to 5.33 (37.6% increase). The Rankine efficiency is decreased slightly, from 9.64% to 9.5% (1.5% decrease), by the slight decrease in turbine

output. The changes in vapor-compression *COP* dominate the corresponding changes in Rankine efficiency to increase the overall *COP* from 0.388 to 0.526 (35.7% increase).

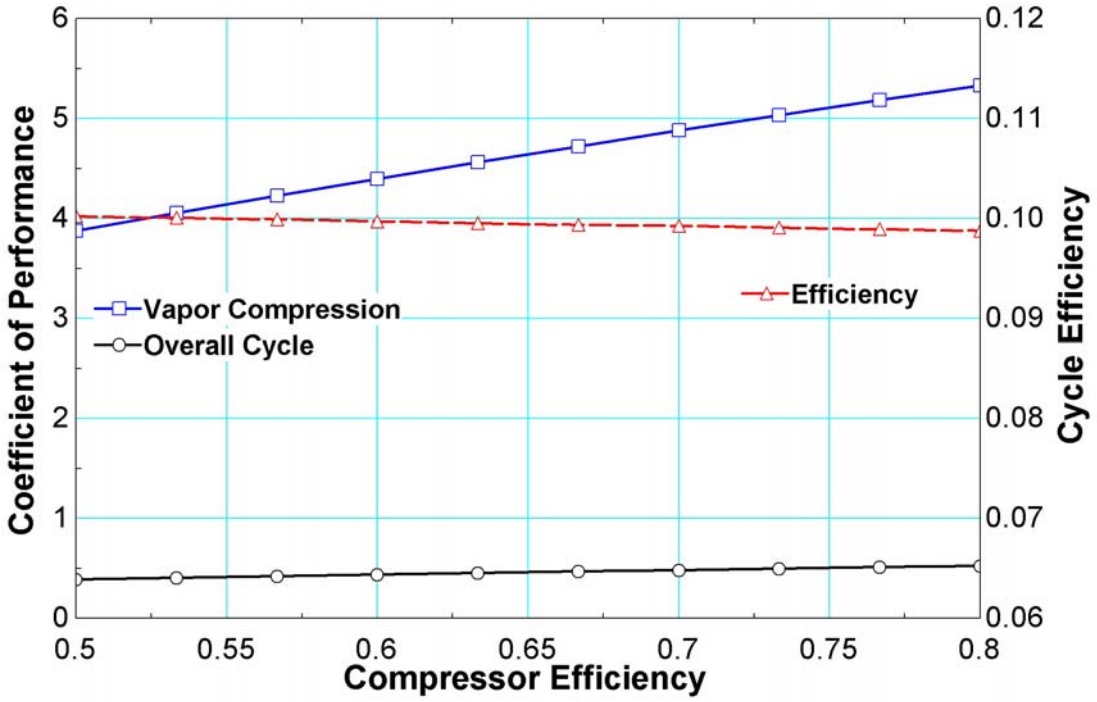

Fig. 74. Effect of Compressor Efficiency on Cycle Performance.

6.4 COMPONENT AIR FLOW RATES

The final parametric analyses for the Rankine/vapor-compression cycle consider the effects of air flow rates through the evaporator and condenser. These flow rates play an important part in establishing the cycle heat sources and sinks and determining the respective loads on each component. Practical ranges for the air flow rate in each component are considered separately.

Heat Rejection Coolant Flow Rate

The condenser connects the two loops in the Rankine/vapor-compression cycle, and is thus a critical component. The effects of a variation in condenser air flow rate from 4.25 m^3/s to 15.10 m^3/s on cycle performance are shown in Fig. 75. As the coolant

flow rate increases, the heat rejection capability of the cycle increases. This in turn improves the evaporator performance, the cooling load, and the cooling cycle *COP*. Thus, the vapor-compression *COP* increases from 4.26 to 4.80 (12.7% increase) as the condenser air flow rate increases from 4.25 m^3/s to 15.10 m^3/s. Similarly the increased heat rejection increases the Rankine cycle efficiency from 8.9% to 9.9% (11.2% increase). Together they raise the overall *COP* from 0.393 to 0.491 (24.9% increase).

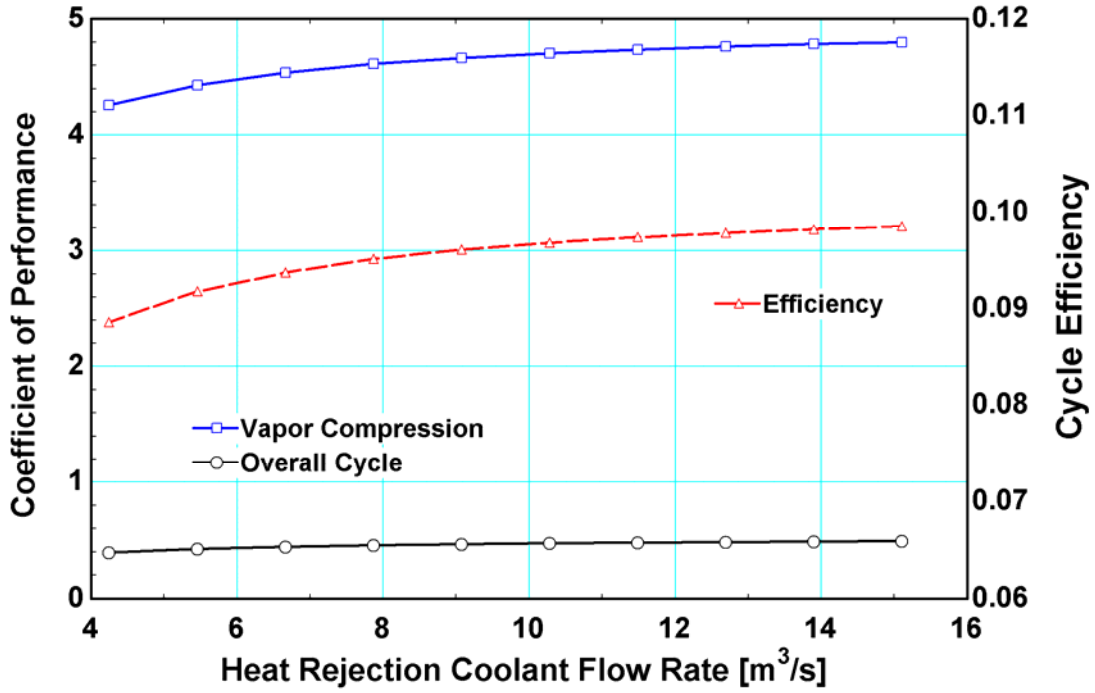

Fig. 75. Effect of Heat Rejection Coolant Flow Rate on Cycle Performance.

Conditioned Air Flow Rate

The effects of changing the conditioned air flow rate from 0.59 m^3/s to 2.36 m^3/s are shown in Fig. 76. As the conditioned air flow rate increases, the cooling load in the evaporator increases. This increases the vapor-compression COP from 4.095 to 4.917 (20.1%). However, it should be noted that cooling duty or cooling *COP* alone are not complete measures of cooling efficacy. As the conditioned air flow rate increases, even though the cooling duty increases, the delivered air temperature can increase, decreasing

comfort. For example, in this case, as the evaporator air flow rate increases from 0.59 m^3/s to 2.36 m^3/s, the cooling load increases from 20.58 to 24.43 kW, but the delivered air temperature increases from 8.18 to 16.52°C. Also, conditioned air flow rates must not be increased to very high levels, because this would lead to excessive noise in the conditioned space. Conditioned air flow rate variation does not affect the other outputs of the cycle appreciably. Thus, the Rankine efficiency shows only a slight decrease, from 9.6% to 9.5%. The overall COP increases from 0.4094 to 0.4876 (19.1% increase) over this range of air flow rates.

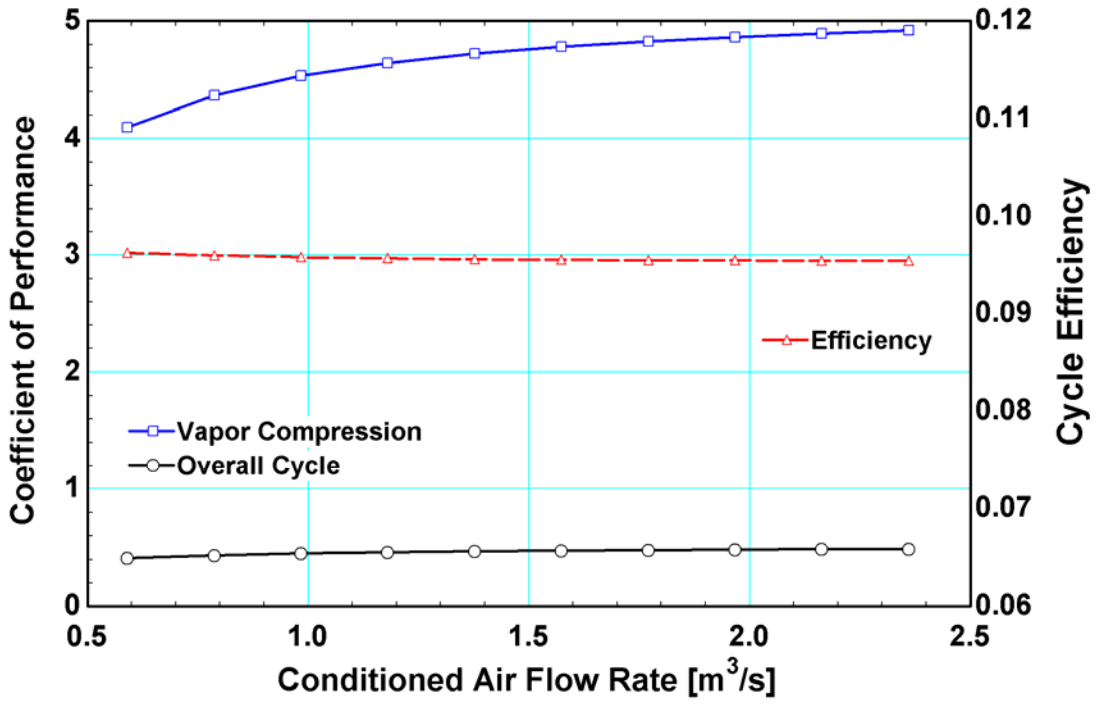

Fig. 76. Effect of Conditioned Air Flow Rate on Cycle Performance.

CHAPTER SEVEN: ASSESSMENT AND CONCLUSIONS

Two thermodynamic cycles were investigated in this study: the Cascade Absorption/Vapor-Compression (CAVC) cycle and the Organic Rankine/Vapor-Compression (ORVC) cycle. The CAVC cycle is a novel cycle designed to provide low-temperature cooling by utilizing an available heat source and environmentally benign working fluids. The ORVC cycle has been described in previous work [5, 17] and is reconsidered in this study with a modern organic working fluid. A thermodynamic model of each cycle was developed to evaluate the cycle performance under varying operating conditions. Model predictions were computed through mass, species and energy conservation equations for each component in the two cycles. The heat exchange components of each cycle were sized with a *UA* based on baseline conditions; this value was fixed during parametric analyses of operating conditions to ensure a realistic assessment of a system subjected to operational variations. Results of the thermodynamic analyses of each cycle are discussed here, followed by an assessment of each cycle within the context of available heat-driven cycles.

7.1 SUMMARY OF CAVC CYCLE PERFORMANCE MODELING

The CAVC cycle utilizes a heat source with temperatures as low as 175°C to provide cooling at a temperature of -40°C. The cycle uses only environmentally benign fluids to achieve this purpose: water-lithium bromide (H_2O-LiBr) and carbon dioxide (CO_2). Other available absorption cycles would need to use the ammonia-water (NH_3-H_2O) working pair to reach cooling temperatures below 0°C. By cascading heat transfer between the H_2O-LiBr absorption cycle and CO_2 vapor-compression cycle, the CAVC

cycle is able to provide low temperature cooling temperatures with benign working fluids, while maintaining an overall cycle performance comparable to that of the traditional single-stage absorption cycle. The CAVC cycle could be used in many sensitive applications were low cooling temperatures are needed but toxic or caustic chemicals are not allowable. One such application is a naval ship which requires low-temperature, high-heat-flux cooling over large surface areas for on-board electronics. In this application, the CAVC cycle could also provide space conditioning and water heating for the ship, without any additional fuel requirement.

The baseline CAVC system configuration was modeled under the operating conditions of the naval ship application. Approximately 200 MW of exhaust heat at temperatures of 175-275°C would be available from the gas turbines of the ship. The naval ship application has the significant advantage of proximity to an excellent heat sink: the ocean. Ocean temperatures of 25-40°C were used to simulate conditions from the coasts near New England to the Middle East. An exhaust temperature of 250°C and a seawater temperature of 35°C were used for baseline performance calculations. In the baseline configuration, 51 MW of electronics cooling would be provided at -40°C, along with 82 MW of space conditioning cooling at 5°C. The overall *COP* of the cycle is predicted to be 0.594, with an absorption cycle COP of 0.78 and a vapor-compression *COP* of 2.17. The absorption cycle *COP* is very good for a single-stage H_2O-LiBr cycle due to the heat sink being seawater. The vapor-compression *COP* is excellent for a CO_2 cycle, due to the 5°C heat sink provided to the cycle by the absorption cycle. This low temperature heat sink allows the CO_2 vapor-compression cycle to operate in subcritical conditions, rather than the usual supercritical conditions for this cycle. The compressor

of the vapor-compression loop requires 23 MW of electricity input, which is essentially the only energy cost of the system.

Parametric analyses were conducted on the heat rejection temperature, exhaust heat temperature, compressor power input, and H_2O-LiBr solution flow rate of the CAVC cycle. The baseline operating conditions and calculated component *UA*s were held constant as each parameter was varied individually. As the heat rejection temperature rises from 25°C to 40°C, the overall *COP* of the cycle decreases from 0.64 to 0.57. This decreased cycle performance is caused by a decreased ability to reject heat, which reduces the amount of exhaust heat energy absorbed by the cycle. As exhaust heat temperature rises from 175°C to 275°C, the overall *COP* increases from 0.53 to 0.61. The increased performance is due to increased refrigerant generation in the desorber, which allows increased heat duties in the evaporators. The compressor power input was varied from 17 to 48 MW, which resulted in a decrease in overall *COP* from 0.64 to 0.46. As compressor power increases, a larger portion of the heat duty is transferred in the low-temperature evaporator than in the medium-temperature evaporator, with associated penalties in overall cycle performance. Finally, as the H_2O-LiBr solution flow rate increases from 350 kg/s to 1300 kg/s, the overall *COP* peaks at 0.61 when the flow rate is set to 450 kg/s. The solution flow rate influences the amount of water vapor generated in the desorber, which affects overall cycle performance. Through the parametric analyses, crystallization risks were identified as both the exhaust heat temperature and H_2O-LiBr solution flow rate varied, which limits these parameters to <250°C and >700 kg/s, respectively.

The performance of the CAVC cycle is also affected by the configuration of the coupling loop that absorbs heat from the CAVC absorber and condenser and rejects it to the sea water. The baseline configuration for the heat rejection coupling loop is a series flow with the absorber being cooled before the condenser. Two additional configurations were considered: (1) a series flow with the condenser cooled first and (2) a parallel flow with half the coupling fluid flow cooling each component. The overall performance impact of the coupling loop configuration is small. The overall *COP* of the baseline, absorber-to-condenser series configuration is 0.594. The overall *COP* of the condenser-to-absorber series configuration is 0.599, and the overall *COP* of the parallel configuration is 0.595. The parallel configuration COP could possibly be improved by resizing the condenser and absorber *UA*s for half the cooling flow. The condenser-to-absorber configuration provides slightly improved cooling capacity, increasing the low-temperature cooling duty by 0.2 MW and the medium-temperature duty by 1.3 MW.

In applications where high temperature heat sources are available, a double-effect configuration of the absorption loop of the CAVC cycle increases overall cycle cooling capacity and total-energy-input-based cycle performance. A baseline model was developed for the double-effect CAVC cycle, utilizing an exhaust heat temperature of 300°C. As in the baseline single-effect CAVC model, a seawater heat rejection temperature of 35°C and a low cooling temperature of -40°C were used for baseline double-effect performance calculations. In this baseline configuration, 89 MW of electronics cooling would be provided at -40°C, along with 143 MW of space conditioning cooling at 5°C. These cooling capacities are nearly twice as large as the single-effect cooling capacities. However, a similar increase in HX heat transfer surface

area is required to provide the increase capacities. The compressor power required (41 MW) is also nearly twice as much as the single-effect compressor load. The overall *COP* of this baseline double-effect CAVC cycle is 0.96, with an absorption cycle COP of 1.37 and a vapor-compression *COP* of 2.17.

Parametric analyses were conducted on exhaust heat temperature. The baseline operating conditions and calculated component *UA*s were held constant as each parameter was varied individually. As exhaust heat temperature rises from 275°C to 300°C, with a fixed total solution mass flow rate of 1121 kg/s, the overall *COP* remains constant at 0.96. Crystallization issues occur at temperatures higher than 300°C when the solution mass flow rate is held constant. A flow rate control system would be required to maintain LiBr concentrations ≤65.0%. With maximum LiBr concentration set to 65.0%, the exhaust heat temperature was raised from 300°C to 400°C and the corresponding overall COP decreased from 0.95 to 0.76. The decreased performance is due to the increased total solution mass flow rate required to maintain LiBr concentrations, while the increase in total H_2O refrigerant flow rate is relatively small. In addition, the desorber temperatures increase, while the decrease in evaporator temperatures is relatively small. Therefore, the increase in exhaust heat input load is much greater than the corresponding increase in cooling capacity, leading to lower *COP* values.

Lastly, the CAVC cycle performance is compared to the performance of a cycle likely to be used in similar applications: a two-stage vapor-compression cycle. The two-stage vapor-compression cycle could also provide low temperature cooling with benign working fluids. However, the cascade cycle clearly outperforms an equivalent two-stage vapor-compression cycle over the range of operating conditions investigated. With 52.7

MW of compressor input power, the cascade cycle used completely for -40°C cooling provides 111.5 MW cooling at a heat rejection temperature of 30°C and 95.4 MW cooling at 40°C. The two-stage cycle requires 75 MW of compressor power input at 30°C and 76 MW at 40°C to provide the same cooling capacities. The cascade cycle savings in electricity demand compared to the two-stage cycle rises from 22 MW at 30.00°C to 23 MW at 40.00°C. Therefore, when a source of waste heat is available, the CAVC cycle is preferable to the two-stage vapor-compression cycle.

The analyses of the novel CAVC discussed above have shown the potential for this cascaded heat-driven cooling system. If waste heat input is considered "free" energy and not included as an input in the COP calculation, the overall COP of the cycle is as high as 8. Compared to an equivalent vapor-compression system, which could not utilize such waste heat sources, the cascaded absorption/vapor-compression cycle avoids up to 31% electricity demand. In addition, the natural refrigerants used in this cycle make it an excellent candidate for sensitive applications where traditional absorption cycles could not be used. The critical challenge of this system is the development of the H_2O evaporator/CO_2 condenser component that couples the absorption and vapor-compression loops. The large pressure differential in this component and the simultaneous processes of evaporation and condensation across small temperature differences will require careful and specialized component design.

7.2 SUMMARY OF COUPLED ORVC CYCLE PERFORMANCE MODELING

The ORVC cycle has been considered for use on military vehicles [5] to provide space-conditioning from the waste heat from the engine and by Wang et al. [58] as an alternative to portable battery-powered vapor-compression systems. The refrigerants of the military vehicle prototype and the Wang et al. cycle model were R-11 and isopentane, respectively. Performance data are not available for the military vehicle prototype. The Wang et al. model aimed to capitalize on the energy density of hydrocarbon fuel to replace heavy batteries; therefore, the model utilized heat source temperatures that were unusually high for organic Rankine cycle operation. Therefore, no performance data are available on the ORVC cycle that accurately characterize its potential as a heat-driven cooling system for low-grade heat recovery. (Much of the literature on organic Rankine cycles is only for power generation applications, and not for the turbo-compressor driven cooling cycles.) The cycle was reconsidered here under typical heat recovery operating conditions, using a refrigerant well-suited to the application.

The baseline ORVC system utilizes a waste heat temperature of 125°C to provide cooled air at 13.66°C from a conditioned return air temperature of 26.67°C. The baseline ambient temperature is 35°C. The ambient and conditioned return air temperatures are determined by Air-conditioning and Refrigeration Institute (ARI) standards. Under these conditions, the coupled Rankine/vapor-compression cycle yields 23.14 kW of cooling with an overall *COP* of 0.46. The baseline *COP* of the vapor-compression loop is 4.64, while the efficiency of the Rankine loop is 9.56%.

Parametric analyses were conducted on the waste heat source temperature, heat rejection temperature, turbo-compressor efficiencies, and ambient and conditioned air

flow rates of the ORVC cycle. The baseline operating conditions and calculated component *UA*s were held constant as each parameter was varied individually. As the waste heat source temperature increases from 80°C to 170°C, the overall *COP* of the cycle increases from 0.2 to 0.57 due to the higher availability energy input to the cycle. As the heat rejection temperature increases from 20°C to 40°C, the overall *COP* decreases from 0.68 to 0.40. This decrease in cycle performance is due to the decreased ability to reject heat. The turbine efficiency was varied from 80% to 95%, resulting in an increase in overall *COP* from 0.43 to 0.48. The compressor efficiency was varied from 50% to 80%, resulting in an overall *COP* increase from 0.39 to 0.53. As the heat rejection air flow rate through the condenser increases from 4.25 m^3/s to 15.1 m^3/s, the overall *COP* increases from 0.393 to 0.491 due to the increased heat rejection capability. As the conditioned air flow rate increases from 0.59 m^3/s to 2.36 m^3/s, the overall COP rises from 0.41 to 0.49. However, *COP* is not the only measure of cycle performance and it is important to note that the delivered air temperature increases from 8.18 to 16.52°C as conditioned air flow rate rises.

The analysis of the ORVC cycle conducted here does not compare favorably to the Wang et al. study [17], which predicted an overall COP of 0.96 to 1.3 for this cycle. Wang et al. considered high boiler operating temperatures, from 116°C to 227°C, and a compressor efficiency of 0.9. These high temperatures from direct fuel-fired sources rather than waste heat, and high compressor efficiency account for some of the *COP* difference. Documentation of the achievement of such high compressor efficiencies in actual practice is not available in the literature at this time. In addition, Wang et al. used a regenerator to enable the superheated temperature boost in the boiler, which adds

considerably to the cycle performance and represents a considerable departure from waste-heat driven systems. However, for the cycle without the regenerator, Wang et al. predict a COP of 0.83 at a boiler operating temperature of 116°C. At the same boiler operating temperature (which corresponds to a 150°C waste heat source temperature) and the same compressor efficiency, the model described here predicts a *COP* of 0.67. The reasons for this discrepancy are not clear, but could be attributed to different working fluids and/or modeling methods. For example, Wang et al. does not clearly describe the accounting of temperature differences between the external fluids and the working fluid, while the model discussed here accounts for these realistic penalties using a *UA-LMTD* approach.

The ORVC cycle requires one more heat exchanger (the boiler) than a conventional vapor-compression cycle, and it may provide an alternative to absorption systems .An ammonia-water absorption cycle operating under similar conditions to those discussed here provides a nominal COP of 0.63 [4]. The performance of the ORVC cycle is expected to be lower, but this deficiency could be overcome by the ability to recover low-temperature waste heat and the minimal number of required components. However, the cycle does require a turbo-compressor. Though turbo-compressor technology is the subject of development efforts, the expansion and compression efficiencies of the component, size, and mechanical reliability will probably prove to be the critical challenges.

7.3 ASSESSMENT OF ORVC AND CAVC POTENTIAL IN CONTEXT OF AVAILABLE HEAT DRIVEN CYCLES

The heat-driven cycles discussed in Chapters One and Two are revisited here to provide context and an assessment of the potential use for the CAVC and ORVC cycles. An overview of key cycle characteristics is presented in Table 13 and Table 14. The values listed for each cycle are taken from the literature discussed in Chapters One and Two. These values are used throughout this section for comparative purposes, though they may not be wholly representative of the entire range of values available for a given system configuration.

The main benefit of the CAVC cycles is shown in Fig. 77, which depicts the input heat source temperature (or desorber temperature) and the cooling temperature (or evaporator temperature) of each cycle and lists the associated *COP*s. Lighter shaded regions represent a range of input and/or cooling temperatures, with the corresponding COP range from the lower input heat source temperature to the higher temperature. Cooling temperatures of -40°C are achieved by only three cycles considered here: the CAVC cycle, the double-effect CAVC cycle, and the vapor-exchange (VX) generator/absorber heat exchange (GAX) cycle. When high exhaust heat temperatures are available, the double-effect CAVC provides the highest cycle performance. The higher *COP* of the VX GAX cycle (0.66) compared to the single-effect CAVC cycle (0.53-0.61), could be negated by the increased complexity and the NH_3-H_2O working pair of the VX GAX cycle. The complexity of the cycles considered and the effects of working fluid are further discussed later in this section. In addition, the single-effect CAVC cycle is driven by a lower temperature heat source than the VX GAX cycle

(175°C compared to 215°C). When high heat source temperatures are not available, the clear choice for low-temperature cooling would be the single-effect CAVC cycle.

A major benefit of the ORVC cycle is to utilize low-temperature waste heat. However, Fig. 77 shows that several cycles utilize temperatures as low or lower than the ORVC cycle, with comparable or better cycle performance. The half-effect absorption cycle in particular utilizes a lower temperature (75°C compared to 80°C) to provide a lower cooling temperature (5°C compared to 13.66°C) with a higher COP (0.37 compared to 0.20). Also, these results are for a H_2O-LiBr half-effect cycle; both cycles use environmentally benign working fluids. The primary advantage of the ORVC may be the reduced complexity of the system. However, as discussed later, this advantage is diminished by the importance of a complex mechanical component, the turbo-compressor, and its efficiency in the ORVC cycle performance.

Table 13. Heat-Driven Thermodynamic Cycles Summary – Part 1.

Cycle	Working Fluid	Input Temperature Range*	Heat Rejection / Chilled Water Temperatures	COP	Sources
Open Dehumidifier-Evaporator-Regenerator [OPEN]	H_2O/LiBr	57.2°C	29.4°C / 7.2°C	0.43	Hellmann & Grossman, 1995 [13]
	H_2O/LiCl	65°C	29.5°C / 14.7°C	0.73	Gommed & Grossman, 2007 [31,32]
Half-Effect (Double-Lift) [1/2 E]	H_2O/LiBr	75 - 87°C	40°C / 5°C	0.37 - 0.38	Ma & Deng, 1996 [34]
	NH_3/H_2O	76°C	19°C / -17°C	0.306	Erickson, 1995 [33]
One-Stage, Single-Effect [1S, 1E]	H_2O/LiBr	100 - 120°C	25°C / 3.7°C	0.72 - 0.71	Herold et al., 1996 [5]
	NH_3/H_2O	150°C	40.0°C / -10.0°C	0.549	
Two-Stage, Double-Effect [2S, 2E]	H_2O/LiBr	150°C	87.73°C & 29.72°C / 5.13°C	1.325	Herold et al., 1996 [5]
	NH_3/H_2O	199.5°C †	40.0°C / -10.0°C ‡	0.74	
Two-Stage, Triple-Effect [2S, 3E]	NH_3/H_2O	218.7°C †	33°C / 2°C ‡	1.41	DeVault & Marsala, 1990 [41]
	H_2O/LiBr & NH_3/H_2O	182°C †	35°C / 4°C ‡	1.7	Herold et al., 1996 [5]
	NH_3/H_2O	182°C †	35°C / 4°C ‡	1.5	Ivester & Shelton, 1994 [40]
Three-Stage, Triple-Effect [3S, 3E]	H_2O/LiBr	149 - 260°C	35°C / 5°C	1.5-1.7	Grossman et al., 1994 [12]
	H_2O/LiBr	180°C †	30°C / 5°C ‡	1.645	Herold et al., 1996 [5]
Cascade Absorption/Vapor-Compression [CAVC]	H_2O/LiBr & CO_2	175 - 275°C	35°C / -40°C	0.53 - 0.61	
Double-Effect CAVC [2E CAVC]	H_2O/LiBr & CO_2	275 - 400°C	35°C / -40°C	0.96 - 0.76	
Generator/Absorber Heat Exchange [GAX]	NH3/H2O	174 - 230°C	42.2°C / 10°C	0.75 - 1.05	Engler et al., 1997 [16]
Branched GAX [Br GAX]	NH_3/H_2O	195°C	42.2°C / 10°C	1.08	Engler et al., 1997 [16]
Vapor Exchange GAX [VX GAX]	NH_3/H_2O	215°C	30°C / -40°C	0.66	Rane & Erickson, 1994 [48]
	NH_3/H_2O	215°C	33°C / 3°C	1.88	
Organic Rankine/Vapor-Compression [ORVC]	R245fa	80-170°C	35°C / 13.66°C	0.20-0.57	
	Isopentane	116-227°C †	40°C / 7°C ‡	0.96-1.3	Wang et al., 2004 [17]

† Input Temperature was not specified; desorber outlet temperature is given instead.

‡ Heat Rejection / Chilled Water Temperature was not specified; the condenser / evaporator temperature is given instead.

Table 14. Heat-Driven Thermodynamic Cycles Summary – Part 2.

Cycle	Number of Components **	Advantages	Disadvantages	Critical Components	Sources
Open Dehumidifier-Evaporator-Regenerator [OPEN]	6 (A,D,E,3HX)	Utilize low temperature heat sources	Humidity/Cooling Tradeoffs, Low Lift	Dehumidifier, Regenerator	[13]
	5 (A,D,3HX)				[31,32]
Half-Effect (Double-Lift) [1/2 E]	8 (2A,2D,C,E,2HX)	Utilize low temperature heat sources	Low COP, Complexity		[34]
					[33]
One-Stage, Single-Effect [1S, 1E]	5 (A,D,C,E,HX)				[5]
	6 (A,D,R,C,E,HX)				
Two-Stage, Double-Effect [2S, 2E]	8 (A,2D,2C,E,2HX)	High COP	Requires high temperature heat sources, Complexity		[5]
	12 (2A,2D,3R,C,E,3HX)				
Two-Stage, Triple-Effect [2S, 3E]	10 (2A,2D,2R,2C,2E)	High COP, Triple-effect for NH_3/H_2O	Requires optimized interal heat exchange, Complexity	Internal Heat Exchangers	[41]
	11 (2A,2D,2R,2C,E,2HX)				[5]
	14 (2A,2D,2R,2C,2E,4HX)				[40]
Three-Stage, Triple-Effect [3S, 3E]	11 (A,3D,3C,E,3HX)	Increased COP	Req. high temp. sources, Complexity, Corrosion		[12]
	11 (A,3D,3C,E,3HX)				[5]
Cascade Absorption/Vapor-Compression [CAVC]	9 (A,D,C,2E,2HX,EC,CO)	High Lift, Avoid NH_3/H_2O	Complexity	H_2O Evaporator/ CO_2 Condenser	
Double-Effect CAVC [2E CAVC]	11 (A,D,C,2E,3HX,EC,DE,CO)	High COP, High Lift, Avoid NH_3/H_2O	Complexity	H_2O Evaporator/ CO_2 Condenser	
Generator/Absorber Heat Exchange [GAX]	6 (A,D,R,C,E,HX)	High COP	Requires high temperature heat sources	Generator/Absorber Heat Exchanger	[16]
Branched GAX [Br GAX]	6 (A,D,R,C,E,HX)	High COP	Req. high temp. sources	Gen/Abs HX	[16]
Vapor Exchange GAX [VX GAX]	13 (2A,2D,2R,C,E,5HX)	High COP, High Lift	Req. high temp. sources, Complexity	Internal Heat Exchangers	[48]
	13 (2A,2D,2R,C,E,5HX)				
Organic Rankine/Vapor-Compression [ORVC]	4 (B,C,E,TC)	Utilize low temperature heat sources	Low COP	Turbo-Compressor	
	5 (B,C,E,RHX,TC)				[17]

* Cycle Component Codes: A - Absorber, D - Desorber, B - Boiler, R - Rectifier, C - Condenser, E - Evaporator, HX - Recuperative Heat Exchanger, EC - Evaporator/Condenser, DE - Desorber/Condenser, CO - Compressor, TC - Turbo-Compressor

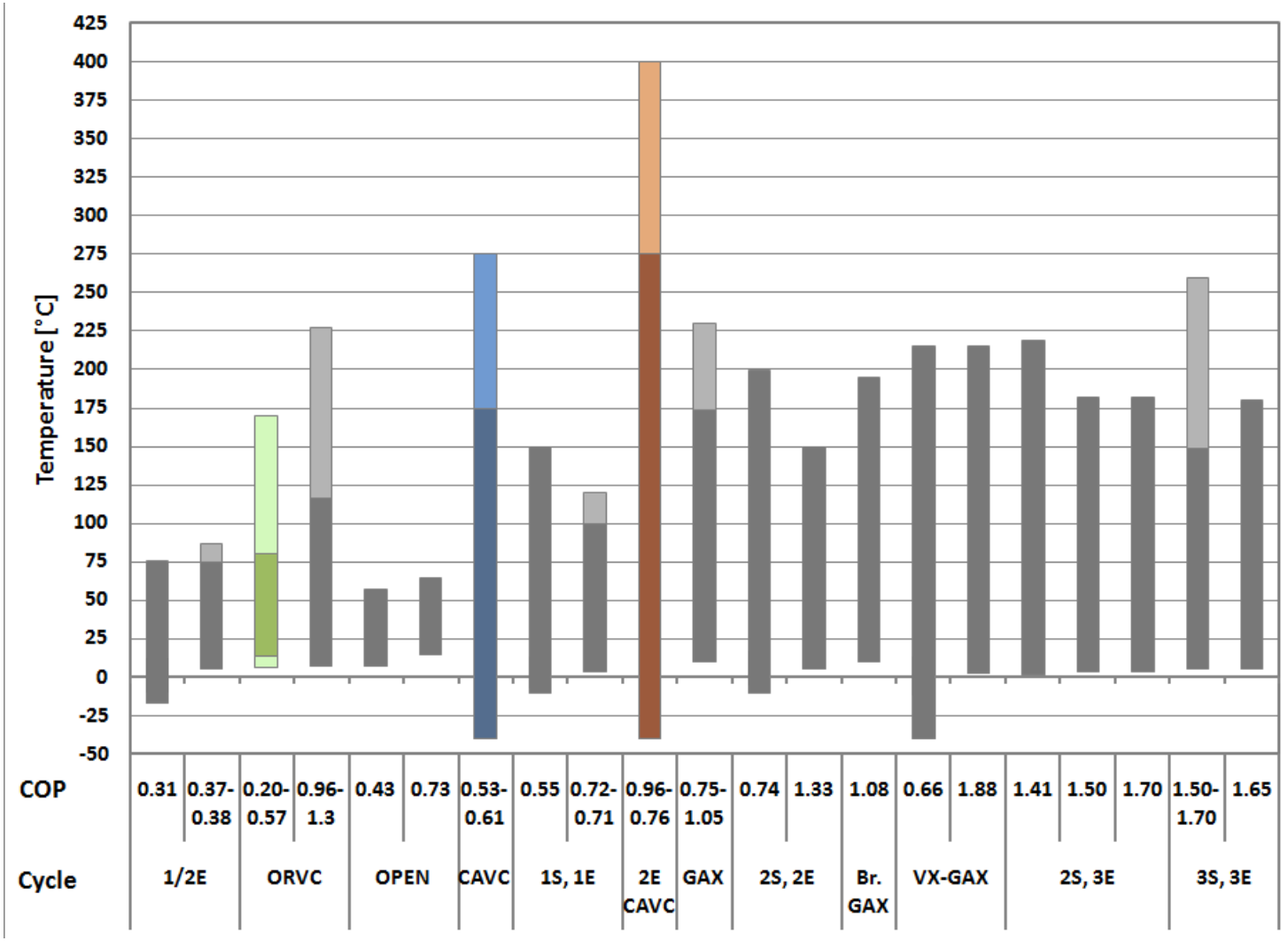

Fig. 77. Heat-Driven Cycle Input and Cooling Temperatures and COP. Multiple COP values and temperatures for each cycle correspond to the various results found in the literature and tabulated in Tables 12 and 13.

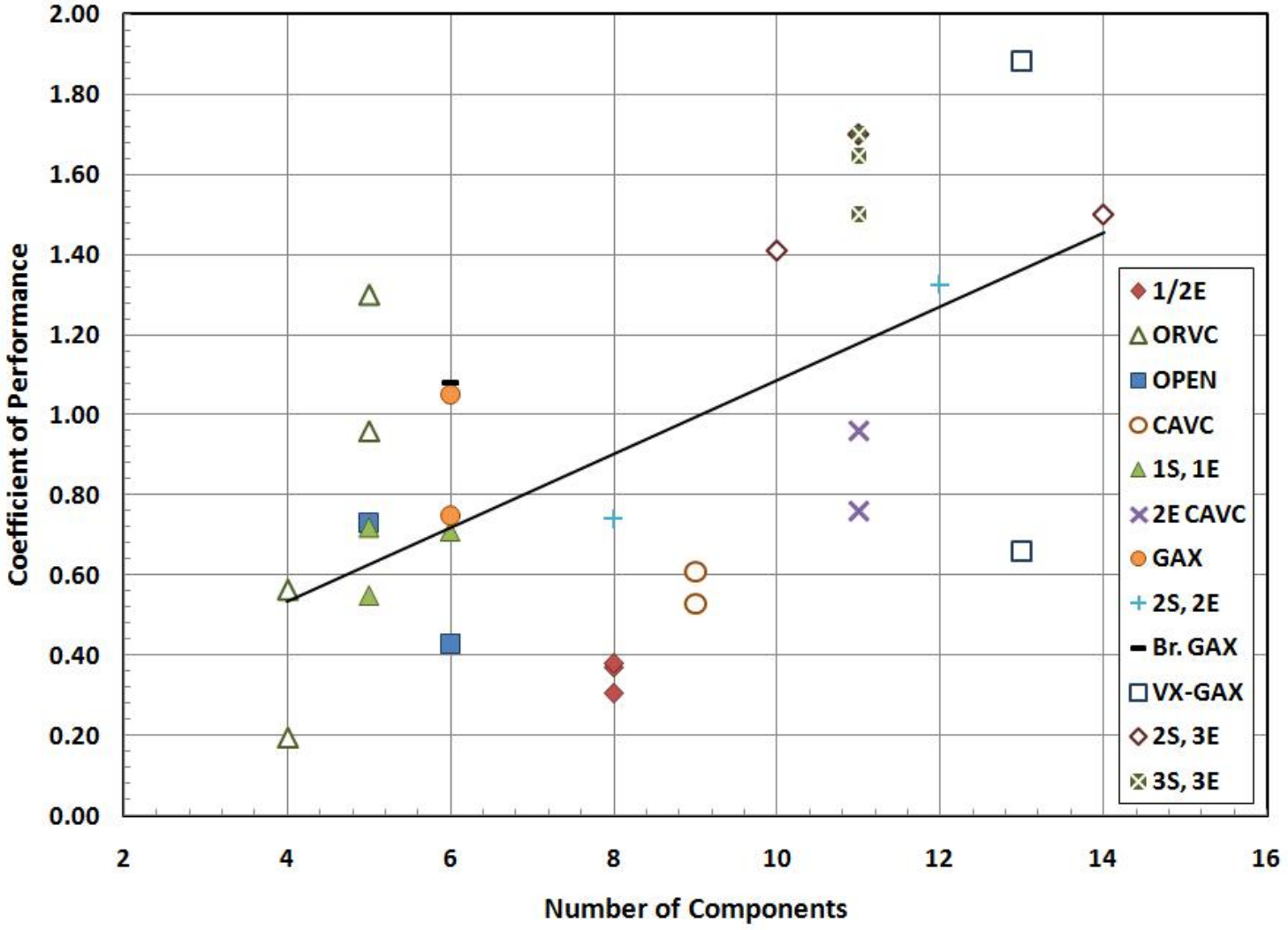

Fig. 78. Heat-Driven Cycle Performance as a function of complexity.

Fig. 78 illustrates the approximate relationship between cycle performance and COP. Generally, increased cycle complexity is associated with increased cycle performance; otherwise, the additional complexity may not be justified. The measure of complexity used in this figure is the number of major components required by the cycle: absorbers, desorbers, boilers, rectifiers, condensers, evaporators, heat exchangers, compressors, and turbo-compressors. This simple measure of complexity yields a surprisingly accurate depiction. For example, the ratio of performance to complexity of the low-temperature heat source ORVC cycle is shown in Fig. 78 as average or below average, despite only requiring four components. This depiction is consistent with the fact that one of the four required components in the ORVC cycle is a turbo-compressor, which increases cycle complexity more than other single components such as heat exchangers. However, the high-temperature heat source ORVC cycle is above average, because the increased cycle performance outweighs the complexity of the turbo-compressor. Likewise, the GAX cycles and the two-stage, triple-effect cycle, which were specifically developed to provide increased cycle performance, are above average despite the relatively high number of components. As discussed in the previous paragraph, cycle complexity can determine the appropriate use of cycles that are similar in performance, such as the single-effect CAVC and VX GAX cycles or the ORVC and half-effect cycle. Although the CAVC cycle is below average by this measure, the equivalent VX GAX cycle is even worse. Both cycles are likely to require sophisticated control of flow rates; therefore, the greater number of components required by the VX GAX cycle may be the largest difference in complexity. The ORVC cycle has the advantage in complexity over the half-effect cycle. However, in low-temperature heat source applications (80°C

ORVC, 75°C half-effect), the poor ORVC cycle performance is likely to outweigh its reduced complexity. If warmer heat source temperatures (170°C) are available and medium temperature cooling (13.66°C) is required, the reduced complexity may justify the decrease in cycle performance. Also, the lower number of components makes for a much more compact system, more suitable for small applications like residences.

The final cycle characteristic considered here is the cycle working fluid. The CAVC and ORVC cycles have been studied here in part due to their ability to use environmentally benign working fluids. As discussed in Chapter One, the working fluids considered in these cycles (H_2O-LiBr, CO_2 and R245fa) are non-toxic and have minimal adverse effect on the environment. The toxic nature of the NH_3–H_2O working pair has been addressed. Isopentane is also a dangerous chemical that is explosive when mixed with air and causes severe irritation upon exposure. Environmental considerations may be crucial in sensitive applications, such as the naval ship example for the CAVC cycle. Even in non-sensitive applications, the effects of system operation on the environment at large should be considered. The choice of working pair comes with several conditions apart from the environmental concerns. The H_2O-LiBr requires subatmospheric operating pressures and is limited by the freezing point of water. Care must be taken to avoid crystallization conditions and the introduction of air into the system. On the other hand, the NH_3–H_2O working pair is corrosive and therefore necessitates the use of steel tubing and components. Rectification is required in NH_3–H_2O systems to remove water vapor from the ammonia vapor stream exiting the desorber. Even with rectification, performance penalties occur as the small amount of water remaining in the vapor stream condenses and accumulates in the evaporator. These considerations affect the choice of

an appropriate system for a particular application. Here, the CAVC may gain another advantage over the VX GAX cycle, which must use the NH_3–H_2O working pair to provide low-temperature cooling. The ORVC cycle gains no edge over the single-stage cycle, as they both utilize environmentally benign working fluids.

The potential of the two cycles analyzed in this work relies on an available source of waste heat. Unless the ratio of electricity prices to primary fuel prices becomes very large, burning primary energy to operate these cycles will not be economically viable. In addition, the CAVC cycle must be liquid-cooled, to avoid crystallization as discussed in Chapter 2. Therefore, a readily available liquid heat sink at ambient temperatures, such as the ocean, increases the practicality of the system. The ORVC can be air-cooled, eliminating the need for hydronic loops and the associated equipment. This lowers initial costs and may make up for the lower level of performance when compared to the single-stage cycle, especially in situations where a heat source is freely available and air-conditioning is needed.

7.4 RECOMMENDATIONS

Several modifications can be made to increase the predicted performance of the Rankine- and absorption-based cycles. In the Rankine-based case, an improvement to the cycle has already been discussed in Section 2.2.2. Wang et al predicted a higher COP (0.96) by using isopentane as a refrigerant and adding a regenerator. The volatile and flammable nature of isopentane makes it an environmentally undesirable refrigerant, but some improvement may be seen by adding the regenerator to the R245fa cycle discussed here. The potential for improvement is greater in the absorption-based case by incorporating

more sophisticated controls in the double-effect absorption topping cycle and improving the vapor-compression bottoming cycle.

7.4.1 Crystallization Controls in Double-Effect Absorption Cycle

The cascaded absorption/vapor-compression cycle modeling effort thus far has pointed to the potential for high COPs across the range of operating conditions. The baseline double-effect CAVC model and exhaust heat temperature parametric analysis have shown that the double-effect absorption loop significantly improves cycle performance when high exhaust heat temperatures are available. However, the double-effect cycle performance is limited by crystallization issues. A variable total solution flow rate was introduced to avoid crystallization limits in this investigation, which resulted in decreased cycle performance as exhaust heat temperature increased. It is possible that other methods of crystallization control could yield higher *COP*s and further investigations should identify other potentially effective control methods.

7.4.2 Enhancements to CO_2 Vapor Compression Cycle

It was noted that the CO_2 exiting the expansion valve is at a quality of about 32% at the baseline conditions. This implies that only 68% of the available heat of evaporation is being used for providing low temperature cooling. This figure can be improved considerably by incorporating heat or work recovery devices into the cycle. Therefore the following enhancements should be investigated:

- Incorporation of a suction line heat exchanger between the evaporator outlet and the condenser outlet. This heat exchanger uses the cold evaporator outlet stream to cool the CO_2 exiting the condenser. The resulting decrease in CO_2 enthalpy results in less flashing across the expansion valve, so that the refrigerant will enter

the evaporator at a lower quality, leading to additional cooling capacity. The tradeoff is that the CO_2 enters the compressor at a higher temperature and entropy, which might lead to excessive condenser superheat. These tradeoffs should be evaluated as a function of suction line heat exchanger effectiveness.

- Another technique to recover energy internally from the cycle is to replace the expansion valve with a recovery device that extracts work from the refrigerant expanding from the condenser pressure to the evaporator pressure. This recovered work is used to offset external power requirements in the compressor, leading to improved CO_2 cycle COPs. The improvements in cycle performance due to incorporation of such a recovery device should be evaluated.

Other related cycle performance issues include the potential to use the rejected heat from the absorption cycle for water heating purposes. For the reject heat to be used effectively, the water must be at a minimum above 40°C. This water temperature can be further increased by lowering the cooling water flow rate for the absorption cycle. However, if the flow rate is decreased significantly, the absorber and condenser pressures will rise, leading to lower cycle performance. The trade-off analyses between cooling, water heating, and coolant pumping power requirements should be evaluated to find the optimal flow rates for each load requirement.

REFERENCES

1. *Annual Energy Review 2007*, Energy Information Administration, p. 221.
2. Rankine, W. J. M., 1859, *A Manual of the Steam Engine and Other Prime Movers*, Richard Griffin and Company, London and Glasgow.
3. Erickson, D. C., 1992, *Vapor Exchange Duplex Gax Absorption Cycle*, Patent 5,097,676.
4. Herold, K. E., Radermacher, R., and Klein, S. A., 1996, *Absorption Chillers and Heat Pumps*, CRC Press, Boca Raton, Florida, p. 286.
5. McDonald, J. L., 1969, *Status Report on Development of Military, Waste-Heat-Powered Environmental Control Systems*, U.S. Army Mobility Equipment Research and Development Center, Fort Belvoir, Virginia.
6. Perry, R. H., and Green, D. W., 1997, *Perry's Chemical Engineers' Handbook*, McGraw-Hill.
7. American Society of Heating, Refrigeration, and Air-Conditioning Engineers, 2006, *Ashrae Handbook - Refrigeration*.
8. Hung, T. C., Shai, T. Y., and Wang, S. K., 1997, "A Review of Organic Rankine Cycles (Orcs) for the Recovery of Low-Grade Waste Heat," *Energy*. **22**(7): pp. 661-667.
9. Christensen, R. N., and Santoso, M., 1990, "An Evaluation of a Rankine Cycle Driven Heat Pump," *Heat Recovery Systems and CHP*. **10**(2): pp. 161-175.
10. Wu, S., and Eames, I. W., 2000, "Innovations in Vapour-Absorption Cycles," *Applied Energy*. **66**(3): pp. 251-266.
11. Schweigler, C., Demmel, S., and Ziegler, F., 1999, *Single-Effect/Double-Lift Chiller: Operational Experience and Prospect*, in *International Sorption Heat Pump Conference*, C. Schweigler, et al., Editors, ZAE Bayern, Munich, Germany. p. 533-539.
12. Grossman, G., Wilk, M., and DeVault, R. C., 1994, "Simulation and Performance Analysis of Triple-Effect Absorption Cycles," *Proceedings of the ASHRAE Winter Meeting, Jan 23-26 1994*, New Orleans, LA, USA, Vol. 100, ASHRAE, Atlanta, GA, USA, pp. 452-462.
13. Hellmann, H.-M., and Grossman, G., 1995, "Simulation and Analysis of an Open-Cycle Dehumidifier-Evaporator-Regenerator (Der) Absorption Chiller for Low-Grade Heat Utilization," *International Journal of Refrigeration*. **18**(3): p. 177.
14. Garimella, S., Christensen, R. N., and Lacy, D., 1996, "Performance Evaluation of a Generator-Absorber Heat-Exchange Heat Pump," *Applied Thermal Engineering*. **16**(7): pp. 591-604.
15. Lior, N., 1977, "Solar Energy and the Steam Rankine Cycle for Driving and Assisting Heat Pumps in Heating and Cooling Modes," *Energy Conversion*. **16**(3): pp. 111-123.
16. Engler, M., Grossman, G., and Hellmann, H. M., 1997, "Comparative Simulation and Investigation of Ammonia-Water: Absorption Cycles for Heat Pump Applications," *International Journal of Refrigeration*. **20**(7): pp. 504-516.
17. Wang, H., Drost, K., and Peterson, R., 2004, "Thermodynamic Performance of a Miniature Expander/Compressor Heat-Actuated Heat Pump," *Collection of*

Technical Papers - 2nd International Energy Conversion Engineering Conference, Aug 16-19 2004, Providence, RI, United States, Vol. 3, American Institute of Aeronautics and Astronautics Inc., Reston, VA 20191, United States, pp. 1455-1461 BN - 1563477157.

18. Pacala, S., and Socolow, R., 2004, "Stabilization Wedges: Solving the Climate Problem for the Next 50 Years with Current Technologies," *Science*. **305**(5686): pp. 968-972.
19. 2008, *Energy Infocard*, Energy Information Administration (EIA), U.S. Department of Energy.
20. Hammar, T., 1999, *The Case of Chp in Denmark - and Perspectives to Other Countries*, Danish Energy Agency.
21. Bergmeier, M., 2003, "The History of Waste Energy Recovery in Germany since 1920," *Energy*. **28**(13): pp. 1359-1374.
22. Stephan, K., 1983, "History of Absorption Heat Pumps and Working Pair Developments in Europe," *International Journal of Refrigeration*. **6**(3): pp. 160-166.
23. Ziegler, F., 1999, "Recent Developments and Future Prospects of Sorption Heat Pump Systems," *International Journal of Thermal Sciences*. **38**(3): pp. 191-208.
24. Perez-Blanco, H., 1984, "Absorption Heat Pump Performance for Different Types of Solutions," *International Journal of Refrigeration*. **7**(2): pp. 115-122.
25. American Society of Heating, Refrigeration, and Air-Conditioning Engineers, 2005, *Ashrae Handbook - Fundamentals*.
26. McQuiston, F. C., Parker, J. D., and Spitler, J. D., 2000, *Heating, Ventilation, and Air Conditioning: Analysis and Design*, John Wiley & Sons, Inc., New York, NY.
27. Saleh, B., Koglbauer, G., Wendland, M., and Fischer, J., 2007, "Working Fluids for Low-Temperature Organic Rankine Cycles," *Energy*. **32**(7): pp. 1210-1221.
28. Ramaswamy, V., Boucher, O., Haigh, J., Hauglustaine, D., Haywood, J., Myhre, G., Nakajima, T., Shi, G. Y., and Solomon, S., 2001, *Radiative Forcing of Climate Change*, in *Climate Change 2001: The Scientific Basis. Contribution of Working Group I to*

the Third Assessment Report of the Intergovernmental Panel on Climate Change, J.T. Houghton, et al., Editors, Cambridge University Press, Cambridge, United Kingdom and New York, NY, USA, p. 881.

29. Honeywell, 2000, *Genetron 245fa: Applications Development Guide*.
30. Klein, S. A., 2003, *Engineering Equation Solver*, F-Chart Software.
31. Gommed, K., and Grossman, G., 2004, "A Liquid Desiccant System for Solar Cooling and Dehumidification," *Journal of Solar Energy Engineering*. **126**(3): pp. 879-885.
32. Gommed, K., and Grossman, G., 2007, "Experimental Investigation of a Liquid Desiccant System for Solar Cooling and Dehumidification," *Solar Energy*. **81**(1): pp. 131-138.
33. Erickson, D. C., 1995, "Waste-Heat-Powered Icemaker for Isolated Fishing Villages," Atlanta, GA, USA, Vol. 101, ASHRAE, pp. 1185-1188.
34. Ma, W. B., and Deng, S. M., 1996, "Theoretical Analysis of Low-Temperature Hot Source Driven Two-Stage Libr/H2o Absorption Refrigeration System," *International Journal of Refrigeration*. **19**(2): pp. 141-146.

35. Goodheart, K. A., 2000, *Low Firing Temperature Absorption Chiller System*, in *College of Engineering, Mechanical Engineering*, University of Wisconsin-Madison, Madison, WI, p. 182.
36. Burgett, L. W., Byars, M. D., and Schultz, K., 1999, "Absorption Systems: The Future, More Than a Niche?," *International Sorption Heat Pump Conference*, Munich, Germany, Lang Offsetdruck GmbH, pp. 13-24.
37. Wardono, B., and Nelson, R. M., 1996, "Simulation of a Double-Effect Libr/H2o Absorption Cooling System," *ASHRAE Journal*. **38**(10): p. 5.
38. Misra, R. D., Sahoo, P. K., and Gupta, A., 2005, "Thermoeconomic Evaluation and Optimization of a Double-Effect H 2o/Libr Vapour-Absorption Refrigeration System," *International Journal of Refrigeration*. **28**(3): pp. 331-343.
39. Alefeld, G., 1983, "Double-Effect, Triple-Effect and Quadruple-Effect Absorption Machines," *16th International Congress of Refrigeration*, Paris, Vol. 2, pp. 951-956.
40. Ivester, D. N., and Shelton, S. V., 1994, "Varying Heat Exchanger Parameters in the Triple-Effect Absorption Cycle," *Proceedings of the International Absorption Heat Pump Conference, Jan 19-21 1994*, New Orleans, LA, USA, Publ by ASME, New York, NY, USA, pp. 243-250 BN - 0-7918-0698-7.
41. DeVault, R. C., and Marsala, J., 1990, "Ammonia-Water Triple-Effect Absorption Cycle," *ASHRAE Transactions*. **96**(1): pp. 676-682.
42. Garimella, S., Lacy, D., and Stout, R. E., 1997, "Space-Conditioning Using Triple-Effect Absorption Heat Pumps," *Applied Thermal Engineering*. **17**(12): pp. 1183-1197.
43. Grossman, G., Zaltash, A., Adcock, P. W., and De Vault, R. C., 1995, "Simulating a 4-Effect Absorption Chiller," *ASHRAE Journal*. **37**(6): p. 6.
44. Ziegler, F., and Alefeld, G., 1987, "Coefficient of Performance of Multistage Absorption Cycles," *International Journal of Refrigeration*. **10**(5): pp. 285-295.
45. Altenkirch, E., and Tenckhoff, B., 1914, *Absorptionskaeltemaschine Zur Kontinuierlichen Erzeugung Von Kaelte Und Waerme Oder Acuh Von Arbeit.*, Patent 278,076.
46. Scharfe, J., Ziegler, F., and Radermacher, R., 1986, "Analysis of Advantages and Limitations of Absorber-Generator Heat Exchangeanalyse Des Avantages Et Des Limites De L'échange De Chaleur De L'absorbeur-Générateur," *International Journal of Refrigeration*. **9**(6): pp. 326-333.
47. Erickson, D. C., Anand, G., and Papar, R. A., 1996, "Branched Gax Cycle Gas Fired Heat Pump," *Energy Conversion Engineering Conference, 1996. IECEC 96. Proceedings of the 31st Intersociety*, Vol. 2, pp. 1078-1083 vol.2.
48. Rane, M. V., and Erickson, D. C., 1994, "Advanced Absorption Cycle: Vapor Exchange Gax," New York, NY, USA, Publ by ASME, pp. 25-32.
49. Prigmore, D., and Barber, R., 1975, "Cooling with the Sun's Heat Design Considerations and Test Data for a Rankine Cycle Prototype," *Solar Energy*. **17**(3): pp. 185-192.
50. Takizuka, T., Takada, S., Yan, X., Kosugiyama, S., Katanishi, S., and Kunitomi, K., 2004, "R&D on the Power Conversion System for Gas Turbine High Temperature Reactors," *Nuclear Engineering and Design*. **233**(1-3): pp. 329-346.

51. Grossman, G., and Perez-Blanco, H., 1982, "Conceptual Design and Performance Analysis of Absorption Heat Pumps for Waste Heat Utilization," *International Journal of Refrigeration*. **5**(6): pp. 361-370.
52. Vliet, G. C., Lawson, M. B., and Lithgow, R. A., 1982, "Water-Lithium Bromide Double-Effect Absorption Cooling Cycle Analysis.," *Technical and Symposium Papers Presented at the 1982 Semiannual Meeting of the American Society of Heating, Refrigerating and Air-Conditioning Engineers, Inc.*, Houston, TX, USA, Vol. 88, ASHRAE, Atlanta, Ga, USA, pp. 811-823.
53. Vliet, G. C., and Kim, J., 1983, "Modeling of Double Effect Water-Lithium Bromide Absorption Cycle.," *18th Intersociety Energy Conversion Engineering Conference: Energy for the Marketplace. Volume 4: Energy Storage & Conversion.*, Orlando, FL, USA, AIChE, New York, NY, USA, pp. 1900-1905.
54. Kaushik, S. C., Tomar, E. S., and Chandra, S., 1984, "Thermal Modelling of a Double Effect Generation Absorption Refrigeration Cycle for Solar Space Conditioning.," *Solar World Congress, Proceedings of the 8th Biennial Congress of the International Solar Energy Society.*, Perth, Aust, Vol. 1, Pergamon Press, Oxford, Engl, pp. 359-364 BN - 0-08-029947-4.
55. Maizza, V., and Maizza, A., 2001, "Unconventional Working Fluids in Organic Rankine-Cycles for Waste Energy Recovery Systems," *Applied Thermal Engineering*. **21**(3): pp. 381-390.
56. Ziegler, F., 2002, "State of the Art in Sorption Heat Pumping and Cooling Technologies," *International Journal of Refrigeration*. **25**(4): pp. 450-459.
57. Cyprus Foote Mineral, 1995, *Lithium Bromide, Technical Data, Bulletin 145*.
58. Cheung, K., Hwang, Y., Judge, J. F., Kolos, K., Singh, A., and Radermacher, R., 1996, "Performance Assessment of Multistage Absorption Cycles," *International Journal of Refrigeration*. **19**(7): pp. 473-481.